On the origins of prompt features in time-resolved laser-induced incandescence measurements of metal and carbonaceous nanoparticles

by

Stephen C. Robinson-Enebeli

A thesis

presented to the University of Waterloo

and the University of Duisburg-Essen

in fulfillment of the

thesis requirement for the degree of

Doctor of Philosophy

in

Mechanical and Mechatronics Engineering (Nanotechnology)

Waterloo, Ontario, Canada/Disuburg, NRW, Germany 2025

© Stephen C. Robinson-Enebeli 2025

Examining committee membership

The following served on the Examining committee for this thesis based on a cotutelle agreement between the University of Waterloo and the University of Duisburg-Essen. The decision of the Examining Committee is by majority vote.

External examiner	Reza Kholghy Associate Professor Department of Mechanical and Aerospace Engineering Carlton University
Supervisors	Kyle J. Daun Professor Department of Mechanical and Mechatronics Engineering University of Waterloo
	Christof Schulz Professor Department of Mechanical and Process Engineering University of Duisburg-Essen
Internal member	Sebastian Kaiser Professor Department of Mechanical and Process Engineering University of Duisburg-Essen
Internal-external member	Germán Sciani Professor Department of Chemistry University of Waterloo

Author's declaration

I hereby declare that I am the sole author of this thesis. This is a true copy of the thesis, including any required final revisions, as accepted by my examiners.

I understand that my thesis may be made electronically available to the public.

Abstract

Synthetic nanoparticles have become highly beneficial in many applications, including, for example, catalytic conversion, enhancing the functionality of electronic devices, targeted drug delivery in medicine, and purifying water through the removal of bacteria and heavy metals. Nanoparticles are often synthesized through gas-phase synthesis, where the nanoparticles are formed in a bath gas, resulting in a nanoparticle aerosol. Such aerosols are also unintentionally emitted through processes such as welding or combustion. The benefits and negative impacts of nanoaerosols significantly depend on their properties, such as particle size and concentration. Laser and optical-based characterization techniques can provide such information in an *in situ* and time-resolved manner.

Time-resolved laser-induced incandescence (TiRe-LII) is a widely used laser-based diagnostic for soot characterization and is increasingly being applied to non-carbonaceous nanoparticles. The technique involves heating nanoparticles in an aerosol to incandescent temperatures with a laser and recording their radiative emissions with a photodetector, as they cool to the temperature of the bath gas. Nanoparticle properties such as size and concentration are obtained from temporally- and spectrally-resolved measurements through inference techniques that involve regressing a TiRe-LII instrument model to the data. Accurate and reliable inference of the nanoaerosol properties relies on the robustness of the instrument model. Unfortunately, previously developed models do not fully describe experimental observations, and the reported discrepancies need to be reconciled to improve fundamental understanding, modeling capabilities, and ultimately measurements. These discrepancies include effects previously termed excessive absorption and anomalous cooling. The effect of excessive absorption is observed when the measured particle temperatures exceed the values predicted by the related model, and the anomalous cooling was related to the effect that occurred when the measured particle cooling rate, immediately following the peak-temperature phase, is faster than what is predicted based on the model.

This thesis work addresses these reported data–model discrepancies, providing insight into laser–nanoparticle interactions in the context of TiRe-LII and the impact of certain experimental conditions. In particular, it is shown that for metal nanoparticle aggregates, radiative properties are enhanced compared to isolated metal nanoparticles, and laser energy absorption becomes spatially nonuniform within aggregates. Under laser heating, the primary nanoparticle may melt; subsequently, the aggregates may partially sinter or coalesce, which further alters their radiative properties as a function of time, phenomena that do not occur in the case of soot. Furthermore, the existence of nanoparticles of different sizes within the aerosol and spatial energy variations across the irradiating laser sheet influence the data in ways that are not accounted for in current TiRe-LII instrument models. The investigations combined theoretical modeling and experimental work. The modeling utilized several light absorption models to explore the light–matter interactions between nanoaerosols and the electromagnetic field of the laser. The experimental component employed calibrated, time- and spectrally-resolved detection techniques to observe the radiative emissions from irradiated particles within the aerosol. The findings of this thesis contribute to a deeper understanding of laser–nanoparticle interactions and open new avenues for further research in this area.

Zusamenfassung

Synthetische Nanopartikel haben sich in vielen Anwendungsbereichen als äußerst nützlich erwiesen, darunter beispielsweise bei der katalytischen Umwandlung, der Verbesserung der Funktionalität elektronischer Geräte, der gezielten Verabreichung von Medikamenten in der Medizin und der Reinigung von Wasser durch die Entfernung von Bakterien und Schwermetallen. Nanopartikel werden häufig durch Gasphasensynthese hergestellt, bei der die Nanopartikel in einem Badgas gebildet werden, wodurch ein Nanopartikel-Aerosol entsteht. Solche Aerosole werden auch unbeabsichtigt durch Prozesse wie Schweißen oder Verbrennung freigesetzt. Die Vorteile und negativen Auswirkungen von Nanoaerosolen hängen in hohem Maße von ihren Eigenschaften wie Partikelgröße und Konzentration ab. Laser- und optische Charakterisierungstechniken können solche Informationen in situ und zeitaufgelöst liefern.

Die zeitaufgelöste laserinduzierte Inkandeszenz (TiRe-LII) ist ein weit verbreitetes laserbasiertes Untersuchungsverfahren zur Charakterisierung von Rußpartikeln und wird zunehmend auch für nicht-kohlenstoffbasierte Nanopartikel eingesetzt. Bei dieser Technik werden Nanopartikel in einem Aerosol mit einem Laser auf Glühtemperaturen erhitzt und ihre Strahlungsemissionen mit einem Fotodetektor aufgezeichnet, während sie auf die Temperatur des Badgases abkühlen. Nanopartikel-Eigenschaften wie Größe und Konzentration werden aus zeitlich und spektral aufgelösten Messungen durch Inferenztechniken gewonnen, bei denen ein TiRe-LII-Instrumentenmodell auf die Daten zurückgeführt wird. Eine genaue und zuverlässige Ableitung der Nanoaerosoleigenschaften hängt von der Robustheit des Instrumentenmodells ab. Leider beschreiben die bisher entwickelten Modelle die experimentellen Beobachtungen nicht vollständig, und die berichteten Diskrepanzen müssen ausgeglichen werden, um das grundlegende Verständnis, die Modellierungsfähigkeiten und letztlich die Messungen zu verbessern. Zu diesen Diskrepanzen gehören Effekte, die bisher als übermäßige Absorption und anomale Abkühlung bezeichnet wurden. Der Effekt der übermäßigen Absorption wird beobachtet, wenn die gemessenen Partikeltemperaturen die vom entsprechenden Modell vorhergesagten Werte überschreiten, und die anomale Abkühlung stand im

Zusammenhang mit dem Effekt, der auftrat, wenn die gemessene Partikelabkühlungsrate unmittelbar nach der Spitzentemperaturphase schneller war als die auf der Grundlage des Modells vorhergesagte.

Diese Doktorarbeit befasst sich mit den berichteten Diskrepanzen zwischen Daten und Modellen und liefert Erkenntnisse über die Wechselwirkungen zwischen Laser und Nanopartikeln im Zusammenhang mit TiRe-LII und den Auswirkungen bestimmter Versuchsbedingungen. Insbesondere wird gezeigt, dass bei Metallnanopartikelaggregaten die Strahlungseigenschaften im Vergleich zu isolierten Metallnanopartikeln verbessert sind und die Laserenergieabsorption innerhalb der Aggregate räumlich ungleichmäßig wird. Unter Lasererwärmung kann das primäre Nanopartikel schmelzen; anschließend können die Aggregate teilweise sintern oder koaleszieren, was ihre Strahlungseigenschaften als Funktion der Zeit weiter verändert – ein Phänomen, das bei Ruß nicht auftritt. Darüber hinaus beeinflussen das Vorhandensein von Nanopartikeln unterschiedlicher Größe innerhalb des Aerosols und räumliche Energieunterschiede über die bestrahlende Laserschicht hinweg die Daten in einer Weise, die in den aktuellen TiRe-LII-Instrumentenmodellen nicht berücksichtigt wird. Die Untersuchungen kombinierten theoretische Modellierung und experimentelle Arbeit. Die Modellierung nutzte mehrere Lichtabsorptionsmodelle, um die Licht-Materie-Wechselwirkungen zwischen Nanoaerosolen und dem elektromagnetischen Feld des Lasers zu untersuchen. Der experimentelle Teil verwendete kalibrierte, zeit- und spektralaufgelöste Detektionstechniken, um die Strahlungsemissionen von bestrahlten Partikeln innerhalb des Aerosols zu beobachten. Die Ergebnisse dieser Arbeit tragen zu einem tieferen Verständnis der Wechselwirkungen zwischen Laser und Nanopartikeln bei und eröffnen neue Wege für die weitere Forschung auf diesem Gebiet.

Acknowledgement

I appreciate the efforts invested by my supervisors, Dr. Kyle Daun and Dr. Christof Schulz, in overseeing the progress of this research. Their involvement contributed to ensuring that the work presented in this thesis, along with its overall structure and clarity, was of a high standard.

I acknowledge the contributions of my colleague and collaborator, Dr. Sina Talebi-Moghaddam, and thank him for his support and patience during the infancy period of my understanding of light-matter interactions.

I express my sincere gratitude to Dr. Erdal Alkyildiz for his steadfast and reliable support in assembling the experimental setups. His elegant solutions to experimental issues, and the speed at which he achieved them, always left me in awe and directly contributed to the success of the experiments I performed at the University of Duisburg-Essen.

I am appreciative of the help and support from all technicians and administrative personnel at both the Mechanical and Mechatronics Engineering Department at the University of Waterloo and the Institute for Energy and Materials Processes – Reactive Fluids (EMPI) at the University of Duisburg-Essen. Navigating technical issues and the administrative network was a little less frustrating with their support.

I extend recognition to all of my colleagues from both the Waterloo Laboratory for Inverse Analysis and Thermal Sciences (WatLIT) and the EMPI research groups. Numerous discussions, both formal and informal, and assistance proved to be helpful in navigating various challenges encountered during the modeling and experimentation phases of the project. Also, importantly, our shared social interactions brightened the experience of it all.

I also extend my appreciation to colleagues at the National Research Council in Ottawa, Canada and other colleagues I met at conferences, seminars, and workshops. Their discussions and input in this work added value to the outcomes in ways that extended its reach and relevance.

The financial support provided by the Natural Sciences and Engineering Research Council of Canada (NSERC), as well as the Indigenous and Black Engineering and Technology (IBET) program, is acknowledged. These funding sources facilitated the continuation of the work and supported various components of the research effort.

I am thankful for the steadfast mental and emotional support of my parents – Robinson and Irene, my brothers – Reuben, Peter and Gregory, and family and friends throughout the course of this academic pursuit.

I am deeply grateful for the overwhelming support of my wife, Hiba Natsheh. Being away from you was the hardest part of all, but you always kept me grounded and lightened all my burdens.

To

Past and present

Survivors of colonial structure

Again, and again, and again

Different faces, same vein

Ignored now

For reparations later

Recurring, over and over

Liberty and self-determination

Can start now



Table of contents

Examining committee membership ..... **ii**

Author's declaration ..... **iii**

Abstract ..... **iv**

Zusamenfassung ..... **vi**

Acknowledgement ..... **viii**

List of figures ..... **xv**

List of tables ..... **xxiii**

Nomenclature ..... **xxiv**

List of symbols xxiv

Latin characters xxiv

Greek characters xxvii

Common superscripts and subscripts xxviii

List of abbreviations xxix

Chapter 1 Introduction **1**

1.1. Motivation of the work 1

1.2. Literature background of TiRe-LII 4

1.2.1. The advent of LII and its use for soot diagnostics 4

1.2.2. Developments in LII and its use for synthetic nanoparticle diagnostics 7

1.3. Problem statement and content overview 10

Chapter 2 Theoretical background for basic TiRe-LII modeling **13**

2.1. The heat transfer submodel 14

2.2. The spectroscopic submodel 20

Chapter 3 Effect of nanoparticle aggregation and sintering **23**

3.1. Introduction 24

3.2. Modifications to the basic TiRe-LII model 26

3.2.1. Modified heat transfer model 26

3.2.2. Modified spectroscopic model 29

3.3. Sintering models for aggregates 32

3.4. Experimental apparatus 33

3.4.1. Excitation and Detection Systems 33

3.4.2. Aerosol generation 34
3.5. Results and discussion 37
3.5.1. Comparison of LII signals 37
3.5.2. Variation of peak pyrometric temperatures with laser fluence 37
3.5.3. Enhanced absorption due to aggregate structure 39
3.5.4. Apparent anomalous cooling from grain-boundary sintering 42
3.6. Conclusions 46

Chapter 4 Absorption properties of metal nanoparticle aggregates during time-resolved laser-induced incandescence 47
4.1. Introduction 48
4.2. Modeling the temperature and optical properties of metal aggregates 49
4.2.1. Modified heat transfer model 49
4.2.2. Modified spectroscopic model 50
4.2.3. Aggregate modeling 52
4.2.4. Absorption modeling 53
4.2.4.1. Mie theory 53
4.2.4.2. Multi-sphere T-matrix 54
4.2.4.3. Discrete dipole approximation 54
4.3. Results and discussion 55
4.3.1. Absorption cross-section distribution within metal aggregates 55
4.3.2. Aggregate absorption cross-sections in the aerosol 60
4.3.3. Effect of sintering on the absorption cross-section of metal aggregates 63
4.4. Conclusions 68

Chapter 5 Effect of laser-induced sintering and coalescence 70
5.1. Introduction 71
5.2. Experimental Setup 71
5.3. Measurement models 72
5.3.1. TiRe-LII model 72
5.3.2. Modeling of aggregate sintering, coalescence, and absorption properties of metal nanoparticles 74
5.3.3. Data regression 75
5.4. Results and discussion 76
5.4.1. Analyzing the extent of sintering by the peak of the LII signal 76
5.4.2. Predicting the impact of coalescence on the LII signal 80
5.4.3. Analysis of the pyrometrically-determined peak temperatures 84
5.4.4. Quantities-of-interest inference from prompt and delayed LII signals 87
5.5. Conclusions 92

Chapter 6 Interpreting pyrometric temperatures measured during laser-induced incandescence on iron nanoparticles 94
6.1. Introduction 95
6.2. TiRe-LII measurement model 96
6.3. Results and discussion 98
6.3.1. Assessing the accuracy of the pyrometric temperature 98

6.3.2. Effects of polydispersity on the effective pyrometric temperature 99
6.4. Conclusions 104

Chapter 7 Investigating the apparent anomalous cooling of soot during laser-induced incandescence experiments 106
7.1. Introduction 107
7.2. TiRe-LII measurement model 108
7.2.1. Heat transfer model for soot 108
7.2.2. Spectroscopic submodel 112
7.3. Experimental procedure 113
7.4. Results and discussion 117
7.4.1. Measured pyrometric soot temperatures 117
7.4.2. Apparent anomalous cooling and calculation of the TAC 119
7.4.3. Effects of nonuniform fluence 121
7.4.4. Effects of particle size polydispersity 124
7.4.5. Quantification of the magnitude of apparent anomalous cooling 127
7.5. Conclusions 131

Chapter 8 Conclusions and future work 133
8.1. Summary and key contributions 133
8.1.1. Aggregation effects 134
8.1.2. Sintering, coalescence, and morphology changes 134
8.1.3. Particle polydispersity and nonuniform fluence effects 135
8.2. Ongoing and future work 136
8.2.1. LII fluence curve and nonuniform fluence profiles for metal nanoparticles 136
8.2.2. Consolidated LII-sintering-nonuniformities model 137
8.2.3. Changes in successive LII signal traces 138
8.2.4. Appropriate light absorption models for metal nanoparticles 139
8.2.5. Quantifying uncertainties in estimated TACs 140
8.2.6. Optimal wavelength excitation for TiRe-LII on metal nanoparticles 140
8.2.7. Experiments on other elemental materials 143
8.2.8. In-flame LII and soot optical properties 143
8.3. Final remarks 144

References 146

Extended analyses and supporting data 160
Appendix A Supplementary information 160
A.1 Melting model for metal nanoparticles 160
A.2 Peak temperatures of core–oxide nanoparticle structures 161
A.3 Temperature history of molybdenum nanoparticles in different gases 162
A.4 Refractive index of small particles 163
A.5 Multisphere T-matrix method (MSTM) convergence study 164
A.6 Discrete dipole approximation (DDA) mesh study 165
A.7 Melting point depression 166
A.8 Energy released from sintering 167
A.9 Regression of the laser heating model to the LII signal 167

A.10 Sampling efficiency of soot particles....168
Appendix B Influence of nonuniform fluences on iron nanoparticle pyrometric temperatures 170
B.1 Modeling the spatially nonuniform fluence for iron nanoparticles....170
B.2 Combined effects of polydispersity and nonuniform fluence on the effective pyrometric temperature 173
B.3 Assessing the simulated fluence curve....176
B.4 Assessing the inference technique....177

List of figures

Figure 1-1: A schematic showing the overview of the LII technique. 3

Figure 2-1: A schematic showing the major heat transfer processes occurring during the TiRe-LII technique. 13

Figure 3-1: **(a)** Excessive absorption phenomenon exhibited by Fe and Mo (computed from this work assuming isolated primary particles) and Ni [16] and **(b)** Anomalous cooling phenomenon adapted from Ref. [19]. $Q_{abs,\lambda}^{exp}$ and $Q_{abs,\lambda}^{Mie}$ is the absorption efficiency determined from experiments and computed from Mie theory, respectively, for a primary particle with diameter of d_p at an excitation wavelength, λ. $T_{p,pyro}$ is the pyrometric aerosol temperature and T_g is the temperature of the bath gas. 24

Figure 3-2: **(a)** Temperature evolutions showing the growing discrepancy, as a function of diameter, between the pyrometric temperature and the temperature computed from the heat transfer model for three monodisperse aerosols, and **(b)** Temperature evolutions showing the discrepancy, as a function of size distribution width, between the pyrometric temperature and the average thermodynamic temperatures; gray lines show the temperatures of the different size classes within the aerosol. Simulations are performed with the properties of Fe nanoparticles irradiated at a fluence of 2.45 mJ/mm^2 31

Figure 3-3: Excitation and detection systems used to conduct TiRe-LII experiments 34

Figure 3-4: **(a)** Spark discharge generation and **(b)** aerosolization system used and the TEM micrographs of SDG-produced (at a spark frequency of 270 Hz) Fe and aerosolized Mo nanoaggregates. Particles flow directly from the aerosolization system into the LII chamber. 35

Figure 3-5: The distribution of the **(a)** primary particle, **(b)** number of particles per aggregate, and **(c)** equivalent diameter of the SDG-generated Fe aerosol. The equivalent diameter distribution is computed from the mean of the primary particle distribution. 36

Figure 3-6: Primary particle size distribution of the aerosolized Mo nanocolloid. 36

Figure 3-7: TEM images and size distributions of **(a)** Fe, and **(b)** Mo nanoparticles irradiated on the TEM grid 36

Figure 3-8: Sample of 40-shot averaged LII traces and pyrometric temperatures for **(a)** Fe nanoparticles in N_2, and **(b)** Mo nanoparticles in Ar, irradiated at a fluence of 2.45 mJ/mm^2. 37

Figure 3-9: Peak pyrometric temperatures measured from the Fe and Mo aerosols as a function of laser fluence. 38

Figure 3-10: Simulated pyrometric temperature curves for the Fe nanoaerosol with a morphology consisting of one isolated 6-nm diameter primary particle, and an aggregate of 126 primary particles. 40

Figure 3-11: Absorption enhancement of a 6 nm diameter Fe nanoparticle by an aggregate consisting of 126 primary particles having diameters of 6 nm and $k_f = 1.3$ and $D_f = 1.78$, normalized by the geometric cross-section of a volume equivalent sphere. The spectral absorption efficiency of the volume equivalent sphere of the aggregate is plotted for comparison. The spectral absorption efficiency of a Fe aggregate is computed with MSTM, while those of the spheres are found using Mie theory. 40

Figure 3-12: Modeled peak thermodynamic temperatures for: **(a)** an aerosol of monodisperse aerosol of iron spheres as a function of particle size, and **(b)** polydisperse aerosols composed of iron spheres, each having diameters that obey lognormal distributions sharing the same mean but different widths. 41

Figure 3-13: Pyrometric temperatures of Mo aerosol as a function of time, showing the duration of the anomalous cooling (shaded region). Particles are irradiated at a fluence of 2.41 mJ/mm^2. The gas temperature is taken as 293 K, and the peak temperature of the Mo aerosol is 2395 K. 42

Figure 3-14: (a) Peak pyrometric temperatures, and **(b)** Pyrometric temperature profiles from aerosols of Mo nanoparticles in various motive gases. 43

Figure 3-15: (a) Changes in absorption efficiency between Mo aggregates of various sizes and a fully sintered sphere having the same d_v at a wavelength of 445 nm and 747 nm; **(b)** corresponding change in the pyrometric temperature as a function of N_p. 44

Figure 3-16: Evolution of grain boundary distance (Eq. (3.14)) between two Mo nanoparticles and the diffusivity at the grain boundary (Eq. (3.16)). 45

Figure 4-1: Refractive indices of solid and liquid iron used in this work. 53

Figure 4-2: Spatial distribution of the effective absorption cross-section at 1064 nm of primary particles with uniform diameters of 6 nm ($x_p = 0.0177$) within iron aggregates of $N_p = 20$, 70, 130, and 250 randomly oriented relative to the EM-field, computed by MSTM, relative to the absorption of an isolated sphere. The aggregates have fractal parameters of $k_f = 1.3$ and $D_f = 1.78$. $C_{pp,abs,\lambda}$ is the absorption cross-section of an isolated primary particle. The refractive index of solid iron is used in the model [147]. 56

Figure 4-3: Absorption cross-sections of primary particles within a strongly anisotropic (chain-like) and a more isotropic (compact) aggregate normalized to the absorption cross-section of an isolated primary particle. The insets show the morphology of the aggregates and locations of enhanced absorption. The refractive index of solid iron is used in the model [147]. 57

Figure 4-4: Temporal variation of the effective temperature derived from the theoretical TiRe-LII signal for the highest and lowest absorbing primary particles in an iron aggregate of 250 primary particles, and that of the aggregate computed by summing emissions from thermally-isolated primary particles and using the total absorption cross-section of the aggregate; irradiated at 1064 nm. The bath gas is N_2 at 295 K and 1 bar and the laser fluence is 2.5 mJ/mm^2. Temperatures of the spheres and aggregate from integrated emission are computed from two-color pyrometry, by taking the ratio of the signals at 445 and 747 nm and using the absorption function of solid iron at the corresponding wavelengths. The Inset is the distribution, $\mathbf{C}_{abs,\lambda} \cdot \mathbf{I}_{b,\lambda}$, within the aggregate at a detection wavelength of 445 nm. The refractive index of solid iron is used [147] 59

Figure 4-5: Distribution of the absorption properties of 100 random iron aggregates with identical Np and identical fractal parameters. **(a)** Ratio of absorption between strongest and weakest absorbing primary particle, and **(b)** total absorption cross-section of the aggregates. 60

Figure 4-6: Orientation-dependent absorption cross-sections of an iron aggregate consisting of 130 primary particles irradiated at 1064 nm. **(a)** Ratio of the effective absorption cross-section of the highest to lowest absorbing sphere within the aggregate. **(b)** Total aggregate absorption cross-section at varying orientations. The bottom right inset shows the varying angles of incidence relative to the target frame. The color maps were generated in MATLAB from grid-based mapping of the MSTM results with no interpolation..... 62

Figure 4-7: Absorption cross-section of iron aggregates as a function of primary particle overlap for laser-sintered aggregate considering mass conservation; the aggregate is shown at 0 %, 30 %, 70 %, and 100 % primary particle overlap. Results are normalized to the computed $C_{\mathrm{abs},\lambda}$ for the 70 primary particle aggregate at point contact at the 450 nm wavelength; the refractive index of molten iron from Ref. [148] is used.. 65

Figure 4-8: Temperature evolution of **(a)** a 70 primary particle aggregate in point contact, for a case where uniform temperatures within the aggregare is assumed and another where thermal isolation is assumed, a sintered with a 70 % overlap, and a coalesced sphere and **(b)** a 255 nm diameter isolated iron particle (gas: N_2, Fluence: 2.5 mJ/mm^2) and aerosolized iron nanoparticles from experiments of Kock *et al.* [22], Sipkens *et al.* [19], and Robinson-Enebeli *et al.* [171]. All simulated temperatures are computed with the heat transfer submodel, except as otherwise mentioned. The refractive index of molten iron from Ref. [148] is used in the model..... 67

Figure 5-1: Modified detection setup with four-color (4C) detection wavelengths..... 72

Figure 5-2: (a) Measured LII signals at four detection wavelengths obtained from iron nanoparticles irradiated at a laser fluence of 2.7 mJ/mm^2 **(b)** Corresponding apparent pyrometric temperatures computed by a weighted nonlinear regression of the modeled spectral intensity (Eq. (2.22)) to the measured signals at four detection wavelengths centered at 445, 550, 650, and 747 nm. The pyrometric temperatures are estimated with a refractive index corresponding to molten iron [103]. 76

Figure 5-3: Average absorption cross-section of an ensemble of iron aggregates containing aggregate sizes of N_p = 30, 50, 70, 100, 135, 200 drawn from $\ln\mathcal{N}(126, 1.77)$ computed from DDA at different sintering stages. The increase, and eventual decrease of $C_{\mathrm{abs},\lambda}$ as the aggregate sinters from point contact is due to increasing dipole interaction at the sintering sites before reaching a maximum, after which $C_{\mathrm{abs},\lambda}$ reduces due to the increasing structural compactness [171]..... 77

Figure 5-4: Spectral distribution of the LII emission at the time of the maximum LII signal **(a)** Simulations for sintering stages with C_ov = 0 %, 25 %, 50 %, 75 %, and 100 % which are all assumed to be at the same temperature of 3,300 K, **(b)** Measured calibrated signal from iron nanoparticle aerosols. In all cases, emission intensities are normalized to the shortest emission wavelength. 78

Figure 5-5: Temperature dependence of the characteristic grain boundary sintering time of two iron nanoparticles with equal diameters of 6 nm..... 80

Figure 5-6: Temperature increase related to coalescence of aggregates as a function of primary particle size computed from the released surface free energy due to reduction in specific surface area..... 81

Figure 5-7: Simulated temperature profiles after laser heating for several conditions: A 6-nm diameter primary particle (dark blue), an aggregate unaffected by sintering (200 primary particles of 6 nm in diameter in point contact, red), and an equivalent sphere (35 nm) of the aggregate (yellow). Three scenarios following the step model transitioning from aggregate to sphere: A single aggregate in point contact (purple), an ensemble of aggregates in point contact (green), and a single partially sintered aggregate (black). All simulations are compared to the measured experimental temperature. A mid-range fluence of about 2.7

mJ/mm^2 in the range of fluences used during experiments was used in both simulations and the experiment shown here..... 82

Figure 5-8: Apparent particle temperatures derived from LII signals as a function of laser fluence, compared with simulated temperatures for iron nanoparticles with a diameter distribution of ln$\mathcal{N}$(56 nm, 2) obtained from Eqs. (2.1), (2.17), and (2.23) (Model, no sintering) and simulated temperatures from an aggregate size distribution of ln$\mathcal{N}$(200, 1.8) with sintering and surface energy release considered (Model, sintering). Peak temperatures from the literature are obtained from Refs. [19,22,87] and re-evaluated with the $E(\mathbf{m}_\lambda)$ determined from refractive indices obtained from ellipsometry [103]. 85

Figure 5-9: Temporal variation of the LII signal for iron nanoparticles irradiated at varying laser fluence **(a)** Linear plot of signal detected at 747 nm. **(b)** Semi-logarithmic plot of the measured signal detected at 445 and 747 nm. 87

Figure 5-10: Regression of the LII model (Eqs. (2.1) and (5.1)) to the data at a tdelay of **(a)** 0 ns and **(b)** 100 ns. 88

Figure 5-11: Inferred QoIs from Case I including, **(a)** d_p, **(b)** σ, **(c)** α, and **(d)** T_peak as a function of tdelay at difference laser fluences. Inferrences from the lowest fluence may be unreliable due to the large noise levels in the data. 89

Figure 5-12: Comparison of the rate of evaporative cooling for iron nanoparticles with diameters of 150 and 250 nm, cooling from the same peak temperature of 3300 K..... 90

Figure 5-13: Inferred QoIs from Case II including, **(a)** d_p, **(b)** σ, **(c)** T_peak as a function of tdelay at difference laser fluences. 91

Figure 5-14: Residuals of the LII model regression to the emitted signals for different laser fluence at time delays of **(a)** 0 ns **(b)** 50 ns **(c)** 100 ns, and, **(d)** 200 ns. For each fluence, the residuals are averaged from those at the detection wavelength of 445, 650, and 747 nm. 92

Figure 6-1: (a) Discrepancy between the temporal evolution of the thermodynamic and the pyrometric temperature of a 55-nm diameter iron nanoparticle irradiated with a uniform fluence of 2.5 mJ/mm^2 and **(b)** Compared to the particle thermodynamic peak temperature, the percent error of the peak temperature determined from color pyrometry using Rayliegh approximation..... 99

Figure 6-2: (a) Particle thermodynamic temperature as a function of particle diameter for varying fluences of 0.25, 0.5, 0.75, 1, 1.75, 2.5, 3.5, and 4 mJ/mm^2. **(b)** Volume normalized $C_{\mathrm{abs}\lambda=1064}$ for varying particle diameters. **(c)** Comparison of the thermodynamic temperature and the effective pyrometric temperature at varying particle diameters.....100

Figure 6-3: The peak temperature of the particle ensemble as estimated by the temperature of the hottest and the least hot particles, $T_\mathrm{p,max}$, and, $T_\mathrm{p,min}$, respectively, the pyrometric temperature of the particle ensemble, Tp,pyroeff, the bulk sensible thermodynamic temperature of the particle ensemble in the probe volume, $T_\mathrm{pv,thermo}$, and the particle thermodynamic temperature of the volume equivalent diameter of the ensemble, $T_\mathrm{dp,vol}$, all normalized to the temperature of the peak thermodynamic temperature of the mean particle diameter for a particle size distribution with a mean of 20 nm and irradiated with a laser fluence of **(a)** 1.5 mJ/mm^2, **(b)** 2.5 mJ/mm^2, **(c)** 3.5 mJ/mm^2, and a particle size distribution with a mean of 50 nm and irradiated with a laser fluence of **(d)** 1.5 mJ/mm^2, **(e)** 2.5 mJ/mm^2, **(f)** 3.5 mJ/mm^2.....101

Figure 6-4: The effective pyrometric temperature, $T_{\mathrm{p,pyro}}^{\mathrm{eff}}$, the thermodynamic temperature of the probe volume, $T_{\mathrm{pv,thermo}}$, the temperature of the volumetric equivalent diameter of the aerosol, $T_{\mathrm{dp,vol}}$, and the temperatures of randomly sampled diameters within the probe volume, $T_{\mathrm{p,thermo}}$, for different aerosol distributions with a mean diameter of 56 nm and a geometric standard deviation of and irradiated at a fluence of, respectively, **(a)** 1.2, and 2.5 mJ/mm^2 **(b)** 1.25, and 2.5 mJ/mm^2 **(c)** 1.5, and 2.5 mJ/mm^2 **(d)** 2, and 2.5 mJ/mm^2 **(e)** 1.5, and 3.25 mJ/mm^2, and **(f)** 2.5, and 3.25 mJ/mm^2.....103

Figure 6-5: The effective pyrometric temperature of an iron aerosol with a mean diameter of 56 nm and various geometric standard deviations irradiated at a fluence of 2.5 mJ/mm^2.....104

Figure 7-1: TiRe-LII experimental setup, **(a)** Soot aerosol (i) in-flame at HAB = 42 mm, (ii) extracted and diluted in various gases, **(b)** laser excitation, and **(c)** detection set-up.....115

Figure 7-2: Fluence profiles with varying nonuniformity (termed "weakly" and "strongly") used in this work and corresponding distributions at two laser pulse energy levels. Black solid lines in the histograms represent best-fit distributions.....116

Figure 7-3: Pyrometric temperatures for soot entrained in argon and heated with a laser of **(a)** weakly and **(b)** strongly nonuniformity across the cross-section, and **(c)** direct comparison of the temperature history for similar fluences at both levels of fluence uniformities. Representative laser energy distributions for both fluence nonuniformities are shown in Figure 7-2.....118

Figure 7-4: Peak pyrometric temperatures of soot heated with a laser of **(a)** weakly and **(b)** strongly nonuniformity across the cross-section.....119

Figure 7-5: Pyrometric temperatures obtained from a weakly and strongly nonuniform laser profile at similar average fluence levels for soot aerosolized in Ar. Measurement and regression to the conduction model, Eq. (7.13).....120

Figure 7-6: Inferred TACs at all considered fluences for soot heated with a laser of **(a)** weakly and **(b)** strongly nonuniformity across the cross-section. Uncertainty bounds represent one standard deviation of the mean. The corresponding fluences for the weakly and strongly nonuniform fluence profiles are comparable to those shown in Figure 7-3, for each respective case.....120

Figure 7-7: (a) Pyrometric temperatures obtained for fluence profiles with varying level of nonuniformity having a lognormal distribution with increasing geometric standard deviations (1.01, 1.35, 1.5, 1.6, 1.75, 2, and 2.5). Also shown are the results for a Gaussian fluence profile with a standard deviation of 13 % of the mean fluence, obtained from shot-to-shot measurements from Ref. [192]. **(b)** Corresponding pyrometric temperatures on a logarithmic scale with one set of pyrometric temperatures regressed to the conduction model (Eq. (7.13)). Bath gas: Ar ($\alpha = 0.25$, $T_{\mathrm{g}} = 296$ K).....122

Figure 7-8: (a) Sensitivity of each fluence class to the pyrometric temperature for the related fluence profile of (In$\mathcal{N}$(0.6 mJ/mm^2, 1.75)). **(b)** Temporal variation of pyrometric temperature simulated with the same nonuniform fluence as in (a) compared to simulations with uniform fluences of 0.6, 1.4 (maximum positive sensitivity in (a)), 1.9 (maximum negative sensitivity in (a)), and 5 mJ/mm^2. The shaded area represents the region between the temperature profiles corresponding to the fluences associated with positive and negative peaks in sensitivity. Bath gas: Ar ($\alpha = 0.25$, $T_{\mathrm{g}} = 296$ K).....123

Figure 7-9: Temperature histories of **(a)** primary particle diameters for $N_{\mathrm{p}} = 192$, and **(b)** aggregate sizes for $d_{\mathrm{p}} = 28.3$ nm for a $F_{\mathrm{o}} = 1.9$ mJ/mm^2. Aerosol bath gas is taken as Ar ($\alpha = 0.25$, $T_{\mathrm{g}} = 296$ K). 125

Figure 7-10: Pyrometric temperature histories for different aggregate distributions of soot irradiated at uniform fluences of **(a)** 0.6 mJ/mm^2, and **(b)** 1.9 mJ/mm^2. Bath gas: Ar ($\alpha = 0.25$, $T_g = 296$ K). 125

Figure 7-11: Comparing sublimative and conductive cooling powers, at peak temperature, for conditions of varying uniform fluences as a function of **(a)** primary particle diameters, and **(b)** aggregate sizes. Aerosol bath gas is taken as Ar ($\alpha = 0.25$, $T_g = 296$ K). 126

Figure 7-12: Inferred heat transfer rates from measured pyrometric temperatures compared to the heat transfer rates predicted by the conduction model for soot heated with a laser of **(a)** weak and **(b)** strong nonuniformity across the cross-section, having a measured mean fluence of 1.02 and 0.25 mJ/mm^2, respectively. The apparent anomalous cooling region is shaded. Bath gas: CO_2. 127

Figure 7-13: Estimated magnitude of apparent anomalous cooling (Eq. (7.17)) for soot heated with a laser of **(a)** weak and **(b)** strong nonuniformity across the cross-section at similar fluences. 128

Figure 7-14: Estimated magnitude of apparent anomalous cooling for soot aerosolized in different bath gases and irradiated with laser fluence profiles of weak and strong nonuniformity. 129

Figure 7-15: Comparing the conductive and sublimative cooling power, at peak temperature, for soot particles in different bath gases. Results are for $d_p = 28.3$ nm, $N_p = 192$, $F_o = 1.75$ mJ/mm^2 and $\alpha = 0.16$, 0.083, 0.1, 0.25, and 0.16, for He, CH_4, N_2, Ar, and CO_2, respectively, inferred from the current data set for the laser cross-section of weak nonuniformity (with a measured average fluence of ~0.57 mJ/mm^2). 130

Figure 7-16: (a) Pyrometric temperature history of soot particles in He and CO_2. **(b)** Simulated magnitude of apparent anomalous cooling as a function of bath gas. Results are for $d_p \sim \mathcal{N}(28.3\text{ nm}, 6.5)$, $N_p \sim \ln\mathcal{N}(192, 1.98)$, $F_o = \ln\mathcal{N}(0.6\text{ mJ/mm}^2, 1.75)$ and $\alpha = 0.16$, 0.083, 0.1, 0.25, and 0.16, for He, CH_4, N_2, Ar, and CO_2, respectively, inferred from the current data set for the laser cross-section of weak nonuniformity (with a measured fluence of ~0.57 mJ/mm^2). 131

Figure 8-1: Simulated LII fluence curves for iron nanoparticles with diameters of 10, 15, 20, 25, and 30 nm. The particle thermodynamic temperatures are used the temperature metric. 137

Figure 8-2: (a) PDFs described by $\ln\mathcal{N}(56\text{ nm}, 2)$ having different concentrations by volume (including 0%, 5%, 10%, and 20%) of particles having diameters of ~250 nm ± 5% in the probe volume, and **(b)** the corresponding increase in the temperature profiles computed from $T_{pv,thermo}$ and $T_{p,pyroeff}$ (Only 20% covolume concentration level is shown for $T_{p,pyroeff}$). 139

Figure 8-3: The calibrated intensities at detection wavelengths of 390 nm, 500 nm, 684 nm, and 797 nm from spark discharge-generated iron nanoparticles irradiated with laser wavelengths of **(a)** 1064 nm, **(b)** 532 nm, and **(c)** 355 nm; and their corresponding fluence curves. 142

Figure 8-4: (a) Regression of the free molecular conduction model to the TiRe-LII data; in-flame soot at 42 mm HAB at a fluence of ~0.5 mJ/mm^{2}and extracted soot diluted in Ar at a fluence of ~0.8 mJ/mm^2.; and **(b)** Magnitude of apparent anomalous cooling for extracted and in-flame soot (HAB = 42 mm) at a fluence of 0.566 mJ/mm^2 and 0.77 mJ/mm^2, respectively. Uncertainty bars represent one standard deviation of the mean. 144

Figure A-1: Temporal temperature variation of a laser-irradiated iron aggregate ($N_p = 135$) at 2 mJ/mm^2 (using Eq. (3.1)) compared to the absorbed laser energy, which shows the instant when melting is registered through change in mateiral properties. The change in morphology upon melting is not considered here. 161

Figure A-2: **(a)** TEM micrograph of coalesced iron aggregates showing signs of an oxide layer, and **(b)** Comparing the thermodynamic peak temperatures of iron spheres to an iron core–shell structure with a 2.5 nm oxide layer thickness. Laser irradiation is assumed to be 2.45 mJ/mm^2. 162

Figure A-3: A 45-nm diameter spherical molybdenum nanoparticle cooling down from peak temperature of 4600 K in different batch gases. 163

Figure A-4: **(a)** Size-dependent permittivity of iron nanoparticles computed from Eq. (A.3) **(b)** Corresponding absorption function. Data for particle diameters of 1, 3, 5, and 10 nm and bulk are shown. 164

Figure A-5: MSTM computed absorption efficiency vs. number of orders of expansion required in the vector spherical harmonic expansion for a 70 primary-particle liquid iron aggregate.....165

Figure A-6: Comparing the accuracy of the DDA method to that of Mie theory for a molten iron sphere with a diameter of 6 nm irradiated at 1064 nm. The refractive index of molten iron are used according to Ref. [104]. 166

Figure A-7: The magnitude of energy released upon coalescence from aggregates with primary particle diameters ranging from 4–100 nm and N_p = 10, 100, 200, 500, and 1000, the energy released after coalescence. The melting point depression as a function of particle diameter is also shown. 167

Figure A-8: Temporal variation of the LII signal for iron nanoparticles irradiated at varying laser fluence **(a)** Linear plot of signal detected at 747 nm. **(b)** Semi-logarithmic plot of the measured signal detected at 445 and 747 nm. 168

Figure A-9: Visual observation of the sampling efficiency of different bath gases. 169

Figure A-10: Estimated soot volume fraction of soot aerosolized in different bath gases and irradiated with **(a)** a weakly nonuniform and **(b)** a strongly nonuniform fluence.....169

Figure A-11: TEM micrographs of soot aerosolized in **(a)** He and **(b)** Ar. 1695

Figure B-1: Demonstrating the computation of the pyrometric temperatures using the condition of non-uniform fluence with uniform particle sizes (56 nm). Shown here: **(a)** Several temperature evolutions of the particles irradiated with the various fluences present in the probe volume; **(b)** incandescence emissions of the irradiated particles at detection wavelengths of 445 and 747 nm; **(c)** integrated intensity obtained from integrating incandescence emissions that have been weighted by the fluence distribution $p(F_\mathrm{o})$, shown in the inset; **(d)** the pyrometric temperature obtained from color pyrometry of the integrated incandescent emissions from a probe volume irradiated with a non-uniform fluence profile. The observed discontinuities in the temperature and intensity profiles are due to change in refractive index between the solid and liquid phases of iron.....171

Figure B-2: **(a)** PDFs of different fluence distributions considered, and **(b)** a visual illustration of randomly sampled fluence values present in the probe volume for a top-hat, irregular and normal (σ = 10% F_o) distribution. 172

Figure B-3: **(a)** Temperature profiles of a monodisperse aerosol with particle diameters of 56 nm, irradiated with increasingly wide fluence distributions with a mean of 2.5 mJ/mm^2, and **(b)** the corresponding increase in the Tp,pyroeff for the different fluence distributions considered. 173

Figure B-4: Effective pyrometric temperatures of various conditions of mono- and polydispersity of the size distribution and uniform and nonuniform distribution of the laser fluence. 174

Figure B-5: The effective pyrometric temperature of different conditions of size and fluence distributions within the probe volume including a monodisperse aerosol with **(a)** 56 nm and **(b)** 200 nm particles in diameter and a normally distributed fluence of $\mathcal{N}(2.5\ \mathrm{mJ/mm^2}, 13\%\mathrm{F_o})$, and a top-hat laser fluence of **(c)** 2.5 $\mathrm{mJ/mm^2}$ and **(d)** 2.5 $\mathrm{mJ/mm^2}$ irradiating particles that distributed as $\mathrm{In}\mathcal{N}(56\ \mathrm{nm}, 2)$. The grey curves are the various size classes and fluence regions within the probe volume.....174

Figure B-6: Simulated fluence curves for different combinations of distributions in size and fluence. Polydisperse size distributions have a mean of 56 nm and nonuniform fluence distributions have a mean of 2.5 $\mathrm{mJ/mm^2}$.....176

Figure B-7: Comparing the model fit to the synthetic data for **(a)** a narrow distribution in size, $\mathrm{In}\,\mathcal{N}(56$ nm, 1.001) and fluence, $\mathcal{N}(2.5\mathrm{mJ/mm^2}, 0.01\%F_\mathrm{o})$, and **(b)** a wide distribution in size, $\mathrm{In}\,\mathcal{N}(56$ nm, 2) and fluence, $\mathcal{N}(2.5\mathrm{mJ/mm^2}, 13\%F_\mathrm{o})$.....178

Figure B-8: Including the information on fluence distribution in the inference and comparing the fit to the synthetic data.....180

List of tables

Table 3-1: Thermophysical properties of iron and molybdenum used in this work..... 29

Table 3-2: Parameters used to evaluate Eq. (3.14) for molybdenum. 45

Table 5-1: Parameters used to evaluate Eq. (5.1) for Fe nanoparticles. 79

Table 7-1: Thermophysical and model properties of soot used in this work. 111

Table B-1: Inferred QoIs with a narrow distribution in size, In$\mathcal{N}$(56 nm, 1.001) and fluence, $\mathcal{N}$(2.5mJ/mm^2, 0.01%F_o), and a wide distribution in size, In$\mathcal{N}$(56 nm, 2) and fluence, $\mathcal{N}$(2.5mJ/mm2, 13%F_o) 179

Table B-2: Infered QoIs and associated percent difference when including the fluence distribution in the inference procedure.....180

Nomenclature

This section provides a summary of the nomenclature used throughout the thesis, except in the Extended analyses and supporting data section (Appendices), where the nomenclature has been clearly described upon usage. The section is organized into two sections, including the List of symbols, which is further organized into Latin characters, Greek characters, and Commonly used superscripts/subscripts, and the List of abbreviations.

List of symbols

As this work incorporates multiple bodies of literature, inconsistencies in nomenclature occasionally arise. In such cases, the specific chapter to which the inconsistency is limited is stated in parentheses beside the symbol.

Latin characters

Symbol	**Definition**
B	Regression constant
c_0	Speed of light in vacuum
c_g	Mean thermal speed of the gas molecules
c_m	Specific heat capacity of the material
c_v	Mean thermal speed of the evaporated species
C_λ	Calibration factor
$C_{\mathrm{abs},\lambda}$	Spectral absorption cross-section
C_abs	Absorption cross-section
C_ext	Extinction cross-section
C_OV	Primary particle overlap factor

C_{v0}	Initial fraction of vacancy sites
d_{eff}	Effective particle diameter
d_p	Diameter of a spherical particle
D_0	Diffusion pre-exponential factor
D_f	Aggregate fractal dimension
D_{gb}	Grain boundary diffusivity
$\mathbf{E}$	Electric field
E_i	Pre-collision energy
E_o	Post-collision energy
$E(\mathbf{m}_\lambda)$	Spectral absorption function
$f(t)$	Temporal laser fluence profile
F_o	Laser fluence
h	Planck's constant
H_{ref}	Reference molar enthalpy of vaporization
ΔH_v	Molar enthalpy of vaporization
$I_{b,\lambda}$	Spectral blackbody intensity
J_λ	Spectral incandescence intensity
k	Thermal conductivity
k (Chapter 4)	Wave number (relating to discrete dipole approximation)
k_λ	Imaginary component of the complex index of refraction
k_B	Boltzmann's constant
k_f	Aggregate prefactor
Kn	Knudsen number
l_n	Neck length
L	Length scale
m_g	Mass of the gas molecule
m_p	Mass of a particle
m_v	Atomic mass of the evaporated species
$\mathbf{m}_\lambda$	Spectral complex index of refraction
M_v	Molar mass of the material

n_λ	Real component of the complex index of refraction
n_g	Molecular number density of the gas molecules
n_v	Molecular number density of the evaporated species
N_A	Avogadro constant
$N_\mathrm{g}^{''}$	Molecular number flux of the gas
N_p	Number of primary particles per aggregate
$N_\mathrm{v}^{''}$	Molecular number flux of the evaporated species
p_g	Gas pressure
p_ref	Reference pressure
p_v	Vapor pressure of the evaporated species
$p_\mathrm{v,o}$	Vapor pressure of the bulk material
$\mathbf{P}$	Light Polarization
q_laser	Rate of laser absorption
q_cond	Rate of conduction heat loss
q_cont	Rate of conduction heat loss in the continuum regime
q_evap	Rate of evaporation heat loss
q_rad	Rate of radiative heat loss
Q	Activation enthalpy
$Q_{\mathrm{abs},\lambda}$	Spectral absorption efficiency
r	Primary particle radius
R	Universal gas constant
R_s	Specific gas constant
R_g	Radius of gyration
t	time
T	Temperature
T_agg	Aggregate temperature
T_cr	Critical temperature
T_g	Gas temperature
T_p	Particle temperature
T_peak	Nanoparticle peak temperature

T_{ref}	Reference temperature
U_{internal}	Internal energy
V_{p}	Volume of a particle
x_{p}	Size parameter
$\mathbf{x}$	Coordinates of primary particle centroids

Greek characters

Symbol	**Definition**
α	Thermal accommodation coefficient (TAC)
β	Evaporation coefficient
β (Chapter 4)	Polar angle
γ_{s}	Surface tension
γ_{sv}	Surface energy
δ	Boundary layer thickness
δ_{gb}	Grain boundary thickness
ζ_{rot}	Rotational degrees-of-freedom of gas molecules
η	Viscosity
λ	Wavelength
λ_{laser}	Laser Wavelength
λ_{MFP}	Mean free path
Λ	Intensity scaling factor (ISF)
ρ	Density
σ	Standard deviation of a normal distribution
σ_{g}	Geometric standard deviation of a lognormal distribution
τ	Characteristic sintering time
Ω	Atomic volume

Common superscripts and subscripts

Subscript/Superscript	Definition
0	Initial
λ	Spectral
agg	Aggregate
b	Boiling point
coalesc	Property after coalescence
eff	Effective
exp	Experimental
g	Gas
gb	Grain boundary
i, j, k	Indices
laser	Property of the laser
m	Material
m	Melting point (temperature only)
Mie	Mie-predicted
mod	Modeled
p	Particle
pp	Primary particle
pyro	Pyrometric
Rayleigh	Rayleigh-predicted
ref	Reference
v	Vapor
w	Detection wavelength
w (Chapter 4)	Angular frequency

List of abbreviations

Abbreviation	Definition
AAC	Aerodynamic aerosol classifiers
CCA	Cluster-cluster aggregation
DDA	Discrete dipole approximation
DMA	Differential mobility analyzer
DLS	Dynamic light scattering
EM	Electromagnetic
FMR	Free molecular regime
HAB	Height-above-burner
ISF	Intensity scaling factor
LII	Laser-induced incandescence
LIF	Laser-induced fluorescence
MD	Molecular dynamics
MSTM	Multisphere T-Matrix
pdf	Probability density function
PMT	Photomultiplier tube
QoI	Quantities-of-interest
RDG-FA	Rayleigh-Debye-Gans Fractal aggregate
TAC	Thermal accommodation coefficient
TEM	Transmission electron microscopy
TiRe-LII	Time-resolved laser-induced incandescence
RDG-FA	Rayleigh-Debye-Gans fractal aggregate
UV-Vis	Ultraviolet visible

Chapter 1

Introduction

1.1. Motivation of the work

Nanoparticles are increasingly becoming important in science and engineering for fundamental and application-related investigations. Metal nanoparticles, as well as oxides and composites, have shown benefits to medicine for hyperthermia cancer therapy and to the renewable energy sector for the improvement of solar cells, both due to their efficiency in converting light to heat as a result of their light absorption characteristics [1,2]. In the field of medicine, in addition to bioimaging, they have been used as drug delivery tools to encapsulate and deliver drugs to targeted locations owing to their biocompatibility [3]. In the environmental sector, they have been used to treat water by removing heavy metal contaminants through adsorption [4]. They are also used as optical sensors, catalysts, and UV filters due to their tunable absorption properties, large surface area, and high refractive indices, respectively [5,6]. Most of the properties of metal nanoparticles are strongly size- and morphology-dependent and need to be well-characterized to understand their properties and to appropriately and optimally apply them for their various intended purposes. As a consequence of these unique properties and growing applications, the demand for nanoparticles has grown substantially and will continue to do so as additional applications of nanoparticles emerge due to an increased understanding of their attributes. Amongst the many synthesis routes, gas-phase techniques have shown promise in making materials with high specific surface areas and without surface coatings, as well as scalability to meet this increasing demand [7,8]. As such, there is a need to effectively characterize the properties of the gas-phase synthesized nanoparticles during production and handling in the aerosol phase to meet the requirements of intended purposes.

In addition to their many benefits, metal nanoparticles, or generally nanoparticle aerosols, can also be harmful due to unintentional release into the atmosphere during industrial processes such as welding and

grinding [9]. In the case of soot, they can have a significant net positive radiative forcing and consequently contribute to the warming of the Earth's surface by trapping the outgoing radiation and reflecting solar radiation into space. Aerosols, clouds, and their interactions have been identified as the largest uncertainties associated with predicting future climate change due to uncertainties in their distribution and properties. Aerosol–cloud interactions amplify their climate impact by influencing the formation and lifetime of clouds, their ability to reflect sunlight, rainfall production, and the chemical composition of the atmosphere through potential chemical reactions on their surfaces [10,11]. Because their harmful properties also depend on their size and morphology, composition, as well as concentration [9], there is a similar need to characterize airborne nanoparticles to ensure air quality standards are met, the workplace is kept safe, and their role in Earth's changing climate is accurately assessed.

Several nanoparticle characterization techniques, including scanning electron microscopy (SEM), transmission electron microscopy (TEM), and dynamic light scattering (DLS), have been used extensively to characterize the size and morphology of sampled nanoparticles. However, these *ex situ* techniques disallow gas-phase characterization or, in the case of DLS, are limited to colloidal measurements. In addition, they do not provide *in situ* information during nanoparticle formation. While some existing techniques, such as differential mobility analysis (DMA) and aerodynamic aerosol classification (AAC), allow inline characterization of nanoaerosols, they have limitations due to the influence of aerosol sampling from reactive environments. In the case of DMA, the uncertainty of the number of charges per particle introduces errors in the estimation of the size distribution of nanoparticles within the aerosol [12]. In the case of AAC, the lower and upper limits of detectable size classes are limited by diffusion losses and particle impaction, respectively [13].

Laser- and optical-based diagnostics are increasingly being used to characterize gas-phase synthesized nanoparticles [8]. One such laser-based characterization technique is time-resolved laser-induced incandescence (TiRe-LII), which is *in situ* and provides temporally- and spatially-resolved aerosol attributes [8,14–16]. A schematic of the technique is shown in Figure 1-1. LII has so far mainly been used for soot diagnostics [17]. It involves using a nanosecond Nd:YAG laser pulse, typically at a wavelength of 1064 nm or its harmonics, to heat aerosolized nanoparticles to incandescent temperatures and record the subsequent thermal emission with optical detectors such as photomultiplier tubes (PMT) or a streak camera using either band pass filters or spectrometers for signal detection at one or more wavelengths. In time-resolved LII (TiRe-LII), the signal is observed as a function of time while the particles thermally equilibrate with

the bath gas by various heat transfer processes [18]. The rate at which the nanoparticles cool, and in the case of metal nanoparticles, the peak temperature, are size-dependent [16,19,20], and the total intensity of the recorded signals depends on the volume fraction (*i.e.*, the nanoparticle concentration in the probe volume). These dependences allow for the inference of particle size, morphology, and volume fraction within the aerosol [21], collectively called the quantities-of-interest (QoIs). Inferring the QoIs involves regressing the TiRe-LII model (which consists of a heat transfer and a spectroscopic submodel) to the recorded data. The technique also provides an opportunity to infer other properties, such as the thermal accommodation coefficient (TAC) that defines the efficiency of heat conduction away from the nanoparticle [22] and some thermodynamic and optical properties of the nanoparticles [23–26].

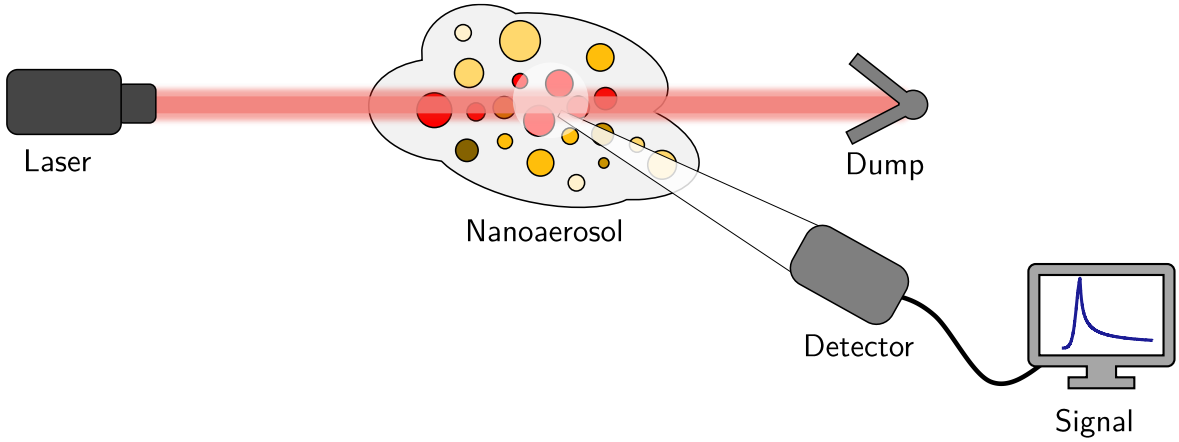


Figure 1-1: A schematic showing the overview of the LII technique.

The reliability of the technique and, consequently, the robustness of the QoI estimates, from experimental data, heavily depend on the accuracy of the LII model that hinges on the complete understanding of the various phenomena that may be occurring during laser heating and nanoparticle cooling. Various deviations from idealized assumptions (often called "anomalies" in literature) have been observed in LII data that are yet to be explained or accounted for by the current LII model [19,27,28]. These apparent anomalies are likely rooted in an incomplete understanding of the experimental conditions and the laser–nanoparticle interactions, in the context of LII, which may lead to unreliable estimates of the QoIs.

The research described in this thesis proposes several sources of the observed apparent anomalies through an extensive investigative exploration involving both experimental and theoretical modelling work. This work provides both evidence and predictive capabilities that, together, offer further insights into and

beyond the technique and hence contribute to the reliability of TiRe-LII diagnostics and the body of knowledge that is laser-nanoparticle interactions.

1.2. Literature background of TiRe-LII

In this section, the origins of the TiRe-LII technique are presented, as well as a review of the body of work that has contributed to its current state-of-the-art development.

1.2.1. The advent of LII and its use for soot diagnostics

Weeks and Duley [29] were the first to recognize that emissions from a laser-heated carbonaceous (as well as alumina) particle aerosol can be used to infer particle size by using an energy balance model to predict the dependence of the time of maximum light emission on the particle diameters. Eckbreth [30], who observed the signal as an unwanted broadband interference in Raman measurements, studied the phenomenon, which he called "laser-modulated incandescence", by irradiating soot particulates in a laminar propane diffusion flame with a dye laser. He formulated an evaporation model and studied the particle vaporization and pyrometric temperatures (*i.e.*, the temperature of an object determined from emitted thermal radiation and the object's radiative properties) as a function of laser energy, although, these efforts were aimed at reducing incandescence interference during laser Raman diagnostics. Melton [17] used the phenomenon as a purposeful optical diagnostic technique for soot. He modelled the emitted blackbody incandescence radiation and recognized that its intensity depends on the soot volume fraction. Melton also developed a heat transfer model based on an energy balance that considered the evolution of the internal energy of the particles, particle heating by laser absorption and cooling by evaporation, conduction, and radiation; although he showed that radiation is a comparably insignificant source of heat loss. These works laid the foundation for the LII technique that flourished in the years that followed.

Many of the works focused on determining the temperature and volume fraction distribution of soot particles in a flame by monitoring the intensity of the emitted incandescence at multiple wavelengths [31–33]. Will *et al.* [34] determined the spatial distribution of soot particle sizes in a flame by computing the ratio of the measured incandescence images taken with cameras at two different cooling times and comparing it to the computed diameter dependence of the ratio. Mewes *et al.* [35] used a similar method to size particles by determining the ratio of the time-integrated signals at two different cooling periods, but introduced an

additional approach that used the ratios of the emitted signals at two different detection wavelengths. Alternative to using ratios to determine particle sizes, Roth *et al.* [36] estimated the particle size distribution of soot in a laminar diffusion flame by inverting a Fredholm integral equation of the first kind (IFK) that modelled the time dependence of the incandescence signals. Particles were found to undergo changes during irradiation. In particular, Dasch [37] found that there is mass loss by evaporation under laser irradiation that becomes significant with increasing laser fluences, and Vander Wal *et al.* [38–41] showed that irradiated soot particles undergo partial graphitization that changes their morphology and potentially their optical properties. These findings showed that the technique was not entirely non-intrusive, and these changes need to be accounted for during the QoI estimation from the LII data.

Several works also focused on best experimentation and detection practices for LII. Vander Wal and Weiland [42] noted that the LII technique depends on the excitation and detection wavelengths, the laser fluence, detection timing and duration, and the number concentration of particles. They found that proper selection of wavelengths and detection timing can reduce interference from non-LII emissions such as the short-lived laser-induced fluorescence (LIF) from the polycyclic aromatic hydrocarbons (PAH) species formed in the flames. Other studies investigated similar parameters for the LII technique, including optimal excitation and detection wavelengths [33,35,40], the best range of laser fluences [33], optimal detector gating, and time-delays to eliminate LIF [33,40,43,44], error-minimization practices through proper calibration techniques [35,45], and the dependence on laser spatial uniformity [46]. Mansmann *et al.* [47] provided additional LII calibration techniques to ensure that the PMTs are used appropriately, maintaining their linear response regime, which can be challenging due to the large dynamical range in signal intensities.

Following the previously discussed works that established LII as a reliable optical technique, it became a standard soot diagnostic as many subsequent studies applied the technique while providing further insight into the TiRe-LII technique [48–54]. Several works focused on investigating the heat transfer processes taking place during the cooling of the laser-irradiated nanoparticles and other parameters that were relevant to the technique. McManus *et al.* [55] introduced a thermionic emission cooling term. Smallwood *et al.* [56] investigated the proper modelling of soot evaporation. Liu *et al.* [57] performed direct simulation Monte Carlo (DSMC) to study heat conduction from soot aggregates, where they quantified shielding effects (caused by "hidden" particles within the aggregates that do not participate in conduction as they normally would) and the effects of varying thermal. Snelling *et al.* [58] estimated the thermal accommodation coefficient (TAC) as well as the soot absorption function. Kuhlmann *et al.* [59] also studied the heat

conduction between nanoparticles and the surrounding gas and noted the importance of TAC in LII heat transfer modelling and the uncertainties surrounding its true value. Liu *et al.* [60] showed how nanoparticle polydispersity can affect results under low-fluence laser irradiation and accounted for the effects in the LII model.

In 2005, LII scientists met at the first international workshop on laser-induced incandescence to discuss the experimental and theoretical fundamentals of soot measurements by LII, leading to a detailed overview and summary by Schulz *et al.* [21] describing the current state of the LII technique. They compared nine LII heat transfer and spectroscopic models and found significant variation between models, which led to the conclusion that there was a general lack of understanding of the physical processes that underlie the LII technique. They also provided detailed discussions on experimental issues and uncertainties involving laser fluences and profiles used, the spectral absorption function of soot, emission detection methods, and procedures in evaluating the LII signal to obtain QoIs such as the volume fraction and particle size distributions. The following year, Michelsen *et al.* [18] provided a detailed comparison of ten LII models used for soot diagnostics to investigate the reason for the variability between LII models, all of which were found to be a modified version of the Melton [17] model with varying complexities. Some models considered that the temperature, as well as the volume and heat capacity of the particles, varied with time, leading to a more elaborate expression of the internal energy. Some models considered laser energy absorption of the particles by solving the full Mie theory rather than approximating in the Rayleigh regime. The Michelsen model considered additional absorption terms that accounted for saturation of linear, single-photon and multiphoton absorption. Some of the models for radiative cooling accounted for the re-absorption of background emissions from the hot gases in the flame. Most of the models considered conduction in the free molecular regime, where the mean free path of the gas is larger than the particle sizes, while some modeled conduction in the transition regime where the mean free path of the gas is comparable to the particle sizes. The sublimation models varied considerably depending on how the mass loss from the soot particles were modeled, what species sublimed (C_1 through C_5), and the partial pressure of the particles. The Michelsen model accounted for thermionic emission as an additional cooling term and oxidation of the particles as an additional heating term. There was great variability amongst models due to uncertainty in the absorption functions of the soot particles, the TAC, the sublimation models, the additional heat gain and loss terms, and overall model complexity.

Daun *et al.* [27] reported the effect of "anomalous cooling" of soot, where, immediately following the peak temperature, the particles undergo a super-exponential drop in temperature, inconsistent with the LII model, that lasted for about 50 ns before being consistent with the model and cooling exponentially as expected. None of the contemporary models were able to reproduce the observed super-exponential cooling, and subsequent work also observed the phenomenon [28]. Despite the model uncertainties, deficiencies, and variability, LII continues to be a useful soot diagnostic for both size and volume fraction characterization measurements [28,61–63].

1.2.2. Developments in LII and its use for synthetic nanoparticle diagnostics

Significant progress was and continues to be made in applying LII as a soot diagnostics [64]; however, during the emergence of the technique, Filippov *et al.* [65] recognized that it could also be applied as a diagnostic to particle aerosols consisting of a variety of other materials. They carried out experiments on carbon (C), silver (Ag), and titanium nitride (TiN) nanoparticles and determined the size distribution of the particles by inverting an IFK similar to the work reported by Roth *et al.* [36]. They accounted for particle melting that may occur for most materials other than soot, which sublimates. Vander Wal *et al.* [66] carried out explorative LII experiments on tungsten (W), iron (Fe), molybdenum (Mo), and titanium (Ti) nanoparticle aerosols. They found that at laser fluences above 1 J/cm^2, the spectrally resolved signals contained non-LII emissions that they determined to be due to recombinative chemiluminescence that originated from the evaporated species. The non-LII emissions decreased in intensity after long cooling times and were prominent mostly at shorter detection wavelengths; only LII emissions persisted at longer cooling times. They proposed and ruled out other possible non-LII emissions, including excited state emissions from the ambient gases, emissions from electronically excited vaporized species, particle photoluminescence, and particle plasmon resonances. They also showed that the particles undergo significant mass loss at higher laser fluences, which reduced the intensity of the LII signal. Vander Wal *et al.* [67] performed LII on metal (Fe and nickel, Ni) catalyzed carbon structures and determined that the elevated temperatures resulting from a blackbody-emission analysis were in reality due to broadband plasma emission that did not exhibit any emission from atomic, molecular, and cluster electronic transitions. The absence of narrowband emission was attributed to the excitation at 1064 nm, which, below the fluences of 0.8 J/cm^2 applied, does not lead to electronic excitation. Other combinations of LII and non-LII emissions, collectively referred to as laser-

induced emissions (LIE), were also observed from titania (TiO_2) particles irradiated at high fluences [62].

Starke *et al.* [68] performed the first simultaneous inference of the particle diameter and the TAC for Fe nanoparticles. They determined the QoIs by choosing appropriate values of the TAC and particle diameter that best regressed the LII model to the measured normalized LII signal. They found that the TAC for iron was significantly lower than that of soot. Stephens *et al.* [15] were able to determine the composition of different materials within an aerosol by using LII to monitor the particle temperature during vaporization. This was achieved based on the fact that, with increasing laser fluence, the temperature of the particle plateaus close to the boiling point of its constituent element. Murakami *et al.* [69] conducted LII on Mo nanoparticles aerosolized in He, Ar, N_2, and CO_2 and found that the intensity as a function of fluence was gas-dependent after the onset of evaporation. They also found that the LII-recovered particle diameters, determined through a fit of the heat transfer model to the temperature histories of the particles, were also gas-dependent due to the varying degrees of freedom accessed and vibrational frequencies of the different gas species, which determine the available modes of energy accommodation. Additionally, they observed atomic emission lines for evaporated Mo at shorter detection wavelengths that decrease with increasing detection delay after the laser pulse. Kock *et al.* [22] recovered the primary particle diameters of aerosolized iron aggregates using LII. They noted that the surface areas of primary particles within open structured aggregates are preserved and hence will be the relevant size in the LII analysis. Many other works have applied LII to metal nanostructures [16,19,70–72], metal oxides [62,73,74], and metalloids [75–78].

Daun *et al.* [79] reviewed the proposed techniques for recovering particle sizes from TiRe-LII data. They noted that implicit methods that sought to minimize the difference between the modelled and experimental data were more robust and practical than explicit methods that directly inverted the LII model, as was done by Roth *et al.* [36], since the explicit methods needed the rarely available information of the minimum and maximum diameters within the aerosol for successful inversion. However, they also found that implicit methods are ill-posed due to noise in the measured data and perturbations introduced by uncertainties in the model parameters, which include the TAC and the radiative properties of the particles. In some cases, where implicit inference methods were employed, the particle diameters and the TAC could not be independently inferred [80]. Daun *et al.* [81] introduced molecular-dynamics simulations (MD) to investigate gas–surface interaction physics and independently infer the TAC. They performed simulations for both graphite (as a surrogate for soot [81]) and various metals [82]. Independently inferred TACs could then be

used to improve LII-derived particle sizes. Other works have employed MD simulations to independently estimate the TAC between metal nanoparticles and gas molecules [75,83].

As opposed to soot with its high variability, the radiative properties of metals have been well studied [84–86] and, if appropriate, can be modelled by Drude theory [19,78]. Eremin *et al.* [23] suggested that the radiative properties of both carbon and metal nanoparticles could be particle size-dependent. Other works by Eremin *et al.* [24,87] also studied how the thermodynamic properties of metal nanoparticles differed from the bulk, particularly their melting and boiling points. Sipkens *et al.* [88] employed the Bayesian inference framework to infer the particle sizes and TACs of Fe nanoparticles aerosolized in different gases. This approach provided an estimate of the credibility intervals of the QoI estimates and allowed the use of prior knowledge during the inference procedure, which reduces ill-posedness.

Menser *et al.* [77] performed LII experiments on Si nanoparticles synthesized in a microwave plasma reactor. They found that the nanoparticles reached temperatures well above the boiling point of Si and attributed this to superheating of the nanoparticles due to the laser heating rate being higher than the evaporative cooling rate during the laser pulse. They also found unusual variations in the volume fraction of the particles during the laser pulse; the volume fraction is expected to remain constant and drop only due to evaporative mass loss. At lower fluences, less than 5 mJ/mm^2, the volume fraction remained constant. At medium fluences (5–30 mJ/mm^2), there was a rapid drop in the volume fraction, which they claim could not be due solely to evaporation and suggested that bremsstrahlung from a generated plasma could be contributing to the measured signal. At higher fluences, greater than 30 mJ/mm^2, there was an increase in the parameter, which they attributed to the limited temporal resolution of the detector that caused signal broadening.

Sipkens *et al.* [19] characterized Fe, Ag, and Mo nanoparticles aerosolized in different gases through Bayesian inference with LII data. Their analysis uncovered that the temperature history of the Ag nanoparticles decayed more rapidly than expected when compared to typical LII temperature decays. For Mo, a rapid decay of the pyrometric temperatures was observed after the peak with similar characteristics as the apparent anomalous cooling previously observed for soot [27]. The peak pyrometric temperatures reached by laser-heated nanoparticles, including Fe, Ag, and Mo, exceeded the values predicted by the LII laser absorption model, an observation that constitutes the anomaly termed “excessive absorption”.

There have been attempts to explain these effects of excessive absorption and apparent anomalous

cooling. Talebi-Moghaddam *et al.* [89] investigated the possibility that bremsstrahlung emission from a laser-induced plasma surrounding the nanoparticles could interfere with the LII signal, and inverse bremsstrahlung could enhance laser absorption within the aerosol. They found that the plasma is expected to form at laser fluences above 1 J/cm^2 due to thermionically emitted electrons from the nanoparticles that collide with neutral bath gas species and emit neutral broadband bremsstrahlung emissions that are more prominent at shorter wavelengths. They noted that metal nanoparticles absorb and emit light in the Mie regime, instead of the previously assumed Rayleigh regime, due to their large refractive indices [20]. Accounting for Mie absorption and emission reduced the magnitude of the excessive absorption effect as observed by Sipkens *et al.* [19], although not completely. In addition, Talebi-Moghaddam *et al.* [90] found that gold (Au) and Ag nanoparticles did not emit incandescence upon 1064-nm irradiation but instead multiphoton-induced photoluminescence, which had short time scales that were temporally aligned with the laser profile. Sipkens *et al.* [91] provided a review on the current state of LII diagnostics of non-soot nanoparticles and highlighted many of the challenges and open questions that have been discussed hitherto.

A summary of the specific diagnostic challenges addressed in this work is presented in the next section, along with a chapter-wise summary of the revealed solutions.

1.3. Problem statement and content overview

Due to the significant efforts invested in developing LII as a diagnostic tool, the technique has become a standard in nanoparticle aerosol characterization. Nevertheless, gaps remain in the fundamental understanding of the LII process. This work specifically addresses the anomalies that have been observed in the LII data including the 'excessive absorption' phenomenon, where irradiated nanoparticles reach pyrometric temperatures higher than those predicted by the LII laser absorption model, and the 'apparent anomalous cooling' phenomenon, where nanoparticles, immediately following peak pyrometric temperatures, cool down at a rate faster than that predicted by the LII heat transfer model. The basic form of the LII model used in most applications is presented in Chapter 2. This work combines experimental and simulation approaches to explain the anomalies by investigating the influence of nanoparticle aggregates—and their temporal morphological changes during laser irradiation—as well as the nonuniformity of certain model parameters on the LII signal. These aspects are discussed in detail throughout the thesis and are briefly summarized as follows:

The information presented in Chapter 3 discusses the experimental results conducted on Fe and Mo nanoparticles to explore the effects of metal nanoparticle aggregation and sintering. Complemented with simulations, the results show that particle aggregation enhances the absorption properties of metal nanoparticles, and for metals with high melting points, grain-boundary sintering of the constituent primary particles alters the absorption of the aggregates, which manifests in a rapid drop in the pyrometric temperature.

The analysis presented in Chapter 4 predicts, through simulation using various light absorption models, additional ways in which aggregation and sintering may influence the LII data. It is shown that light absorption within metal aggregates is highly nonuniform, with the predicted nonuniformity increasing with aggregate size. The non-uniformity of light absorption causes hotspots within the aggregates that allow the primary particles to reach higher-than-predicted peak pyrometric temperatures. Furthermore, as the irradiated metal nanoparticles heat up, they sinter, causing overlapping primary particles, which further enhances the absorption properties of the aggregates.

The discussion in Chapter 5 explores how emissions from metal aggregates, through various sintering changes, influence the spectrally resolved TiRe-LII signal. The timescales of sintering and eventual coalescence of the aggregates are discussed as they relate to relevant LII timescales. It is found that the exothermic process of coalescence is expected to cause further particle heating during laser irradiation. Furthermore, it is concluded that while aggregates are fully coalesced by the peak of the time-resolved emission, and that non-LII interferences are likely absent, the current LII heat transfer model cannot account for the temperature decay trends observed in the data immediately following peak temperatures.

The content in Chapter 6 examines the influence of particle polydispersity on the interpretation of the pyrometric temperatures of metal nanoparticles. It is shown that polydispersity results in a wide range of particle temperatures that contribute to the recorded TiRe-LII data. In particular, hot particles within the aerosol result in higher-than-expected pyrometric temperatures. These particles may then cool down through evaporation and influence the pyrometric temperature decay, resulting in a faster-than-expected decay rate following the peak temperatures. The error resulting from the approximation of monodispersity when estimating the pyrometric temperatures results in features consistent with the observed ‘excessive absorption’ and ‘apparent anomalous cooling’.

The analysis in Chapter 7 extends the considerations of the previous chapter, with the consideration of

fluence nonuniformities, to explain the 'anomalies' observed for soot LII, where it is also found that particle polydispersity and nonuniform fluence irradiation may also explain the observed soot LII data. However, in the case of soot, particle polydispersity has less of an influence on the pyrometric peak temperatures compared to metal nanoparticles. Additionally, it is shown that the 'apparent anomalous cooling' effect observed for soot is bath gas-dependent due to the varying gas conductivities.

The information in Chapter 8 includes a summary and conclusion of the findings of the thesis work and lays the path forward for future work.

Extended analyses and supporting data (Appendices) are included to supplement and expand upon the main thesis content. Appendix A contains the supplementary information that are referenced throughout the core chapters, and Appendix B contains information that extends the analysis presented in Chapter 6 through preliminary investigation of the effects of nonuniform fluences on the incandescent emissions from iron nanoparticles.

Chapter 2

Theoretical background for basic TiRe-LII modeling

As can be concluded from the work by Michelsen *et al.* [18] and Lemaire and Mobtil [63], the LII model is highly modifiable and modular depending on the applicable heat transfer terms present during the process. Hence, to provide the theoretical background, the LII model presented in this chapter is the basic instrument model for LII analysis on isolated spherical nanoparticles in the literature. The model consists of two submodels: the heat transfer model that predicts the temperature evolution of the aerosol depending on the considered heat loss and gain terms, and the spectroscopic model that predicts the observed temporal and spectral incandescence from the heated nanoaerosol at a defined temperature. Figure 2-1 shows a schematic of the major heat transfer processes occurring during the LII measurement.

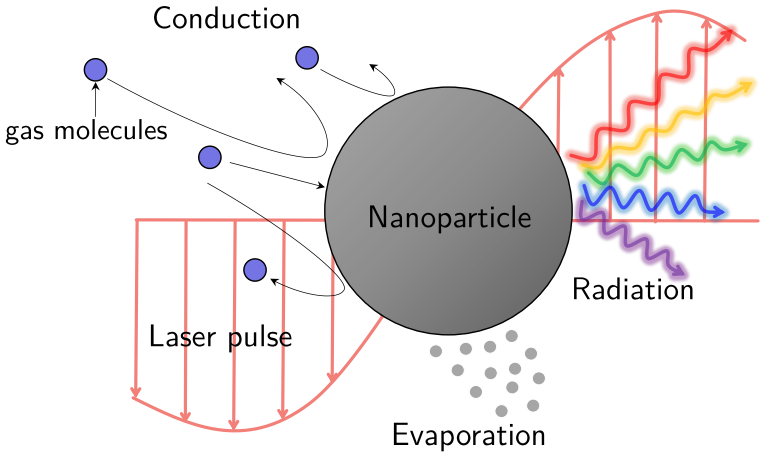


Figure 2-1: A schematic showing the major heat transfer processes occurring during the TiRe-LII technique.

2.1. The heat transfer submodel

The heat transfer submodel predicts the temperature evolution of the nanoparticles through an energy balance that equates the internal energy of the particle to all contributing heat loss and gain terms [17],

$$\dot{U}_{\text{internal}} = q_{\text{laser}}(t, d_{\text{p}}) - q_{\text{evap}}(T_{\text{p}}, d_{\text{p}}) - q_{\text{cond}}(T_{\text{p}}, d_{\text{p}}), \tag{2.1}$$

where $\dot{U}_{\text{internal}}$ is the rate of change of the internal energy of the nanoparticle, $q_{\text{laser}}(t,\ d_{\text{p}})$ is the time-dependent laser energy absorbed by the nanoparticle, and $q_{\text{evap}}(T_{\text{p}},\ d_{\text{p}})$ and $q_{\text{cond}}(T_{\text{p}},\ d_{\text{p}})$ are energy losses from the nanoparticle, at temperature T_{p}, due to evaporation and conduction, respectively; all energy transfer terms depend on nanoparticle diameter, d_{p}. Other cooling terms, such as radiation and thermionic emission, are negligible at commonly encountered temperatures (< 5000 K) [19] and fluences (< 10 mJ/mm^2) [89]. Melting is generally not considered, but during the emergence of LII on metal nanoparticles, Filipov *et al.* [65] proposed a melting model that acts as a cooling term during heating and a heating term during cooling due to latency effects, although, results show that the latent heat associated with melting is negligible during the LII process as discussed in Appendix A.1. In addition, as discussed by Michelsen [92], in the case of soot, exothermic oxidation at the particle surface may occur during irradiation, releasing heat. Soot, under laser irradiation, undergoes crystalline restructuring (*i.e.*, graphitization/annealing) [39], which is accounted for by an exothermic annealing model [92]. These heat transfer processes have been estimated to be orders of magnitude less significant than those considered in Eq. (2.1) [64]. While molten metal particles are expected to recrystallize during cooling, the associated heat transfer contribution has not been addressed in the literature but is commonly assumed to be negligible [91]. Material phase change effects between solid and molten states are incorporated into the model by switching between material properties of both states at the melting point of the material.

The mass loss from the nanoparticle due to evaporation is modelled according to

$$\frac{\mathrm{d}m_{\text{p}}}{\mathrm{d}t} = -M_{\text{v}}\,\frac{q_{\text{evap}}\left[T_{\text{p}}\left(d_{\text{p}}\right)\right]}{\Delta H_{\text{v}}\left(T_{\text{p}}\right)}, \tag{2.2}$$

where M_{v} is the molar mass of the material, m_{p} is the mass of the nanoparticle, and $\Delta H_{\text{v}}(T_{\text{p}})$ is the temperature-dependent molar enthalpy of vaporization, which is found at any temperature with reference

to a defined temperature according to Watson's equation,

$$\Delta H_{\mathrm{v}}\left(T_{\mathrm{p}}\right)=H_{\mathrm{ref}}\left[\frac{T_{\mathrm{cr}}-T_{\mathrm{p}}}{T_{\mathrm{cr}}-T_{\mathrm{ref}}}\right]^{8}, \tag{2.3}$$

where T_{ref} is the reference temperature, H_{ref} is the heat of vaporization at the reference temperature, and T_{cr} is the vapor-liquid critical temperature of the nanoparticle material (*i.e.* the temperature beyond which the liquid and vapor phases of the material are indistinguishable). Equations (2.1) and (2.2) are solved simultaneously to predict the temperature evolution. The nanoparticle diameter may change over time due to mass loss from evaporation and a decrease in density due to thermal expansion. The instantaneous particle diameter can be found from

$$d_{\mathrm{p}}\left(T_{\mathrm{p}},m_{\mathrm{p}}\right)=\left[\frac{6m_{\mathrm{p}}}{\pi\rho_{\mathrm{m}}(T_{\mathrm{p}})}\right]^{1/3}, \tag{2.4}$$

where $\rho_{\mathrm{m}}(T_{\mathrm{p}})$ is the temperature-dependent density of the material.

The internal energy term in Eq. (2.1) is expressed as

$$\dot{U}_{\mathrm{internal}}=\frac{\mathrm{d}}{\mathrm{d}t}\left(m_{\mathrm{p}}\left(T_{\mathrm{p}}\right)c_{\mathrm{m}}\left(T_{\mathrm{p}}\right)T_{\mathrm{p}}\left(t\right)\right), \tag{2.5}$$

where $c_{\mathrm{m}}(T_{\mathrm{p}})$ is the temperature-dependent heat capacity of the material and $m_{\mathrm{p}}=\rho_{\mathrm{m}}(T_{\mathrm{p}})\pi d_{\mathrm{p}}^{3}/6$ is the mass of the nanoparticle. While some works consider all terms to be time-dependent [18], it is more common to consider all terms, except temperature, to be time-independent and express the internal energy as

$$\dot{U}_{\mathrm{internal}}=\rho_{\mathrm{m}}\left(T_{\mathrm{p}}\right)c_{\mathrm{m}}\left(T_{\mathrm{p}}\right)\frac{\pi d_{\mathrm{p}}^{3}}{6}\frac{\mathrm{d}}{\mathrm{d}t}\left(T_{\mathrm{p}}\left(t\right)\right), \tag{2.6}$$

and the temporal temperature dependency of the material properties accounts for the time dependency.

The temperature within the small nanoparticles becomes uniform within a few picoseconds [92], which is faster than the timescale of the laser pulse (~ns). In addition, the Biot number computed for metal nanoparticles in the timescale of laser heating is in the order of 10^{-16} [16], suggesting that the particle can be assumed as isothermal during laser heating. However, if the temporal phase change, such as melting, is slow within the nanoparticle, it would be necessary to account for any existing temperature gradient, and

the internal energy model will need to account for the different phases within the nanoparticle [92,93]. An existing aggregate morphology will also introduce nonuniform spatial heating and temperature gradients within the nanoparticle, as discussed in Chapter 4.

The laser absorption term is expressed as

$$q_{\text{laser}}(t, d_{\text{p}}) = F_{\text{o}} f(t) C_{\text{abs},\lambda_{\text{laser}}}(\mathbf{m}_{\lambda}, d_{\text{p}}), \tag{2.7}$$

where F_{o} is the laser fluence, $f(t)$ is the temporal profile of the laser that integrates to unity, and $C_{\text{abs},\lambda\text{laser}}$ is the absorption cross-section at the laser wavelength and for an isolated primary particle is estimated as $C_{\text{abs},\lambda\text{laser}} = \pi d_{\text{p}}^2/4 Q_{\text{abs},\lambda\text{laser}}$, where $Q_{\text{abs},\lambda\text{laser}}$ is the spectral absorption efficiency of the nanoparticle at the laser wavelength, which can be computed with the full Mie theory or, if appropriate, in the Rayleigh limit [16,20,94]. When the nanoparticles are aggregated, $C_{\text{abs},\lambda\text{laser}}$ is computed with other light scattering models, as discussed in Chapter 3 – Chapter 5. The absorption model by Michelsen *et al.* [18] for soot accounts for linear and multiphoton absorption that leads to the photodesorption of carbon species. While no photodesorbing species have been reported for metal nanoparticles, Talebi-Moghaddam *et al.* [90] predicted that plasmonic nanoparticles should not emit incandescence due to their low absorption cross-section at 1064 nm but instead exhibit photoluminescence that originates from multiphoton absorption. There are currently no models in the LII literature that account for this phenomenon during the laser heating of metal nanoparticles.

The evaporation model is modelled according to

$$q_{\text{evap}}\left(T_{\text{p}}, d_{\text{p}}\right) = \frac{\Delta H_{\text{v}}\left(T_{\text{p}}\right)}{M_{\text{v}}} \frac{\mathrm{d}m_{\text{p}}}{\mathrm{d}t}, \tag{2.8}$$

where $\Delta H_{\text{v}}(T_{\text{p}})$ is the temperature-dependent molar enthalpy of vaporization given by Eq. (2.3), M_{v} is the molar mass of the material and $\mathrm{d}m_{\text{p}}/\mathrm{d}t$ is the rate of mass conversion to vapour species given by

$$\frac{\mathrm{d}m_{\text{p}}}{\mathrm{d}t} = \pi d_{\text{p}}^2 N_{\text{v}}'' \frac{M_{\text{v}}}{N_{\text{A}}}, \tag{2.9}$$

where N_{A} is Avogadro's constant and N_{v}'' is the molecular flux of evaporated species away from the nanoparticle, given by [20]

$$N_{\mathrm{v}}'' = \frac{1}{4}\beta n_{\mathrm{v}} c_{\mathrm{v}} = \frac{1}{4}\beta \frac{p_{\mathrm{v}}}{k_{\mathrm{B}} T_{\mathrm{p}}} \sqrt{\frac{8 k_{\mathrm{B}} T_{\mathrm{p}}}{\pi m_{\mathrm{v}}}}\,, \tag{2.10}$$

where β is the evaporation coefficient defining the fraction of evaporating species that recondense back into the nanoparticle [95], n_{v} and c_{v} are the molecular number density and the mean thermal speed of the evaporated species, respectively, k_{B} is the Boltzmann constant, m_{v} is the atomic mass, and p_{v} is the vapor pressure of the evaporative species. Equation (2.10) implicitly assumes that evaporation from the nanoparticle occurs in the free molecular Knudsen regime where the size of the evaporated species is smaller than the mean free path of the bath gas [96] suggesting that evaporated species might have minimal effects on the bath gas dynamics; however, Memarian *et al.* [96], using direct simulation Monte Carlo (DSMC) simulations, showed that the onset of evaporation causes a snow plough effect where the evaporated species push away surrounding bath gas molecules however, this effect has not been incorporated into LII models. While Michelsen [92] considers photodesorption of carbon clusters from a soot particle, this phenomenon, as well as bond-breaking processes, does not occur for the elemental metal nanoparticles considered in this work since there are no adsorbed species expected on the surface of the metal nanoparticles.

Assuming quasi-equilibrium between the nanoparticle surface and evaporated gas species, the partial pressure, p_{v}, at any temperature can be found from the Clausius-Clapeyron equation [20],

$$p_{\mathrm{v}} = p_{\mathrm{ref}} \exp\left[\frac{\Delta H_{\mathrm{v}}\left(T_{\mathrm{p}} - T_{\mathrm{ref}}\right)}{R T_{\mathrm{p}} T_{\mathrm{ref}}}\right], \tag{2.11}$$

where p_{ref} and T_{ref} are the reference pressure and temperature, respectively, of the saturated vapour, and R is the universal gas constant. At the relevant length scale, surface curvature effects cause an increase in the surface energy and are accounted for with the Kelvin equation [97],

$$p_{\mathrm{v}} = p_{\mathrm{v,o}} \exp\left[\frac{4\gamma_{\mathrm{s}}\left(T_{\mathrm{p}}\right)}{d_{\mathrm{p}} \rho\left(T_{\mathrm{p}}\right) R_{\mathrm{s}} T_{\mathrm{p}}}\right], \tag{2.12}$$

where $p_{\mathrm{v,o}}$ is the unadjusted vapour pressure of Eq. (2.11), $\gamma_{\mathrm{s}}(T_{\mathrm{p}})$ is the temperature-dependent surface tension of the nanoparticle, and R_{s} is the specific gas constant of the surrounding gas. The partial pressure model assumes quasi-equilibrium across the phase interface, which may not be the case under conditions of

laser irradiation. There are currently no LII models that account for such non-equilibrium processes. However, work by Menser *et al.* [98] on silicon nanoparticles provides validation of the evaporation model, but only during the cooling phase after excitation with a high laser fluence of 100 mJ/mm^2.

Conduction of heat away from the nanoparticles by the bath gas is commonly modelled in the free molecular regime [77,99], since the size of the nanoparticle is smaller than the mean free path of the gas molecules. This regime is defined by the Knudsen number, $Kn = \lambda_{\mathrm{MFP}}/L >> 1$, where L is the characteristic length of the nanoparticle, defined as the radius, and λ_{MFP} is the mean free path of the gas that has several expressions based on, for example, gas dynamics, dynamic viscosity, or thermal conductivity [100]. Conduction occurs as an incident flux of gas molecules that scatter from the surface of the nanoparticles and carry away energy, governed by [101]

$$q_{\mathrm{cond}}\left(T_{\mathrm{p}}, d_{\mathrm{p}}\right) = \alpha\pi d_{\mathrm{p}}^2 N_{\mathrm{g}}^{''} \left\langle E_o - E_i \right\rangle_{\mathrm{max}}, \tag{2.13}$$

where α is the thermal accommodation coefficient (TAC) that defines the efficiency of energy transfer between the particle and the gas molecule during each scattering event, $N_{\mathrm{g}}^{''}$ is the molecular number flux of incident gas molecules governed by

$$N_{\mathrm{g}}^{''} = \frac{1}{4} n_{\mathrm{g}} c_{\mathrm{g}} = \frac{1}{4} \frac{p_{\mathrm{g}}}{k_{\mathrm{B}} T_{\mathrm{g}}} \sqrt{\frac{8 k_{\mathrm{B}} T_{\mathrm{g}}}{\pi m_{\mathrm{g}}}}, \tag{2.14}$$

where n_{g} and c_{g} are the molecular number density and the mean thermal speed of the bath gas molecules, respectively, T_{g} is the temperature of the bath gas, k_{B} is the Boltzmann constant, and m_{g} and p_{g} are the molecular mass and partial pressure of the bath gas, respectively. In Eq. (2.13), E_{i} and E_{o} are the incident and outgoing energy, respectively, of a gas molecule during a scattering event, and $< \cdot >$ denotes the mean. The maximum outgoing energy is defined at the temperature of the heated nanoparticle, T_{p}, and $\langle E_{\mathrm{o}}\text{-}E_{\mathrm{i}} \rangle_{\mathrm{max}}$ is the maximum average energy transfer allowed by the Second Law of Thermodynamics, which the TAC adjusts to account for the imperfect energy transfer during scattering events. Daun [101] used molecular dynamics (MD) simulations to estimate the value of the TAC between various gas molecules and a soot surface. Gas molecules can accommodate energy in several modes, including normal- and tangential-translational modes, rotational modes, and vibrational modes; the total energy transferred or accommodated is the sum of all energies accommodated in each mode. It was shown that the accommodation in the vibrational mode is negligible, the normal- and tangential-translational modes accommodate a maximum

energy of $k_B(T_p - T_g)$, and the rotational mode maximally accommodates $(\zeta_{rot}/2)k_B(T_p - T_g)$, where ζ_{rot} is the number of rotational degrees-of-freedom with $\zeta_{rot} = 0$ for monoatomic gases such as Ar, He and Ne; $\zeta_{rot} = 2$ for linear polyatomic gases such as CO, N_2, and CO_2; and $\zeta_{rot} = 3$ for non-linear polyatomic gases such as CH_4 and C_2H_6. The maximum energy transfer is then modelled according to

$$\left\langle E_o - E_i \right\rangle_{max} = 2k_B\left(T_p - T_g\right) + \frac{\zeta_{rot}}{2}\left(k_B\left(T_p - T_g\right)\right) = \left(2 + \frac{\zeta_{rot}}{2}\right)k_B\left(T_p - T_g\right). \tag{2.15}$$

The overall TAC that defines the amount of energy transfer is the average of all TACs associated with each mode. The TAC was found to reduce with increasing gas molecular mass and complexity [27]; however, faster nanoparticle cooling occurs as energy transfer increases with increasing gas molecular mass and complexity. Since energy was found to be readily accommodated in the translational modes, the reduction in TAC was attributed to the increasingly available internal modes of accommodation within complex gas molecules that are not efficiently filled as compared to simpler gas molecules [27]. However, it was found by Robinson-Enebeli *et al.* [16], from experiments on Ni nanoparticles, that the TAC for CO_2 was larger than that of monatomic gas molecules, which they attributed to chemisorption of the gas molecule to the surface of the heated nanoparticle. They hypothesize that chemisorption causes an increase in the residence time of the gas molecule on the surface of the nanoparticle and consequently increases the amount of energy transferred. Several MD simulations have also been performed for nanoparticle surface-gas molecule systems in the context of LII [75,99,102].

When the sizes of the nanoparticles are comparable to or larger than the mean free path of the gas, intermolecular collisions within the vicinity of the particle will influence the local temperature field in the gas, and thus the overall heat transfer rate. To calculate the conduction heat transfer from a large particle, in this work, Fuchs' boundary sphere method [100] is used, in which the gas is subdivided into a free molecular domain that surrounds the nanoparticle, which is in turn enveloped by the continuum domain. These two domains are separated by the boundary sphere. The solution proceeds to solve for the unknown boundary sphere temperature by setting the free molecular heat transfer rate between the particle and the boundary sphere equal to the continuum heat transfer rate (used when the size of the nanoparticles is much larger than the mean free path of the gas) between the boundary sphere and the equilibrium gas,

$$q_{\text{cont}} = 4\pi\left(2\delta + d_{\text{eff}}\right)\int_{T_{\text{p}}}^{T_{\text{g}}} k\left(T_{\text{p}}\right)\mathrm{d}T\,, \tag{2.16}$$

where δ is the boundary layer thickness (usually taken to be the mean free path of the gas at the bath gas temperature), d_{eff} is the particle diameter based on effective surface area for heat conduction [60], and $k(T)$ is the thermal conductivity of the gas. The mean free path of the gases is computed from the Maxwell mean free path formulation according to Ref. [100].

2.2. The spectroscopic submodel

The spectroscopic submodel is based on the radiative transfer equation (RTE) for a non-scattering optically thin medium (*i.e.*, no reabsorption within the aerosol), hence only the gain due to emission is considered from the RTE. For an aerosol consisting of polydisperse spherical unaggregated nanoparticles, the emitted incandescence is modelled according to

$$J_{\lambda}\left(t\right) = C_{\lambda}\Lambda\int_{0}^{\infty} p\left(d_{\text{p}}\right)C_{\text{abs},\lambda}\left(d_{\text{p}},\mathbf{m}_{\lambda}\right)I_{\text{b},\lambda}\left[T_{\text{p}}\left(t,d_{\text{p}}\right)\right]\mathrm{d}\left(d_{\text{p}}\right), \tag{2.17}$$

where C_{λ} is a detector intensity calibration factor, Λ is an intensity scaling factor (ISF) that accounts for the volume fraction of nanoparticles within the aerosol, $p(d_{\text{p}})$ is the probability density value of the nanoparticle diameter, d_{p}, within the aerosol, $C_{\text{abs},\lambda} = \pi d_{\text{p}}^{2}/4\,Q_{\text{abs},\lambda}$ is the absorption cross section, where $Q_{\text{abs},\lambda}$ is the spectral absorption efficiency of the nanoparticle at the wavelength, λ, of the nanoparticle with diameter d_{p} and complex index of refraction $\mathbf{m}_{\lambda}$, and $I_{\text{b},\lambda}[T_{\text{p}}(t,d_{\text{p}})]$ is the spectral blackbody distribution emitted by a nanoparticle with diameter d_{p} and temperature, T_{p}, at a time, t.

The spectral blackbody intensity is given by

$$I_{\text{b},\lambda} = \frac{2\pi h c_{0}^{2}}{\lambda^{5}\left[\exp\left(\dfrac{hc_{0}}{k_{\text{B}}\lambda T_{\text{p}}}\right)-1\right]}, \tag{2.18}$$

where h is Planck's constant, c_0 is the speed of light in a vacuum, and k_{B} is Boltzmann's constant.

When the particle is small compared to the wavelength of the irradiating wave, $x_{\text{p}} << 1$, and is of a

material with a small refractive index, $|\mathbf{m}_\lambda| x_\mathrm{p} << 1$, then the particle absorbs energy volumetrically, and the spectral absorption efficiency can be determined by the Rayleigh approximation [94]

$$Q_{\mathrm{abs},\lambda}^{\mathrm{Rayliegh}} = 4 x_\mathrm{p} E(\mathbf{m}_\lambda), \tag{2.19}$$

where $E(\mathbf{m}_\lambda)$ is the spectral absorption function given by

$$E(\mathbf{m}_\lambda) = -\operatorname{Im}\left(\frac{\mathbf{m}_\lambda^2 - 1}{\mathbf{m}_\lambda^2 + 2}\right) = \frac{6 n_\lambda k_\lambda}{\left(n_\lambda^2 - k_\lambda^2 + 2\right)^2 + 4 n_\lambda^2 k_\lambda^2}. \tag{2.20}$$

The refractive indices of materials are generally obtained from experiments such as ellipsometry [84–86,103,104], which involves measurements on bulk samples or thin films of a material of interest. For some metals, they can also be determined from models such as the Drude model [94], where the optical properties are mostly due to the behaviour of free electrons, which more often applies to liquid or melted metals [105]. For metals where bound electrons undergo interband transitions and also contribute to the optical behaviour of the material, for example, in transition metals where the *d*-band electrons overlap and cross into the conduction band [84,105], the refractive index may be predicted using Lorentz-Drude theory [94].

During laser heating, particles of different sizes reach different temperatures, and the emitted signal is determined from Eq. (2.17); however, if the pdf of the particle size distribution is sufficiently narrow, the aerosol can be approximated as being monodisperse, and Eq. (2.17) can be simplified to

$$J_\lambda\left(t\right) = C_\lambda \mathcal{A} C_{\mathrm{abs},\lambda}\left(d_\mathrm{p}, \mathbf{m}_\lambda\right) I_{\mathrm{b},\lambda}\left[T_\mathrm{p}\left(t, d_\mathrm{p}\right)\right]. \tag{2.21}$$

The temperature of the nanoparticle ensemble is usually estimated by a pyrometric temperature, $T_{\mathrm{p,pyro}}$. When incandescence data from multiple wavelengths are available, both $T_{\mathrm{p,pyro}}$ and ISF of the nanoaerosol are determined by a non-linear minimization scheme according to

$$\begin{bmatrix} T_{\mathrm{p,pyro}} \\ B \end{bmatrix} = \underset{T,B}{\arg\min} \left\{ \left\| \begin{matrix} J_{\lambda_1}^{\mathrm{exp}} - J_{\lambda_1}^{\mathrm{mod}} \Big/ \sigma\left(J_{\lambda_1}^{\mathrm{exp}}\right) \\ \vdots \\ J_{\lambda_w}^{\mathrm{exp}} - J_{\lambda_w}^{\mathrm{mod}} \Big/ \sigma\left(J_{\lambda_w}^{\mathrm{exp}}\right) \end{matrix} \right\|_2^2 \right\}, \tag{2.22}$$

where B is an effective regression constant containing information about the ISF [106], $J_{\lambda,\mathrm{w}}^{\mathrm{exp}}$ is the experimentally measured incandescence at the w^{th} detection wavelength, with a corresponding experimental standard deviation $\sigma(J_{\lambda,\mathrm{w}}^{\mathrm{exp}})$ and $J_{\lambda,\mathrm{w}}^{\mathrm{mod}}$ is the modeled incandescence signal at the w^{th} wavelength; all variables in Eq. (2.22) are time-dependent. The modelled incandescence is determined by Eq. (2.17) or (2.21). Since one defining temperature is determined for the aerosol even under conditions of polydispersity, the temperature is referred to as an effective temperature. When incandescence signals at two wavelengths are used in the Rayleigh limit, Eq. (2.22) can be simplified by a closed-form solution according to two-colour ratio pyrometry. Taking the ratio of the incandescence data at the two wavelengths, invoking Wien's approximation (where the exponential term in Eq. (2.18), $\exp(hc_0/k_{\mathrm{B}}\lambda T) >> 1$), and isolating the temperature, results in

$$T_{\mathrm{p,pyro}} = \frac{hc_0}{k_{\mathrm{B}}}\left(\frac{1}{\lambda_2}-\frac{1}{\lambda_1}\right)\left[\ln\left(\frac{J_{\lambda,1}}{J_{\lambda,2}}\frac{E\left(\mathbf{m}_{\lambda,2}\right)}{E\left(\mathbf{m}_{\lambda,1}\right)}\left(\frac{\lambda_1}{\lambda_2}\right)^{6}\right)\right]^{-1} . \tag{2.23}$$

The advantage of using Eq. (2.22) or (2.23) in the Rayleigh limit is that the diameters of the nanoparticles are not required to determine the temperature of the aerosol; however, when the full Mie theory or any other light scattering models are used to model the absorption efficiency of the particles, *a priori* knowledge of the diameters is required. The accuracy of the pyrometric temperature for the metal nanoparticle ensemble is briefly discussed in Chapter 3 and assessed in detail in Chapter 6.

The LII model is implemented in MATLAB, which can be found on GitHub (https://github.com/s27robin/SRE-LIIcodes) along with documentation. Implementations of all models introduced later in this thesis can also be found on the provided GitHub.

The foregoing summary of the TiRe-LII model does not consider non-idealities that can affect the LII process, such as aggregation of nanoparticles, temporal morphology changes, or nonuniformity in particle morphologies or laser irradiation. The following chapters provide experimental evidence of the effects of such non-idealities and account for them through modifications to the TiRe-LII model.

Chapter 3

Effect of nanoparticle aggregation and sintering[1]

The content of this chapter examines the apparent excessive absorption and apparent anomalous cooling phenomena reported in laser-induced incandescence measurements on metal nanoparticles by considering the effects of aggregate structure and sintering. Experimental investigations are conducted on iron and molybdenum aerosols, which have different melting points and thus respond differently to the laser pulse.

[1] Information presented in this chapter is based on the published work:
Robinson-Enebeli, S., Talebi-Moghaddam, S., and Daun, K. J., 2023, "Time-resolved Laser-induced Incandescence on Metal Nanoparticles : Effect of Nanoparticle Aggregation and Sintering," Appl. Phys. B, **129**(25).

3.1. Introduction

The excessive absorption phenomenon refers to laser-heated nanoparticles reaching peak experimental temperatures that exceed theoretical predictions based on their absorption cross-sections calculated using electromagnetic theory. Apparent anomalous cooling is characterized by a more rapid decay in experimental pyrometric temperatures immediately after the peak, compared to the rates predicted by existing cooling models [16,19,90]. These deviations from the TiRe-LII model are shown in Figure 3-1.

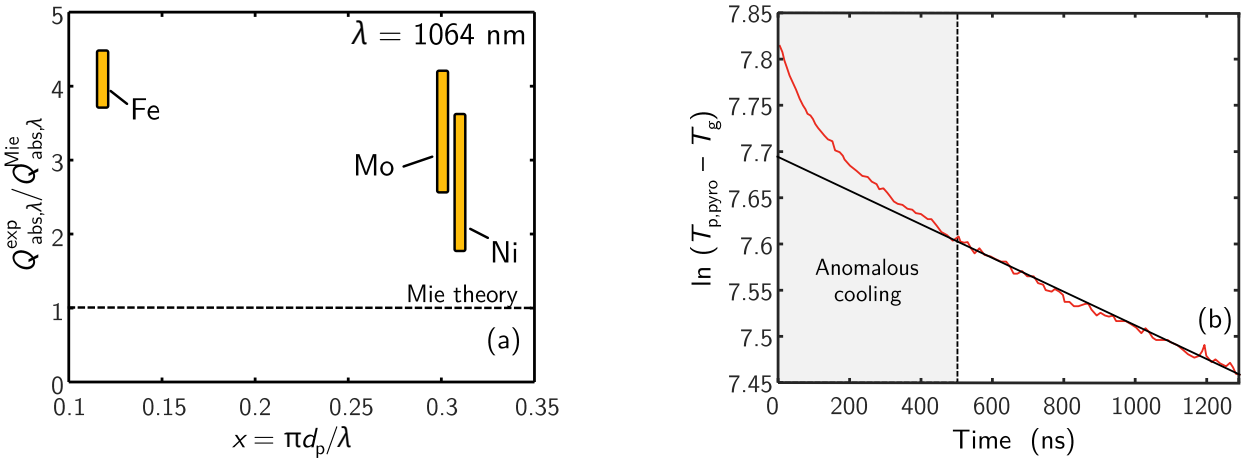


Figure 3-1: **(a)** Excessive absorption phenomenon exhibited by Fe and Mo (computed from this work assuming isolated primary particles) and Ni [16] and **(b)** Anomalous cooling phenomenon adapted from Ref. [19]. $Q^{exp}_{abs,\lambda}$ and $Q^{Mie}_{abs,\lambda}$ is the absorption efficiency determined from experiments and computed from Mie theory, respectively, for a primary particle with diameter of d_p at an excitation wavelength, λ. $T_{p,pyro}$ is the pyrometric aerosol temperature and T_g is the temperature of the bath gas.

Several hypotheses have been proposed to explain these phenomena. Talebi-Moghaddam *et al.* [90] explained the apparent excessive absorption of noble metal nanoparticles by demonstrating that the measured LII signal, under 1064 nm irradiation, does not originate from incandescence, but rather multiphoton-induced photoluminescence. For other metals, the pyrometrically inferred peak temperature may be inflated due to corruption of the LII signals by broadband neutral bremsstrahlung, which could happen at fluences above 10 mJ/mm^2 [89], and enhanced absorption of the metal nanoparticles may be a result of inverse bremsstrahlung heating. Talebi-Moghaddam *et al.* [20] also showed that some reports of excessive absorption in the literature could be attributed, in part, to improper use of the Rayleigh approximation of Mie theory to model the absorption cross-sections of metal nanoparticles. Eremin *et al.* [23] observed apparent enhanced absorption cross-sections in metal aerosols produced by photolysis of $Fe(CO)_5$ using an excimer laser,

followed by a second LII laser pulse. They suggest that this effect may depend, in some way, on the particle diameter, which was controlled by changing the delay between the excimer laser pulse and the LII pulse.

In contrast to the enhanced absorption phenomenon, which is more pronounced for metal nanoparticles, apparent anomalous cooling has been observed in LII measurements on both carbonaceous [27,28] and metal [16,19,107] aerosols, although it is unclear whether these observations may be attributed to the same underlying cause. Both Gurentsov *et al.* [107] and Sipkens *et al.* [19] report a rapid temperature decrease of Mo nanoparticles following the peak temperature. If neutral bremsstrahlung occurs, Talebi-Moghaddam *et al.* [89] also speculate that the apparent anomalous cooling effect could be due to the gradual dissipation of a laser-induced plasma surrounding the particle, leading to a corresponding decay in the signal corruption and drop in pyrometric temperature. Altman [108] has additionally speculated that the prolonged electron relaxation could explain the apparent anomalous cooling phenomenon.

In all LII studies on metal nanoparticles discussed hitherto, the aerosolized nanoparticles were modeled as isolated spheres, while, in reality, the particles are often nanospheres arranged in an aggregate structure. This conceptual simplification is mostly benign for soot, since, according to the Rayleigh-Debye-Gans Fractal Aggregate (RDG-FA) theory [109], the absorption cross-section of the aggregate is approximated by the sum of the absorption cross-sections of the primary particles (multiple scattering within the aggregate is neglected). However, RDG-FA theory does not generally apply to aggregates of metal nanospheres [20]. Moreover, laser-induced changes in aggregate morphology may change the spectral absorption cross-section during excitation and cooling, consequently biasing the pyrometrically inferred temperatures.

In this chapter, TiRe-LII measurements are described for aerosols of iron nanoparticles generated using a spark discharge generator, and for molybdenum aerosols produced by atomizing a commercial powder dispersed in water. Results from laser-heated Fe nanoparticles showed that accounting for aggregation reduces the magnitude of excessive absorption but does not eliminate this phenomenon completely. Measurements on Mo nanoparticles reveal that the rapid temperature decay of the nanoparticle ensemble, immediately following the peak, is independent of the bath gas, which disallows the possibility that apparent anomalous cooling is due to bremsstrahlung contamination of the signal. Instead, simulations on laser-heated Mo nanoparticles suggest that grain boundary sintering of the nanoaggregate during laser heating changes the absorption properties of the nanoaerosol, which manifests as a rapid cooling immediately after the peak pyrometric temperature.

3.2. Modifications to the basic TiRe-LII model

3.2.1. Modified heat transfer model

Modifications are made to the basic model presented in Chapter 2 to consider aerosols consisting of aggregates of nanospheres. The number of primary particles per aggregate, N_p, or, alternatively, the radius of gyration, R_g, usually obeys a wide distribution due to the random processes underlying aggregate assembly [110]. These parameters are empirically related by $N_\mathrm{p} = k_\mathrm{f}(2R_\mathrm{g}/d_\mathrm{p})^{D_\mathrm{f}}$, where D_f and k_f are the fractal dimension and prefactor, respectively, which together define the aggregate morphology. D_f defines the openness and compactness of the aggregates, such that a higher value of D_f represents more compact aggregates.

Accordingly, three scenarios are considered: (1) the aerosol may consist of isolated spheres of nonuniform diameter; (2) it may consist of nonuniformly-sized aggregates containing uniformly sized primary particles; and (3) the aggregates may partially sinter upon laser heating into a different morphology, and, in a limiting case, coalesce into an aerosol of nonuniformly-sized spheres. Note that throughout this thesis work, the term "aggregate" is used to describe both agglomerates, where the primary particles are weakly bound (*e.g.*, point contact) and aggregates, where the primary particles are strongly bound (*e.g.*, sintered), to be consistent with the LII literature.

In the case of an aerosol of metal aggregates, during an LII measurement, the temperature of an aggregate containing N_p nanoparticles with no overlap or necking, T_agg, is governed by [60,111]

$$\frac{\pi}{6} d_\mathrm{p}^3 N_\mathrm{p} \rho_\mathrm{m} c_\mathrm{m} \frac{\mathrm{d}T_\mathrm{agg}}{\mathrm{d}t} = q_\mathrm{laser,agg}(t, d_\mathrm{p}, N_\mathrm{p}) - q_\mathrm{evap,agg}\left[T_\mathrm{agg}\left(d_\mathrm{p}, N_\mathrm{p}\right)\right] - q_\mathrm{cond,agg}\left[T_\mathrm{agg}\left(d_\mathrm{p}, N_\mathrm{p}\right)\right], \quad (3.1)$$

where ρ_m and c_m are the density and specific heat of the bulk nanoparticle material, respectively, d_p is the diameter of the primary particles within the aggregate, $q_\mathrm{evap,agg}$ and $q_\mathrm{cond,agg}$ are the evaporation and conduction heat transfer losses of the aggregate, respectively, and $q_\mathrm{laser,agg}$ is the amount of laser heat absorbed by the aggregate. The model assumes that the aggregates are made of uniform primary particles; hence, temperature non-uniformities within the aggregate induced by polydisperse primary particle sizes are neglected. (Nonuniform heating of the aggregate due to local field enhancements is considered in Chapter

4). Analysis of electron micrographs of sampled aggregates, discussed in later sections, shows that the primary particle distributions are sufficiently narrow to support this assumption.

The rate of mass loss from the aggregate is due to uniform evaporation from each particle within the aggregate and is given by [111]

$$\frac{\mathrm{d}m_\mathrm{p}}{\mathrm{d}t} = -M_\mathrm{v}\,\frac{q_\mathrm{evap,agg}\left[T_\mathrm{agg}\left(d_\mathrm{p}, N_\mathrm{p}\right)\right]}{\Delta H_\mathrm{v} N_\mathrm{p}} \tag{3.2}$$

where m_p is the mass of the nanoparticle, and M_v and ΔH_v are the molar mass and latent heat of evaporation of the bulk nanoparticle material, respectively; ΔH_v is computed by Watson's equation [112]. The diameter of each primary particle is assumed to change over time due to mass loss from evaporation and a decrease in density due to thermal expansion. The instantaneous primary particle diameter can be found from

$$d_\mathrm{p}\left(T_\mathrm{p}, m_\mathrm{p}\right) = \left[\frac{6m_\mathrm{p}}{\pi\rho_\mathrm{m}(T_\mathrm{agg})}\right]^{1/3}, \tag{3.3}$$

and the instantaneous equivalent volumetric diameter of the aggregate can be computed from $d_\mathrm{v} = d_\mathrm{p}(T_\mathrm{p}, m_\mathrm{p})\cdot(N_\mathrm{p})^{1/3}$.

The evaporative cooling term of the aggregate is modelled according to [111]

$$q_\mathrm{evap,agg}\left(T_\mathrm{p}, d_\mathrm{p}\right) = \pi d_\mathrm{p}^2 N_\mathrm{p} N_\mathrm{v}'' \frac{\Delta H_\mathrm{v}}{N_\mathrm{A}} \tag{3.4}$$

where $N_\mathrm{v}'' = n_\mathrm{v}c_\mathrm{v}/4$ is the number flux of evaporated molecules from the particle surface-gas interface, $n_\mathrm{v} = p_\mathrm{v}/(k_\mathrm{B}T_\mathrm{p})$, and $c_\mathrm{v} = [8k_\mathrm{B}T_\mathrm{p}/(\pi m_\mathrm{v})]^{1/2}$ are the number density and mean thermal speed of evaporated molecules, respectively (m_v is the atomic mass), and N_A is Avogadro's number. The curvature-adjusted vapour pressure is estimated as in Chapter 2 at the temperature of the aggregate with the Kelvin equation (*cf.*, Eq. (2.12)).

To model conduction from an aggregate, an equivalent diameter, d_eff, that considers shielding, is defined according to [60]

$$d_{\mathrm{eff}} = d_{\mathrm{p}} \left(\frac{N_{\mathrm{p}}}{k_{\mathrm{h}}} \right)^{1/D_{\mathrm{h}}}, \tag{3.5}$$

where k_{h} and D_{h} are fractal parameters defined by TAC-dependent quadratic expressions determined from a direct simulation Monte Carlo (DSMC) simulation performed by Liu *et al.* [60] that takes into account the shielding effect of soot aggregates (numerically generated by the cluster-cluster aggregation (CCA) algorithm [110]) during heat conduction with the bath gas. When considering an isolated primary particle, d_{eff} is equal to d_{p}. For an aggregate having a conduction equivalent diameter, d_{eff}, that is small compared to the mean free path, λ_{MFP}, of the buffer gas, *i.e.*, the Knudsen number, $Kn = \lambda_{\mathrm{MFP}}/d_{\mathrm{eff}} >> 1$ [113], conduction occurs in the free molecular regime (FMR) [101],

$$q_{\mathrm{FMR,agg}} \left(T_{\mathrm{agg}}, d_{\mathrm{p}} \right) = \pi d_{\mathrm{eff}}^2 N_{\mathrm{g}}'' \alpha \left(2 + \frac{\zeta_{\mathrm{rot}}}{2} \right) k_{\mathrm{B}} \left(T_{\mathrm{agg}} - T_{\mathrm{g}} \right), \tag{3.6}$$

where $N_{\mathrm{g}}'' = n_{\mathrm{g}} c_{\mathrm{g}}/4$ is the incident gas molecular flux on the surface of the nanoparticle, $n_{\mathrm{g}} = p_{\mathrm{g}}/(k_{\mathrm{B}} T_{\mathrm{g}})$ is the gas molecular number density, $c_{\mathrm{g}} = [8 k_{\mathrm{B}} T_{\mathrm{agg}}/(\pi m_{\mathrm{g}})]^{1/2}$ is the mean thermal speed of the gas, and p_{g}, m_{g}, and T_{g} are the pressure, molecular mass, and temperature of the buffer gas, respectively, α is the thermal accommodation coefficient (TAC). Equation (3.6) does not include the vibrational modes of the gas molecules. Estimates of the conduction heat transfer losses in the transition and continuum regime are determined according to the Fuchs boundary sphere model presented in Chapter 2 at the aggregate temperature for a diameter, d_{eff}.

The heat gain term $q_{\mathrm{laser,agg}}$ is modelled according to

$$q_{\mathrm{laser,agg}}(t, d_{\mathrm{p}}) = F_{\mathrm{o}} f(t) C_{\mathrm{abs},\lambda} \left(\mathbf{m}_{\lambda}, d_{\mathrm{p}}, N_{\mathrm{p}}, k_{\mathrm{f}}, D_{\mathrm{f}} \right), \tag{3.7}$$

where F_0 is the laser fluence, $f(t)$ is the temporal laser profile, and $C_{\mathrm{abs},\lambda}(\mathbf{m}_{\lambda}, d_{\mathrm{p}}, N_{\mathrm{p}}, k_{\mathrm{f}}, D_{\mathrm{f}})$ is the absorption cross-section of the target. The absorption cross-section for an isolated nanosphere is $C_{\mathrm{abs},\lambda} = Q_{\mathrm{abs},\lambda}(\mathbf{m}_{\lambda}, d_{\mathrm{p}}) \cdot (\pi d_{\mathrm{p}}^2/4)$ where $Q_{\mathrm{abs},\lambda}(\mathbf{m}_{\lambda}, d_{\mathrm{p}})$ is the absorption efficiency computed from Mie theory with a refractive index of $\mathbf{m}_{\lambda}$. In the case of aggregates, $C_{\mathrm{abs},\lambda} = Q_{\mathrm{abs,agg},\lambda}(\mathbf{m}_{\lambda}, d_{\mathrm{p}}, N_{\mathrm{p}}, k_{\mathrm{f}}, D_{\mathrm{f}}) \cdot (\pi d_{\mathrm{v}}^2/4)$, where $Q_{\mathrm{abs,agg},\lambda}$ is the absorption efficiency of the aggregate, assumed to consist of spheres in point contact, and $d_{\mathrm{v}} = d_{\mathrm{p}} \cdot (N_{\mathrm{p}})^{1/3}$ is the volumetric equivalent diameter of the aggregate. $Q_{\mathrm{abs,agg},\lambda}$ is computed from the Multi-Sphere T-Matrix

(MSTM) method [9,10] for a randomly oriented aggregate at the laser wavelength, λ, and defined with respect to the equivalent diameter of the aggregate.

Equations (3.1) and (3.2) are solved simultaneously, starting from an initial temperature taken to be that of the bath gas. These equations also apply to aerosols consisting of isolated nanospheres. The thermodynamic properties of iron and molybdenum used in this model are provided in Table 1.

Table 3-1: Thermophysical properties of iron and molybdenum used in this work.

Property	**Fe**	**Mo**
T_m[K]	1811	2896
T_b [K]	3124	4913
$\rho_p(T_p)$ [kg/m^3]	$T_p > T_m$: –0.64985T_p + 8171 [114]	$T_p > T_m$: 9100 – 0.6(T_p–T_m)
	$T_p < T_m$: 7874	$T_p < T_m$: 9100 – 0.5(T_p–T_m) [115]
$c_p(T_p)$ [×M_v J/(kg·K)]	T_p < 1667 K : 17.64 + 1.232×10$^{-2}T_p$	$T_p > T_m$: (34.2+0.00113(T_p– T_m))
	1667<$T_p \leq T_m$: –2.38+ 3.161×10$^{-2}T_p$	$T_p < T_m$: (151.78+0.00565(T_p– T_m)).(0.29+0.0000989.(T_p– T_m)) [115]
	$T_p > T_m$: 46.632, [116]	
H_{ref} [J/mol]	340 × 10^3 [117]	597.71 × 10^3 [117]
p_{ref} [Pa]	101325	101325
T_{ref} [K]	3124	4913
T_{cr} [K]	9340 [118]	14588 [118]
$\gamma_s(T_p)$ [N/m]	1.826 – (T_p – T_m).(0.35).(10^{-3}) [119]	2.11 [120]
M_v [kg/mol]	55.85 × 10^{-3}	95.94 × 10^{-3}

3.2.2. Modified spectroscopic model

For aerosols containing aggregates, the number of primary particles per aggregate is defined by a probability density function (PDF), $p(N_p)$, and the measured incandescence is given by

$$J_\lambda\left(t\right) = C_\lambda \Lambda \int_0^\infty p\left(N_p\right) C_{abs,\lambda}\left(\mathbf{m}_\lambda, d_p, N_p, k_f, D_f\right) I_{b,\lambda}\left[T_{agg}\left(t, N_p, d_p\right)\right] \mathrm{d}N_p \,, \tag{3.8}$$

where C_λ is the calibration constant, Λ is the intensity scaling factor (ISF) that accounts for the volume fraction of nanoparticles [77,106], and $I_{b,\lambda}$ is the blackbody spectral intensity at the aggregate temperature, $T_{agg}(t,N_p,d_p)$. When the aerosol is envisioned as consisting of aggregates having uniform d_p and N_p, Eq. (3.8) simplifies to

$$J_\lambda\left(t\right) = C_\lambda \Lambda C_{abs,\lambda}\left(\mathbf{m}_\lambda, d_p, N_p, k_f, D_f\right) I_{b,\lambda}\left[T_{agg}\left(t, N_p, d_p\right)\right]. \tag{3.9}$$

Equation (3.8) can also be used to model emitted incandescence from an aerosol containing isolated spheres, where the PDF defines the distribution of the sphere diameters, and the absorption efficiency can be computed from Mie theory.

The experimental incandescence signals measured at any two detection wavelengths can be used to find the pyrometric temperature which represents an "effective" temperature, T_{eff}, of the nanoparticle ensemble

$$T_{\mathrm{p,eff}} = \frac{hc_0}{k_{\mathrm{B}}}\left(\frac{1}{\lambda_2}-\frac{1}{\lambda_1}\right)\left[\ln\left(\frac{J_{\lambda,1}}{J_{\lambda,2}}\frac{C^{\mathrm{eff}}_{\mathrm{abs},\lambda 2}\left(\mathbf{m}_\lambda, d_{\mathrm{p}}, N_{\mathrm{p}}, k_f, D_{\mathrm{f}}\right)}{C^{\mathrm{eff}}_{\mathrm{abs},\lambda 1}\left(\mathbf{m}_\lambda, d_{\mathrm{p}}, N_{\mathrm{p}}, k_f, D_{\mathrm{f}}\right)}\left(\frac{\lambda_1}{\lambda_2}\right)^5\right)\right]^{-1}, \tag{3.10}$$

where h, c_0, and k_{B} are Planck's constant, the speed of light, and the Boltzmann constant, respectively, and $C^{\mathrm{eff}}_{\mathrm{abs},\lambda}$ is the effective absorption cross-section of the aerosol that considers all size classes. When considering spheres that emit radiation in the Rayleigh regime, which occurs when the phase function, $|\mathbf{m}_\lambda|\pi d_{\mathrm{p}}/\lambda$, and size parameter, $\pi d_{\mathrm{p}}/\lambda$, are both much less than unity [94,109,121], $Q_{\mathrm{abs},\lambda} = 4\,(\pi d_{\mathrm{p}}/\lambda)E(\mathbf{m}_\lambda)$, where $E(\mathbf{m}_\lambda)$ is the spectral absorption function given by

$$E(\mathbf{m}_\lambda) = -\operatorname{Im}\left(\frac{\mathbf{m}_\lambda^2-1}{\mathbf{m}_\lambda^2+2}\right). \tag{3.11}$$

In this scenario, the pyrometric nanoparticle temperature simplifies to

$$T_{\mathrm{p,pyro}} = \frac{hc_0}{k_{\mathrm{B}}}\left(\frac{1}{\lambda_2}-\frac{1}{\lambda_1}\right)\left[\ln\left(\frac{J_{\lambda,1}}{J_{\lambda,2}}\frac{E\left(\mathbf{m}_{\lambda,2}\right)}{E\left(\mathbf{m}_{\lambda,1}\right)}\left(\frac{\lambda_1}{\lambda_2}\right)^6\right)\right]^{-1}. \tag{3.12}$$

A thermodynamic average temperature of the nanoparticles within the aerosol in the probe volume can be calculated if the size distribution and temperatures of each size class within the aerosol are known accurately. For example, for an aerosol containing isolated, nonuniformly sized spheres

$$T_{\mathrm{pv,thermo}} = \frac{\int_0^\infty T\left(d_{\mathrm{p}}\right)c_{\mathrm{m}}\left(T_{\mathrm{p}}\right)\rho_{\mathrm{m}}\left(T_{\mathrm{p}}\right)d_{\mathrm{p}}^3 p\left(d_{\mathrm{p}}\right)\mathrm{d}\,d_{\mathrm{p}}}{\int_0^\infty c_{\mathrm{m}}\left(T_{\mathrm{p}}\right)\rho_{\mathrm{m}}\left(T_{\mathrm{p}}\right)d_{\mathrm{p}}^3 p\left(d_{\mathrm{p}}\right)\mathrm{d}\,d_{\mathrm{p}}}. \tag{3.13}$$

A similar equation may be written for an aerosol containing nonuniformly-sized aggregates of identical spheres, by substituting $p(N_{\mathrm{p}})$ in place of $p(d_{\mathrm{p}})$.

An advantage of Eq. (3.12) is that the pyrometric temperatures do not rely on the nanoparticle morphology; thus, the spectroscopic and heat transfer models may be applied sequentially to recover the quantities-of-interest. However, since the Rayleigh approximation to Mie theory is usually invalid for the metal nanoparticle sizes studied using LII, the pyrometric temperature computed in this manner loses its physical significance [20]. Consequently, there is nonuniform heating of the isolated nanospheres and the aggregates within the aerosol since the absorption cross-section is no longer proportional to $N_\mathrm{p} d_\mathrm{p}^3$ (*i.e.*, no volumetric heating of the aggregates as opposed to the case of soot, where RDG-FA applies). Figure 3-2a shows that the pyrometric temperatures, computed using Eq. (3.12), will increasingly underpredict the thermodynamic temperature of the nanoparticles as particle diameter increases. This is because the laser absorption model computes the absorption efficiencies from Mie theory, and pyrometry increasingly becomes invalid as $\frac{C_{\mathrm{abs},\lambda 2}}{C_{\mathrm{abs},\lambda 1}}$ deviates progressively from the approximate ratio of $\frac{\lambda_1}{\lambda_2}\frac{E(\mathbf{m}_{\lambda 2})}{E(\mathbf{m}_{\lambda 1})}$. This is discussed in more detail in Chapter 6. Nevertheless, pyrometry provides a general indication of the instantaneous temperature of the nanoparticles within the probe volume and can be used as a tool to reduce the dimension of the available data when inferring nanoaerosol attributes using inverse analysis techniques [19,20]. However, Figure 3-2b shows that the pyrometric temperature may differ significantly from the average thermodynamic temperature of the nanoparticles within the aerosol.

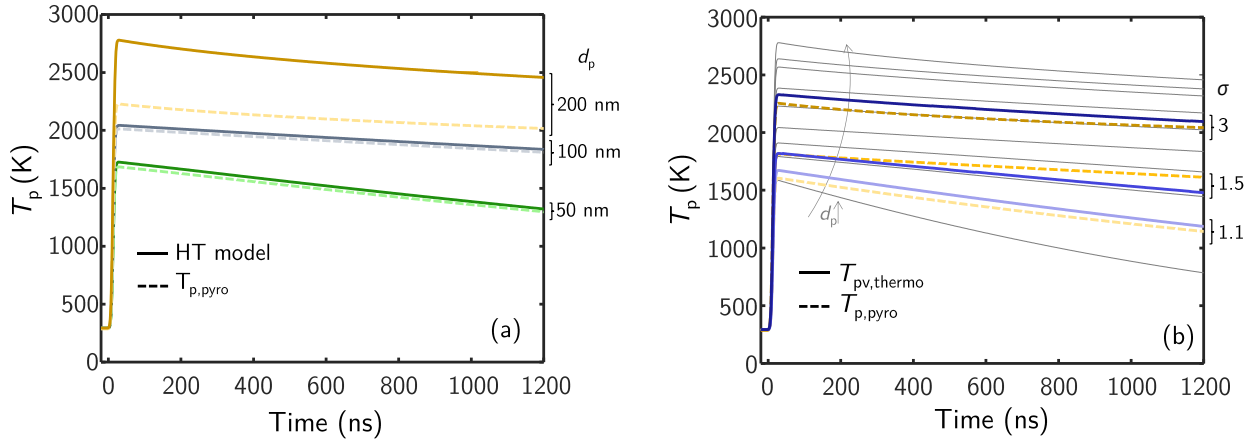


Figure 3-2: (a) Temperature evolutions showing the growing discrepancy, as a function of diameter, between the pyrometric temperature and the temperature computed from the heat transfer model for three monodisperse aerosols, and **(b)** Temperature evolutions showing the discrepancy, as a function of size distribution width, between the pyrometric temperature and the average thermodynamic temperatures; gray lines show the temperatures of the different size classes within the aerosol. Simulations are performed with the properties of Fe nanoparticles irradiated at a fluence of 2.45 mJ/mm^2.

As aggregates are heated during laser irradiation, their morphologies change through sintering, which affects the emission cross-section of the aggregate.

3.3. Sintering models for aggregates

As metal aggregates heat up, upon laser irradiation, they may undergo grain boundary diffusion sintering or viscous sintering at elevated temperatures, depending on their melting points [122].

When aggregates within the aerosol remain below their melting point, they sinter through grain boundary diffusion [122]. For an identical two-sphere system, the evolution of the neck length, l_n, is modeled according to [122]

$$l_n\left(t\right) = l_n\left(t_{-1}\right) + \Delta l_n\,, \tag{3.14}$$

where t and t_{-1} are the current and past time steps, respectively, and

$$\Delta l_n = \frac{1}{l_n^{\,5}} \frac{16 D_{gb}\left(T\right)\delta_{gb}\gamma_{sv}\Omega d_{p0}^2}{4 k_B T_{gb}}\,\Delta t\,, \tag{3.15}$$

where the grain boundary diffusivity for single crystals is

$$D_{gb} = D_0 \exp\left(-\frac{Q}{R T_{gb}}\right), \tag{3.16}$$

and D_0 and Q are the pre-exponential factor and activation enthalpy, respectively, δ_{gb} is the grain boundary thickness which is the initial size of the monomer d_{p0} (at $l_{n0} = d_{p0}/2$), k_B is the Boltzmann constant, R is the gas constant, γ_{sv} is the surface energy, Ω is the atomic volume, Δt is the sampling time, and T_{gb} is the temperature at the grain boundary. While the activation energy is considered constant in this work, it has been shown to be size-dependent through the size-dependent melting of the nanoparticles (*cf.*, Appendix A.7), which results in faster sintering and coalescence for smaller particles [123]. Equations (3.14) and (3.15) are solved with the boundary condition of $l_{n0} = d_{p0}/2$. In this case, one would expect the laser pulse to temporally modify the aggregate structure, and hence its spectral absorption cross-section.

If the aggregates are heated to temperatures above their melting point, they sinter through viscous

flow, which is much faster than grain boundary diffusion [124]. The aggregates have a characteristic sintering time of [125]

$$\tau = \frac{\eta r_0}{\gamma_s}\left(\frac{N_p}{2}\right)^{\left(1/2-D_f/6\right)}, \tag{3.17}$$

where η and γ_s are the viscosity and surface tension of the material, and r_0 is the initial radius of the primary particles within the aggregate. The time scale for viscous sintering is below a nanosecond for the aggregates in this study, suggesting that particles heated beyond their melting point should, in principle, form nanospheres almost immediately. Detailed comparative analysis between the sintering and laser irradiation timescales is presented in Chapter 5.

Although there are other mechanisms of sintering, such as surface diffusion or lattice/volume diffusion [122,126], only grain boundary and viscous sintering are densifying mechanisms characterized by shrinkage as a consequence of particle centers approaching each other. Such densifying mechanisms also tend to dominate at high temperatures, such as those relevant to this work [126]. Low-melting-point metals are expected to undergo viscous sintering at high temperatures since they become amorphous upon melting.

3.4. Experimental apparatus

This section describes the excitation and detection systems used to collect the experimental LII signals, as well as the aerosol generation systems used to produce the synthesized metal nanoparticles.

3.4.1. Excitation and Detection Systems

TiRe-LII experiments were conducted using the apparatus shown in Figure 3-3. The excitation system consists of a 1064 nm Nd:YAG laser operated at 20 Hz with a Gaussian pulse duration of 8 ns at FWHM. The laser pulse passes through beam-forming optics to control the power and cross-section of the final laser pulse contained within the probe volume. The laser fluence is controlled using two half-wave plates and a polarizer, made more uniform through an aperture, and the resulting beam is then relay-imaged to produce a 2 mm × 1.3 mm beam cross-section at the probe volume location. Emissions from the heated aerosol are focused onto a fiber optic cable using collection optics consisting of two achromatic doublets of focal lengths 210 mm and 100 mm. The fiber optic cable transmits the probe volume emissions to the detection system,

consisting of a demultiplexing system which uses a series of dichroic mirrors and bandpass filters to decouple the light into two wavelength bands centred at (445 nm ± 32 nm, and 747 nm ± 29 nm), which are then imaged onto two PMTs. Signals were normalized to the 747 nm band using a tungsten-halogen light source (Thorlabs, SLS202L), with known emission spectra at 2800 K, following a calibration procedure similar to the one described in Ref. [47]. A detailed description of the calibration procedure can be found in the Appendix of Ref. [127]. The LII data collected and analyzed in this chapter are available on GitHub (https://github.com/s27robin/SRE-PhD-LII-exp_data).

3.4.2. Aerosol generation

Aerosols of Fe and Mo aggregates are produced using the systems shown in Figure 3-3. An aerosol of Fe nanoaggregates in N_2 (at a feed pressure of 1.2 bar) was generated using a spark discharge generator (SDG, PALAS GFG 1000, *cf.*, Figure 3-4a) equipped with pure iron electrodes (ARMCO® – 99.85 % iron) and operated at 270 Hz. In principle, it is possible to supply the SDG with various motive gases, but the gas species affect the morphology of the nanoparticle [128]. Therefore, comparing LII signals collected from SDG-generated nanoparticles in different gases is not straightforward. For this reason, the SDG is operated using N_2 exclusively. The spark discharge generation system is operated under positive pressure (achieved through the flow of the bath gas) to reduce the infiltration of oxygen and eventual particle oxidation.

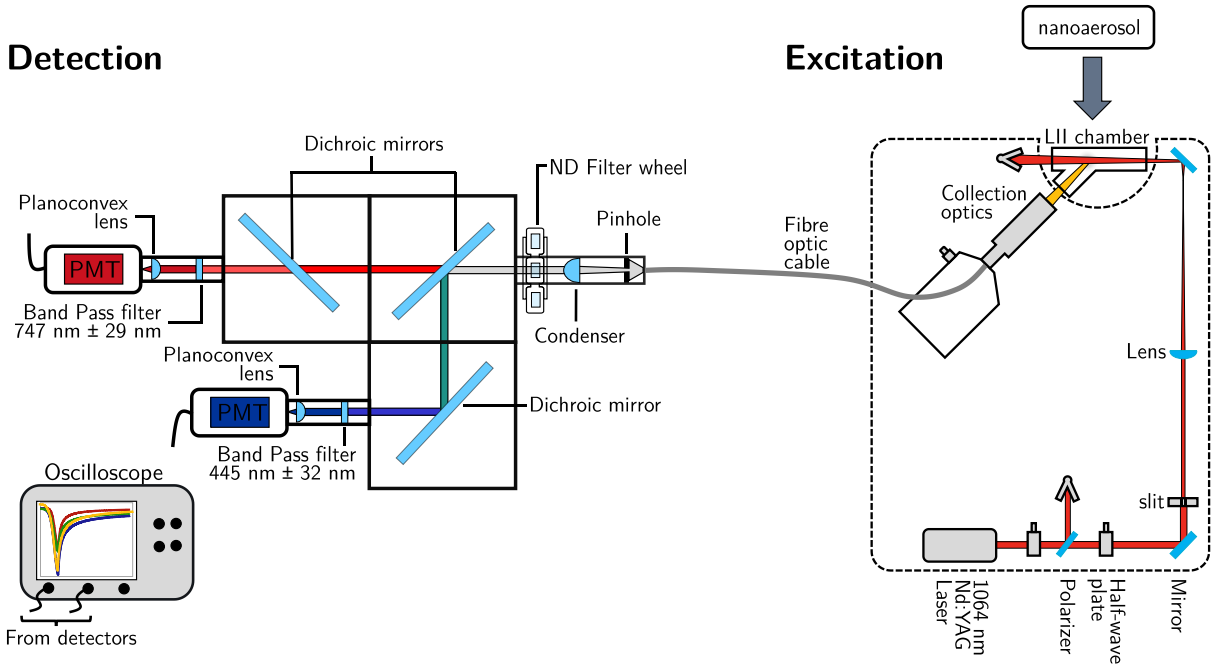


Figure 3-3: Excitation and detection systems used to conduct TiRe-LII experiments.

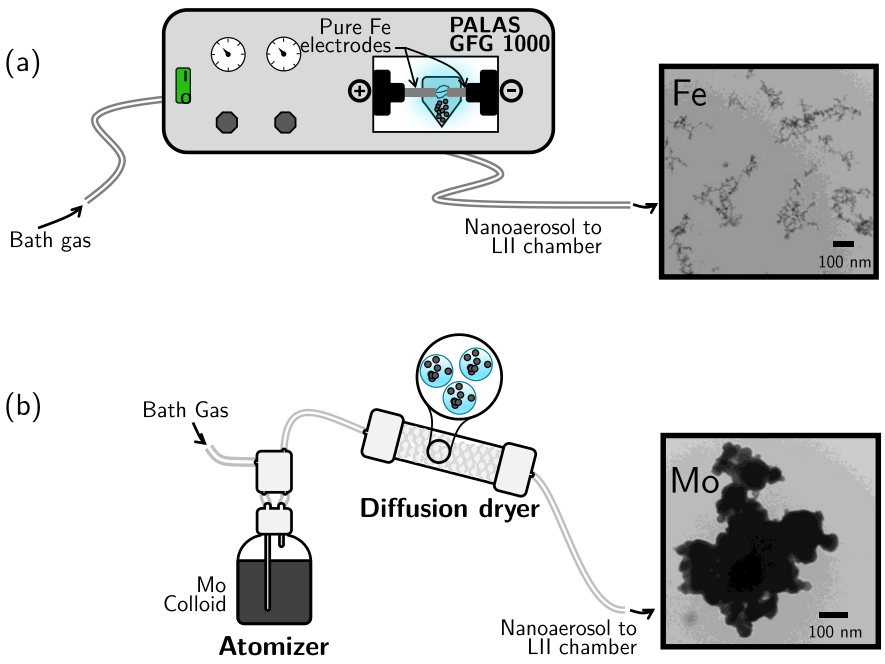


Figure 3-4: (a) Spark discharge generation and **(b)** aerosolization system used and the TEM micrographs of SDG-produced (at a spark frequency of 270 Hz) Fe and aerosolized Mo nanoaggregates. Particles flow directly from the aerosolization system into the LII chamber.

TEM grids were populated with an electrostatic sampler (ESPNano – Model 100, 10 – 20 s sampling time). Size distribution analysis of 96 nanoparticles and 24 aggregates using ImageJ [129] showed that the primary particles within aggregates were lognormally-distributed as $\ln\mathcal{N}(6.02\text{ nm}, 1.3)$. The number of particles per aggregate was inferred to be $\ln\mathcal{N}(126, 1.77)$ based on total surface area according to Ref. [130], assuming a projected area exponent of unity. Figure 3-5 highlights that the distribution of the number of particles per aggregate is wider than the primary particle size distribution, suggesting that aggregate sizes within the aerosol mostly differ by N_p, which supports the approximation of uniform d_p underlying Eq. (3.8).

A colloidal solution of Mo nanopowder (MilliporeSigma) was aerosolized using a pneumatic atomizer (Model 3067 Constant Output Atomizer) with Ar, He, Ne, N_2, or CO_2 bath gases, each supplied at a pressure of 20 psi (*cf.*, Figure 3-4b). The wet aerosol flows through a diffusion dryer before entering the probe volume. The Mo aggregates showed varying degrees of compactness and openness; a representative TEM micrograph is shown in Figure 3-4. Size distribution analysis of 125 nanoparticles showed the primary size distribution $\ln\mathcal{N}(32.9\text{ nm}, 1.2)$ (*cf.* Figure 3-6). The analysis of the number of particles per aggregate was inconclusive due to the low number of aggregates observed on the TEM micrographs, which ranged from 40 to 200 particles per aggregate.

To explore how the particles may respond to the laser pulse, TEM-sampled nanoaggregates are directly irradiated with one laser shot with a fluence of 2.45 mJ/mm^2. As seen in Figure 3-7a, the Fe aggregates coalesce into isolated spheres that are much larger than the estimated volumetric diameter of the aggregates, *cf.* Figure 3-5c. It is possible that several aggregates on the TEM grid may merge into a single large sphere.

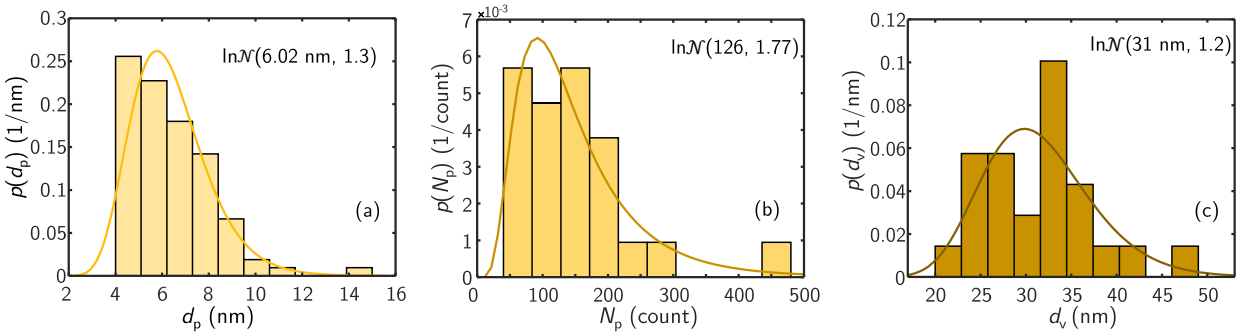


Figure 3-5: The distribution of the **(a)** primary particle, **(b)** number of particles per aggregate, and **(c)** equivalent diameter of the SDG-generated Fe aerosol. The equivalent diameter distribution is computed from the mean of the primary particle distribution.

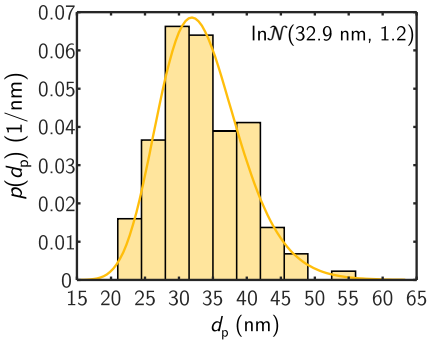


Figure 3-6: Primary particle size distribution of the aerosolized Mo nanocolloid.

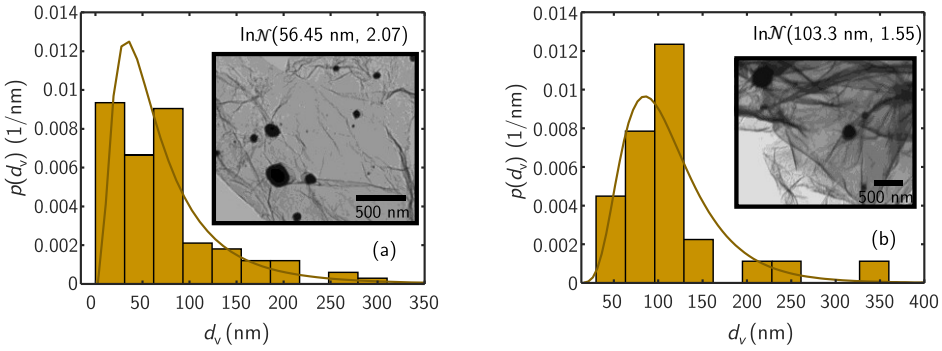


Figure 3-7: TEM images and size distributions of **(a)** Fe, and **(b)** Mo nanoparticles irradiated on the TEM grid.

3.5. Results and discussion

3.5.1. Comparison of LII signals

Figure 3-8a and b show typical LII traces for the Fe and Mo aggregates in N_2 at a fluence of 2.45 mJ/mm^2. Signals are produced by averaging over 40 shots. Unless otherwise stated, all pyrometric temperatures are computed with Eq. (3.12), using refractive indices obtained from Ref. [103] for Fe and Ref. [86] for Mo at 3000 K, with the understanding that the pyrometric temperature is an approximation of the true temperature due to polydispersity as discussed previously. Signals from the Fe aerosol are weaker and noisier due to low concentrations from the SDG and smaller aggregate sizes compared to Mo. The Mo aerosol reaches higher peak temperatures.

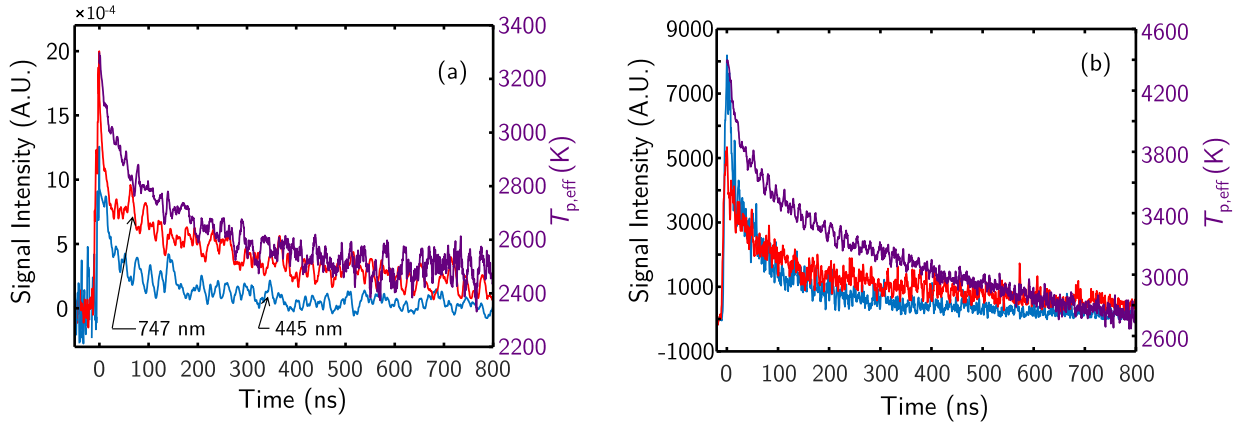


Figure 3-8: Sample of 40-shot averaged LII traces and pyrometric temperatures for **(a)** Fe nanoparticles in N_2, and **(b)** Mo nanoparticles in Ar, irradiated at a fluence of 2.45 mJ/mm^2.

3.5.2. Variation of peak pyrometric temperatures with laser fluence

Figure 3-9 shows how the peak pyrometric temperatures measured from the Fe and Mo aerosols vary with laser fluence. While one may expect that higher temperatures are reached by nanoparticles with larger absorption cross-sections, this is not necessarily the case. For the same particle morphology, according to Mie theory, Fe nanoparticles will absorb more 1064 nm radiation compared to Mo nanoparticles. However, because Fe nanoparticles have a larger thermal mass (the coefficient of $\mathrm{d}T/\mathrm{d}t$ in Eq. (3.1)) than Mo

nanoparticles for a given spectral absorption cross-section, the Mo nanoparticles reach higher temperatures for the same laser fluence.

The peak pyrometric temperatures for the Mo aerosols are higher than the melting point of bulk molybdenum (2869 K) and greatly exceed the peak temperatures reported by Sipkens *et al.* [19] (*cf.*, Figure 3-1b) at similar fluences and nanoparticle sizes. The peak temperatures for the Mo aerosol in this study increase approximately linearly with fluence, while those of the Fe aerosols remain approximately constant at a temperature slightly above the boiling temperature of iron at atmospheric pressure, 3135 K. Due to its low melting point, any increase in the laser energy absorbed by the Fe nanoparticles is offset by increased evaporative cooling. A slight superheating effect would be expected because the temporal width of the laser pulse is shorter than the characteristic time of evaporation [77]. Notably, Gurentsov *et al.* [107] reported a similar behaviour, in the considered fluence range, for their measurements on Mo aerosol, with a plateau at ~4000 K at increasing fluences up to 6 mJ/mm^2.

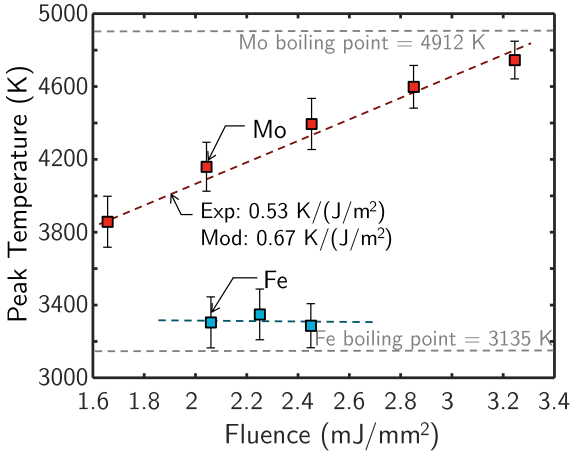


Figure 3-9: Peak pyrometric temperatures measured from the Fe and Mo aerosols as a function of laser

In the case of Mo nanoparticles, the peak temperature should increase linearly with fluence if the evaporative cooling in Eq. (3.1) is negligible. Equating the increase in sensible energy to the laser heating term results in

$$\frac{\mathrm{d}T_{\mathrm{peak}}}{\mathrm{d}F_{\mathrm{o}}} = \frac{3}{2}\frac{Q_{\mathrm{abs},\lambda} d_{\mathrm{v}}^2}{d_{\mathrm{p}}^3 N_{\mathrm{p}} \rho_{\mathrm{m}} c_{\mathrm{p}}}, \tag{3.18}$$

where d_{v} is the volumetric-equivalent diameter of the nanoaggregate, $Q_{\mathrm{abs},\lambda}$ is the volumetric spectral absorption efficiency of the aggregate, and all other terms are as defined in Eqs. (3.1) and (3.7). With a

simulated aggregate structure consisting of 40 primary particles, each with a diameter of 33 nm, and fractal parameters, $k_f = 1.3$ and $D_f = 1.78$, the slope of the peak temperature as a function of fluence is 0.67 K/(J/m^2) which is consistent with the experimental value of 0.53 K/(J/m^2) within modelling error that may originate from the uncertainty of the aggregate structure (*cf.*, Chapter 4 andChapter 5) or nonuniform fluence (discussed in Chapter 7 and Appendix B). At higher fluences, a plateau in the peak pyrometric temperatures is expected in the vicinity of the boiling point of Mo, similar to that observed for Fe nanoparticles.

3.5.3. Enhanced absorption due to aggregate structure

LII measurements on metal nanoparticles are often interpreted as originating from isolated spheres without considering aggregation [19,22,71]. Following this assumption, the simulated temperature evolution of a 6 nm Fe nanoparticle aerosolized in N_2 and irradiated with a fluence of 2.45 mJ/mm^2 results in a peak pyrometric temperature of about 1477 K, as seen in Figure 3-10. However, Figure 3-11 shows that aggregates have a significantly larger absorption cross-section and that the aggregate structure also enhances the absorption cross-section when compared to a volumetric equivalent sphere due to multiple scattering effects within the aggregate that enhance the exciting field [131], as discussed further in Chapter 4. (Simulated aggregates are generated using the CCA algorithm [110]). Assuming an aggregate structure consisting of 126 primary particles, each having a diameter of 6 nm, as per the analysis of the TEM micrographs, and with $k_f = 1.3$ and $D_f = 1.78$, the enhanced absorption cross-section results in a peak pyrometric temperature of 2068 K. As an extreme scenario, the model assumes that each aggregate maintains its structure throughout the heating process and does not sinter into a sphere, which would otherwise reduce the absorption cross-section. While surface energy that is released during aggregate sintering and coalescence may further increase the estimated temperatures, the absorption enhancement due to aggregation is also stunted in the process to an extent that is not compensated by the released surface energy. This is discussed further in Chapter 5.

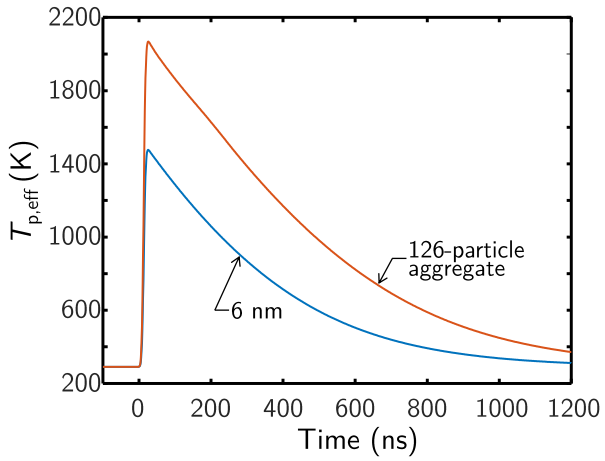


Figure 3-10: Simulated pyrometric temperature curves for the Fe nanoaerosol with a morphology consisting of one isolated 6-nm diameter primary particle, and an aggregate of 126 primary particles.

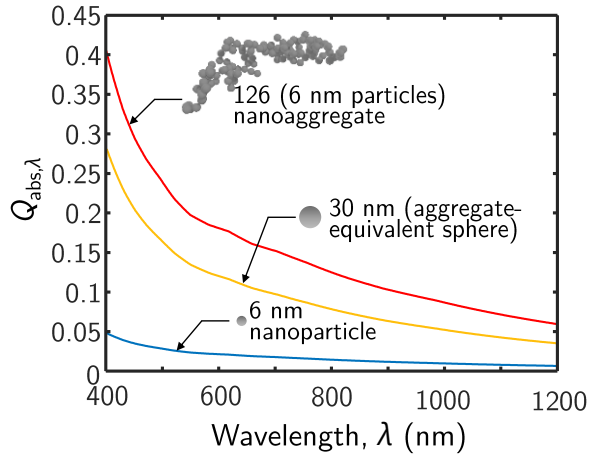


Figure 3-11: Absorption enhancement of a 6 nm diameter Fe nanoparticle by an aggregate consisting of 126 primary particles having diameters of 6 nm and $k_f = 1.3$ and $D_f = 1.78$, normalized by the geometric cross-section of a volume equivalent sphere. The spectral absorption efficiency of the volume equivalent sphere of the aggregate is plotted for comparison. The spectral absorption efficiency of a Fe aggregate is computed with MSTM, while those of the spheres are found using Mie theory.

Using Eq. (3.17) with a viscosity of 10.5 mPa·s [132], surface tension of 1.8 J/m^2 [133], and an aggregate morphology of 126 × 6 nm diameter particle with a $D_f = 1.78$, the characteristic viscous sintering time of the aggregate is estimated to be ~0.04 ns, suggesting that the aggregates sinter into spheres well before the end of the laser pulse (~8 ns). Characteristic sintering times are discussed further in Chapter 5.

To examine how sintering may impact the peak pyrometric temperature, the incandescence signal from monodisperse aerosols containing particles of different diameters is modeled with Eqs. (3.1) and (3.8), and

the peak pyrometric temperature is then calculated using Eq. (3.12). Figure 3-12a shows that the peak temperature increases as a function of equivalent diameter to a maximum of 2356 K at 255 nm, and then decreases with further increase in diameter (reasons behind this trend are discussed in Chapter 6). This decrease is due to the large thermal mass of the larger particles that are large enough to counteract the increase in the absorption cross-section in the energy balance equation.

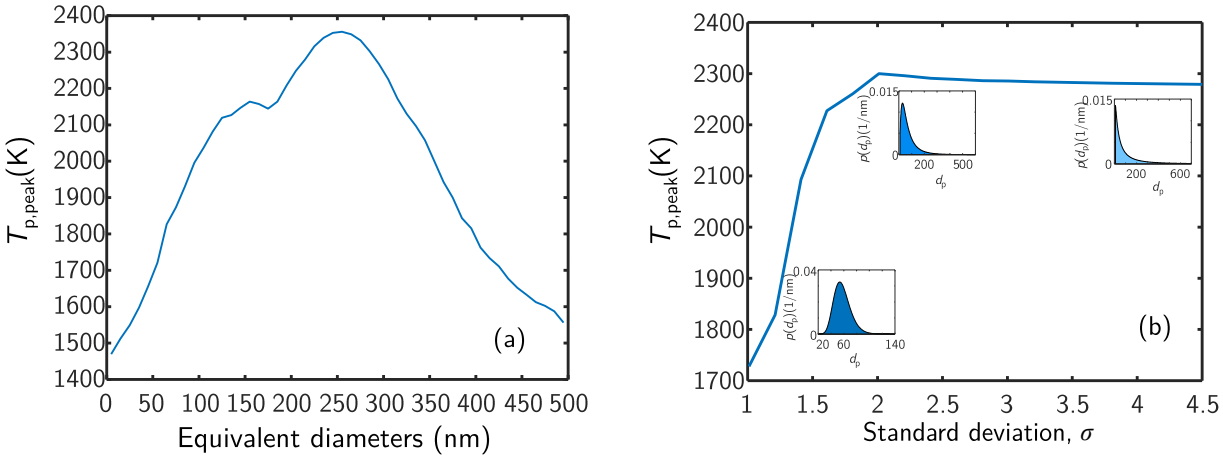


Figure 3-12: Modeled peak thermodynamic temperatures for: **(a)** an aerosol of monodisperse aerosol of iron spheres as a function of particle size, and **(b)** polydisperse aerosols composed of iron spheres, each having diameters that obey lognormal distributions sharing the same mean but different widths.

Figure 3-12b examines how the polydispersity of particle sizes may affect the pyrometric temperature by considering the peak pyrometric temperatures of aerosols containing particles having diameters that are distributed according to different lognormal PDFs, but with the same mean diameter of 57 nm. The peak temperatures of the aerosol increase with an increase in the standard deviation. This is because the largest particles have a larger influence on the incandescence signal, both due to their larger absorption cross-section and the fact that they reach higher peak temperatures.

Since Fe nanoparticles readily oxidize when exposed to air [134] and form a thin oxide shell, the possibility of absorption enhancement by an iron core – oxide shell structure is also considered. However, results based on absorption efficiencies computed from Mie theory for a thin shell thickness of 2.5 nm show only a slight peak pyrometric temperature increase of ~100 K for a range of iron cores between 70 – 270 nm (*cf.*, Appendix A.2).

3.5.4. Apparent anomalous cooling from grain-boundary sintering[2]

The apparent anomalous cooling effect is apparent from the rapid decay in pyrometric temperature observed in Figure 3-8b for Mo after the peak temperature. During pure conduction cooling, Eq. (3.1) can be written as $\log(T_{\mathrm{p,eff}} - T_{\mathrm{g}}) = C_1 t + C_2$ [27,127], where C_1 is a constant dependent on the thermal accommodation coefficient and the degrees-of-freedom of the buffer gas molecule (detailed derivation is shown in Chapter 7), and C_2 is a regression constant. It is more apparent in Figure 3-13, which shows the logarithm of the difference between particle temperature and gas temperature versus time. In the absence of evaporative cooling (since pyrometric temperatures remain below the evaporation threshold for Mo), this temperature difference represents the "driving potential" for conduction, and, in conduction-dominated cooling, one would expect the temperature to decay roughly exponentially, or linearly on a semilog plot [101]. Instead, Figure 3-13 reveals a period of enhanced temperature decay that lasts approximately 400 ns. This timescale was found to increase with increasing fluence. The apparent drop in temperature has been labelled $\Delta T_{\mathrm{p,eff}}$.

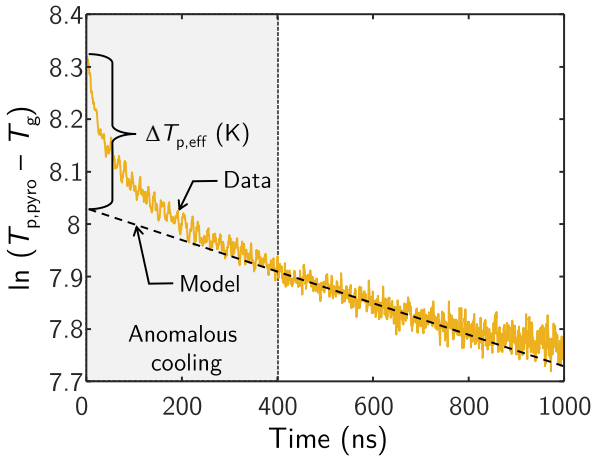


Figure 3-13: Pyrometric temperatures of Mo aerosol as a function of time, showing the duration of the anomalous cooling (shaded region). Particles are irradiated at a fluence of 2.41 mJ/mm^2. The gas temperature is taken as 293 K, and the peak temperature of the Mo aerosol is 2395 K.

Several alternate hypotheses have been proposed to explain this phenomenon. First, it has been speculated in the literature that enhanced absorption and apparent anomalous cooling may be due to contamination

[2] In this work, Dr. Sina Talebi-Moghaddam estimated the absorption properties on molybdenum aggregates using the multisphere T-matrix (MSTM) method, and contributed to the simulation of grain boundary sintering of a molybdenum dimer.

of the LII signal by inverse bremsstrahlung absorption and neutral bremsstrahlung emission, respectively, due to a plasma enveloping the nanoparticle. Talebi-Moghaddam *et al.* [89] show that neutral bremsstrahlung emissions should be gas-dependent due to the electron momentum cross-section increasing with an increase in polarizability; hence, more polarizable gas molecules should produce more bremsstrahlung emissions from the aerosol and affect the peak pyrometric temperatures. On the contrary, Figure 3-14a demonstrates that the peak pyrometric temperatures are approximately independent of the bath gas. This discounts the possibility that the apparent anomalous cooling phenomenon is due to neutral bremsstrahlung. Furthermore, since bremsstrahlung emission is due to the scattering of the thermionically emitted electrons off both the ionized nanoparticles and the more abundant bath gas neutrals, one would expect that emissions from interactions with bath gas neutrals would be dominate those originating from interactions with ionized nanoparticles, which should further exacerbate the effect of bath gas type which are absent from the current results [89]. These findings are consistent with the theoretical calculations from Talebi-Moghaddam *et al.* [89] that predict that no bremsstrahlung emissions are expected at laser fluences below 10 mJ/mm^2. While Figure 3-14b shows that the time-resolved pyrometric temperatures have the same initial temperature decay regardless of the bath gas, the temperature profiles differ slightly at later cooling times. Simulations of isolated spherical molybdenum nanoparticles in different gases suggest that this discrepancy at later cooling times may be due to the different conductive cooling powers of the bath gas species (*cf.,* Appendix A.3). This is discussed in more detail, for soot, in Chapter 7.

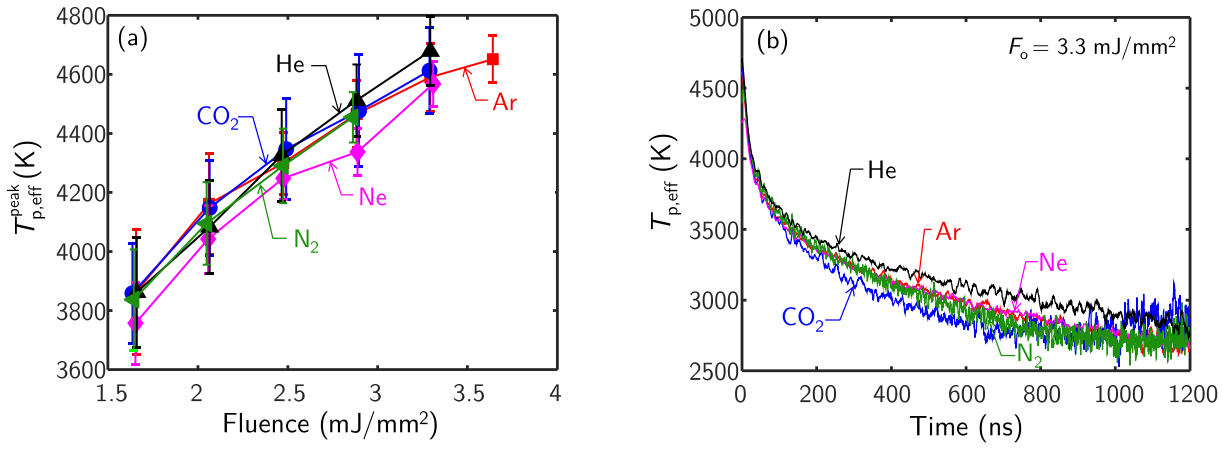


Figure 3-14: (a) Peak pyrometric temperatures, and **(b)** Pyrometric temperature profiles from aerosols of Mo nanoparticles in various motive gases.

Since the pyrometric temperatures of the Mo nanoaerosol reach temperatures above the melting point of molybdenum, one would expect Mo nanoaggregates to sinter through the viscous mechanism over a

timescale similar to those predicted for the Fe nanoparticles. This observation is supported by the TEM images shown in Figure 3-7b. Nevertheless, explored here is the possibility that the observed pyrometric temperature decay may not be indicative of the true thermodynamic temperature of the particles, but rather a spectroscopic phenomenon caused by laser-induced morphological changes to the particle that occur over a similar timescale, *i.e.*, grain boundary diffusion. This exploration is grounded in the possibility that the true temperature of some aggregate size classes may not reach the observed pyrometric temperature (Figure 3-2) but remain at temperatures that favor grain boundary sintering. Since the absorption cross-sections of aggregates are much larger than spheres of equivalent volume (*cf.*, Figure 3-11), these unmelted aggregates would increasingly influence the pyrometric temperature as the particles cool.

The potential effect of such a scenario on the pyrometric temperature is illustrated by comparing the spectral absorption efficiencies of 10 randomly-oriented aggregates with those of a fully-sintered sphere after the laser pulse. Figure 3-15a shows that the spectral absorption efficiency at the lower detection wavelength (445 nm) drops significantly due to sintering, while the spectral absorption efficiency at the higher detection wavelength (747 nm) remains mostly unchanged. Therefore, the ratio of $Q_{\text{abs},\lambda 1}/Q_{\text{abs},\lambda 2}$ in Eq. (3.10) will drop during and after laser heating, leading to an apparent drop in temperature, $\Delta T_{\text{p,eff}}$, as shown in Figure 3-15b, which also shows that the magnitude of the drop increases for larger aggregates. The variation in pyrometric temperature is consistent with what is observed experimentally over the apparent anomalous cooling period.

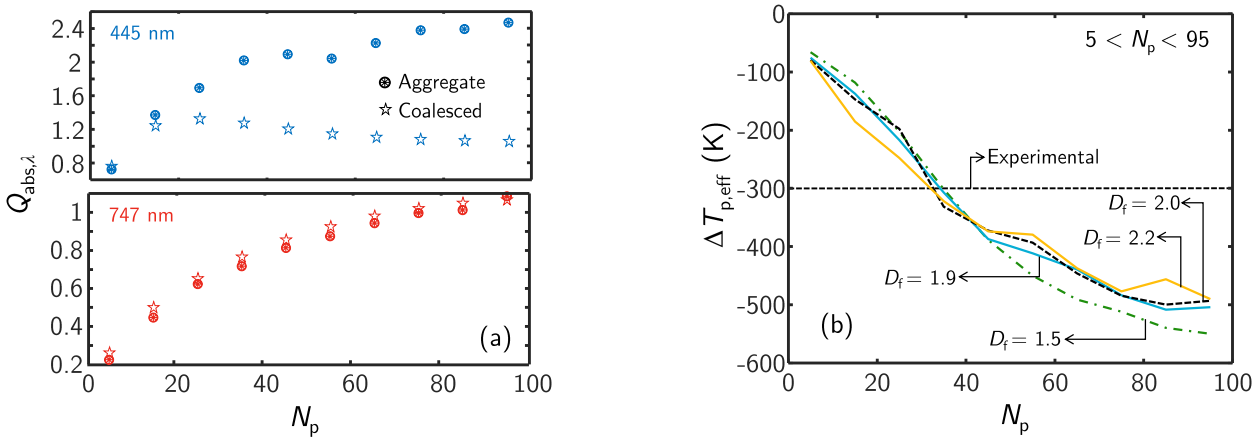


Figure 3-15: (a) Changes in absorption efficiency between Mo aggregates of various sizes and a fully sintered sphere having the same d_v at a wavelength of 445 nm and 747 nm; (b) corresponding change in the pyrometric temperature as a function of N_p.

Equations (3.15) and (3.16) are evaluated to determine the timescale of an assumed grain boundary sintering of Mo nanoaggregates. The temperature history of the nanoparticles is obtained from the simulated

temperature of a 45 nm Mo nanoparticle irradiated with a fluence of 2 mJ/mm^2 and reaches a peak temperature of 2380 K. The nanoparticles are assumed to still be in point contact at the peak temperature, at which point they begin to sinter.

Figure 3-16 shows the temporal evolution of the grain boundary neck length and diffusivity of a two-sphere system modelled according to Eq. (3.14) , with parameters shown in Table 3-2.

Table 3-2: Parameters used to evaluate Eq. (3.14) for molybdenum.

Parameter	**Value**
D_0 [cm^2/s]	0.1 (single crystal grain boundary) [135]
Q [kCal/mol]	92.2 [135]
γ_{sv} [J/m^2]	0.1 [136,137]
δ_{gb} [nm]	d_p (= 45 nm)
Ω [m^3]	$(4\pi/3)\ a^3$
	a is the atomic radius of Mo taken as 139 pm [117]

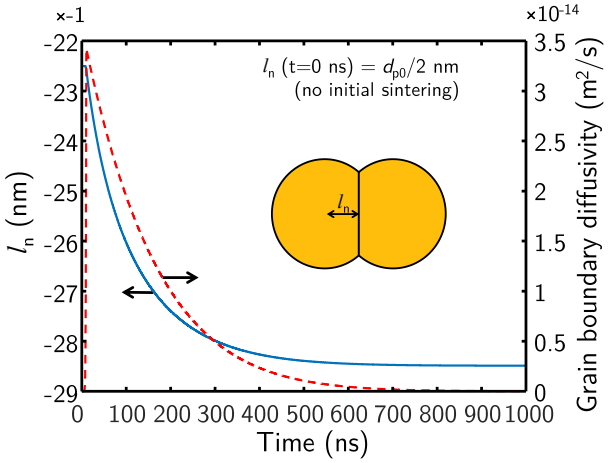


Figure 3-16: Evolution of grain boundary distance (Eq. (3.14)) between two Mo nanoparticles and the diffusivity at the grain boundary (Eq. (3.16)).

From Figure 3-16, the grain boundary neck length and diffusivity reach steady-state between 400 – 500 ns, which suggests that morphology changes continue to occur for a few hundred nanoseconds following the peak temperature. The time scale of evaluated grain boundary sintering is consistent with the time scale of apparent anomalous cooling, further suggesting that sustained morphology changes after the laser pulse could be contributing to the apparent rapid drop in temperature. However, further investigation still needs to be carried out to ascertain the exact time scale of sintering for the Mo nanoaggregates and how this may affect the observed pyrometric temperature.

3.6. Conclusions

Several hypotheses have been advanced to explain the observed deviations from the TiRe-LII model, including excessive absorption and anomalous cooling in the LII data of metal nanoparticles, including the possibility of signal corruption due to bremsstrahlung emission from a plasma. However, this study suggests a simpler explanation: the spectroscopic model used in most LII studies on metal aerosols assumes that the particles exist as isolated nanospheres, which is often not the case.

From the analysis of Fe nanoaerosols, it was found that although aggregation enhances the absorption cross-sections of the nanoparticles, simulated peak pyrometric temperatures still do not reach experimentally observed pyrometric temperatures. Irradiated TEM samples showed that the Fe aggregates rapidly coalesce through viscous forces during laser heating, and calculated viscous sintering times indicated full sintering to occur before the peak temperature is reached, suggesting that observed emissions may come from large, sintered spheres.

Although the pyrometric temperatures of the Mo aerosols suggested that viscous sintering may occur, the duration of the apparent anomalous cooling phenomena is consistent with the timescales required for grain sintering. Moreover, the change in absorption cross-section as the particles sinter would manifest as a drop in temperature. It is speculated that some of the aggregates do not reach the melting point of Mo, and these aggregates dominate the LII signal due to their much larger absorption cross-section compared to fully sintered spheres.

The simulated aggregates in this chapter consist of primary particles in point contact; however, some overlap between primary particles may be present due to partial sintering, which may intensify the electromagnetic field during laser heating of the aggregate through an “antenna effect”, thereby further enhancing the absorption cross-section [138]. This scenario is further explored in the next chapter.

Chapter 4

Absorption properties of metal nanoparticle aggregates during time-resolved laser-induced incandescence[3]

The research presented in this chapter explores how nonuniform absorption within metal nanoparticle aggregates, aggregate morphology and orientation, and sintering of primary particles may affect TiRe-LII signals from metal nanoparticle aerosols. The investigations consist of numerical simulations to predict the absorption properties of the aggregates during laser irradiation. Several light scattering models, including the Mie theory, the multi-sphere T-matrix method, and the discrete dipole approximation method, are used to determine aggregate absorption properties depending on the considered morphology, which could be either isolated spherical primary particles, aggregates of primary spheres in point contact, or overlapping primary particles.

[3] Information presented in this chapter is based on the published work:
Robinson-Enebeli, S., Schulz, C., and Daun, K. J., 2024, "Investigating the Absorption Properties of Metal Nanoparticle Aggregates during Time-Resolved Laser-Induced Incandescence," J. Quant. Spectrosc. Radiat. Transf., **322**, p. 109009.

4.1. Introduction

The incomplete understanding of the laser–nanoparticle interaction during laser heating, as well as the impact of laser-induced morphological changes on the absorption cross-section, are possible sources of reported deviations from straightforward analysis, including effects previously termed as excessive absorption and apparent anomalous cooling, that are yet to be fully explained [19,20,139]. While the use of the full Mie theory model improved temperature estimates over those predicted from improper use of the Rayleigh approximation, temperature predictions remain below experimental pyrometric temperatures [20]. The analysis presented in Chapter 3 shows that accounting for metal nanoparticle aggregation and sintering effects may partially resolve the reported effects [139]. However, other factors that may arise due to nanoparticle aggregation need further investigation for a fuller understanding of how the aggregate structure may influence the TiRe-LII signal.

Laser-induced incandescence is most frequently applied to soot-laden aerosols, where isolated particles are in the Rayleigh regime or, if aggregated, their absorption can be modeled by the Rayleigh–Debye–Gans fractal aggregate (RDG-FA) theory. Therefore, all particles within a soot aggregate absorb proportionally to their volume because their dipoles oscillate in phase within the electromagnetic field throughout the entire particle. Due to the large refractive indices of metals, metal nanoparticle aggregates are expected to couple strongly with the electric EM-field due to their dipoles oscillating out of phase and interacting with each other, which can lead to nonuniform absorption of laser radiation within a particle, for example, by the primary particles within a metal nanoparticle aggregate. The resulting inhomogeneous temperature distribution within the aggregates may then affect the pyrometrically-inferred temperature, which is often used in TiRe-LII to infer attributes of the metal aerosol. Temperature nonuniformities may also occur within the aerosol due to different aggregate morphologies or different orientations of similarly shaped aggregates relative to the direction of wave propagation, stemming from a significant variability of absorption cross-sections of the aggregates within the aerosol.

Primary particles within synthesized metal aggregates may be sintered to a certain degree as a consequence of laser heating, as shown in the TEM micrographs of SDG-synthesized iron nanoparticles in Figure 3-4, which may impact the absorption cross-section of the aggregate [139]. The degree of partial sintering may be amplified due to laser-induced changes to the particle morphology as the aggregates heat

up. While primary particle overlap has little to no effect on the absorption properties of soot aggregates in the wavelength range relevant to TiRe-LII [140], this is not the case for metal aggregates that couple more strongly to the electric field and provide greater electrical conductivity across the structure. In a loosely connected aggregate, temperature gradients may be present in the initial phase, during, and immediately after laser heat-up, which introduces additional difficulties in defining effective aggregate temperatures to be used in TiRe-LII models.

The objective in this chapter is to show the effects of nonuniform heating of metal aggregates and their subsequent sintering on the TiRe-LII data. The distribution of absorption cross-sections of primary particles in point contact within iron aggregates of differing morphologies is computed using the multi-sphere T-matrix (MSTM), and the resulting temperature distribution is investigated. The discrete dipole approximation (DDA) method is used to investigate the effect of sintering on the absorption properties of the iron aggregates. It is shown that there are absorption nonuniformities within the aggregates that increase with increasing aggregate sizes and may contribute to excessive absorption and anomalous cooling for aggregates with minimal overlap between primary particles. The fractal dimension of a metal aggregate also has a strong effect on the absorption cross-sections of the individual primary particles within the aggregate. For the moderately anisotropic iron aggregates considered here, the total absorption cross-section varies weakly with orientation. Additionally, partial sintering as a result of laser heating enhances the total absorption cross-section of the aggregate in a manner that depends on wavelength.

4.2. Modeling the temperature and optical properties of metal aggregates

In this section, the modified heat transfer and spectroscopic submodel specific to this work is presented. The aggregate generation models and the corresponding absorption models are also presented. These models are used to interpret the LII data later in the chapter.

4.2.1. Modified heat transfer model

The heat transfer submodel used in this chapter is identical to that presented in Chapter 3, with the following additions and caveats:

i. The nanoparticle can be either an isolated primary particle, an aggregate with primary particles in point contact, or an aggregate with overlapping primary particles to represent partial particle sintering.

ii. The volume of a partially sintered aggregate of spheres is determined from a Monte Carlo algorithm, and $N_{\mathrm{p}}^{\mathrm{eff}} = 6\,V_{\mathrm{p}}/\pi d_{\mathrm{p}}^{3}$ is the volume-equivalent number of primary particles ($N_{\mathrm{p}}^{\mathrm{eff}}$ is taken as the nearest integer of the result). When primary particles are in point contact, $N_{\mathrm{p}}^{\mathrm{eff}}$ is equivalent to N_{p} and $V_{\mathrm{p}} = N_{\mathrm{p}}\pi d_{\mathrm{p}}^{3}/6$, where V_{p} is the volume of the particle. The expression for $N_{\mathrm{p}}^{\mathrm{eff}}$ models an aggregate with overlap as a point contact aggregate with a certain number of particles, $N_{\mathrm{p}}^{\mathrm{eff}}$, that has a similar volume as the aggregate with primary particle overlap. This approximation becomes less reasonable with increasing overlap and may become invalid when the overlap exceeds 50 %, which would require modification of the heat transfer model to appropriately account for the surface area of the aggregate.

iii. The evaporation model assumes that the primary particles remain in point contact during mass loss after laser heating, which may not be the case due to sintering.

iv. The absorption efficiency of the aggregate is computed from the Multi-Sphere T-Matrix (MSTM) method [9,10] for a randomly oriented aggregate at the laser wavelength, λ, and is defined with respect to the equivalent diameter of the aggregate. The MSTM algorithm provides the absorption cross-sections of individual primary particles, which are summed to obtain the absorption cross-section of the aggregate [141]. When the aggregate is sintered, the entire cross-section of the aggregate is found using the discrete dipole approximation (DDA) [142].

4.2.2. Modified spectroscopic model

When analyzing TiRe-LII signals from soot particles, it is common practice to assume that the soot aggregate is isothermal at any instant, and the temperature may be found from the absorbed laser energy calculated using the total absorption cross-section of the aggregate [111,143], as well as the signal emitted by the aggregate. Previous studies have also reported an enhancement of soot absorption properties due to aggregation that results in multiple scattering within the aggregate [109,111,144–146], although this effect is found to be small for soot aggregates having primary particles less than 30 nm in diameter [143].

These assumptions are unlikely to apply to metal aggregates, however, due to their strong coupling with the external EM-field, as depicted by their large refractive indices, causing significant local field

enhancements [147]. Consequently, primary particles in the aggregate may absorb very different amounts of laser energy, leading to significant temperature variations within the aggregate depending on the extent of thermal coupling between the primary particles. Partial sintering of the metal aggregate that results in larger electrically conductive structures may also alter the absorption properties.

Consequently, a more detailed equation is needed to describe emission from the laser-heated metal nanoparticle aggregates within a probe volume than is normally used in LII studies of soot. The instantaneous emission from a probe volume of aggregates may be written as

$$J_\lambda\left(t\right) = C_\lambda \Lambda \sum_{N_\mathrm{p}} p\left(N_\mathrm{p}\right) \int_{\mathbf{x}} \mathbf{C}_{\mathrm{abs},\lambda}\left(\mathbf{m}_\lambda, d_\mathrm{p}, \mathbf{x}, N_\mathrm{p}\right) \cdot \mathbf{I}_{\mathrm{b},\lambda}\left[\mathbf{T}\left(d_\mathrm{p}, \mathbf{x}, t\right)\right] p\left(\mathbf{x}\right) \mathrm{d}\mathbf{x} \tag{4.1}$$

where C_λ is a calibration constant, Λ is the intensity scaling factor (ISF) that accounts for the volume fraction of nanoparticles [77,106], d_p is the primary particle diameter, and $\mathbf{x}$, $\mathbf{C}_{\mathrm{abs},\lambda}$ $\mathbf{I}_{\mathrm{b},\lambda}$, and $\mathbf{T}$ are vectors of dimension N_p containing the centroid location, spectral absorption cross-section, blackbody spectral intensities, and temperatures of the primary particles, respectively, in a given aggregate at time t. Equation (4.1) assumes that N_p and $\mathbf{x}$ are uncorrelated and N_p is considered a pseudo-continuous variable ranging from zero to infinity, even though it is an integer starting at one.

The inner integral of Eq. (4.1) is taken over all possible aggregate geometries of size class N_p, weighted by the joint probability density of the primary particle location, $p(\mathbf{x})$. In practice, this may be approximated by averaging over aggregates sampled from the cluster–cluster aggregate (CCA) algorithm [110],

$$\begin{aligned} &\int_{\mathbf{x}} \mathbf{C}_{\mathrm{abs},\lambda}\left(\mathbf{m}_\lambda, d_\mathrm{p}, \mathbf{x}, N_\mathrm{p}\right) \mathbf{I}_{\lambda,\mathrm{b}}\left[\mathbf{T}\left(d_\mathrm{p}, \mathbf{x}, t\right)\right] p\left(\mathbf{x}\right) \mathrm{d}\mathbf{x} \\ &\quad \approx \frac{1}{N_\mathrm{p}} \sum_{k=1}^{N_\mathrm{p}} \mathbf{C}_{\mathrm{abs},\lambda}\left(\mathbf{m}_\lambda, d_\mathrm{p}, \mathbf{x}^k, N_\mathrm{p}\right) \mathbf{I}_{\lambda,\mathrm{b}}\left[\mathbf{T}\left(d_\mathrm{p}, \mathbf{x}^k, t\right)\right], \quad \mathbf{x}^k \sim p\left(\mathbf{x}\right) \text{ (CCA)} \end{aligned}, \tag{4.2}$$

which produces aggregates with uniformly sized primary particles in point contact. In other words, the CCA algorithm samples aggregate geometries from an underlying distribution described by $p(\mathbf{x})$ following a Markov-chain Monte-Carlo procedure.

Once the inner integral is evaluated, the summation over N_p is carried out with each aggregate size weighted by its probability within the probe volume, $p(N_\mathrm{p})$. The number of primary particles per aggregate, N_p, or, equivalently, the radius of gyration, R_g, usually obeys a wide distribution due to the random processes

that underly aggregate assembly. These parameters are empirically related by $N_\mathrm{p} = k_\mathrm{f}(2R_\mathrm{g}/d_\mathrm{p})^{D\mathrm{f}}$, where k_f and D_f are the fractal prefactor and fractal dimension, respectively. All of the modeled iron aggregates in this work do not exceed 270 nm in any direction.

If the particles within a probe volume emit and absorb in the Rayleigh regime in the case of spheres [20] or can be approximated by Rayleigh–Debye–Gans fractal aggregate (RDG-FA) theory in the case of aggregates [109], Eq. (4.1) can be computed at two wavelengths and the ratio taken to determine an effective pyrometric temperature, $T_\mathrm{p,pyro}$, of the probe volume estimated by two-color pyrometry according to Eq. (2.23). It is assumed that the estimated spectral absorption cross-section in any direction is equal to the spectral emission cross-section in that direction, following Kirchhoff's law. The instantaneous effective temperature of the particle ensemble may be interpreted as a representative average temperature of the particles within the probe volume. This procedure is standard for analyzing TiRe-LII data from soot particles and is also appealing for analyzing metal nanoparticles since the effective temperature does not depend on particle size, which is often the sought-after parameter [20]. There are, however, a number of factors that distance this temperature from the thermodynamic particle temperature, especially for metal nanoparticles. These include: (1) the inapplicability of the Rayleigh model or, for aggregates, the RDG-FA model, to represent the absorption cross-section of sintered and non-sintered metal aggregates; (2) the fact that the particles may not be isothermal. These issues are explored later in the chapter.

4.2.3. Aggregate modeling

Random aggregates are generated using the tunable CCA algorithm [110], which produces aggregates with uniformly sized primary particles in point contact.

Primary particles may sinter during laser heating via grain boundary diffusion or, if they are liquefied upon heating by the laser pulse, they coalesce through viscous flow [124,125]. Overlap of primary particles during sintering is simulated by multiplying the centroid locations of the primary particles by $(1 - C_\mathrm{ov})$, where C_ov is the overlap factor,

$$C_\mathrm{ov} = \frac{r_i + r_j - d_{ij}}{r_i + r_j}; \qquad 0 \geq C_\mathrm{ov} \geq 1\,, \tag{4.3}$$

where r_i and r_j are the radii of primary particles i and j, respectively, and $d_{ij}$is the distance between their centers. Necking, defined as the accumulation of material around the primary particle contact sites that

results in a narrow neck between primary particles, was neglected but can occur during the sintering process. In the case of laser-induced sintering at low enough fluences to assume negligible mass loss, the volume of the aggregate is adjusted after simulating sintering to conserve mass by increasing the diameters of the primary particles by equal amounts.

The aggregate is considered solid prior to laser heating and molten after laser heating, leading to coalescence. The absorption cross-sections of iron is modeled with bulk refractive indices of solid and molten states obtained from Ref. [148] and [149], respectively, as shown in Figure 4-1. Size [150] and temperature [86,151] dependence of the refractive index are not considered in this work, but, as determined in Appendix A.4, for the size classes considered in this thesis work, there is a negligible influence on the resulting optical properties.

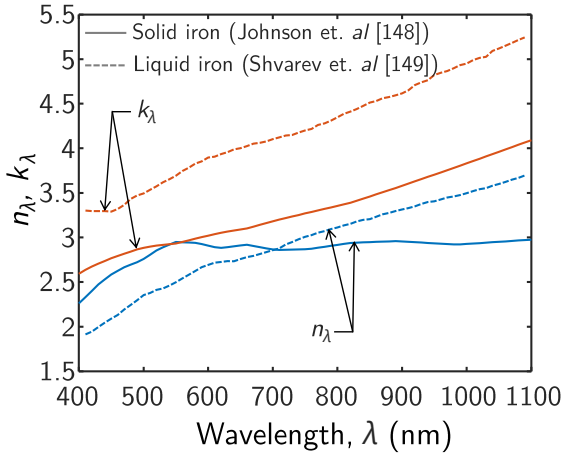


Figure 4-1: Refractive indices of solid and liquid iron used in this work.

4.2.4. Absorption modeling

The absorption efficiency of the particle is computed for three scenarios: an isolated sphere, an aggregate consisting of primary particles in point contact, and an aggregate with primary particles with a defined overlap. The absorption efficiencies for these scenarios are computed using Mie theory [94], the multi-sphere T-matrix method [141], and the discrete dipole approximation [142], respectively.

4.2.4.1. Mie theory

The equations for Mie scattering and absorption are derived by solving the Maxwell equations in spherical polar coordinates with field boundary conditions at the surface of the particle [94,150]. The exact analytical

solution for an isolated spherical particle has the form of an infinite summation of Riccati Bessel functions that depend on the refractive index of the material and the size parameter $x_p = \pi d_p/\lambda$ [94,150]. In this work, the Mie theory computation is carried out in the MATLAB program implemented by Schäfer *et al.* [152].

4.2.4.2. Multi-sphere T-matrix

Mie theory can be extended to model the absorption cross-section of aggregates consisting of spheres in point contact by virtue of the linearity of the Maxwell equations and boundary conditions [150]. The approach employs the superposition of the incident and scattered fields from each constituent primary particle to obtain the EM-field surrounding the aggregate as a whole. The scattered field from each particle is represented by an expansion of spherical wave functions about the particle origin [153]. The boundary conditions of each particle consist of the incident field and the scattered field from all other particles in the aggregate. The scattering coefficients of the particles within the aggregate are related linearly, through a transition (T) matrix, to the Mie scattering coefficients that originate from the incident field [153]. In summary, the absorption cross-section of each constituent sphere is calculated due to the incident field and the scattered field from other particles within the aggregate, and the total absorption cross-section of the aggregate is then the sum of the absorption cross-sections of the primary particles [153].

In this work, the T-matrix method is implemented according to Mackowski and Mishchenko [141] using the MSTM version 3.0 code. In this implementation, when $x_p << 1$ and the refractive indices are large, care must be taken to ensure that the expansion terms converge [153].

4.2.4.3. Discrete dipole approximation

The discrete dipole approximation (DDA) provides a numerical solution to the Maxwell equations by approximating a geometry with a finite array of polarizable points (dipoles) that are coupled together by the incident electric field and the electric fields of the other dipoles [154]. Each dipole has a polarization $\mathbf{P}_j = \alpha_j \mathbf{E}_j$, where α_j is the dipole polarizability at j and $\mathbf{E}_j$ is the electric field at a location $\mathbf{r}_j$ due to the incident field, along with contributions from all other dipoles. The polarization of each dipole is related to the incident field, $\mathbf{E}_{\mathrm{inc},j}$, through an interaction matrix $\mathbf{A}_{kj}$ that includes retardation effects and scattering from other dipoles.

$$\sum_{k=1}^{N} \mathbf{A}_{jk} \mathbf{P}_k = \mathbf{E}_{\mathrm{inc},j} \tag{4.4}$$

Once Eq. (4.4) has been solved to obtain the polarization of each dipole, the extinction and absorption cross-sections are determined by

$$C_{\text{ext}} = \frac{4\pi k}{\left|\mathbf{E}_0\right|^2} \sum_{j=1}^{N} \text{Im}\left(\mathbf{E}_{\text{inc},j}^{*} \cdot \mathbf{P}_j\right) \tag{4.5}$$

$$C_{\text{abs}} = \frac{4\pi k}{\left|\mathbf{E}_0\right|^2} \sum_{j=1}^{N} \left\{ \text{Im}\left[\mathbf{P}_j \cdot \left(\alpha_j^{-1}\right)^{*} \mathbf{P}_j^{*}\right] - \frac{2}{3} k^3 \left|\mathbf{P}_j\right|^2 \right\} , \tag{4.6}$$

where $k = \omega/c_0$ in eqns. (4.5) and (4.6).

This method requires that: (1) $|\mathbf{m}_\lambda| 2\pi d/\lambda \lesssim 1$, where $\mathbf{m}_\lambda$ is the spectral refractive index of the material and d is the dipole spacing; and (2) d is small enough to appropriately capture the target geometry. Criterion (1) is usually satisfied when $|\mathbf{m}_\lambda - 1| \lesssim 3$ [155]. When the refractive index becomes too large, the accuracy of DDA drops and a smaller value of d compared to that suggested by criterion (1), *i.e.*, a larger number of dipoles, is needed to improve accuracy. The DDA method is implemented using DDSCAT 7.3 [142].

4.3. Results and discussion

4.3.1. Absorption cross-section distribution within metal aggregates

Primary particles within a metal nanoparticle aggregate are expected to absorb varying amounts of light due to local variations in the EM-field, induced by multiple scattering within aggregates [109,146,147]. The extent of this effect and its dependence on aggregate size were investigated with four differently sized aggregates: N_p = 20, 70, 130, and 250. Aggregates were generated with the CCA algorithm [110] with a prefactor $k_\text{f} = 1.3$, a fractal dimension $D_\text{f} = 1.78$, and uniform primary particle diameters of 6 nm, which is consistent with the SDG-synthesized nanoaggregates shown in Figure 3-4. The absorption efficiency for each primary particle within the randomly-oriented aggregates at a laser wavelength of 1064 nm was computed by MSTM [141].

Figure 4-2 shows the distributions of effective absorption cross-sections of primary particles within the aggregates normalized to that of an isolated sphere, indicating that the entire structure increases in absorption efficiency compared to the same number of isolated spheres. The effective absorption cross-sections are highly

nonuniform, and the heterogeneity increases with N_p. All primary particles within the aggregates experience absorption enhancements of at least a factor of 1.1 relative to an isolated sphere; in the smallest aggregate, the absorption enhancement of the highest absorbing primary particle is 2.05, while it is 2.66 in the largest aggregate. Assuming the aggregate structure remains unchanged during laser excitation, and that the primary particles remain thermally-isolated during heating, this would lead to a difference between the highest and lowest absorbing primary particles within the aggregate of ~1340 K at the peak temperatures at a fluence of 2.45 mJ/mm^2 with the lowest absorbing sphere reaching temperatures of ~1600 K. Parts of the aggregate that reach temperatures that exceed the melting point will likely sinter and coalesce.

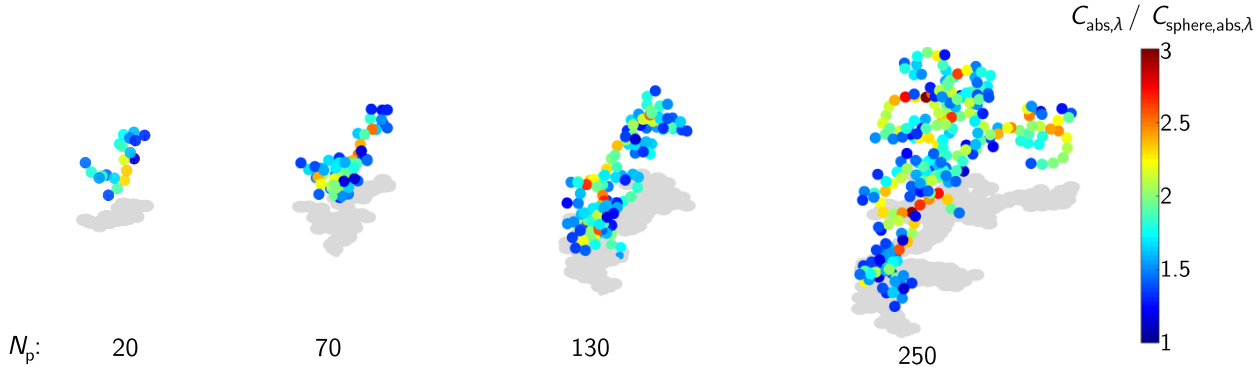


Figure 4-2: Spatial distribution of the effective absorption cross-section at 1064 nm of primary particles with uniform diameters of 6 nm ($x_p = 0.0177$) within iron aggregates of $N_p = 20$, 70, 130, and 250 randomly oriented relative to the EM-field, computed by MSTM, relative to the absorption of an isolated sphere. The aggregates have fractal parameters of $k_f = 1.3$ and $D_f = 1.78$. $C_{pp,abs,\lambda}$ is the absorption cross-section of an isolated primary particle. The refractive index of solid iron is used in the model [148].

The absorption non-uniformities observed in the aggregate originate from EM-field enhancement through multiple scattering [109,147]. Markel *et al.* [156] have shown, through a scale-invariant analysis, that such nonuniformities are properties of fractals. They originate from fluctuations of the local field within the fractal that then cause an enhancement of the optical properties. These nonuniformities arose from interactions of the external EM-field-induced dipole field of the particles [157] (*i.e.*, multiple scattering as discussed in Refs. [109,146,147,158]). Stockman [159] shows that the fluctuations are highly chaotic and the local fields exhibit inhomogeneous localizations that originate from the dipolar eigenmodes. The local fields can be highly concentrated within regions that are smaller than the wavelength of the exciting electromagnetic wave [157,160,161]. Such localized modes have been observed experimentally for silver aggregates [161]. Other studies show that an increase in local anisotropy of the aggregate contributes to locally enhanced fields, and isotropy provides compensating effects that cancel out [162,163].

To investigate the effect of anisotropy, two aggregates of extreme fractal structures but identical N_p, with $D_f = 1.3$ and $k_f = 1.3$ for the anisotropic, chain-like aggregate and $D_f = 2.2$ and $k_f = 2.2$ for the more isotropic, compact aggregate, are analyzed and shown in Figure 4-3.

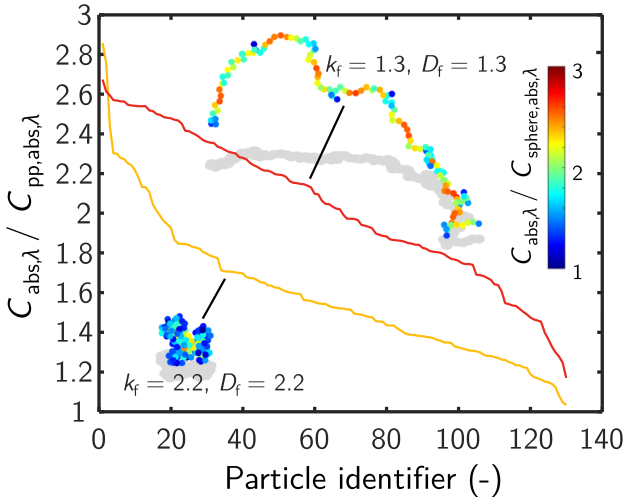


Figure 4-3: Absorption cross-sections of primary particles within a strongly anisotropic (chain-like) and a more isotropic (compact) aggregate normalized to the absorption cross-section of an isolated primary particle. The insets show the morphology of the aggregates and locations of enhanced absorption. The refractive index of solid iron is used in the model [148].

It is seen that a few particles in the compact aggregate absorb more strongly than any particle in the chain-like aggregate. However, more particles in the anisotropic chain-like aggregate generally have larger absorption cross-sections compared to the compact aggregate. Primary particle absorption cross-sections in the compact aggregate rapidly decrease compared to those in the chain-like aggregate, leading to a larger total absorption cross-section for the chain-like aggregate. Karpov *et al.* [163] show that it is the degree of local anisotropy (in a defined aggregate region) that determines the enhancement of the local EM-field, and not the entire aggregate structure. Therefore, a possible explanation for the strongly absorbing particles in the compact aggregate is that these particles are in locations of strong constructive interference from scattered light that are not cancelled out due to local anisotropy. Additionally, simulations by Quinten [147] show that near-field enhancements in locations called "hot spots" can occur already within aggregates of minimal anisotropy from constructive interference. This suggests that nonuniform absorption and the locations of high absorption enhancements are the results of a combination of local anisotropy and constructive interference of intense multiply scattered light from neighboring particles.

Each primary particle within an aggregate can be assumed to reach a homogeneous temperature during the laser pulse since the phonon mean free paths of most metals at room temperature range from 4 to 10 nm, and the phonon relaxation time is in the order of picoseconds [164]. On the other hand, the thermal contact between primary particles in point contact is expected to be much weaker, so the highly nonuniform absorption cross-sections of metal aggregates suggest that they cannot be modeled as isothermal, as is normally done for soot aggregates [111,143]. Accordingly, a temperature based on the emitted incandescnce can be computed in two ways: (1) by assuming each particle within the aggregate is thermally isolated and summing over all their emitted radiation (*i.e.*, Eq. (4.1) while assuming all aggregates have the same size) and computing a temperature from pyrometry (using the cross-sections of each particle that are estimated by the MSTM model); (2) assuming an isothermal aggregate temperature and using the total absorption cross-section of the randomly-oriented aggregate estimated by the MSTM model to predict the temperature using Eq. (3.1).

Figure 4-4 compares the pyrometric temperature that one would observe for a hypothetical uniform-temperature aerosol of the aggregate in question using two-color pyrometry according to Eq. (2.23) for these two scenarios, along with the thermodynamic temperatures of the primary particles having the largest and smallest absorption cross-sections, and thus the highest and lowest temperatures. The peak effective temperature of the fully thermalized aggregate is ~400 K lower compared to the case of thermally isolated primary particles and cools more slowly due to the large heat capacity of the aggregate. A rapid temperature reduction is observed for the highest absorbing particle, which is driven primarily by evaporation. When evaporation from all spheres is considered in the case of thermally isolated primary particles, this manifests as a rapid temperature reduction of the aggregate, which the TiRe-LII model would not otherwise predict under the assumption of an isothermal aggregate.

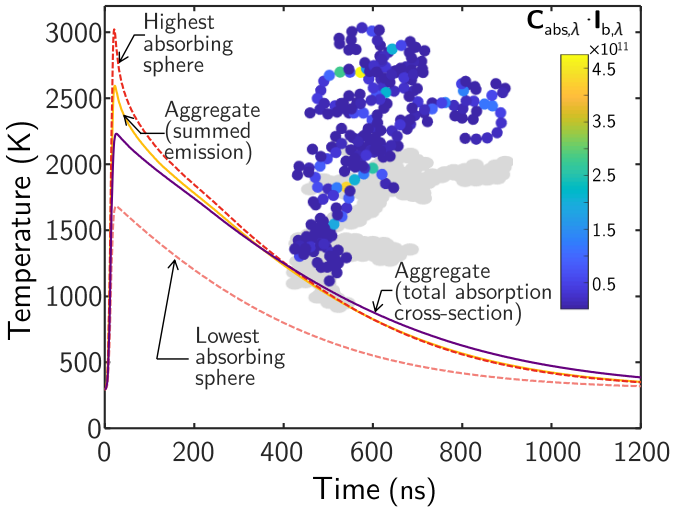


Figure 4-4: Temporal variation of the effective temperature derived from the theoretical TiRe-LII signal for the highest and lowest absorbing primary particles in an iron aggregate of 250 primary particles, and that of the aggregate computed by summing emissions from thermally-isolated primary particles and using the total absorption cross-section of the aggregate; irradiated at 1064 nm. The bath gas is N_2 at 295 K and 1 bar and the laser fluence is 2.5 mJ/mm^2. Temperatures of the spheres and aggregate from integrated emission are computed from two-color pyrometry, by taking the ratio of the signals at 445 and 747 nm and using the absorption function of solid iron at the corresponding wavelengths. The Inset is the distribution, $\mathbf{C}_{abs,\lambda} \cdot \mathbf{I}_{b,\lambda}$, within the aggregate at a detection wavelength of 445 nm. The refractive index of solid iron is used [148].

Previous studies identified anomalous cooling for molybdenum nanoparticles, characterized by an initial rapid reduction in temperature below the melting point of the metal that lasted for ~400–500 ns [19,139], while a similar rapid reduction in temperature for iron nanoparticles was attributed to evaporation of the nanoparticles to which the TiRe-LII model was regressed [19]. The results of Figure 4-4 show both a higher peak temperature and its rapid reduction for aggregates, suggesting that nonuniform heating also contributes to the initial rapid reduction in temperature and introduces a cooling phenomenon similar to anomalous cooling, which has not been previously identified for iron nanoparticles but was attributed to evaporation. This phenomenon is further enhanced by sintering, as discussed later. However, when primary particles coalesce or sinter upon laser heating [139], the aggregate structure moves to thermal equilibrium more quickly due to better thermal contact between the particles.

4.3.2. Aggregate absorption cross-sections in the aerosol

The particle temperatures within the aerosol depend on the different aggregate morphologies in the probe volume due to their different absorption and emission characteristics in the EM-field. This makes it necessary to understand how the distribution of particle absorption cross-sections may vary in the aerosol.

Sampled aggregate morphologies differ by morphological parameters (k_f, D_f, d_p, and N_p) and consequently, their absorption cross-sections are different from each other. However, as seen from Figure 4-3, it is the local structure that defines the absorption cross-sections, *i.e.*, the exact location of the particles within the aggregate. Therefore, aggregates with identical fractal parameters may have different absorption cross-sections due to the different positions of their primary particles. To investigate absorption properties or aggregates within the aerosol, the absorption cross-sections of 100 randomly sampled aggregates with parameters of $k_f = 1.3$, $D_f = 1.78$, $d_p = 6$ nm, and $N_p = 130$ are computed. Figure 4-5a shows the distribution of the ratios of the absorption cross-sections of the highest to the lowest absorbing sphere, which gives an indication of the absorption nonuniformities within the aggregates, and Figure 4-5b shows the distribution of the total absorption cross-section of the aggregates.

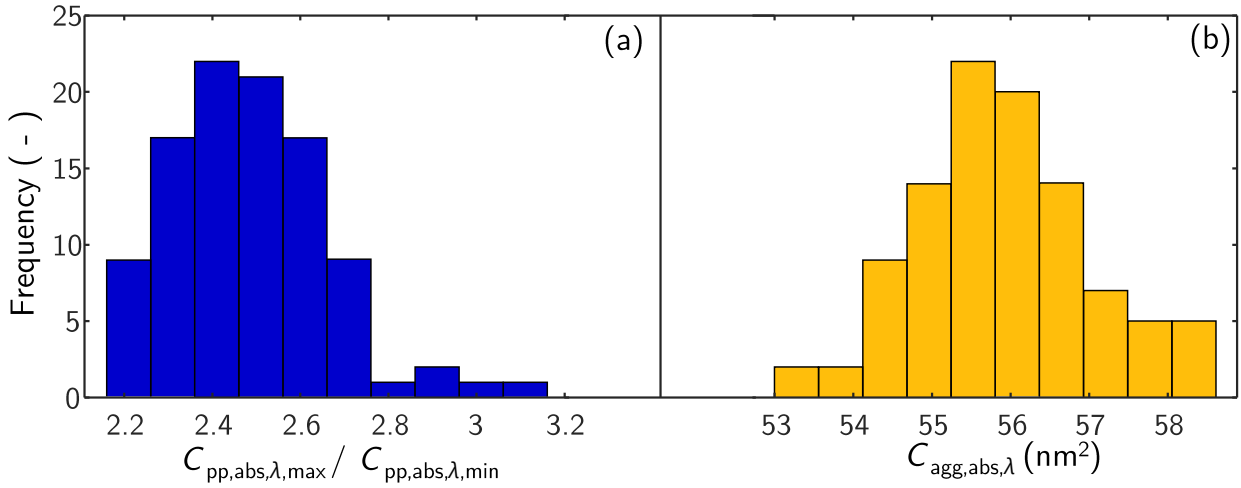


Figure 4-5: Distribution of the absorption properties of 100 random iron aggregates with identical Np and identical fractal parameters. **(a)** Ratio of absorption between strongest and weakest absorbing primary particle, and **(b)** total absorption cross-section of the aggregates.

Variations in particle positions between similarly structured aggregates translate into a variation of approximately 10 % in the total absorption cross-section of the aggregate, with a mean and standard deviation of 56 and 1.15 nm^2, respectively. Results from Figure 4-5 show that the absorption properties of a metal

nanoparticle aggregate are not unique to the aggregate fractal parameters. The models of laser absorption, Eq. (3.1), and emitted incandescence, Eq. (4.1), do not define the absorption properties as a function of the fractal parameters but rather by the exact position of the particles in the EM-field. For practical purposes, when modeling aggregates within an aerosol, a representative population of aggregates are generated with identical fractal parameters and the average of their absorption properties is computed; however, this calculation may be computationally intensive for metal aggregates compared to soot aggregates due to the larger refractive indices of metals compared to carbonaceous material.

Thus far, the variance in aggregate absorption has been discussed in the context of the random orientation of aggregates in the EM-field. For a particular aggregate geometry, the absorption properties may vary as a function of orientation with respect to the EM-field, particularly given the anisotropic aggregate structure. Both the MSTM and DDA methods compute the optical properties of a randomly oriented aggregate as the average of its optical properties at all orientations; however, there may be specific orientations that differ greatly from the average, causing a wide distribution in temperature. While aggregates may not have a preferred orientation within the probe volume, it may be informative to investigate the laser irradiation and incandescent emission cross-sections for any one aggregate, since the laser propagation path and detector line-of-sight are typically placed at an angle with respect to each other. Absorption cross-sections as a function of orientation cannot be captured experimentally because the detected signals are a culmination of all aggregate orientations within the aerosol. Figure 4-6a shows the ratio of the absorption cross-sections of the highest to the lowest absorbing sphere at all orientations, and Figure 4-6b shows the total absorption cross-section of the aggregates at the corresponding orientation. Modeling the laser-particle interaction using the aggregate absorption cross-section is equivalent to assuming good thermal contact within the aggregate.

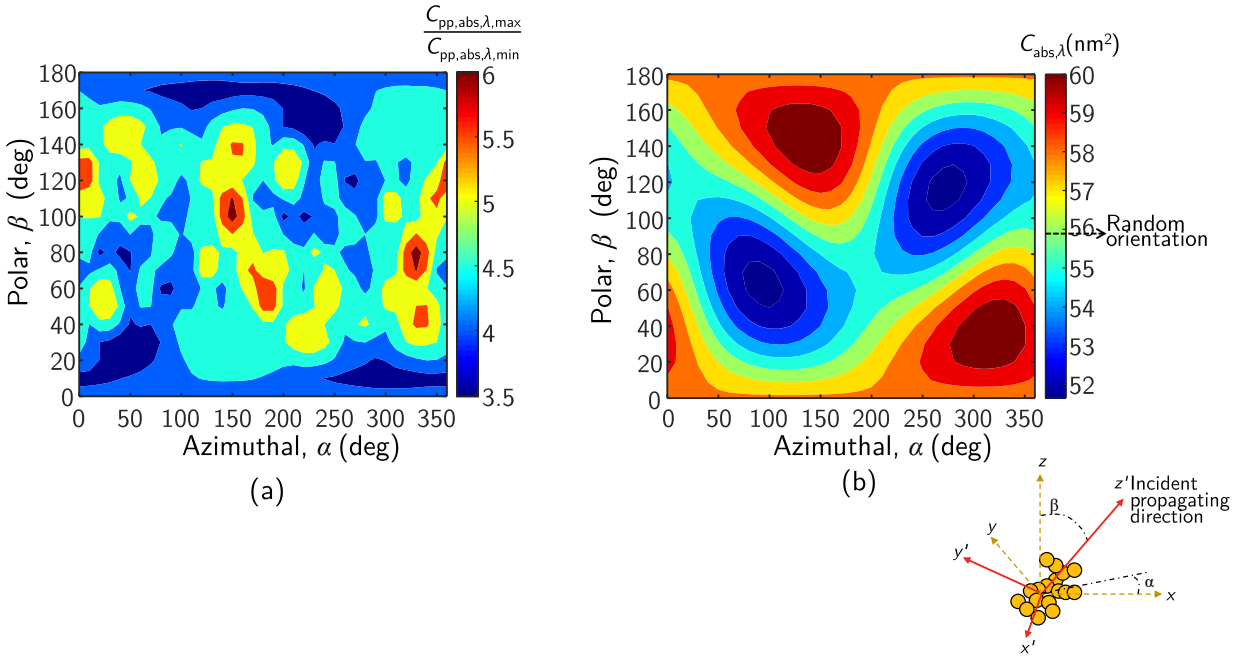


Figure 4-6: Orientation-dependent absorption cross-sections of an iron aggregate consisting of 130 primary particles irradiated at 1064 nm. **(a)** Ratio of the effective absorption cross-section of the highest to lowest absorbing sphere within the aggregate. **(b)** Total aggregate absorption cross-section at varying orientations. The bottom right inset shows the varying angles of incidence relative to the target frame. The color maps were generated in MATLAB from grid-based mapping of the MSTM results with no interpolation.

For the iron aggregate considered in Figure 4-6, there are large variations in the distribution of primary particle absorption cross-sections within the aggregate at different orientations. The large ratios between the highest and lowest absorbing spheres are due to some of the spheres being shielded at particular orientations and hence absorbing less light compared to an isolated primary particle. Such a result is expected if one considers a highly anisotropic aggregate that is oriented towards either the laser or the detector, such that most particles within the aggregate are aligned with the incident or outgoing radiation in that direction [153,165]. However, the total absorption cross-section of the aggregate at all orientations varies only slightly about the random-orientation value, with less than a 10 % difference between the largest and smallest value at an excitation wavelength of 1064 nm. Similar results are obtained at wavelengths in the visible spectrum. Therefore, although the distribution of primary particle absorption cross-sections within the aggregate may differ greatly as a function of orientation, this has little effect on the total absorption of the aggregate. Hence, for an aggregate where the primary particles are in good thermal contact and the aggregate may be modeled as isothermal, the aggregate absorption cross-section is approximately independent of the aggregate orientation in the EM-field or towards the detection optics, and the orientation average value may be considered representative. It follows that any

errors introduced by ignoring the angular dependence of the absorption cross-section relative to the detector are minimal and unbiased. For aggregates with high anisotropy (*cf.*, Figure 4-3, for $D_f = 1.3$ and $k_f = 1.3$), however, large nonuniformities may exist as a function of orientation, and the aggregate cannot be treated as isothermal. One implication of this result is that for sintered aggregates, where uniform temperatures are expected due to the improved thermal contact of the individual primary particles within the aggregate, simulations with few particle orientations are sufficient to obtain representative values for determining the absorption characteristics. This is especially important when using more computationally intensive light scattering models such as DDA. In addition, this suggests that for sintered aggregates that promote a homogeneous temperature, orientation will not have a significant impact on LII. Note, however, that during LII experiments, all aggregate orientations will contribute to the detected spectral emission, which may then be considered an "effective emission" that may be skewed toward aggregates of larger absorption/emission properties in the case where the optical properties strongly depend on orientation.

4.3.3. Effect of sintering on the absorption cross-section of metal aggregates

The effect of sintering on the spectral absorption cross-section and detected incandescence was simulated using DDA. To simulate overlap for an aggregate, the coordinates of the center of each primary particle were multiplied by $(1 - C_{ov})$ (Eq. (4.3)), *i.e.*, spheres shrink towards each other) and the absorption cross-section was computed. The aggregate mass is conserved by increasing the diameter (volume) of the primary particles by equal amounts, *i.e.*, the primary particles remain monodisperse, although in reality, the rate of sintering depends on particle size and number of contacts such that smaller particles and particles with more contacts sinter and grow faster during sintering, causing the size distribution to initially widen before narrowing again [166]. As discussed in Section 3.3, during laser heating, the aggregate may sinter through lattice and grain boundary diffusion at temperatures below the melting point, which creates a necking feature at the grain boundary that is not considered in this work [166]. At higher temperatures, the aggregate material becomes liquid, and sintering and rapid coalescence occur through viscous flow. At laser fluences typical of LII measurements on iron nanoparticles, the peak temperature reaches the melting point of iron within the laser pulse, suggesting that viscous sintering is dominant with a sintering time scale of ~ 10–100 ps computed for an aggregate with $N_p = 120$ and $d_p = 6$ nm based on viscosity and surface tension (as discussed in Chapter 3).

Although nonuniform absorption is expected within the aggregate, when sintering occurs, it becomes invalid to define an absorption cross-section per primary particle within the aggregate since the primary particle no longer interacts in the EM-field with a defined cross-section. An alternative approach may be to analyze the enhancement of the EM-field within the aggregate structure, although this is difficult to visualize for the three-dimensional fractal structure. Instead, the total absorption cross-section of the aggregate is analyzed. This route is justified since sintering results in particle overlap that will increase conduction heat transfer within the aggregate and promote uniform temperatures within the aggregate.

The computation was confined to 380 to 500 nm, where $|\mathbf{m}_\lambda - 1| \approx 3.4$ or lower [149], to reduce errors in the DDA computation due to the growing magnitude of the refractive index at longer wavelengths [142,155]. A total of 18 aggregate orientations spanning the full range of rotations were averaged to obtain the orientationally averaged $C_{\mathrm{abs},\lambda}$. Results from vertically and horizontally polarized EM-fields were also averaged. The accuracy of the DDA method can be assessed for an aggregate with point contact using the MSTM method, and for the fully sintered case using either the Mie theory equations or the MSTM method. A mesh refinement study was conducted, and it was determined that a dipole spacing of 0.3 nm was sufficient to capture the cross-sections accurately. The errors were as low as 2 % in the coalesced case, at lower wavelengths and lower magnitudes of the refractive indices; however, they could grow up to 50 % or more in the case of point contact aggregates at the longest wavelength and high magnitudes of the refractive index. For large refractive indices, DDA-derived cross-sections usually overestimate the true absorption cross-section [155]; however, the general trends in the results, as a function of C_{ov}, remain unchanged as a function of dipole spacing.

Figure 4-7 shows the absorption cross-sections of two different aggregates with $N_{\mathrm{p}} = 20$ and 70 as they are sintered while the aggregate mass is conserved.

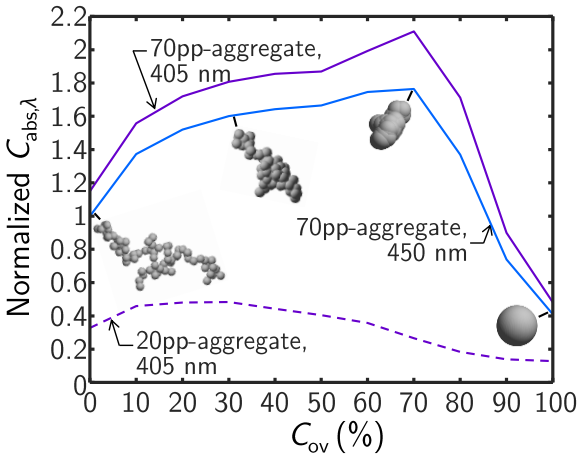


Figure 4-7: Absorption cross-section of iron aggregates as a function of primary particle overlap for laser-sintered aggregate considering mass conservation; the aggregate is shown at 0 %, 30 %, 70 %, and 100 % primary particle overlap. Results are normalized to the computed $C_{abs,\lambda}$ for the 70 primary particle aggregate at point contact at the 450 nm wavelength; the refractive index of molten iron from Ref. [149] is used.

As seen from Figure 4-7, $C_{abs,\lambda}$ increases with an increase in C_{ov} and decreases after reaching a maximum at C_{ov} = 20–30 % for the aggregate with N_p = 20 and C_{ov} = 70 % for the aggregate with N_p = 70.

The initial increase in $C_{abs,\lambda}$ with C_{ov} can be attributed to increased dipole interactions within the aggregate (*i.e.*, increased electrical conductivity) and a change in morphology. The changing morphology influences the absorption cross-section through the antenna effect [167]. Karpov *et al.* [163] show that this effect can be maximized in elongated structures that have maximal anisotropy along the direction of polarization.

The eventual drop in $C_{abs,\lambda}$ is due to the aggregate sintering and eventually coalescing to a more compact structure, thus reducing the radius of gyration. There is a broader peak in the curve for the smaller aggregate of 20 primary particles because the morphological changes towards a sphere are more subtle compared to those of a larger aggregate. Note that in cases where sintering is not due to heating but a consequence of the aggregate synthesis method, there is a rapid reduction in geometric cross-section when the synthesis method produces aggregates with a greater degree of sintered primary particles [168][4]. Experimental validation of the optical properties of the aggregates during sintering may be conducted by sintering the aggregates up to various

[4] This reference is the first version of the work presented in this chapter and published as:
Robinson-Enebeli, S., Schulz, C., Daun, K. J., 2023, "Investigating the Absorption Properties of Metal Nanoparticle Aggregates During Time-Resolved Laser-Induced Incandescence." Begel House Inc.; 2023, p. 19–26. Proceedings of the 11th International Symposium on Radiative Transfer, RAD-23, Thessaloniki, Greece, 12–16 June 2023.

sintering stages by flowing the aerosol through a tube furnace at varying operating conditions [124]. Nanoncolloids of these differently sintered aggregates can then be made for UV-Vis analysis.

In Chapter 3 (*cf.*, Figure 3-4), it was shown that, as molybdenum nanoparticle aggregates undergo laser-induced sintering during TiRe-LII, the ratio of $Q_{\text{abs},\lambda}$ at the shorter detection wavelength to the longer detection wavelength changes drastically. However, the computed ratio of $Q_{\text{abs},\lambda}$ at 380 or 405 nm and 450 or 500 nm for a 70-primary particle iron aggregate with $d_{\text{p}} = 6$ nm and in point-contact was not significantly different from the coalesced aggregate. Simulated absorption cross-sections calculated using the DDA method confirm that this discrepancy can be attributed to the difference in aggregate morphology, with the molybdenum aggregates studied in Chapter 3 having primary particle diameters of 45 nm.

Accurate modeling of the temperature evolution of the laser-induced sintered aggregates would require modifications to the TiRe-LII evaporative and conductive cooling models to account for the evolution of the surface area and size during the sintering process. However, an estimate of the temperature deviation due to laser sintering can be determined for the case of 70 % overlap, where maximum absorption is expected. The absorption cross-section at the excitation wavelength of 1064 nm is computed for a 70 primary particle aggregate using a dipole spacing of 0.1 nm. This spacing, when applied to an isolated primary particle, results in an error of less than 5 % when compared to Mie theory. Then, the heat transfer model is evaluated for the 70 % sintered aggregate as shown in Figure 4-8a. The temperature of the coalesced case, point contact aggregate, and the case of isothermality are also plotted. To show the effect of coalescence (complete sintering), in Figure 4-8b, effective temperature curves from LII measurements made on iron nanoparticles from the literature [19,22,139] are compared to the simulated temperature profile of an isolated primary particle of 255 nm, which should produce the highest peak temperature in an aerosol containing a distribution of isolated sherical particles (*cf.*, Figure 3-12a).

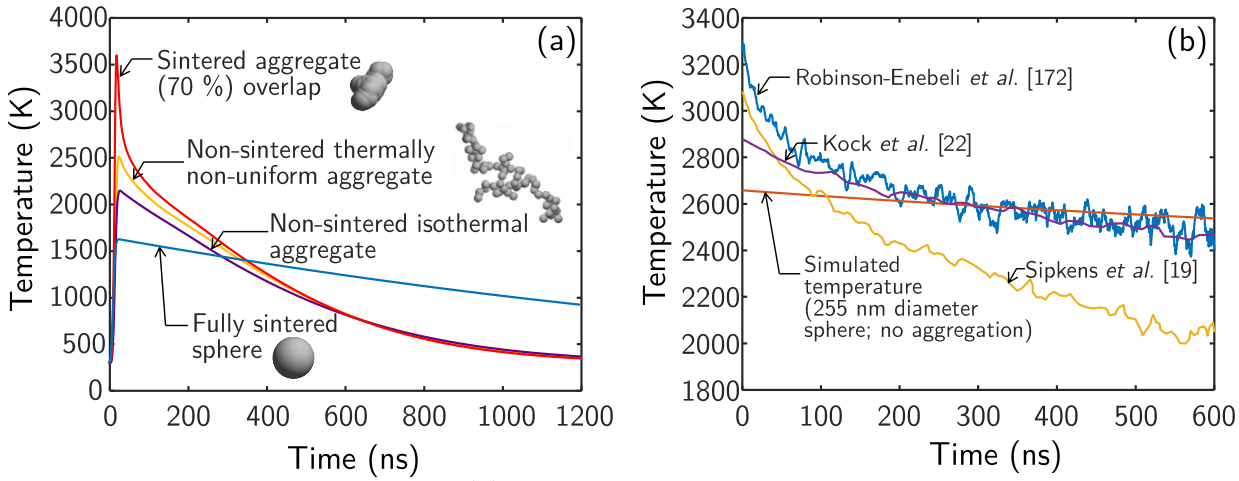


Figure 4-8: Temperature evolution of **(a)** a 70 primary particle aggregate in point contact, for a case where uniform temperatures within the aggregare is assumed and another where thermal isolation is assumed, a sintered with a 70 % overlap, and a coalesced sphere and **(b)** a 255 nm diameter isolated iron particle (gas: N_2, Fluence: 2.5 mJ/mm^2) and aerosolized iron nanoparticles from experiments of Kock *et al.* [22], Sipkens *et al.* [19], and Robinson-Enebeli *et al.* [172]. All simulated temperatures are computed with the heat transfer submodel, except as otherwise mentioned. The refractive index of molten iron from Ref. [149] is used in the model.

As seen in Figure 4-8a, the partially sintered aggregate reached higher peak temperatures compared to the point contact aggregate and rapidly cools down due to evaporation for ~100 ns following the peak temperature. The observed rapid cooling is more prominent for the sintered aggregate compared to the point contact aggregate, which could potentially explain at least some of the apparent anomalous cooling phenomenon. Additionally, the observed anomalous cooling timescale of ~100 ns for iron aggregates is shorter than that of molybdenum nanoparticles of ~400 ns [139]. Note that the current evaporation and conduction models induce more cooling than may be occurring since a higher surface area is used for evaluation. In addition, the temperature of the sintered case assumes the aggregate has already been sintered to a 70 % overlap prior to laser excitation. In order to obtain a more accurate temperature profile, one may need to account for the temporally resolved sintering dynamics [125]. The effects of sintering are expected to mostly influence the rise in temperatures, where most of the morphological changes occur, and consequently, the peak temperature reached, when nanostructures are rapidly heated to temperatures close to their melting point, where viscous sintering is dominant, as is the case in Figure 4-8. However, if the aggregate is not coalesced after the laser pulse, sintering effects will last beyond the duration of the temperature increase. Such effects will also last longer when peak temperatures remain below the melting point where lattice or grain boundary sintering is dominant, which may result in effects lasting up to 400 ns in the case of molybdenum nanoparticles [139].

As observed from Figure 4-8b, if the effects of aggregation are not considered and isolated primary particles are assumed, the rapid drop in the experimental temperatures for the first ~300 ns is not captured by the model. Such a rapid reduction in temperature has been previously attributed to free molecular evaporation [19,22], but results from this work suggest that the effective temperature can rapidly decrease as a result of heat conduction between particles of different temperatures within the aggregate, which is accelerated by sintering. Nonuniform heating may also be enhancing evaporation since primary particles in hot spots reach much higher temperatures, resulting in significant evaporation, further contributing to rapid cooling. Differences between the experimental data shown in Figure 4-8b may be due to morphology differences of the iron particles between the studies. Sipkens *et al.* [19] report that the iron particles were isolated spheres following a distribution of $\ln\mathcal{N}(39.8\text{ nm}, 1.16)$, Kock *et al.* [22] report chain-like synthesized iron aggregates with primary particles distributed according to $\ln\mathcal{N}(26.9\text{ nm}, 1.34)$ and $\ln\mathcal{N}(18.0\text{ nm}, 1.41)$ in Ar and N_2 respectively. Differences in the fluence distribution across the irradiating laser cross-sections may also contribute to descrepancy between the measured data. The role of fluence distributions are discussed in Chapter 7 and Appendix B.

4.4. Conclusions

The investigations in this chapter explored the impact of nonuniform heating of aggregates, aggregate morphology, aggregate orientation with respect to the propagation direction of the EM wave, and sintering-induced primary particle overlap within the aggregate on the TiRe-LII signal. It was found that the absorption cross-section of the individual primary particles varied widely within the aggregates to a degree that increases with increasing aggregate sizes and may contribute to excessive absorption and anomalous cooling for aggregates with minimal overlap between primary particles. In addition, the variation is influenced by a combination of aggregate anisotropies and constructive interference between the scattered EM-fields within the aggregate.

Moreover, for the aggregates considered, primary particles within the aggregate may be shielded from the EM-field at certain orientations, leading to increasingly nonuniform absorption and emission throughout the aggregate. However, the total absorption cross-section of the aggregate varied by less than 10 % over all orientations. This can simplify the computation during TiRe-LII when the aggregate is considered isothermal.

Furthermore, sintering-induced overlap can enhance the absorption properties of the aggregate due to increased electrical conductivity and morphological changes towards a structure that may promote the antenna

effect. Such absorption enhancements by sintered aggregates were shown to significantly increase the peak temperature of the aggregate when compared to point contact aggregates. The computed temperature profile of the partially sintered iron aggregate exhibited an initial rapid drop in temperature previously observed in experimental results, but has been strictly attributed to evaporation.

Further investigations of the behavior of metal aggregates in an EM-field are needed to develop a more complete TiRe-LII model. In particular, the morphological changes from point contact aggregates to partially or fully sintered structures need to be considered through time-resolved sintering models, and the evaporation and conduction models need to be modified to properly account for the evolution of the surface area. In addition, other light scattering models that may be better suited for large refractive index materials such as the finite element method (FEM) [169] or the finite difference time domain method (FDTD) [170] may be used to more accurately compute the absorption cross-section of sintered aggregates, although these methods may be more computationally intensive than the DDA method [171].

In the next chapter, sintering and coalescence during LII are investigated experimentally to provide insight into the relevant time scales involved during nanoparticle laser irradiation and sintering, and how sintering dynamics may impact the experimentally measured pyrometric temperatures.

Chapter 5

Effect of laser-induced sintering and coalescence[5]

The analysis in this chapter investigates how sintering and coalescence may influence the TiRe-LII signals from metal nanoparticle aerosols. The investigations consist of numerical simulations and experimental TiRe-LII measurements on iron aggregates. As a low-melting-point material, laser-heated iron aggregates coalesce into spheres (*i.e.,* fully sinter) before the peak of the LII signal is reached. Coalescence may affect the observed TiRe-LII signals in two ways: (i) the transition from aggregates to spheres reduces the absorption cross-section, which affects both the total absorbed laser energy and the intensity of the emitted incandescence in a wavelength-dependent manner; and (ii) surface energy is converted into sensible energy of the nanoparticles, which increases their peak temperature.

[5] Information presented in this chapter is based on the published work:
Robinson-Enebeli, S., Schulz, C., and Daun, K. J., 2025, "Laser-Induced Incandescence of Iron Nanoparticles: Effects of Laser-Induced Sintering and Coalescence," Appl. Phys. B, **131**(135).

5.1. Introduction

In Chapter 3, it was shown that the aggregate structure can strongly enhance the absorption cross-section and cause significant variations in temperature within the aggregates at a given instant [139,172]. In addition, primary particles within aggregated nanoparticles can partially sinter or the aggregate can coalesce into spheres as a result of laser heating, which will change their absorption cross-section [172]. In Chapter 4, it was hypothesized, through numerical models, that the apparent anomalous cooling effect may be explained by nonuniform aggregate heating that causes some particles to cool through evaporation, which increases the expected cooling rate or by sintering after the particle reaches its peak temperature, via the increased electrical and thermal contact between the primary particles [139].

In this chapter, these hypotheses are assessed using data from LII measurements on an aerosol of iron nanoaggregates formed through a spark discharge process. In particular, sintering and coalescence (*i.e.*, complete sintering of the aggregate into a sphere) are investigated experimentally. Measurements are interpreted using absorption cross-sections modelled using the multi-sphere T-matrix (MSTM) method (point contact), the discrete-dipole approximation (partially sintered), and Mie theory (coalesced). An attempt is made to reproduce the measured pyrometric temperatures while incorporating sintering and coalescence into the LII model. Furthermore, the robustness of prompt LII signals is evaluated under conditions where apparent anomalous cooling dominates. This is performed by monitoring the estimated quantities-of-interest (QoIs) through a time-delayed regression analysis, which revealed that the rapid decay in prompt LII signals is not accounted for by the current evaporative mass loss model.

5.2. Experimental Setup

The experimental setup used in this chapter is identical to that used in Chapter 3 (*cf.*, Figure 3-3 and Figure 3-4); however, two additional detection wavelengths were employed, as shown in Figure 5-1. The LII data collected and analyzed in this chapter are available on GitHub (https://github.com/s27robin/SRE-PhD-LII-exp_data).

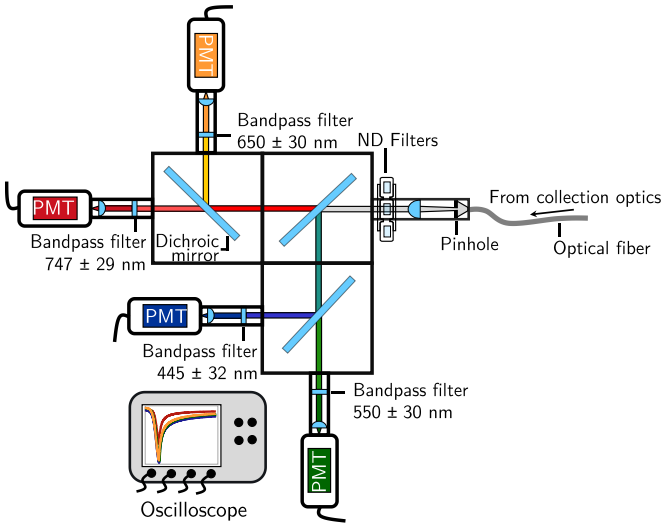


Figure 5-1: Modified detection setup with four-color (4C) detection wavelengths.

5.3. Measurement models

This section presents additional information on the TiRe-LII model, as used for analysis in Chapter 3 and Chapter 4. The aggregate sintering model, and the absorption model are also presented.

5.3.1. TiRe-LII model

The heat transfer submodel for an aggregate, as presented in Chapter 3 and Chapter 4, is used here. When primary particles are in point contact, the laser absorption model computes the absorption cross-section of each primary particle within the aggregate. Because the local EM-field strength is influenced by the surrounding particles in an aggregate, each primary particle may be exposed to different field strengths and thus be heated to different temperatures, as discussed in Chapter 4. The energy absorbed by a non-sintered aggregate equals the sum of energy deposited in the individual particles. Because the metal aggregates are expected to absorb and emit outside of the Rayleigh limit, the local EM-field is strongly influenced by the aggregate structure and, consequently, the primary particles are expected to be at different temperatures at any instant [172].

After the onset of sintering (when primary particles are no longer in point contact but begin to overlap), the resulting aggregate is assumed to absorb laser energy as an electrically and thermally conductive structure, which is isothermal at any given instant. Because of the electrical contact between the particles,

the absorbed energy depends on the total cross-section of the entire aggregate. Consequently, the aggregate temperature depends on the compactness of its initial structure. When the aggregate structure changes upon coalescence, the spherical particle formed from an aggregate would have absorbed more laser energy and would be hotter than a particle with the same diameter and mass that was compact throughout the laser interaction. This effect is discussed further in Section 5.4.2.

The evaporation model assumes that the particles within the aggregate remain in point contact and evaporate independently, which may not be accurate upon melting, sintering, and coalescence. The melting enthalpy is neglected since the energy associated with the solid-to-liquid phase change is orders of magnitude less than the laser heating (*cf.*, Appendix A.1).

When all the aggregates coalesce into spheres, the incandescence signal is modelled as

$$J_\lambda\left(t\right) = C_\lambda \Lambda \int_0^\infty p\left(d_\mathrm{p}^{\mathrm{coalesc}}\right) C_{\lambda,\mathrm{abs}}\left(\mathbf{m}_\lambda, d_\mathrm{p}^{\mathrm{coalesc}}\right) I_{\lambda,\mathrm{b}}\left[T_\mathrm{p}\left(d_\mathrm{p}^{\mathrm{coalesc}}\right)\right] d\left(d_\mathrm{p}^{\mathrm{coalesc}}\right), \tag{5.1}$$

where $d_\mathrm{p}^{\mathrm{coalesc}}$ is the diameter of the coalesced sphere produced by the sintering of an aggregate containing N_p primary particles, and $p(d_\mathrm{p}^{\mathrm{coalesc}})$ is the PDF that describes the diameters of the coalesced spheres. The width of this distribution originates mainly from the polydispersity of the number of primary particles per aggregate, $p(N_\mathrm{p})$, in the original aggregate population. The typical approximation that the primary particles are isolated and absorb in the Rayleigh regime may then be applied, allowing for an effective temperature of the aerosol to be estimated through two-color pyrometry (*cf.*, Section 3.2.2).

At any instant, the pyrometric temperature obtained using this procedure differs from the average sensible temperature of the particle ensemble within the probe volume for several reasons: (1) the particles are polydisperse in size, and therefore are expected to have different temperatures at any instant [20] (this is explored further in Chapter 6); (2) the Rayleigh approximation does not generally hold for metal aggregates nor coalesced metal spheres [94,109,121]; and (3) field enhancement effects within the aggregates during emission may further contribute to nonuniform temperatures (*cf.*, Chapter 4). Therefore, while the pyrometric temperature, $T_{\mathrm{p,pyro}}$, provides a rough indication of the instantaneous "average" temperature (although biased towards hotter particles [139]), it should not be interpreted as a true thermodynamic temperature. Moreover, since all spectroscopic effects mentioned prior change as the particles are heated and melted, they may, at least, partially account for some of the heretofore unexplained transient phenomena in LII measurements. A further time-dependent artifact in the pyrometric temperature may

arise from the fact that the hottest particles in an ensemble might cool faster due to evaporative cooling, even if the pyrometric temperature of the ensemble appears to be lower than the temperature at which significant evaporative cooling occurs (further discussed in Chapter 6).

For iron nanoparticles with diameters greater than ~3 nm, the refractive indices may be taken to be that of the bulk material (*cf.*, Appendix A.4), and are taken to be that of molten iron as reported by Shaverav *et al.* [104]. While the nanoparticles are solid for a short time after the onset of laser irradiation and before melting, only the refractive index of molten iron is considered because the total signal is dominated by the hot molten particles, as discussed further in Section 5.4.1.

5.3.2. Modeling of aggregate sintering, coalescence, and absorption properties of metal nanoparticles

In Chapter 4, it was established that partial sintering enhances the absorption cross-sections of the aggregates, thereby raising the peak temperature compared to what would be expected from an aerosol of isolated spheres. It was also hypothesized that apparent anomalous cooling could be explained, at least in part, by aggregates containing primary particles that are not fully sintered by the time that peak incandescence is reached. At this point, the aggregate structure would lead to localized field enhancements and, therefore, primary particles that may reach temperatures far above the median value. These particles would cool down through evaporation, subsequently manifesting in a rapid drop in the effective temperature decay rate. However, later in this chapter, it will be shown that the particles will have melted and transformed into spheres before the time of peak emission, so the previous hypothesis does not apply to the conditions investigated here (as discussed further in Section 5.4.1).

Synthetic nanoparticle aggregate geometries are generated through the tunable cluster–cluster aggregation algorithm [110] with uniformly sized primary particles similar to Chapter 4, with representative fractal parameters $k_f = 1.19$ and $D_f = 1.82$ [173]. The viscous sintering model is described in Section 3.3. The primary particle diameters and number of particles per aggregate are considered to follow the distributions of $\ln\mathcal{N}(6\text{ nm},\ 1.3)$ and $\ln\mathcal{N}(126,\ 1.77)$, respectively, as determined from analysis of TEM micrographs (*cf.*, Figure 3-4 and Figure 3-5).

The absorption efficiency of the aggregates is computed using the multi-sphere T-matrix (MSTM) method [141] for aggregates consisting of primary particles in point contact, the discrete dipole

approximation (DDA) [142] for sintered aggregates, and Mie theory [94] for fully coalesced spheres. The T-matrix and DDA methods are implemented using MSTM version 3.0 [141] and DDSCAT 7.3 [142], respectively. In this chapter, additional measures are taken to improve the accuracy of the results produced by these models. In the case of MSTM, a larger number of expansion terms is needed to reach convergence compared to what is expected for soot [153], while in the case of DDA, a small dipole spacing is needed. A convergence study showed that 20 expansion terms are needed for the MSTM computation (*cf.*, Appendix A.5), and a mesh study determined that a 0.3 nm dipole spacing was sufficient for the DDA computation (*cf.*, Appendix A.6). For the DDA calculations, 18 aggregate orientations spanning the full range of aggregate rotation were averaged to obtain the orientationally averaged $C_{\lambda,\mathrm{abs}}$. Results from vertically and horizontally polarized EM-fields were also averaged. The biconjugate gradient method was used to iteratively solve for the dipole polarizabilities, which were defined by the filtered coupled dipole method (recommended for large refractive index materials [142]). The ambient environment was taken to be air.

5.3.3. Data regression

Deficiencies in the LII model may be elucidated from the residual between experimental incandescence traces and the corresponding best-fit simulations. In this work, the spectral incandescence data from all detection wavelengths are regressed through least squares minimization following a procedure described in Ref. [16]. The spectral time-resolved signals from all four detection wavelengths are stacked on the time axis for a more effective inference strategy that minimizes the influence of noise in the data, as shown in a previous work [174][6] and as implemented in Ref [16]. The free parameters are the particle diameter d_p, the geometric standard deviation of an assumed log-normal particle-size distribution, σ, the TAC, α, and the peak temperature from which the particles cool, T_peak. The LII signal is computed by evaluating Eqs. (2.1) and (2.17). Regression to the incandescence signal, as opposed to the pyrometric temperatures derived through color pyrometry, avoids the error introduced by the Rayleigh approximation [16,20]. The regression was implemented in MATLAB by first using the genetic algorithm (a heuristic optimization technique implemented with the "*ga*" function in MATLAB), and refined with a gradient-based, deterministic optimization technique (implemented with the "*fmincon*" function in MATLAB).

[6] This is a conference proceeding disseminated as a poster at the NanoOntraio Conference 2021:
Robinson-Enebeli, S., Daun, K. J., 2021, "Effective Wavelength Data Arrangement for Time-Resolved Laser-Induced Incandescence Inference." Proceedings of the NanoOntario Conferences – Remote, Ontario, Canada, November 2021.

5.4. Results and discussion

5.4.1. Analyzing the extent of sintering by the peak of the LII signal

Figure 5-2 shows a typical measured signal and the corresponding pyrometric temperature. While all channels in the detection setup are influenced by Q-switch noise and electronic noise from the surroundings, during the experiment, the 550 nm detection channel was particularly noisy.

Since aggregates are expected to have extinction spectra that are distinct from isolated spheres [175], analyzing the spectral distribution of the peak LII signal may indicate the extent of sintering by the peak of the LII signal. This can be accomplished by comparing the spectral distribution at the LII peak, measured experimentally, with the spectral intensity distributions predicted for aggregates with varying degrees of sintering (*i.e.*, $C_{\mathrm{ov}} = 0$ %, 25 %, 50 %, 75 %, and 100 %) and containing 30, 50, 70, 100, 135, or 200 particles per aggregate. The particle diameter corresponding to 100 % primary particle overlap is equivalent to the volume equivalent diameter of the aggregate according to $d_{100\,\%} = d_{\mathrm{p}}\, N_{\mathrm{p}}^{1/3}$.

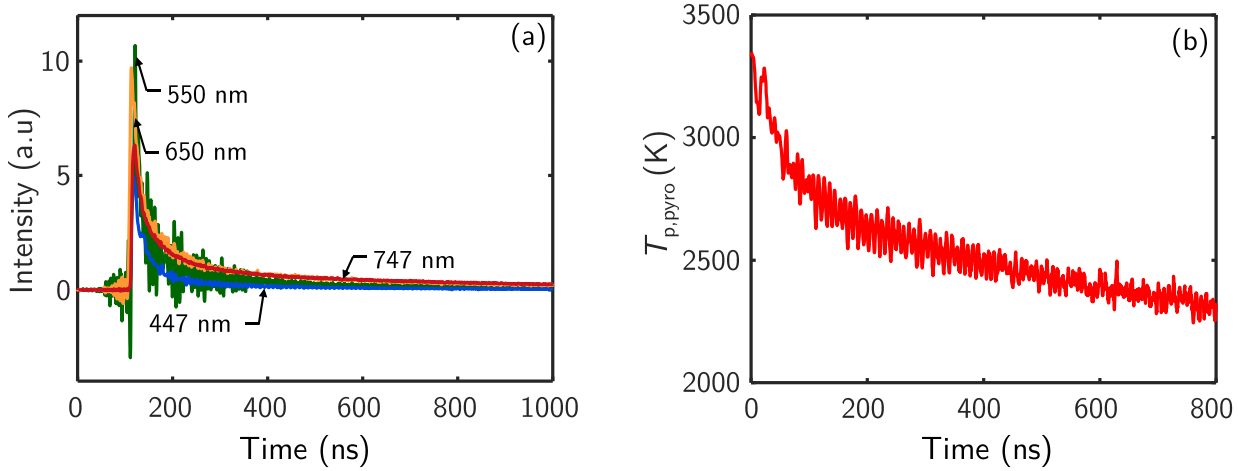


Figure 5-2: (a) Measured LII signals at four detection wavelengths obtained from iron nanoparticles irradiated at a laser fluence of 2.7 mJ/mm^2 **(b)** Corresponding apparent pyrometric temperatures computed by a weighted nonlinear regression of the modeled spectral intensity (Eq. (2.22)) to the measured signals at four detection wavelengths centered at 445, 550, 650, and 747 nm. The pyrometric temperatures are estimated with a refractive index corresponding to molten iron [103].

Modeling the spectrally-resolved peak LII emissions from the particle ensemble requires knowledge of the peak temperature reached by aggregates with different morphologies and varying degrees of sintering. Since

this information is unavailable, it is temporarily assumed that the aggregates reach a uniform peak temperature of 3300 K, estimated by pyrometry (*cf.*, Figure 5-2b). Then, the absorption cross-sections for each size class and sintering stage, computed from DDA at wavelengths of 401, 500, 684, and 797 nm, are weighted by the log-normal distribution, $\ln\mathcal{N}(126, 1.77)$ to get an average absorption cross-section of the ensemble shown in Figure 5-3. The peak of the incandescence signal at each sintering stage and each emission wavelength is then computed using Eq. (2.21) and normalized to the shortest emission wavelength as shown in Figure 5-4a.

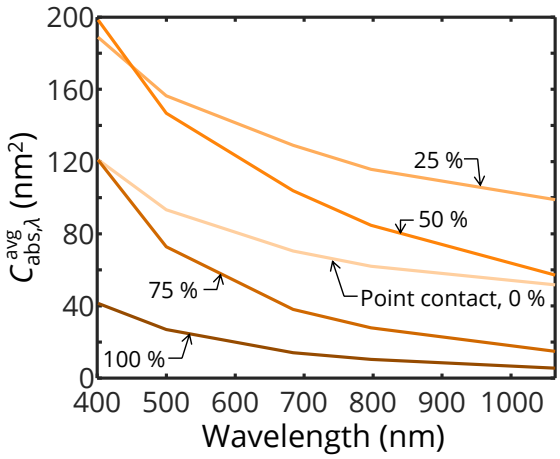


Figure 5-3: Average absorption cross-section of an ensemble of iron aggregates containing aggregate sizes of N_p = 30, 50, 70, 100, 135, 200 drawn from $\ln\mathcal{N}(126, 1.77)$ computed from DDA at different sintering stages. The increase, and eventual decrease of $C_{abs,\lambda}$ as the aggregate sinters from point contact is due to increasing dipole interaction at the sintering sites before reaching a maximum, after which $C_{abs,\lambda}$ reduces due to the increasing structural compactness [172].

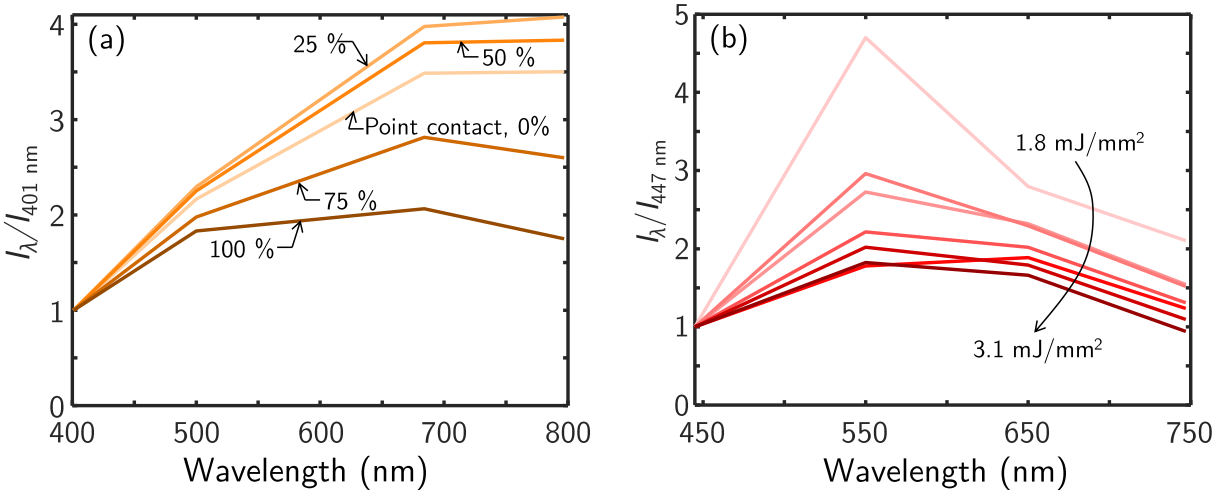


Figure 5-4: Spectral distribution of the LII emission at the time of the maximum LII signal **(a)** Simulations for sintering stages with C_{ov} = 0 %, 25 %, 50 %, 75 %, and 100 % which are all assumed to be at the same temperature of 3,300 K, **(b)** Measured calibrated signal from iron nanoparticle aerosols. In all cases, emission intensities are normalized to the shortest emission wavelength.

Figure 5-4 shows the simulated and measured spectral intensity at the peak incandescence for four detection channels. For the simulation results shown in Figure 5-4a, the normalized spectral intensity increases with wavelength in accordance with the spectral absorption cross-section shown in Figure 5-3. In addition, the spectral distribution of the signal depends on the degree of sintering (*i.e.*, varying C_{ov}). Increasing C_{ov} up to 50 % leads to a slight increase in intensity while maintaining the spectral shape. A further increase in C_{ov} leads to an overall decrease in signal intensity relative to the signal at the shortest wavelength, but it is more pronounced at longer wavelengths, leading to a signal peak at around 700 nm. This trend is consistent with the magnitudes of the absorption cross-sections of each sintering stage shown in Figure 5-3, with the coalesced aggregates (C_{ov} = 100 %) having the lowest $C_{797\ nm,abs}/C_{401\ nm,abs}$ ratio and the 25 % sintering stage having the highest. Figure 5-4b shows that the measured spectral shapes of the LII emission at all laser fluences have signal peaks in the visible range and are most consistent with simulated emission spectra for an aerosol of coalesced aggregates (C_{ov} = 100 %). This observation suggests that the iron aggregates are coalesced, or nearly so, by the time the peak LII signal is reached, which is also consistent with observations of laser-irradiated samples of iron aggregates that show complete coalescence in TEM measurements (*cf.*, Figure 3-7). Note that the measured spectral shape shown in Figure 5-4b peaks around 550 nm, while the simulated data peaks around 700 nm. This difference may be attributed to the fact that the modeled peak incandescence is computed assuming that the particles are at the same peak temperature. However, it is

also noted that the poor signal-to-noise ratio of the 550 nm detection channel (as observed in Figure 5-2a) may also be a contributing factor.

Coalescence during laser heating is consistent with the outcome of Eq. (3.17), which suggests a characteristic viscous sintering (and thus coalescence) time of ~10^{-2} ns, much shorter than the duration of the laser pulse and the estimated measured heat-up time (time from the initial background signal to the peak of the LII signal) that ranges from 8–12 ns at all fluences. Since Eq. (3.17) only predicts the characteristic viscous sintering time, the metal aggregate may begin to sinter through a slower process, such as grain-boundary diffusion [166] at lower temperatures.

Below the melting temperature of a crystalline material, sintering occurs through grain boundary diffusion [122,124]. The characteristic grain boundary sintering time, τ_{gb}, of two equally sized nanoparticles is estimated according to [124]

$$\tau_{gb} = \frac{k_B T r_{p,0}^4}{2\pi D_v C_{v0} \delta_{gb} \gamma_s \Omega}, \tag{5.2}$$

where $r_{p,0}$ is the initial radius of the particles, k_B is the Boltzmann constant, T is the temperature of the particle, γ_s is the surface tension, δ_{gb} is the grain boundary thickness, Ω is the volume of the atomic vacancy, C_{v0} initial fraction of sites occupied by vacancies, and D_v is the vacancy diffusion coefficient. Table 3-2 shows the parameters used to evaluate Eq. (5.1). Figure 5-5 shows that the characteristic sintering time for grain-boundary sintering of iron nanoparticles above 800 K is already less than the laser pulse duration. Note that the surface energy of the iron nanoparticles in the related size range depresses the melting point from 1811 K (bulk) to about 1483 K (*cf.*, Appendix A.7).

Table 5-1: Parameters used to evaluate Eq. (5.1) for Fe nanoparticles.

Parameter	**Value**
D_v [m^2/s]	$A_{gb} \exp(-Q/(RT))$ [176] $A_{gb} = 5.99$[a] $Q = 39750$ cal·mol^{-1} [a] R is the gas constant
C_{v0} [-]	10^{-5} [177]
γ_s [J/m^2]	$1.826 - (T_p - T_m)\ 0.35\times10^{-3}$ [119] T_p and T_m are the particle and melting point temperature, respectively
δ_{gb} [m]	10^{-6} [176]

Ω [m^3]	$(4\pi/3)\ a^3$ a is the atomic radius of Fe taken as 126 pm [117]

[a] Taken as the average value of the b.c.c. and f.c.c. lattice structures.

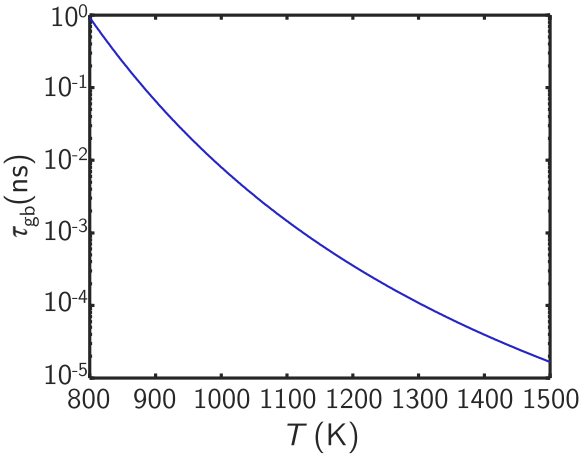


Figure 5-5: Temperature dependence of the characteristic grain boundary sintering time of two iron nanoparticles with equal diameters of 6 nm.

This further suggests that the particles are completely coalesced by the time the peak LII signal is reached. Hence, the hypothesis made in Chapter 4 that suggests apparent anomalous cooling may occur due to nonuniform heating and cooling of the primary particles within the aggregate as a result of the nonuniform laser absorption could not apply to iron aggregates where the particles coalesce as rapidly as predicted by the viscous sintering model.

5.4.2. Predicting the impact of coalescence on the LII signal

Sintering and coalescence are exothermic processes due to the release of surface free energy from the reduction in surface area (*i.e.,* $\gamma_s \Delta A_s$, where ΔA_s is the change of the surface area from an aggregate morphology to a sphere after coalescence). The temperature increase due to the energy gained from the reduction in surface area is

$$\Delta T = \frac{Q_{SE}}{m_{agg} c_p}, \tag{5.3}$$

where Q_{SE} is the surface energy gained through surface reduction, m_{agg} is the mass of the aggregate, c_p is the specific heat, and ΔT is the equivalent temperature increase. From the determined released energy due to coalescence (*cf.*, Appendix A.8), for aggregates with N_p = 10, 100, 1000, the temperature increase as a

function of primary particle diameters (with melting point depression considered) is shown in Figure 5-6. For an aggregate consisting of primary particles having a diameter of 6 nm, the equivalent temperature increase is ~ 270 – 450 K.

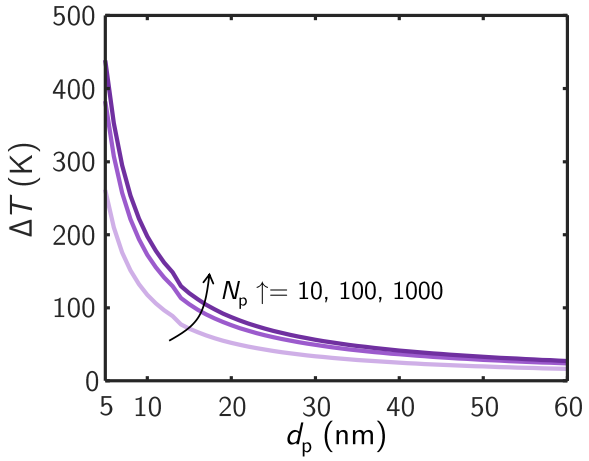


Figure 5-6: Temperature increase related to coalescence of aggregates as a function of primary particle size computed from the released surface free energy due to reduction in specific surface area.

The temperature evolution of laser-heated iron aggregates is modeled as follows. In the initial particle heating phase (*i.e.*, before sintering), the solid aggregates are modeled as being in point contact. Once the melting temperature is reached, the aggregates coalesce immediately into spheres, which is justified by the very short characteristic coalescence time predicted by Eq. (3.17), and the surface energy released according to Eq. (5.3) is added to the sensible energy of the sphere. The resulting temperature, $T_{\mathrm{melt}} + \Delta T$, is then used as an initial particle temperature to calculate the further heat-up by the remainder of the laser pulse, while using the optical properties of the molten sphere.

Figure 5-7 compares different hypothetical scenarios for the modeled particle temperature against the measured effective temperature (light blue) for a laser fluence of 2.7 mJ/mm^2. The two extreme cases are represented by individual 6-nm primary particles and aggregates ($D_{\mathrm{f}} = 1.82$) with 200 primary particles in point contact that are assumed to maintain their original structure. The latter case reaches the highest heat-up temperature because it maintains a large optical cross-section throughout laser heating. Both structures show fast cooling due to their large surface-to-volume ratio and high evaporative cooling.

The purple curve follows the step model described above, where the particle coalesces into a 35-nm diameter sphere upon melting. Since this occurs early in the laser pulse, the peak temperature is far lower than in the previous case because of the strongly reduced absorption cross-section upon coalescence. It is,

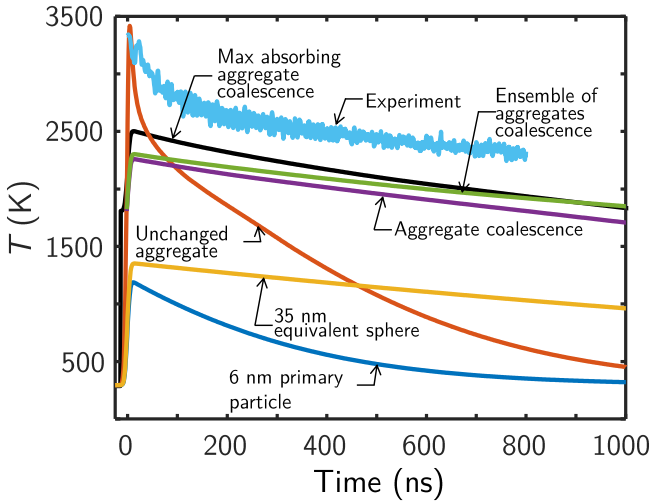


Figure 5-7: Simulated temperature profiles after laser heating for several conditions: A 6-nm diameter primary particle (dark blue), an aggregate unaffected by sintering (200 primary particles of 6 nm in diameter in point contact, red), and an equivalent sphere (35 nm) of the aggregate (yellow). Three scenarios following the step model transitioning from aggregate to sphere: A single aggregate in point contact (purple), an ensemble of aggregates in point contact (green), and a single partially sintered aggregate (black). All simulations are compared to the measured experimental temperature. A mid-range fluence of about 2.7 mJ/mm^2 in the range of fluences used during experiments was used in both simulations and the experiment shown here.

however, significantly higher compared to the scenario in which the particle starts as a 35-nm diameter sphere, since, in the former scenario, the enhanced absorption cross-section of the aggregate prior to melting, combined with the surface energy released during melting, augments the peak temperature by ~900 K. In both cases, the temperature decay is significantly slower compared to the blue and red cases because of the lower surface-to-volume ratio and lower evaporative cooling. In other words, a particle that coalesces during the laser pulse changes its interaction cross-section between laser absorption during heating and emission during cooling and thus would be contributing to the observed apparent "excessive absorption" since the sintered sphere would reach higher temperatures compared to an identically sized sphere with an unchanged morphology during the LII process.

The above scenarios pertain to individual particles and should not be compared directly to the effective temperature, which arises from contributions of all size classes. The green curve in Figure 5-7 shows the modeled effective temperature for an ensemble of aggregates having primary particle diameters of 6 nm and an N_p distribution of $\ln\mathcal{N}(200,\ 1.8)$. The aggregates transform into equivalent spheres upon melting according to the step model described above. The solid aggregates are assumed to absorb light as would an aggregate containing 200 primary particles prior to melting, for computational expediency. However, the

temperature enhancement due to absorbed surface energy and the absorption cross-section of the coalesced spheres are calculated according to the correct size classes. The effective temperature of the ensemble of polydisperse aggregates is higher than that of a monodisperse ensemble because the hottest particles within the ensemble have a disproportionately large influence on the effective temperature [139]. The resulting peak temperature, however, is still below the experimentally determined pyrometric temperature.

In Chapter 4, it was shown that partially sintered aggregates have larger absorption cross-sections compared to point-contact aggregates. While the DDA method can be used to estimate the absorption cross-sections of partially sintered aggregates, the estimates are best used in a comparative capacity (as opposed to using the estimated absolute values) because of the error associated with DDA for large refractive index materials. Instead, a hypothetically maximally absorbing aggregate that results in a vertical increase in temperature prior to coalescence upon melting. According to the step model described above, this leads to an earlier time of coalescence and thus a larger fraction of the laser pulse interacts with the equivalent sphere instead of the aggregate. The combined effect leads to an increase of the predicted peak temperature by ~250 K compared to the point-contact aggregates (Figure 5-7, black). However, even this increased temperature remains below the apparent temperature derived from the measurement. Actual partially sintered aggregates would be expected to have temperatures between the maximally absorbing aggregate and the point-contact aggregate. The convergence of the temperature profile of the maximally absorbing aggregate (black curve) and the ensemble of coalesced aggregates (green curve) at later cooling times indicates that the cooling rates of the ensemble of coalesced aggregates at later cooling times are likely dominated by the cooling of particles within similar size classes to that of the volume-equivalent diameter (due to coalescence) of the maximally absorbing aggregate. Each size class in the ensemble contribute to the measured temperature through the T^4 dependence of the measured intensity. This is discussed further in Chapter 6 and Chapter 7.

While the peak temperature of the aggregate in point-contact (red) is comparable to the experimentally determined pyrometric temperature, this assumes that the aggregate structure remains unchanged, which is unlikely since the particles reach temperatures that exceed the melting point of the primary particles. Compared to the experimental data, the coalesced structure cools down too slowly, while the non-coalesced one is too fast, which might indicate that, in reality, a combination of such structures is present. Noteworthy here is that while particles in the probe volume are expected to equilibrate with the ~300 K bath gas at later cooling times, their slower cooling—due to higher heat capacity and lower surface-to-volume ratio

compared to 6 nm primary particles—is consistent with model predictions in Figure 5-12, where large particles (150 and 250 nm) remain at high temperatures when cooling from the estimated peak pyrometric temperatures.

Note that the aggregate is modeled to absorb laser energy uniformly, and absorption nonuniformities within the aggregate are ignored since sintering will lead to an isothermal aggregate. In addition, it is noted that the MSTM-estimated absorption cross-section is obtained with a larger number of expansion terms (to ensure convergence) than was used in Chapter 3 and Chapter 4, which underestimate the true absorption cross-section (*cf.*, Appendix A.5).

Assuming sudden coalescence from an aggregate structure to a sphere upon melting may excessively simplify the process while also greatly reducing the absorbed laser energy, resulting in lower peak temperatures as seen in Figure 5-7. There is currently no consolidated model to investigate the time-resolved aggregate sintering on the LII signal and temperature.

5.4.3. Analysis of the pyrometrically-determined peak temperatures

Until now, the heating phase of the LII signal has been analyzed to elucidate the laser–nanoparticle interaction; however, it is the cool-down phase of the particles and the associated LII signal that provides information about the particle size distribution and other QoIs. The temporal variation of the LII signal during the cool-down phase can be conceptually divided into prompt and delayed portions; the prompt signal extends from the peak signal to ~50 ns following the peak, which is followed by the delayed signal. The apparent anomalous signal behavior mostly influences the prompt phase [66] but has been observed to last for as long as 400 ns in the case of LII measurements on molybdenum aggregates [19].

Figure 5-8 compares LII fluence curves for iron nanoparticle aggregates reported in the literature with those obtained from the current experimental data. Note that the morphologies of the iron aggregates from the earlier studies all differ from each other and from this work due to the different nanoparticle synthesis and aerosol generation methods used. Sipkens *et al.* [19] used an atomizer and diffusion dryer setup to aerosolize particles in a colloid of chemically synthesized iron nanoparticles and reported isolated spheres following a distribution of ln(39.8 nm, 1.16). Kock *et al.* [22] reported chain-like iron aggregates synthesized in a hot wall flow reactor, resulting in aggregates with primary particles distributed according to ln(26.9

nm, 1.34) and ln(18.0 nm, 1.41) in Ar and N_2, respectively. Eremin *et al.* [70,87] synthesized chain-like iron nanoparticles through photolysis of $Fe(CO)_5$ at room temperature using a Kr–F excimer laser and showed that the resulting aggregates consisted of primary particles that obeyed a lognormal distribution with a mean of about 8 nm. An expected fluence curve can be simulated from an initial aggregate distribution of $N_p \sim \ln\mathcal{N}(200, 1.8)$ (informed by TEM analysis) while also considering the surface energy released during coalescence. This simulation is also compared to the fluence curve corresponding to spheres having the diameters of coalesced aggregates, $\sim\ln\mathcal{N}(56\text{ nm}, 2)$, based on the diameters of spheres generated by capturing iron aggregates on a TEM grid and heating them with the laser pulse (*cf.*, Figure 3-7). The coalesced particles within the aerosol have different peak temperatures and the emitted incandescence signals are integrated, according to Eq. (5.1), and subsequently used to determine simulated pyrometric temperatures. Unlike soot, Figure 5-8 shows that the simulated fluence curves do not exhibit a plateau temperature in the fluence range typical of LII experiments [178] (the plateau region occurs at much higher fluences, *cf.*, Section 8.2.1). The peak pyrometric temperatures obtained from the current measured data are higher than the simulated value. This may be due to the actual size distribution of the coalesced particles within the probe volume being different from the estimated size distribution of the irradiated TEM sampled iron aggregates.

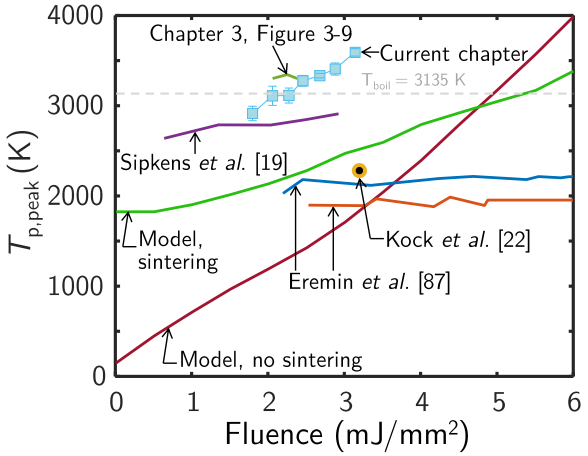


Figure 5-8: Apparent particle temperatures derived from LII signals as a function of laser fluence, compared with simulated temperatures for iron nanoparticles with a diameter distribution of $\ln\mathcal{N}(56\text{ nm}, 2)$ obtained from Eqs. (2.1), (2.17), and (2.23) (Model, no sintering) and simulated temperatures from an aggregate size distribution of $\ln\mathcal{N}(200, 1.8)$ with sintering and surface energy release considered (Model, sintering). Peak temperatures from the literature are obtained from Refs. [19,22,87] and re-evaluated with the $E(\mathbf{m}_\lambda)$ determined from refractive indices obtained from ellipsometry [103].

The prompt LII signals could potentially be corrupted by non-incandescent emissions that could bias the inferred peak temperatures. These emissions may originate from thermal or laser-induced emission of atomic

or molecular gas-phase species [179], recombinative chemiluminescence [66], or plasma emission [89,98]. These signals can differ in temporal characteristics depending on excited state lifetimes and formation kinetics of the related excited species. Vander Wal *et al.* [66] experimentally investigated the interference of non-incandescent emissions by analyzing both spectrally- and time-resolved data based on the assumption that LII signals and the potential interference have highly distinct fluence dependences and temporal characteristics. In particular, significant non-LII interference would result in an inconsistent temporal variation of the total signal as a function of laser fluence. In their strategy, they used a spectrograph to determine wavelengths at which only thermal emissions occurred and those that had other emissions and spectral features present. Then, the time-resolved intensities measured at the wavelengths with and without other emissions and spectral features were plotted on a logarithmic scale at different fluences. On the logarithmic scale, they observed that at wavelengths with only thermal emissions, the slopes of the intensities were similar across all fluences and were likely due to evaporative mass loss while the intensities measured at the wavelengths with other emissions present showed a marked change in the slope of the prompt signal as a function of fluence, which they used as an indicator for the presence of a non-LII signal in the time-resolved data. With this strategy, they showed that, for iron nanoparticles irradiated at 1064 nm, increasing amounts of non-thermal emissions interfere with the LII signal at a range of detection wavelengths below 400 nm, although at much higher fluences (> 9 mJ/mm^2) than those used in this work (≤ 3.14 mJ/mm^2). It has also been shown for titanium dioxide nanoparticles irradiated at 355 nm that the recorded signals contain LIF, LII, and plasma emissions depending on the laser fluence and also occur at different time scales with LII emissions lasting longer than non-LII emissions [180].

Figure 5-9a shows that at all fluences investigated in the current experiments, the LII signal decay indicates similar particle cooling rates with a rapid decay in the prompt signal that lasts longer at the higher fluences. This is consistent with observations from the literature on irradiated iron [22] and nickel [16] nanoparticles and has been associated with evaporative mass loss. To observe the presence of interfering non-LII signals, the recorded signals are also plotted on a logarithmic scale at selected fluences and wavelengths in Figure 5-9b, following a procedure by Vander Wal *et al.* [66]. As seen in Figure 5-9b, for the same detection wavelength, there is no obvious change in the slope of the logarithm of the intensity of the prompt signals as a function of fluence, which, according to the procedure of Vander Wal *et al.* [66], suggests the absence of non-incandescent emissions and the dominance of evaporative cooling. This observation was consistent among all detection wavelengths, and hence, according to the analysis by Vander Wal *et al.* [66],

it also follows that it is unlikely that the signals were affected by appreciable non-incandescent emissions at these wavelengths, and evaporative cooling is dominant.

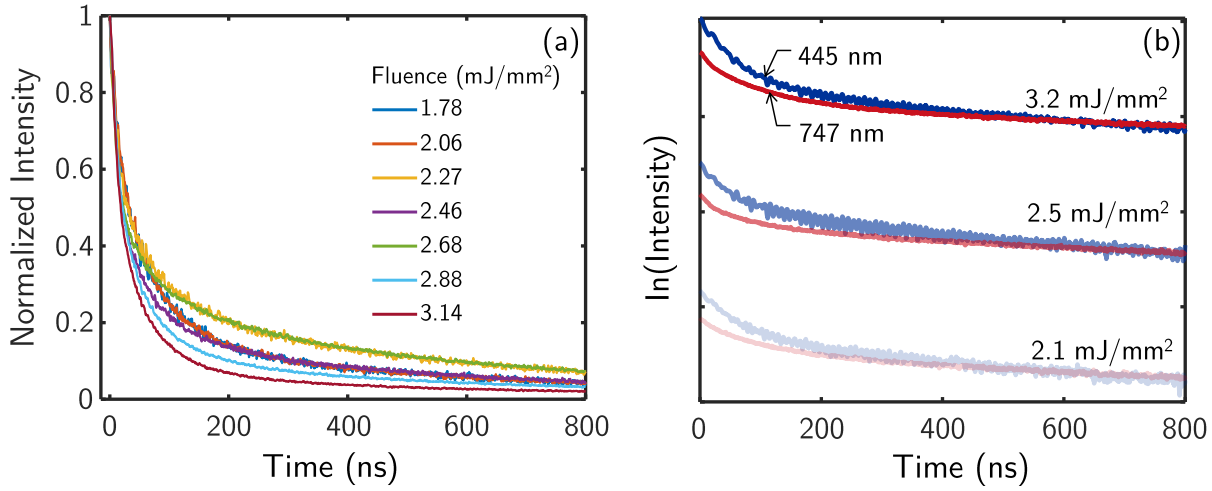


Figure 5-9: Temporal variation of the LII signal for iron nanoparticles irradiated at varying laser fluence **(a)** Linear plot of signal detected at 747 nm. **(b)** Semi-logarithmic plot of the measured signal detected at 445 and 747 nm.

5.4.4. Quantities-of-interest inference from prompt and delayed LII signals

Given the uncertainty attached to the prompt signal, it is common practice to exclude this data when inferring quantities-of-interest like the size distribution parameters from the LII data, up to a certain delay time after the peak incandescence signal [16,43]. In this section, the effect of increasing this delay time and its impact on the parameters inferred from the signal decays are explored. This method of time-delayed detection has also been performed for metal nanoparticle LII [66].

The LII model used to analyze the data assumes that the aerosol consists of isolated molten iron spheres. Only the cool-down phase of the LII signal is included in the regression because, as established in Sections 5.4.1 and 5.4.2, the physical understanding of the heating phase for iron nanoparticles is incomplete (*cf.*, also Appendix A.9 for attempts to include the heating phase in the regression). Accordingly, this treatment imposes a uniform particle temperature equal to the pyrometric temperature inferred from the peak LII signal. However, while this may be reasonable for aerosols of soot particles that absorb and emit in the Rayleigh regime, in the case of metal nanoparticles it introduces an unavoidable, and potentially substantial, model error into the analysis since particles of different sizes and morphologies absorb laser energy and emit

incandescence in a manner that is not proportional to their volume [20], and consequently, the peak particle temperature is expected to be far from uniform.

A total of 30 signals were obtained, each averaged over 200 shots. A weighted nonlinear regression is used to infer two combinations of four QoIs that include the mean particle diameter, d_p, the geometric standard deviation of the distribution, σ, the thermal accommodation coefficient, α, and the model peak temperature, T_{peak}. Case I has the QoI combination: [d_p, σ, α, T_{peak}] and Case II assumes a monodisperse aerosol with the combination: [d_p, α, T_{peak}]. The regression is performed at 450, 650, and 747 nm, avoiding the noisy 550 nm detection channel, and at different time delays, t_{delay}, after peak incandescence. Figure 5-10 shows that the LII modeled data are in better agreement with the experimental data at a longer time delay, t_{delay}, suggesting that, as expected, the model cannot accurately capture the prompt signals.

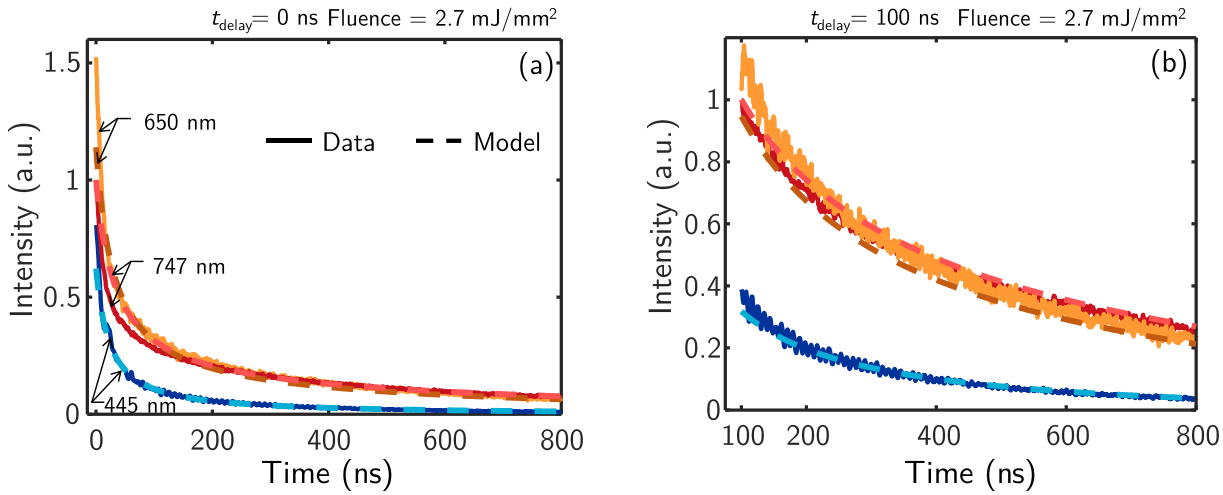


Figure 5-10: Regression of the LII model (Eqs. (2.1) and (5.1)) to the data at a tdelay of **(a)** 0 ns and **(b)** 100 ns.

The inferred QoI from Case I are shown in Figure 5-11. The inferred geometric mean particle diameter ranges from about 100–160 nm at shorter t_{delay}, and this range narrows with increasing t_{delay} to 140–150 nm at the longest time delay of 400 ns. Because the inference procedure imposes a uniform initial temperature for all particle sizes, the inferred size distributions are uniform or nearly uniform ($\sigma \approx 1$). While the true size distribution of coalesced spheres within the aerosol is unknown, examination of iron aggregates deposited on a TEM grid and irradiated with a laser pulse suggests that the aggregates coalesce to a final size distribution of $d_p^{coalesc} \sim \ln\mathcal{N}(56\text{ nm}, 2)$, which is inconsistent with the inferred size distribution. The TEM-estimated final size distribution of the coalesced particles was also inconsistent with the expected

equivalent diameter of ~35 nm produced from the aggregate distribution of $p(N_p) \sim \ln\mathcal{N}(126, 1.77)$ assuming a uniform primary particle diameter of 6 nm. The reason for this discrepancy remains unknown, although, in the case of the particles irradiated on the TEM grid, the coalesced particles may consist of several "merged" aggregates.

The inferred diameters are expected to be biased towards hotter particles since these particles dominate the emitted incandescence. According to Figure 3-12a, the particles with the highest peak pyrometric temperatures have diameters of approximately 150 and 250 nm. In this chapter, the inferred diameters are more in line with the lowest end of this range. Figure 5-12 shows that for the same peak temperature, the evaporative cooling rate for a 150-nm diameter particle is higher than that of a 250-nm diameter particle. In addition, the inferred model peak temperatures, particularly at shorter time delays, are higher than the effective pyrometric temperatures. Hence, the regression tends toward size classes that are more likely to produce the highest temperatures while also having the fastest evaporative cooling following the prompt signal.

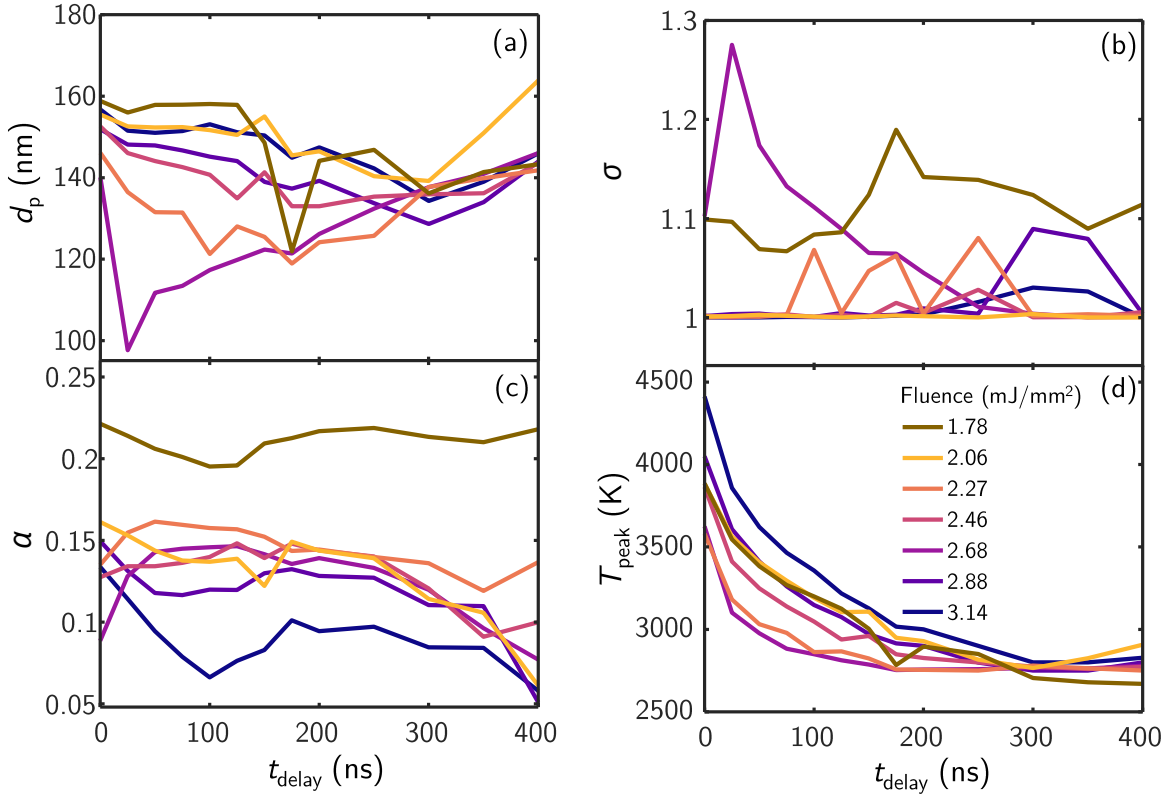


Figure 5-11: Inferred QoIs from Case I including, **(a)** d_p, **(b)** σ, **(c)** α, and **(d)** T_{peak} as a function of tdelay at difference laser fluences. Inferrences from the lowest fluence may be unreliable due to the large noise levels in the data.

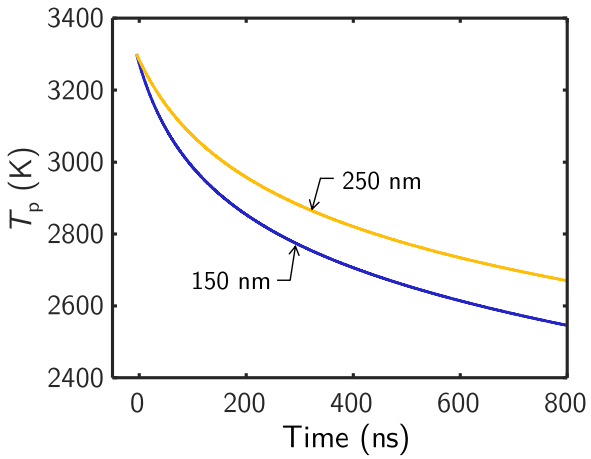


Figure 5-12: Comparison of the rate of evaporative cooling for iron nanoparticles with diameters of 150 and 250 nm, cooling from the same peak temperature of 3300 K.

Excluding the earlier portions of the signals increases the influence of polydispersity on the temperature distributions at later cooling times. Also, while the inferred TACs are "effective" due to the temperature distribution within the probe volume from different size classes, they are consistent with the values reported in the literature (0.05–0.1 [19]). Inferred peak temperatures are also higher than the measured pyrometric temperatures of ~3300 K at a lower t_{delay} but converge to lower temperatures at a longer t_{delay}; however, compared to the pyrometric temperature shown in Figure 5-2b, the temperatures remain higher at longer cooling times. Higher temperatures are inferred compared to the pyrometric temperatures due to the use of the more accurate Mie absorption cross-sections that have a larger $C_{\text{abs},\lambda 2} / C_{\text{abs},\lambda 1}$ ratio compared to the Rayleigh approximations, which have a strong influence on the approximation of the pyrometric temperature. The reduction of the T_{peak} at a longer t_{delay} is expected since the temperatures are lower with the removal of more of the prompt signals (*i.e.*, particles cool with time). The narrowing particle size distribution from all fluences with increasing t_{delay} is not expected and indicates that there may be phenomena close to the peak signal that are not captured by the model.

Case II results are shown in Figure 5-13. Inferred QoIs at $t_{\text{delay}} > 100$ ns are generally consistent with trends observed for Case I. At $t_{\text{delay}} < 100$ ns, the inferred diameters and TACs are much lower, including the goodness-of-fit. It is not clear why smaller diameters and TACs are inferred at $t_{\text{delay}} < 100$ ns; however, this causes lower model peak temperatures to be inferred with prompt signals compared to Case I, which eventually increase at longer time delays when the inferred diameters are consistent with Case I.

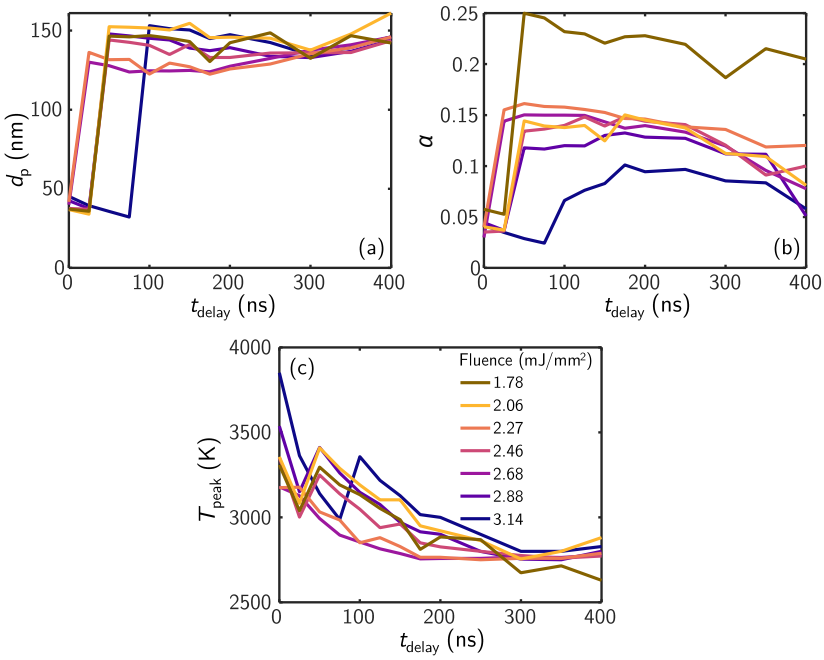


Figure 5-13: Inferred QoIs from Case II including, **(a)** d_p, **(b)** σ, **(c)** T_{peak} as a function of tdelay at difference laser fluences.

Some insight into model deficiencies may be gained from the residual between the measured intensity and the best-fit model. Figure 5-14 shows that, at $t_{delay} = 0$ ns, the residuals at all fluences reduce and converge to zero at $t = 200$ ns, after which the model slightly underestimates the data for some fluences. By $t_{delay} = 100$ ns, all residuals are unbiased for the remaining duration of the LII signal, but this does not mean that the corresponding inferred QoIs are accurate. Figure 5-14 also shows that the evaporation model does not capture the prompt signal decay, with a percent difference of as much as 40 % at the highest fluence of 3.14 mJ/mm^2. In this respect, the assumption of uniform peak particle temperatures may be a leading source of error, which can be eliminated with modifications (such as accurately accounting for time-resolved sintering). While experimental measures could be taken to reduce the contribution from the rapid, unexplained cooling during the prompt signal by avoiding fluences that induce evaporation, Chapter 6 shows that assessing the accuracy of the pyrometric temperature in the context of particle polydispersity may offer additional insight into the observed rapid drop in temperature after the peak temperature.

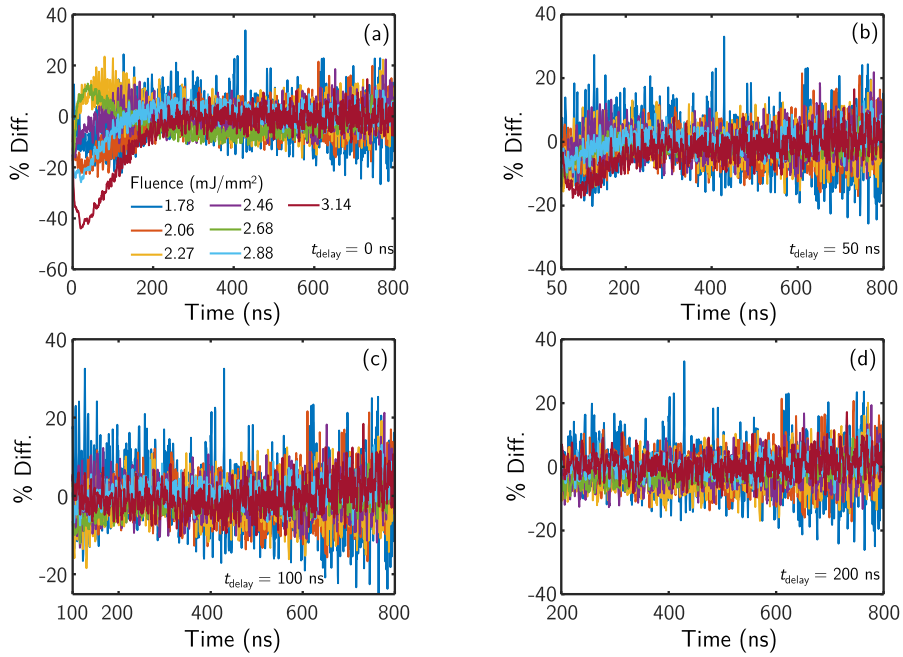


Figure 5-14: Residuals of the LII model regression to the emitted signals for different laser fluence at time delays of **(a)** 0 ns (**b**) 50 ns **(c)** 100 ns, and, **(d)** 200 ns. For each fluence, the residuals are averaged from those at the detection wavelength of 445, 650, and 747 nm.

5.5. Conclusions

This work shows that laser-irradiated iron aggregates are likely to coalesce during the laser pulse once reaching their melting point, producing an aerosol of spheres having diameters determined by the total mass of the original aggregate. This affects the particle temperatures in a number of ways: (1) metal nanoparticle aggregates have significantly larger specific (mass-normalized) absorption cross-sections compared to spheres, which influences the absorbed laser energy per mass; (2) the surface energy of the aggregate is transferred to the sensible energy of the particle upon coalescence, thereby increasing its temperature; (3) the reduced surface-to-volume ratio reduces heat transfer to the surrounding gas, and (4) the absorption cross-section evolves as an aggregate in point contact sinters in a manner that depends on wavelength and likely reduces field-enhancements within the aggregate due to increased electrical contact. (5) Upon coalescence, particle ensembles with initial variations in aggregate size lead to ensembles of similarly-sized spherical particles with strongly varying temperatures, where the apparent temperature is increased because the pyrometric temperature measurement is biased towards the high-temperature part of the distribution.

Based on simulations of viscous sintering and coalescence times, it is concluded that coalescence occurs almost instantaneously during laser heating once the melting temperature has been reached. As a consequence, during the laser pulse, the specific absorption cross-section changes significantly, reducing laser heating. At the same time, the coalescence results in the release of surface energy, increasing the particle temperature. According to the evaluation, the loss in absorbed laser energy due to the reduction in absorption cross-section is far larger than the increase in sensible energy from the reduced specific surface area. Particles gain additional energy through enhanced absorption in the initial phase due to their aggregate history and through conversion of surface energy, thus contributing to the effect of "excessive absorption" described before for metal particles. Nevertheless, the current model can not yet fully explain the peak temperatures and temperature decays observed experimentally. The possibility that the unexpectedly high peak temperatures are due to signal contamination by non-incandescent emissions within the applied fluence range is discounted.

A further complication of the particle coalescence is that the particle peak temperatures are expected to be highly nonuniform in the particle ensemble. Since there is presently no model that adequately explains the details of the laser-heating process during the structural change of the particles, the cooling phase of the signal is analyzed by assuming that all the particles reach a common peak temperature. Analyses were started at varying delay times after the peak LII signal. The analysis showed that the current LII evaporation model does not accurately capture the prompt LII signals; however, the delayed signals are well captured by the conduction model. This may be a result of the assumption of uniform temperature, which is most likely not the case within the probe volume. Consequently, the inferred quantities-of-interest may not be representative of the actual particle diameters after coalescence in the aerosol; rather, they are diameters that most explain the high peak temperatures and rapid rate of evaporation.

In the next chapter, the accuracy assumption of uniform particle temperatures is assessed in detail, including its impacts on the temporal evolution of the experimentally measured pyrometric temperature.

Chapter 6

Interpreting pyrometric temperatures measured during laser-induced incandescence on iron nanoparticles

The analysis presented in this chapter assesses how the simplifying assumptions and approximations made in the previous chapters can impact the interpretation of the aerosol temperature during TiRe-LII experiments on iron nanoparticles. These effects differ from LII on carbonaceous species and are due to the metal particles not obeying Rayleigh conditions in their interaction with light, even for nanometer-sized particles. While Section 3.2.2 briefly discussed the impact of some of these assumptions and particle polydispersity on the pyrometric temperature (*cf.*, Figure 3-2), the investigations in this chapter provide a more in-depth discussion on the topic and show that nonuniformity in the particle size can result in biased temperatures and temporal variations in pyrometric temperature. The results show that, considering particle polydispersity, the resulting pyrometric temperatures possess features that resemble the effects previously termed excessive absorption and apparent anomalous cooling. These findings may be generalized to LII measurements on other metal aerosols.

6.1. Introduction

When estimating the pyrometric temperature of a laser-heated aerosol, often several assumptions and approximations are made concerning the particle morphology. For soot, where light absorption is well described by the Rayleigh approximation, such assumptions are less relevant, as light absorption and emission can be considered proportional to the particle volume independent of shape, and thus all nanoparticles in an aerosol initially reach the same temperature at a given laser fluence. For metal nanoparticles considered in this thesis work, the assumption of monodispersity and the absence of aggregate effects, including field enhancements and sintering, are often used. The pyrometric temperatures derived using such simplifying assumptions are used in previous studies to provide a rough estimate of the instantaneous "average" temperature of the laser-heated aerosol [16,19,22,87], while the temperature of individual particles differs and depends on size, morphology, and orientation. These assumptions and approximations, therefore, can introduce significant uncertainties that complicate the interpretation of pyrometrically-derived temperatures.

In this chapter, the impact of these assumptions and approximations on the interpretation of the pyrometric temperatures – and thus the capability of quantitatively analyzing LII signals – is explored. The results are used to analyze the extent to which previously reported "anomalies" in the LII data, such as the so-called excessive absorption and anomalous cooling phenomena, are in fact related to the underlying erroneous assumptions and might therefore need to be revisited. While iron nanoparticles are used as a case study, because it is the most studied metal in the LII literature [91], effects, previously attributed to "excessive absorption" have also been observed for LII measurements on nickel [16], molybdenum [19,139], silver [19], and gold [90] nanoparticles and "apparent anomalous cooling" has been identified in data collected on iron [139,172], and molybdenum [19,139] nanoaerosols.

Discussions in previous chapters have shown the contribution of metal nanoparticle aggregation, and aggregate sintering and coalescence to the observed effects of initially monodisperse particles. In contrast, the analysis in this chapter considers polydisperse isolated spherical particles as a simplifying first step to investigate the effects of particle polydispersity, which can be further modified to consider aggregate effects.

The work reported in this chapter aims to analyze LII for polydisperse spherical metal nanoparticles and shows its effects on the pyrometrically-derived temperature, which are expected to be exacerbated by aggregate effects. In a polydisperse metal nanoparticle aerosol, where particle heat-up temperatures depend

on individual particle size, some particles may undergo partial or complete evaporation, leading to different energy-loss pathways and thus different temporal variations in particle temperature. Since, at a fixed pulse width, the fraction of particles cooling by evaporation depends on the fluence, the effect also depends on the laser fluence. For practical cases, where the fluence varies spatially and/or temporally, additional complications arise. A preliminary proposal for how to address this issue is presented in Appendix B.

6.2. TiRe-LII measurement model

The heat transfer submodel for isolated spheres, as presented in Chapter 2, is used here with the exception that full Mie theory is used to calculate absorption cross-sections. In this chapter, while unnecessary due to its insignificant contribution to the heat loss as discussed in Chapter 2, the radiative heat loss term is included in the model (*i.e.,* Eq (2.1)) for completeness, according to

$$q_{\mathrm{rad}}\left(T_{\mathrm{p}}, d_{\mathrm{p}}\right) = 4\pi \int_{0}^{\infty} C_{\mathrm{abs},\lambda}\left(\mathbf{m}_{\lambda}, d_{\mathrm{p}}\right) I_{\mathrm{b},\lambda}\left[T_{\mathrm{p}}\left(t, d_{\mathrm{p}}\right)\right] \mathrm{d}\lambda \,. \tag{6.1}$$

The heated aerosol is considered optically thin and contains polydisperse isolated particles irradiated with a uniform fluence. The emitted spectral incandescence J_λ from the aerosol is modeled according to

$$J_{\lambda}\left(t\right) = A_{\lambda} \Lambda \int_{d_{\mathrm{p}}} p(d_{\mathrm{p}}) C_{\mathrm{abs},\lambda}\left(\mathbf{m}_{\lambda}, d_{\mathrm{p}}\right) I_{\mathrm{b},\lambda}\left[T_{\mathrm{p}}\left(t, d_{\mathrm{p}}\right)\right] \mathrm{d}d_{\mathrm{p}} \,, \tag{6.2}$$

where A_λ and Λ are the calibration constant and the intensity scaling factor, respectively, and $I_{\mathrm{b},\lambda}$, is the blackbody intensity. The measured incandescence signal is modeled by an integral of the various incandescence signals emitted from the probe volume due to the different diameters, d_{p}, which are weighted by the corresponding probability density function $p(d_{\mathrm{p}})$. Equation (6.2) does not consider the effects that occur due to nanoparticle aggregation. Accounting for the presence of aggregates will increase the intensity of the predicted incandescence (*cf.*, Chapter 3 and Chapter 4), introduce additional temperature nonuniformities within the probe volume due to nonuniform laser absorption within the aggregate (*cf.*, Chapter 3 and Chapter 4), and increase the internal energy of the nanoparticle due to release of surface energy during coalescence (*cf.*, Chapter 5). Since the goal of the current work is to show the first-order effects of nonuniform particle sizes within the probe volume, a simplified version of the predicted incandescence as presented in Eq. (6.2), ignores the aggregate history of the spheres formed from coalescence.

Evaluating accurate pyrometric temperatures requires information on $p(d_\mathrm{p})$. It is often the goal of LII to determine $p(d_\mathrm{p})$ from experimental data. The commonly used two-color pyrometric temperature is an attractive metric because it is determined independently of the particle size and distribution. Typically, evaluations of the two-color pyrometric temperature either ignore the non-Rayleigh behavior of metal nanoparticles or ignore the particle-size distribution, $p(d_\mathrm{p})$, and thus approximate the particle distribution as monodisperse. This makes the pyrometric temperature an "effective temperature" that – given the strong dependence of the LII signal intensity on temperature – is biased to the high-temperature side of the distribution.

In the literature, the effective pyrometric temperature is often interpreted as a representative temperature that indicates the average internal energy of the particles within the probe volume, *i.e.*, the sensible bulk (*i.e.*, particle ensemble) thermodynamic temperature of the particles. When the temperatures of all particles within the probe volume are known, as well as the size distribution and material properties, the sensible bulk thermodynamic temperature of the probe volume, $T_\mathrm{pv,thermo}$, can be determined as described in Eq. (3.13). Note that $T_\mathrm{pv,thermo}$ differs from the thermodynamic temperature in Eq. (2.1), which indicates the temperature of a single nanoparticle.

One may also attempt to determine an effective diameter of a hypothetical monodisperse aerosol that will have temperatures that may represent the temperature of the particle ensemble. Such a diameter is defined based on the volumetric equivalent diameter of the particle ensemble within the aerosol, given by [20]

$$d_\mathrm{p,vol} = \left(\int_0^\infty d_\mathrm{p}^3 p\left(d_\mathrm{p}\right) \mathrm{d}\, d_\mathrm{p} \right)^{1/3} . \tag{6.3}$$

These temperature metrics, including the particle thermodynamic temperature, the effective pyrometric temperature of the ensemble, the sensible bulk thermodynamic temperature, and the temperature of the volumetric equivalent diameter of the aerosol, are compared to gain further insight into the interpretation of the pyrometric temperature that is most often used in TiRe-LII analysis.

6.3. Results and discussion

6.3.1. Assessing the accuracy of the pyrometric temperature

Two-color pyrometry is often based on the Rayleigh approximation and is commonly used to estimate the temperature of the metal nanoaerosol from measured incandescence. However, Talebi-Moghaddam [20] showed that the often applied Rayleigh approximation is invalid for metal nanoparticles due to the high refractive indices of metal compared to soot. Consequently, the estimated pyrometric temperature of a monodisperse metal nanoaerosol may not accurately predict the thermodynamic temperature of the aerosol (estimated from the heat transfer model for an isolated particle with the same diameter as the particles in the monodisperse aerosol (Eq. (2.1))). However, when the information on the particle size is known, Mie-estimated absorption cross-sections can be used to estimate a more accurate pyrometric temperature of the monodisperse aerosol [20]. Figure 6-1a shows, for a particle diameter of 55 nm, that the time-resolved pyrometric temperature (employing the Rayleigh approximation) of the monodisperse aerosol is not consistent with the predicted thermodynamic temperature, specifically from the peak temperature onwards. The pyrometric temperatures were obtained from simulated incandescence signals at 445 and 747 nm, detection wavelengths that have been used in previous experiments.

Figure 6-1b quantifies the discrepancy, at the peak temperature, between the pyrometric and particle thermodynamic temperatures for different particle diameters. The errors remain within 5 % below ~120 nm, beyond which the effective pyrometric temperature begins to underestimate the particle thermodynamic temperature, reaching a maximum error of approximately 20 %. This trend due to the discrepancy between the arguments $(C_{\mathrm{abs},\lambda 2}\,/\,C_{\mathrm{abs},\lambda 1})\cdot(\lambda_1/\lambda_2)^5$, which would be used to compute the pyrometric temperature if the size information is known (*i.e.*, employing Mie theory, *cf.*, Eq. (3.10)), and $(E(\mathbf{m}_{\lambda 2})/E(\mathbf{m}_{\lambda 1}))\cdot(\lambda_1/\lambda_2)^6$, which is normally used to compute the effective pyrometric temperature of the nanoparticle ensemble using Rayleigh approximation (*cf.*, Eq. (3.12)). Note that while a spherical metal nanoparticle does not absorb the laser energy volumetrically (as soot would in the Rayleigh regime), any ensuing temperature gradient is quickly dissipated in order of picoseconds, based on phonon relaxation times [164]. Figure 6-1 highlights the errors of the pyrometric temperature, due to the Rayleigh approximation, even for cases of monodispersity, which are exacerbated by nonuniform particle sizes as discussed in the following section.

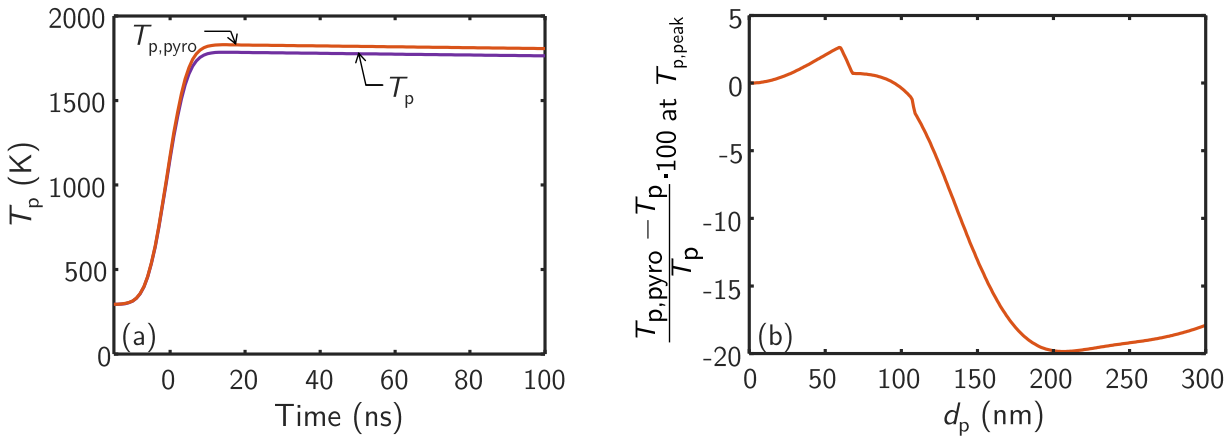


Figure 6-1: (a) Discrepancy between the temporal evolution of the thermodynamic and the pyrometric temperature of a 55-nm diameter iron nanoparticle irradiated with a uniform fluence of 2.5 mJ/mm^2 and **(b)** Compared to the particle thermodynamic peak temperature, the percent error of the peak temperature determined from color pyrometry using Rayliegh approximation.

6.3.2. Effects of polydispersity on the effective pyrometric temperature

The polydispersity of the aerosol particles within the probe volume results in a distribution of instantaneous temperatures, which widens when particles move out of the Rayleigh regime (*i.e.*, for metals and with larger particle size). Figure 6-2a shows the ranges of peak particle thermodynamic temperatures for different spherical particle diameters as a function of laser fluence. As expected, the particles reach higher peak temperatures with increasing laser fluence, with some particle size classes being superheated (*i.e.*, temperature higher than the boiling point of bulk iron) at higher fluences. The trend in peak particle thermodynamic temperatures, at the fluences considered, is dictated by the amount of laser energy absorbed per volume for each particle diameter, as shown in Figure 6-2b. The particle size class of about ~250 nm absorbs the largest laser energy per volume and consequently also reaches the highest peak thermodynamic temperatures. The effective pyrometric temperatures of the particles also follow the same trend as the thermodynamic temperatures, as shown in Figure 6-2c (consistent with results presented in Figure 3-12); however, the difference between the thermodynamic temperature and the pyrometric temperature of the ensemble increases with increasing particle diameters up until a point after which the difference begins to decrease. This trend is consistent with results presented in Figure 6-1b, where the error grows, reaching a maximum for size classes with diameters of ~ 200 nm and then begins to decrease. This trend is due to the amplification of the error from the Rayleigh approximation term (*i.e.*, the $(E(\mathbf{m}_{\lambda 2})/E(\mathbf{m}_{\lambda 1}))\cdot(\lambda_1/\lambda_2)^6$ term in

Eq. (3.12)) by the $J_{\lambda,1}/J_{\lambda,2}$ term that is larger for hotter particles. Hence, this trend is an indication that the error in the pyrometric temperature from the Rayleigh approximation also grows with particle temperature.

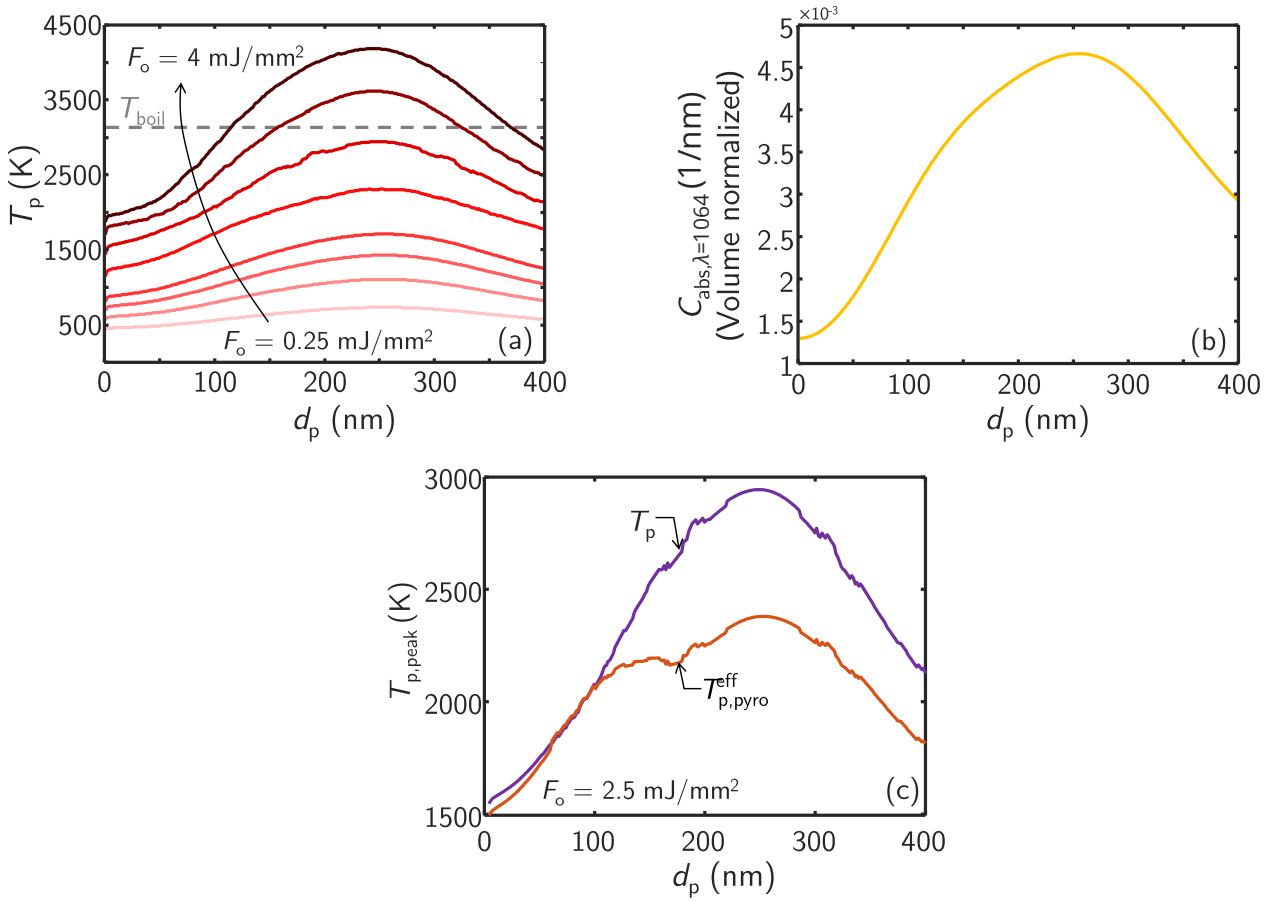


Figure 6-2: (a) Particle thermodynamic temperature as a function of particle diameter for varying fluences of 0.25, 0.5, 0.75, 1, 1.75, 2.5, 3.5, and 4 mJ/mm². **(b)** Volume normalized $C_{abs,\lambda=1064}$ for varying particle diameters. **(c)** Comparison of the thermodynamic temperature and the effective pyrometric temperature at varying particle diameters.

Due to particle size polydispersity, particle temperatures obey a wide distribution within the probe volume at any given instant; however, only one effective incandescence signal is measured, at each detection wavelength, during LII experiments from which effective pyrometric temperatures are determined. Figure 6-3 shows the range of peak temperatures, determined by several metrics, for varying particle size distribution widths with mean diameters of 20 and 50 nm, at laser fluences of 1.5, 2.5, and 3.5 mJ/mm². For each case of mean diameter and fluence, the sensible temperature of the particle ensemble is influenced by the temperatures of every particle present in the aerosol.

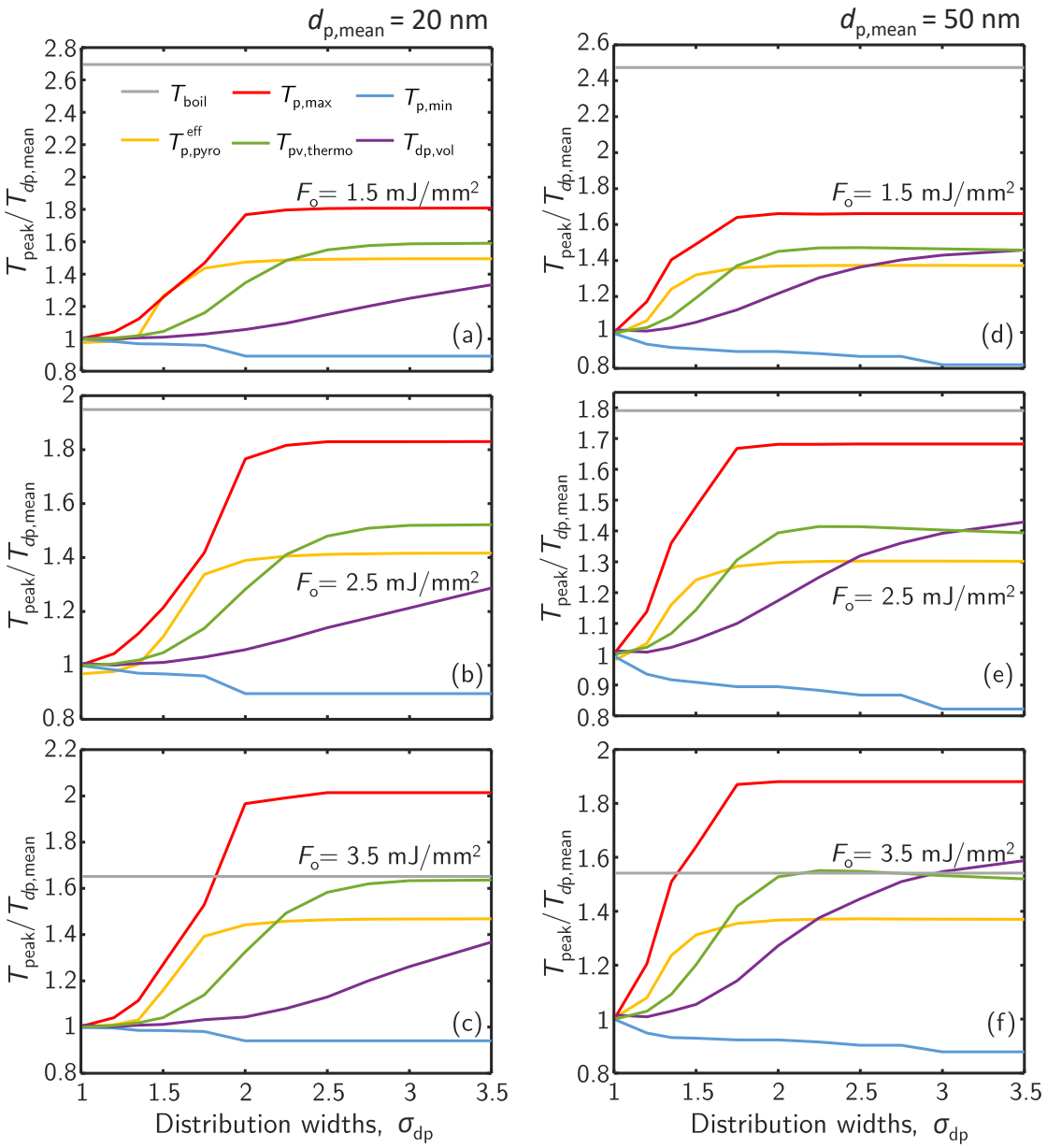


Figure 6-3: The peak temperature of the particle ensemble as estimated by the temperature of the hottest and the least hot particles, $T_{p,max}$, and, $T_{p,min}$, respectively, the pyrometric temperature of the particle ensemble, $T^{eff}_{p,pyro}$, the bulk sensible thermodynamic temperature of the particle ensemble in the probe volume, $T_{pv,thermo}$, and the particle thermodynamic temperature of the volume equivalent diameter of the ensemble, $T_{dp,vol}$, all normalized to the temperature of the peak thermodynamic temperature of the mean particle diameter for a particle size distribution with a mean of 20 nm and irradiated with a laser fluence of **(a)** 1.5 mJ/mm², **(b)** 2.5 mJ/mm², **(c)** 3.5 mJ/mm², and a particle size distribution with a mean of 50 nm and irradiated with a laser fluence of **(d)** 1.5 mJ/mm², **(e)** 2.5 mJ/mm², **(f)** 3.5 mJ/mm².

Per Figure 6-3, for all cases considered, increasing distribution widths lead to a larger temperature difference between the hottest particle, $T_{p,max}$, and the coldest particle, $T_{p,min}$. Other temperature metrics, including

the pyrometric temperature of the particle ensemble, $T_{\mathrm{p,pyro}}^{\mathrm{eff}}$, the bulk sensible thermodynamic temperature of the particle ensemble in the probe volume, $T_{\mathrm{pv,thermo}}$, and the particle thermodynamic temperature of the volume-equivalent diameter of the ensemble, $T_{\mathrm{dp,vol}}$, all lie between $T_{\mathrm{p,max}}$ and $T_{\mathrm{p,min}}$ and increase with distribution widths until they either reach a constant value or the rate at which they increase reduces.

As the particle size distribution widens, larger particles appear in the aerosol; hence, once particles with diameters of ~250 nm are present in the aerosol, $T_{\mathrm{p,max}}$ becomes constant and the rate at which $T_{\mathrm{p,pyro}}^{\mathrm{eff}}$, $T_{\mathrm{pv,thermo}}$, and $T_{\mathrm{dp,vol,}}$ increase begins to decrease as the influence of these particles increases. On the other hand, $T_{\mathrm{p,min}}$ continues to decrease as particles larger than ~250 nm are continually introduced into the aerosol. Note that $T_{\mathrm{pv,thermo}}$ slightly decreases at larger distribution, while $T_{\mathrm{p,pyro}}^{\mathrm{eff}}$ remains fairly constant. In the case of $T_{\mathrm{pv,thermo}}$, this is due to the increasing influence of the larger, lower temperature diameter particles, while in the case of $T_{\mathrm{p,pyro}}^{\mathrm{eff}}$, the trend is due to the T^4 dependence of the incandescence signal, the hottest particles continue to have an outsized influence on the measured incandescence. However, $T_{\mathrm{dp,vol}}$ continues to increase because the volumetric equivalent diameter increases for larger size distributions, but does not reach ~250 nm for the distributions considered, beyond which one would expect it to decrease. Figure 6-3 reveals that it is not straightforward to define a temperature metric to be used for TiRe-LII analysis.

As fluence increases, so do all temperature metrics, with more particles in the ensemble undergoing superheating at a fluence of 3.5 mJ/mm^2.

To investigate the effects of polydispersity on the time-resolved pyrometric temperature, several distributions, described by $\ln\mathcal{N}(56\text{ nm}, \sigma)$, are considered. Figure 6-4a – d shows that for a uniform fluence of 2.5 mJ/mm^2, at narrow size distributions, $T_{\mathrm{p,pyro}}^{\mathrm{eff}}$, $T_{\mathrm{pv,thermo}}$, and $T_{\mathrm{dp,vol}}$ closely agree. However, as the distribution widens and larger particles increasingly contribute to the incandescence signal, all three temperatures increasingly disagree. At narrow-to-moderate distributions, temperatures estimated by $T_{\mathrm{p,pyro}}^{\mathrm{eff}}$ are greater than $T_{\mathrm{pv,thermo,}}$ while the reverse occurs at wider distributions due to the influence of larger particles and growing pyrometric error at larger particle sizes. Figure 6-4e and f show a similar trend for a fluence of 3.25 mJ/mm^2, however, in this case, some particles in the ensemble reach temperatures above the boiling point (*i.e.*, superheating) of iron.

Comparing the time-resolved pyrometric temperature of varying size distributions, as presented in Figure 6-5, shows that the estimated temperatures increase as the size distribution widens at all times.

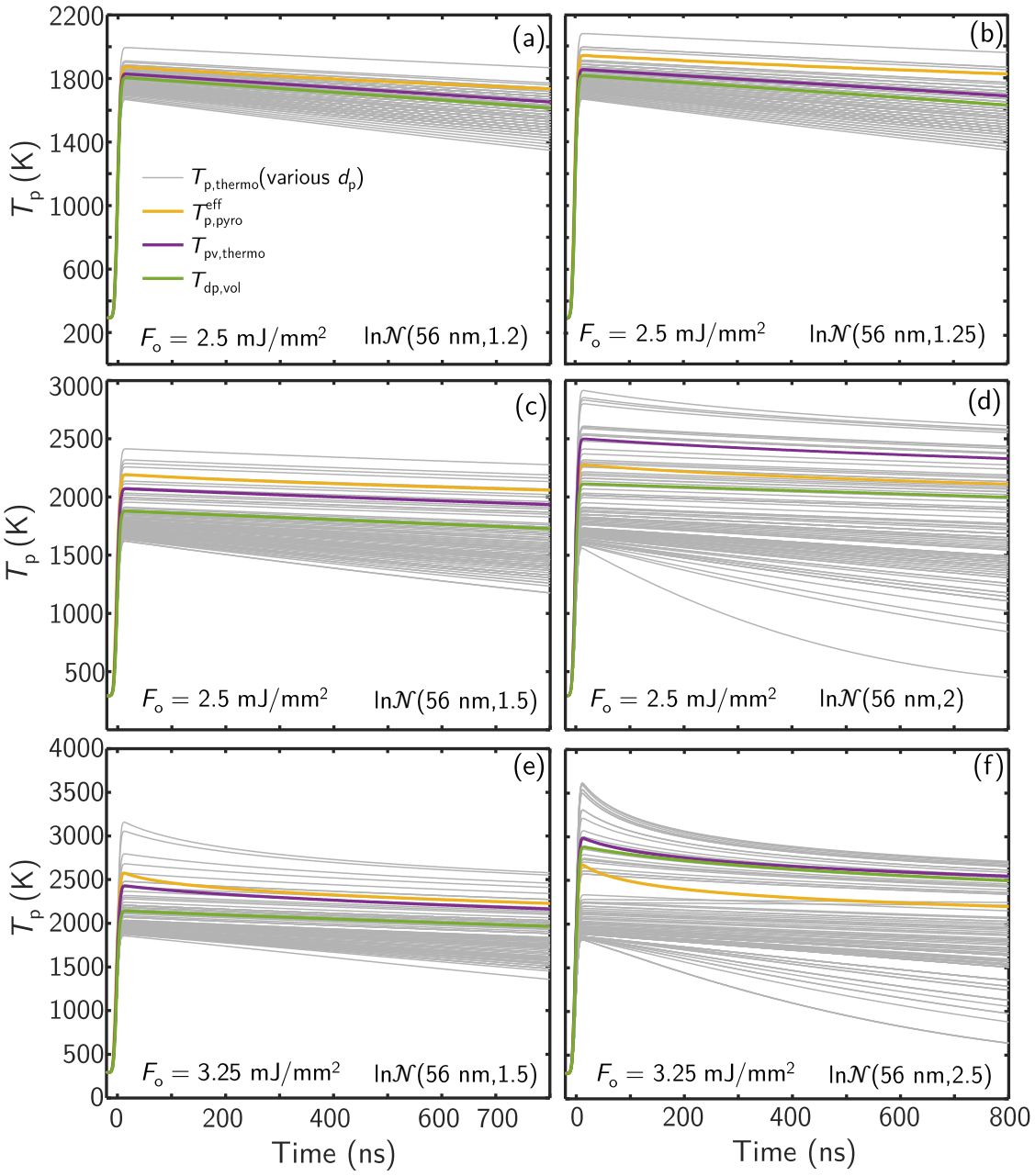


Figure 6-4: The effective pyrometric temperature, $T^{\text{eff}}_{\text{p,pyro}}$, the thermodynamic temperature of the probe volume, $T_{\text{pv,thermo}}$, the temperature of the volumetric equivalent diameter of the aerosol, $T_{\text{dp,vol}}$, and the temperatures of randomly sampled diameters within the probe volume, $T_{\text{p,thermo}}$, for different aerosol distributions with a mean diameter of 56 nm and a geometric standard deviation of and irradiated at a fluence of, respectively, **(a)** 1.2, and 2.5 mJ/mm² **(b)** 1.25, and 2.5 mJ/mm² **(c)** 1.5, and 2.5 mJ/mm² **(d)** 2, and 2.5 mJ/mm² **(e)** 1.5, and 3.25 mJ/mm², and **(f)** 2.5, and 3.25 mJ/mm²

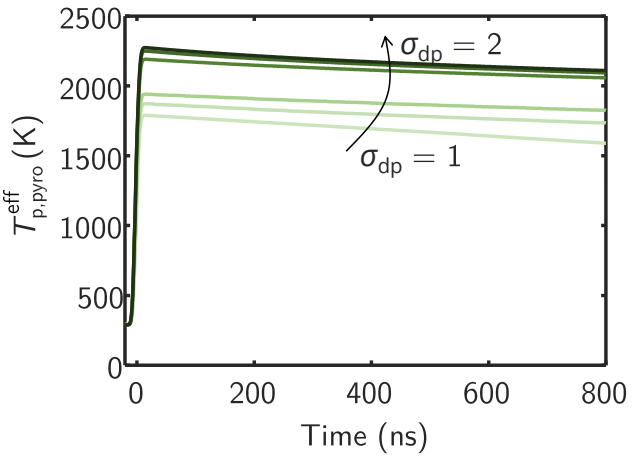


Figure 6-5: The effective pyrometric temperature of an iron aerosol with a mean diameter of 56 nm and various geometric standard deviations irradiated at a fluence of 2.5 mJ/mm^2.

As shown in Figure 6-5, the pyrometric temperatures of the particle ensemble are higher than one would expect if a monodisperse particle distribution is considered and the variations in temperatures due to particle polydispersity are ignored. This observation is consistent with the apparent excessive absorption phenomenon that is reported for metal nanoparticles [16,139,181]. Furthermore, Figure 6-4 shows that the superheated particles will consequently cool through evaporation and influence the pyrometric temperature such that there is a rapid temperature decrease following the peak pyrometric temperature, even though the predicted pyrometric temperatures remain below the boiling point of iron. Preliminary work shows that these observations are exacerbated by nonuniform fluences (*cf.*, Appendix B).

6.4. Conclusions

While the pyrometric temperature has been used extensively in the literature as an estimate of the average thermodynamic temperature of laser-heated aerosols containing metal nanoparticles, the underlying assumptions, including monodispersity and absorption in the Rayleigh regime, are invalid.

This work showed that when the full Mie theory is considered, the polydispersity of particle diameters leads to vastly varying temperatures in the aerosol that are not accounted for when estimating the pyrometric temperatures. In addition, although pyrometry is an attractive metric in TiRe-LII analysis to estimate the temperature of the particles due to its independence of the knowledge of particle size distribution, it is an inaccurate temperature metric, particularly when temperatures vary significantly.

While other temperature metrics were considered, it is not clear which ones may be used for TiRe-LII analysis.

When particle size polydispersity is considered in the TiRe-LII instrument model, the resulting pyrometric temperature profiles exhibit peak temperatures that are higher than would be expected for a monodisperse aerosol. Because the ensemble contains hot, superheated particles that cool through evaporation, the measured pyrometric temperatures decrease more quickly than expected, even when they are still below the level where evaporative cooling would normally dominate. These features bear similarities to the model-experimental data discrepancies termed “excessive absorption” and “apparent anomalous cooling”, respectively, and the results show that they are, at least in part, due to particle sizes that reach high temperatures and consequently cool down through evaporation within the aerosol.

The analyses presented in this chapter are extended through LII experiments on re-aerosolized soot and the consideration of nonuniform fluences in the next chapter to explain the apparent anomalous cooling of soot, the first reported instance of the phenomenon.

Chapter 7

Investigating the apparent anomalous cooling of soot during laser-induced incandescence experiments[7]

The discussions in previous chapters have extensively investigated laser-induced incandescence on metal nanoparticles. In Chapter 6, it was hypothesized that particle polydispersity may be contributing to the reported "anomalies", including excessive absorption and apparent anomalous cooling. In this chapter, this concept, including the consideration of nonuniform fluence, is adapted to soot, for which apparent anomalous cooling was first reported, to explain the phenomenon as it is observed in the soot data. Investigations are performed through experiments on soot entrained in different bath gases and irradiated in the low-fluence regime, where particle sublimation is minimal. It was found that the apparent anomalous cooling phenomenon is caused by the contribution of particles in the probe volume that have been heated beyond the sublimation threshold to the overall incandescence signal, due to nonuniform laser fluence. Particles in these "hot spot" regions feature a faster cooling rate due to sublimation, contributing to the effect of apparent anomalous cooling. Unlike iron nanoparticles, particle-size polydispersity plays a minor but notable role for soot particles due to their Rayleigh regime absorption. Furthermore, the effect depends on the bath-gas composition, which is attributed to differences in species-specific heat transfer.

[7] Information presented in this chapter is based on the published work:
Robinson-Enebeli S., Schulz C., Daun K.J., 2026, "Investigating the apparent anomalous cooling of soot during laser-induced incandescence experiments." Appl. Phys. B, **132**(6).

7.1. Introduction

The reliability of TiRe-LII as a diagnostic depends on the accuracy of the measurement model and the validity of the assumption that the measured emissions arise from incandescence [178]. However, in the case of soot, the incandescence signal may be affected by interference from laser-induced fluorescence (LIF) of polycyclic aromatic hydrocarbons (PAHs) when 266 or 532 nm laser excitation wavelengths are used [33,182] or from non-thermal C_2-Swan band and C_3-Swing band emissions, which are most pronounced at high fluences (> 5 mJ/mm^2) and in the ~300–600 nm detection wavelength range [178,183]. Other commonly observed deviations from the expected signal behavior are of undetermined origin. One such unexplained feature is the so-called anomalous cooling as described by Daun *et al.* [27]. In their experiment, flame-extracted soot was re-aerosolized in different gases and irradiated by a 1064 nm laser at a fluence of 3 mJ/mm^2. Under these conditions, the observed pyrometric temperature (*i.e.*, a representative temperature derived from the emission of the entire particle ensemble) drops faster than one would expect from purely conductive cooling for about 50 ns after the laser pulse, before reaching the expected decay rate.

Snelling *et al.* [28] also reported the apparent anomalous cooling of soot in LII experiments using a 532-nm laser pulse and fluences below 0.26 mJ/mm^2. They hypothesized that the apparent anomalous cooling in the low-fluence regime may be explained by the sublimation of PAHs or graphitization of soot particles, which are endothermic processes and thus reduce the sensible energy. Maffi *et al.* [184] observed apparent anomalous cooling within the first 10–25 ns for soot irradiated at 1064 nm with a fluence of 1.22 mJ/mm^2. Cenker e*t al.* [185] suggested that anomalous cooling may be a possible cause for the discrepancy between LII-derived soot primary particle diameters and TEM sample results.

Talebi-Moghaddam *et al.* [89] attempted to explain the phenomenon through interference from neutral bremsstrahlung. According to this theory, trigger electrons are released from the hot particle and then accelerate in the laser pulse, releasing more electrons in a cascade-like process through impact ionization. The free electrons then decelerate as they scatter from the bath gas molecules, releasing broadband electromagnetic radiation in a manner that depends on the polarizability of the gas molecule. Theoretical calculations showed that, when using a 1064-nm laser, this phenomenon should occur only at fluences greater than 10 mJ/mm^2. A number of other hypotheses could potentially explain this phenomenon, such as laser-induced changes to the particle morphology or optical properties (*e.g.*, graphitization [28]).

The work presented in this chapter investigates the apparent anomalous cooling of soot in the low-fluence regime, where, under the assumption of homogeneous particle heating, no particle sublimation is expected and how the phenomenon varies with bath gas during TiRe-LII experiments. Soot is produced in an ethylene/air diffusion flame and then induced into different bath gases using a venturi eductor. It is shown that particles that have been heated beyond their sublimation threshold, due to nonuniformity in the irradiating laser fluence, contribute significantly to apparent anomalous cooling, with an increase in the phenomenon at higher degrees of fluence nonuniformity across the laser beam. Particle polydispersity also contributes to the effect, but to a lesser extent. It is also found that the bath-gas dependence is due to the different conductive cooling powers of bath gases.

7.2. TiRe-LII measurement model

While the model presented in Chapter 2 for metal nanoparticles can be applied to soot after some modifications, the heat transfer and spectroscopic submodels are present here again, specifically to model soot and to ensure clarity.

7.2.1. Heat transfer model for soot

The time-resolved temperature, $T_\mathrm{p}(t)$, of a soot particle after laser irradiation is governed by

$$\rho_\mathrm{m} c_\mathrm{m} \frac{\pi}{6} d_\mathrm{p}^3 N_\mathrm{p} \frac{\mathrm{d}T_\mathrm{p}}{\mathrm{d}t} = q_\mathrm{laser}(t, d_\mathrm{p}) - q_\mathrm{sub}(T_\mathrm{p}, d_\mathrm{p}) - q_\mathrm{cond}(T_\mathrm{p}, d_\mathrm{p}) \ , \tag{7.1}$$

where c_m and ρ_m are the specific heat and density of soot, N_p is the number of primary nanoparticles, and d_p is the primary particle diameter. The particles are heated according to $q_\mathrm{laser}(t,d_\mathrm{p}) = F_\mathrm{o}\, f(t)\ C_{\mathrm{abs},\lambda}$, where F_o is the laser fluence, $f(t)$ is the temporal laser pulse intensity, $C_{\mathrm{abs},\lambda} = (\pi d_\mathrm{p}^2/4) Q_{\mathrm{abs},\lambda}$ is the absorption cross-section of the soot primary particle, and $Q_{\mathrm{abs},\lambda} = 4\pi d_\mathrm{p} E(\mathbf{m}_\lambda)/\lambda$ is the spectral absorption efficiency modeled in the Rayleigh regime. $E(\mathbf{m}_\lambda)$ is the absorption function, which is approximately wavelength-independent over the LII detection wavelengths and taken as 0.4 for soot in this work, and $\mathbf{m}_\lambda$ is the wavelength-dependent complex refractive index [186]. The terms $q_\mathrm{sub}(T_\mathrm{p},\ d_\mathrm{p})$ and $q_\mathrm{cond}(T_\mathrm{p},\ d_\mathrm{p})$ are the sublimative and conductive cooling rates, respectively. While thermal radiation accounts for the incandescence signal, its

magnitude is much less than sublimative and conductive cooling and can be excluded from the heat transfer model. The initial condition of Eq. (7.1) is taken to be the temperature of the surrounding gas.

Mass loss due to sublimation is considered by solving Eq. (7.1) simultaneously with

$$\frac{\mathrm{d}m_{\mathrm{p}}}{\mathrm{d}t} = -\dot{m}_{\mathrm{sub}}(T_{\mathrm{p}}, d_{\mathrm{p}}) = -m_{\mathrm{v}} \frac{q_{\mathrm{sub}}(T_{\mathrm{p}}, d_{\mathrm{p}})}{\Delta H_{\mathrm{v}} N_{\mathrm{p}}}, \tag{7.2}$$

where m_{v} is the molar mass of the sublimated species and ΔH_{v} is the molar latent heat of vaporization of the nanoparticle. The instantaneous particle diameter is then found from $d_{\mathrm{p}} = \{6m_{\mathrm{p}}(t)/[\pi\rho_{\mathrm{p}}]\}^{1/3}$.

Sublimative cooling is modelled according to [20]

$$q_{\mathrm{sub}}\left(T_{\mathrm{p}}, d_{\mathrm{p}}\right) = A_{\mathrm{sub}} \beta N_{\mathrm{v}}'' \frac{\Delta H_{\mathrm{v}}}{N_{\mathrm{A}}}, \tag{7.3}$$

where A_{sub} is the available surface area for sublimation, which is $\pi d_{\mathrm{p}}^2 N_{\mathrm{p}}$ for a soot aggregate with primary particles in point contact, β is the mass accommodation coefficient, $N_{\mathrm{v}}'' = n_{\mathrm{v}} c_{\mathrm{v}}/4$ is the number flux of sublimated molecules, n_{v} and c_{v} are the number density and mean thermal speed of sublimated molecules, N_{A} is the Avogadro number, and $\Delta H_{\mathrm{v}}/N_{\mathrm{A}}$ is the energy required to sublimate one molecule from the nanoparticle. The mean free speed of the sublimated molecules is $c_{\mathrm{v}} = [8k_{\mathrm{B}}T_{\mathrm{p}}/(\pi m_{\mathrm{v}})]^{1/2}$, while their number density is $n_{\mathrm{v}} = p_{\mathrm{v}}/(k_{\mathrm{B}}T_{\mathrm{p}})$. The vapor pressure of the nanoparticle is found from the Clausius-Clapeyron equation [92,187],

$$p_{\mathrm{v}} = p_{\mathrm{ref}} \exp\left[-\frac{\Delta H_{\mathrm{v}}}{R}\left(\frac{1}{T_{\mathrm{p}}} - \frac{1}{T_{\mathrm{ref}}}\right)\right], \tag{7.4}$$

where R is the universal gas constant, and p_{ref} and T_{ref} are the reference state for the saturated vapor.

When soot particles are smaller than the mean free path of the gas, conductive cooling is modelled in the free molecular regime [101] (*i.e.*, the Knudsen number, $Kn = \lambda_{\mathrm{MFP}}/d_{\mathrm{p}} >> 1$[113], where λ_{MFP} is the mean free path) according to

$$q \quad \left(T_{\mathrm{p}}, d_{\mathrm{p}}\right) = A_{\mathrm{cond}} N'' \left\langle E_{\mathrm{g,o}} - E_{\mathrm{g,}} \right\rangle, \tag{7.5}$$

where A_{cond} is the effective surface area available for conduction, $N_{\mathrm{g}}'' = n_{\mathrm{g}} c_{\mathrm{g}}/4$ is the incident gas molecular flux, $n_{\mathrm{g}} = p_{\mathrm{g}}/(k_{\mathrm{B}}T_{\mathrm{g}})$ is the molecular number density of the gas, $c_{\mathrm{g}} = [8k_{\mathrm{B}}T_{\mathrm{p}}/(\pi m_{\mathrm{g}})]^{1/2}$ is the mean thermal

speed of the gas, and p_g and m_g are the pressure and molecular mass of the buffer gas, respectively. The average change in energy between the incident and scattered gas molecular streams, $<E_{g,o} - E_{g,i}>$, is expressed as a fraction α of the maximum average energy transfer that would occur if the incident molecule were to thermally equilibrate with the particle before reissuing into the gas, where α is the thermal accommodation coefficient (TAC). Assuming that the vibrational modes are frozen during the interaction [27], the maximum average energy transfer is given by

$$\left\langle E_{g,o} - E_{g,i} \right\rangle_{max} = \left(2 + \frac{\zeta_{rot}}{2} \right) k_B \left(T_p - T_g \right), \tag{7.6}$$

where ζ_{rot} is the number of rotational degrees of freedom of the buffer gas, which is zero for monoatomic (He, Ar) gases and two for diatomic (N_2) and linear polyatomic (CO, CO_2, N_2O) gases [101]. When the surrounding gas is an equilibrium mixture of different gases, Eq. (7.5) becomes

$$q_{cond}\left(T_p, d_p\right) = A_{cond}\alpha_{eff}\left\langle E_{g,o} - E_{g,i} \right\rangle_{max} \sum_i N''_{g,i} \ , \tag{7.7}$$

where α_{eff} is the effective (TAC) when the buffer gas is a mixture of two or more gases, $N_{g,i}''$ is the incident gas molecular flux of gas i, while using the appropriate partial pressure of the gas, and α_i is the TAC of gas i.

In the case of aggregates, a portion of the particle surface area is not directly accessible to the incident gas molecules. To account for this, the effective surface area for heat conduction from soot aggregates is modelled according to $A_{cond} = \pi d_{eff}^2 N_p$ [60], where

$$d_{eff} = d_p \left(\frac{N_p}{k_h} \right)^{1/D_h} \ , \tag{7.8}$$

and k_h and D_h are defined by TAC-dependent quadratic expressions reported by Liu *et al.* [60]. When considering an isolated primary particle, d_{eff} is equal to d_p.

When d_{eff} is comparable to or larger than the mean free path of the gas, intermolecular collisions within the vicinity of the particle will influence the local temperature field in the gas, and thus the overall heat transfer rate. To calculate the conduction heat transfer from a large aggregate, in this work, Fuchs' boundary sphere method [100] is used, in which the gas is subdivided into a free molecular domain that

surrounds the nanoparticle, which is in turn enveloped by the continuum domain. These two domains are separated by the boundary sphere. The solution proceeds to solve for the unknown boundary sphere temperature by setting the free molecular heat transfer rate between the particle and the boundary sphere equal to the continuum heat transfer rate (used when the sizes of the aggregates are much larger than the mean free path of the gas) between the boundary sphere and the equilibrium gas,

$$q_{\mathrm{cont,agg}} = 4\pi\left(2\delta + d_{\mathrm{eff}}\right)\int_{T_{\mathrm{p}}}^{T_{\mathrm{g}}} k\left(T_{\mathrm{agg}}\right)\mathrm{d}\,T \tag{7.9}$$

where δ is the boundary layer thickness (usually taken to be the mean free path of the gas at the bath gas temperature), and $k(T)$ is the thermal conductivity of the gas. The mean free path of the gases is computed from the Maxwell mean free path formulation according to Ref. [100].

The thermophysical properties of soot and model parameters used in this work are shown in Table 7-1.

Table 7-1: Thermophysical and model properties of soot used in this work.

Property	**Value**
$\rho_{\mathrm{p}}\,(T_{\mathrm{p}})$ [kg/m^3]	$2303.1 - 7.3106\times10^{-2}T_{\mathrm{p}}$ [92]
$c_{\mathrm{p}}\,(T_{\mathrm{p}})$ [J/(kg·K)]	T_{p}-dependent expression[a] [92,188]
ΔH_{ref} / (J/mol]	$2.05398\times10^{5} + 7.3660\times10^{2}T_{\mathrm{p}} - 0.40713\,T_{\mathrm{p}}^{2} + 1.1992\times10^{-4}T_{\mathrm{p}}^{3} - 1.7946\times10^{-8}T_{\mathrm{p}}^{4} + 1.0717\times10^{-12}T_{\mathrm{p}}^{5}$ [18,189]
β [-]	0.9 [28]
p_{ref} [Pa]	61.5 [18,189]
T_{ref} [K]	3000 [18,189]
E(m) [-]	0.4 [58]
M_{v} [10^3 kg/mol]	$17.179 + 6.8654\times10^{-4}T_{\mathrm{p}} + 2.9962\times10^{-6}T_{\mathrm{p}}^{2} - 8.5954\times10^{-10}T_{\mathrm{p}}^{3} + 1.0486\times10^{-13}T_{\mathrm{p}}^{4}$ [18,189]
k_h [-]	$1.04476 + 0.22329\alpha + 7.14286\times10^{-3}\,\alpha^2$ [60]
D_h [-]	$1.99345 + 0.30224\alpha - 0.11276\alpha^2$ [60]

[a] $\left(\frac{R}{12.01\ \mathrm{g\ /\ mol}}\right)\left\{1.115\left(\frac{597\ \mathrm{K}}{T_{\mathrm{p}}}\right)^{2}\exp\left(\frac{597\ \mathrm{K}}{T_{\mathrm{p}}}\right)\left[\exp\left(\frac{597\ \mathrm{K}}{T_{\mathrm{p}}}\right)-1\right]^{-2} + 1.789\left(\frac{1739\ \mathrm{K}}{T_{\mathrm{p}}}\right)^{2}\exp\left(\frac{1739\ \mathrm{K}}{T_{\mathrm{p}}}\right)\left[\exp\left(\frac{1739\ \mathrm{K}}{T_{\mathrm{p}}}\right)-1\right]^{-2} + \frac{T_{\mathrm{p}}}{8620\ \mathrm{K}}\right\}$

While local fluences may be high enough to induce sublimative cooling, under the assumption of a uniform laser fluence profile, at sufficiently low laser fluences, conduction-dominated cooling is expected, sublimation can be ignored, and Eq. (7.1) can be written as

$$\rho_{\mathrm{p}} c_{\mathrm{p}} \frac{\pi}{6} d_{\mathrm{p}}^{3} N_{\mathrm{p}} \frac{\mathrm{d}T_{\mathrm{p}}}{\mathrm{d}t} = -A_{\mathrm{cond}} \frac{1}{4} \frac{p_{\mathrm{tot}}}{k_{\mathrm{B}} T_{\mathrm{g}}} \sqrt{\frac{8 k_{\mathrm{B}} T_{\mathrm{g}}}{\pi}} k_{\mathrm{B}} \alpha_{\mathrm{eff}} \left(T_{\mathrm{p}} - T_{\mathrm{g}}\right) \sum_{i} x_{\mathrm{g},i} \frac{1}{\sqrt{m_{\mathrm{g},i}}} \left(2 + \frac{\zeta_{\mathrm{rot},i}}{2}\right), \tag{7.10}$$

where p_{tot} is the total pressure of the gases and $x_{\mathrm{g},i}$ are the mole fractions of the constituent gases. Equation (7.10) can be rearranged into a separable ordinary differential equation

$$\frac{\mathrm{d}\left[\theta\left(t\right)\right]}{\mathrm{d}t} = \alpha_{\mathrm{eff}} C_{1} \theta\left(t\right), \tag{7.11}$$

where $\theta(\mathrm{t}) = T_{\mathrm{p}} - T_{\mathrm{g}}$ and

$$C_{1} = -A_{\mathrm{cond}} \frac{1}{4} \frac{P_{\mathrm{tot}}}{T_{\mathrm{g}}} \sqrt{\frac{8 k_{\mathrm{B}} T_{\mathrm{g}}}{\pi}} \left[\rho_{\mathrm{m}}\left(T_{\mathrm{p}}\right) c_{\mathrm{m}}\left(T_{\mathrm{p}}\right) \frac{\pi N_{\mathrm{p}} d_{\mathrm{p}}^{3}}{6}\right]^{-1} \sum_{i} \chi_{\mathrm{g},i} \frac{1}{\sqrt{m_{\mathrm{g},i}}} \left(2 + \frac{\zeta_{\mathrm{rot},i}}{2}\right). \tag{7.12}$$

Equation (7.11) is solved by

$$\ln\left(T_{\mathrm{p}} - T_{\mathrm{g}}\right) = \alpha_{\mathrm{eff}} C_{1} t + C_{2}, \tag{7.13}$$

where C_2 is an integration constant.

Note that while irradiated soot particles aerosolized in a bath gas at room temperature and pressure may conductively cool in the transition regime or the continuum regime if the particles are large enough, the formulation of Eq. (7.10) approximates the heat conduction as strictly occurring in the free molecular regime. Since d_{eff} (Eq. (7.8)) is α-dependent, which results in a nonlinear formulation, the approach employed in Eq. (7.10) is attractive because it allows for a closed-form analytical solution that results in Eq. (7.13). This approximation will overestimate the TACs to an extent that increases as the mean free path of the gas reduces. For a soot particle temperature of 3500K, the TAC is overpredicted between 10% (He) and 30% (CO_2) due to the FMR approximation. Hence, the TACs estimated in this work are referred to as FMR-derived TACs, $\alpha_{\mathrm{eff}}^{\mathrm{FMR}}$.

7.2.2. Spectroscopic submodel

The measured incandescence is due to emission from the particle ensemble containing various primary particle and aggregate sizes that are irradiated by the varying laser fluences within the probe volume, as modeled by

$$J_\lambda\left(t\right)=A_\lambda \Lambda \int_{F_\mathrm{o}}\int_{N_\mathrm{p}}\int_{d_\mathrm{p}} p(d_\mathrm{p})p(N_\mathrm{p})p(F_\mathrm{o})\frac{\pi d_\mathrm{p}^2}{4}N_\mathrm{p}Q_{\mathrm{abs},\lambda}\left(d_\mathrm{p},\mathbf{m}_\lambda\right)I_{\mathrm{b},\lambda}\left[T_\mathrm{p}\left(t,d_\mathrm{p}\right)\right]\mathrm{d}d_\mathrm{p}\mathrm{d}N_\mathrm{p}\mathrm{d}F_\mathrm{o}\,, \tag{7.14}$$

where A_λ and Λ are the calibration constant and the intensity scaling factor, respectively, and $I_{\mathrm{b},\lambda}$, is the blackbody emission intensity. The measured incandescence is due to contributions from all the particles and fluence regions within the probe volume, which are weighted by the corresponding probability density functions, $p(d_\mathrm{p})$, $p(N_\mathrm{p})$, and $p(F_\mathrm{o})$. While $E(\mathbf{m}_\lambda)$ varies slightly with wavelength [181,190], in Eq. (7.14), $Q_{\mathrm{abs},\lambda}$ is estimated with a wavelength-independent approximation of $E(\mathbf{m}_\lambda)$ that is taken as 0.4.

The finite width of $p(F_\mathrm{o})$ is due to nonuniform laser fluence across the beam, which arises from the laser design, alignment, and mode fluctuations. The beam profile may also be affected by interference originating from multiple reflections from surfaces of optical components or beam diffraction. Snelling *et al.* [45] accounted for nonuniform laser fluence by determining an equivalent laser sheet width based on the integrated intensities emitted from the probe volume, while Bladh *et al.* [191] do this by integrating the incandescence signals computed at different locations within the laser sheet weighted by the spatial intensity distribution within the laser profile. Some strategies have discretized the spatial domain in which the energy and mass balance equations are solved [192]. Liu *et al.* [193] capture the laser fluence distribution with a beam profiler from which a fluence histogram is derived that is used to weigh the computed incandescence. Equation (7.14) follows the approach by Liu *et al.* [193].

Equation (7.14) is often further simplified by assuming a monodisperse size distribution and uniform spatial laser fluence, which amounts to ignoring the distributions in $p(d_\mathrm{p})$, $p(N_\mathrm{p})$, and $p(F_\mathrm{o})$,

$$J_\lambda\left(t\right)=A_\lambda \Lambda \frac{\pi d_\mathrm{p}^2}{4}Q_{\mathrm{abs},\lambda}\left(d_\mathrm{p},\mathbf{m}_\lambda\right)I_{\mathrm{b},\lambda}\left[T_\mathrm{p}\left(t,d_\mathrm{p}\right)\right]. \tag{7.15}$$

A pyrometric temperature may be inferred by regressing Eq. (7.15) to the measured incandescence at all detection wavelengths simultaneously (Eq. (2.22)) or by using two-color pyrometry (Eq. (2.23)).

7.3. Experimental procedure

The soot aerosol generation is shown in Figure 7-1, which is similar to the one used by Daun *et al.* [27]. An ethylene/air co-flow laminar diffusion flame is operated at a fuel flow rate of 0.198 slm and an air flow rate

of ~284 slm. Soot is extracted at 42 mm height-above-burner (HAB) using a venturi eductor (Figure 7-1a) having a nozzle orifice diameter of 1.52 mm through which motive gas flows at a rate of 20 l/min. The extracted soot aerosol mixes with the motive gas and enters an optically accessible flow cell for LII measurements. Bath gas dilution of > 95 mol% ensures that additional flame offgas and ambient air have a negligible effect on the measurement [27]. The distribution of the primary particle size d_p is taken as $\mathcal{N}(28.3 \text{ nm}, 6.5 \text{ nm})$ as reported by Tian *et al.* [194] for this type of flame, operating condition, and location, while the number of primary particles per aggregates N_p is inferred from Daun *et al.* [27] as $\ln\mathcal{N}(192, 1.98)$. The resulting aerosol is assumed to be at room temperature (20 °C) upon reaching the LII measurement cell. Visual observations indicated that, at the same motive gas flow rate, heavier gases extracted more soot from the flame than lighter gases. This led to higher soot concentrations entrained in the aerosol, as confirmed by the estimated soot volume fractions (*cf.*, Appendix A.10). However, this did not lead to significantly different levels of aggregation as verified by TEM micrographs (*cf.*, Appendix A.10), since the aerosol dilution is also increased for the heavier gases due to the additional flame offgas and ambient air entrained into the flow through the open end of the sampling probe.

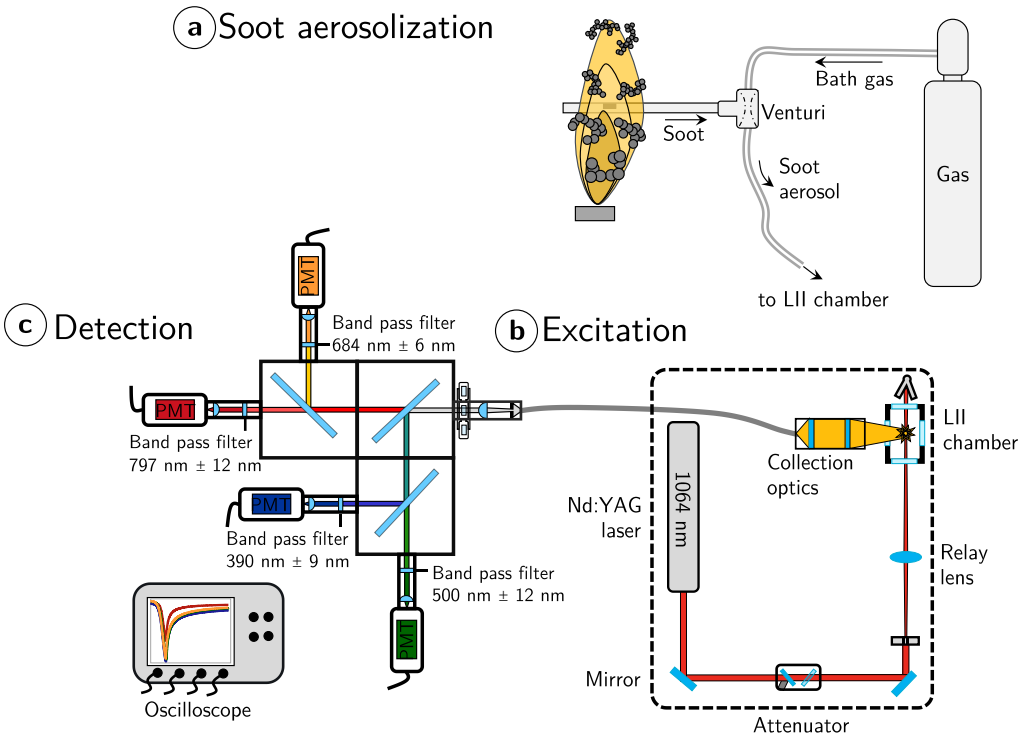


Figure 7-1: TiRe-LII experimental setup, **(a)** Soot aerosol (i) in-flame at HAB = 42 mm, (ii) extracted and diluted in various gases, **(b)** laser excitation, and **(c)** detection set-up.

The laser excitation apparatus is shown in Figure 7-1b. A Nd:YAG laser operated at a repetition frequency of 10 Hz is used to generate a nearly Gaussian temporal profile at 1064 nm with a pulse duration of 8 ns (FWHM). The laser beam passes through a variable attenuator and is then shaped with a 2-mm diameter aperture before being relay-imaged by a convex lens into the LII chamber. Two different laser profiles of varying uniformities were used at fluences ranging from ~0.4–1.6 mJ/mm^2. Beams with varying nonuniformity were generated by changing the location of the aperture in the laser beam profile and measured by a beam profiler (Coherent, LaserCam-HR). While laser beams typically used for LII are more uniform than those shown in Figure 7-2, the different levels of uniformity were selected to provide a basis for studying the influence of fluence inhomogeneity.

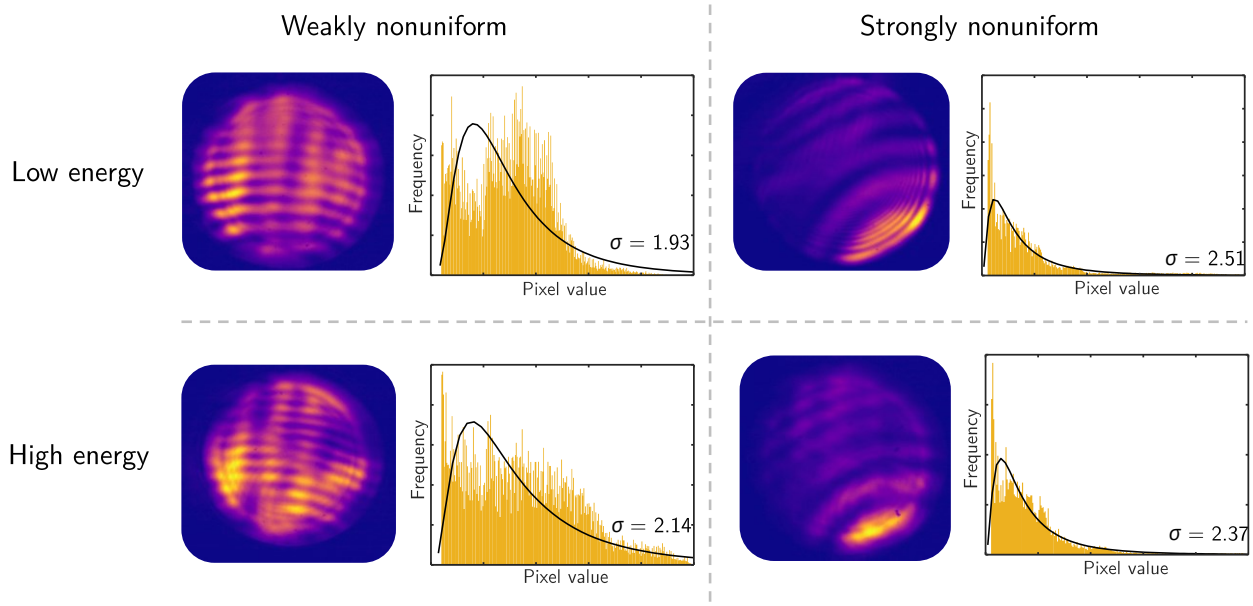


Figure 7-2: Fluence profiles with varying nonuniformity (termed "weakly" and "strongly") used in this work and corresponding distributions at two laser pulse energy levels. Black solid lines in the histograms represent best-fit distributions.

The detector arrangement is shown in Figure 7-1c. LII emission from the probe volume is imaged by two achromatic lenses ($f = 250$ and 100 mm) onto the entrance of an optical fiber (diameter: 1000 µm, numerical aperture: 0.48, length: 2 m, Thorlabs). The fiber is connected to a detector system consisting of a series of dichroic mirrors and bandpass filters that decouple the broadband emission into four separate wavelength ranges (390±9, 500±12, 684±12, and 797±6 nm), directed onto four PMTs with rise times of < 2 ns [195]. The respective signals were recorded every 0.8 ns with a 500-MHz oscilloscope (PicoScope 6404C) using a vertical resolution of 8 bits. The detector system was calibrated with a broadband light source consisting of three halogen lamps mounted in an integrating sphere (LOT K-150WH) and powered with a DC power supply (Gossen Metrawatt SLP 120-80). The calibration procedure is described in Ref. [47] and takes into account wavelength-dependent sensitivity at each detector channel. The LII data collected and analyzed in this chapter are available on GitHub (https://github.com/s27robin/SRE-PhD-LII-exp_data).

7.4. Results and discussion

7.4.1. Measured pyrometric soot temperatures

Figure 7-3 shows examples of pyrometric temperature traces for the weakly and strongly nonuniform fluence profiles. Figure 7-3c specifically shows how the pyrometric temperature history differs for similar fluences at both levels of laser fluence uniformities. Figure 7-4 shows the peak temperatures obtained at different fluences for both beam types and all bath gases used in this work. Using a representative TAC of 0.35 for Ar [27] and a mean aggregate morphology of $d_{\mathrm{p}} = 28.3$ nm and $N_{\mathrm{p}} = 192$, the heat transfer model shows that threshold temperature above which sublimative cooling dominates conductive cooling is approximately 3530 K, which is consistent with the temperatures at which the LII signal generated from the particle ensembles starts to transition into the plateau zone as shown in Figure 7-4.

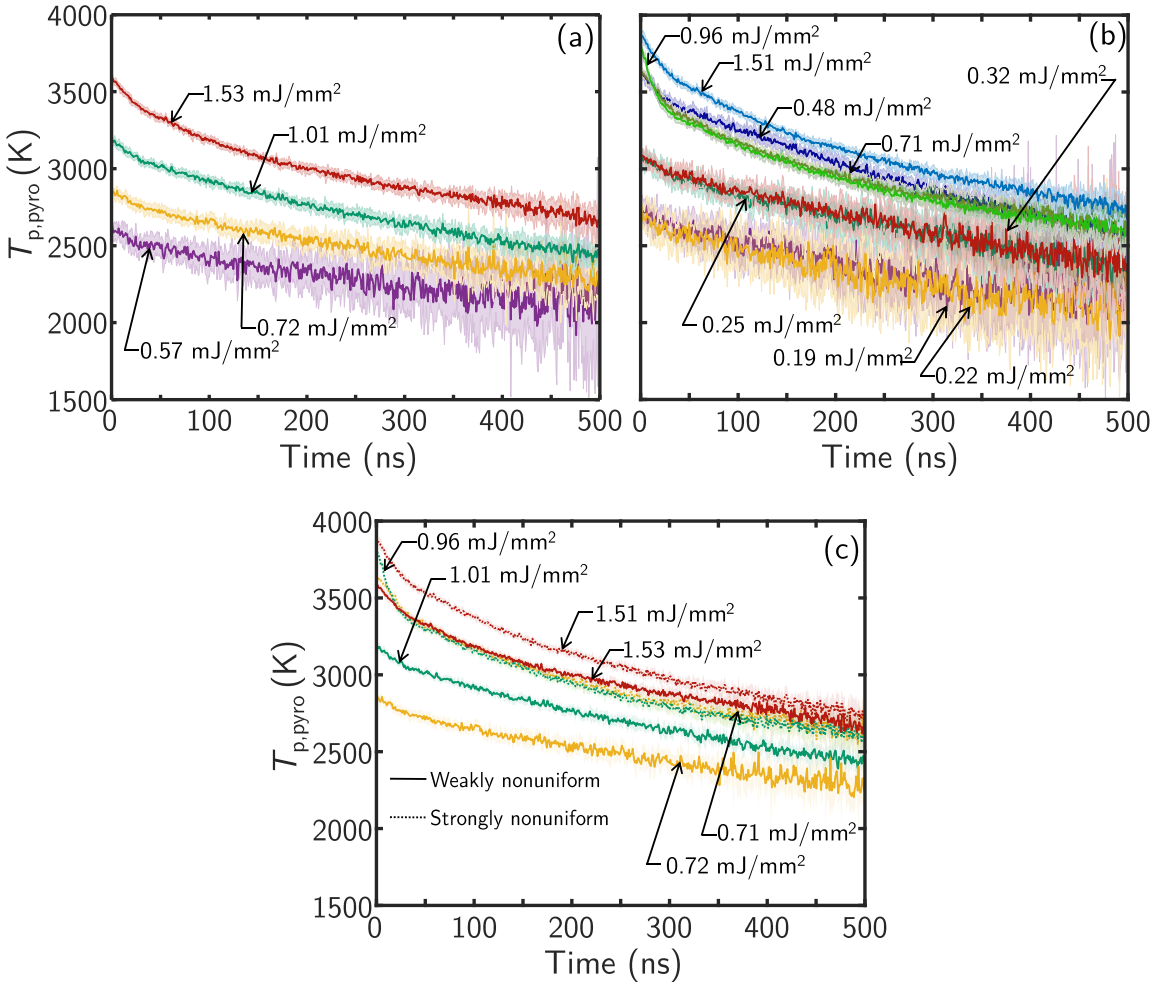


Figure 7-3: Pyrometric temperatures for soot entrained in argon and heated with a laser of **(a)** weakly and **(b)** strongly nonuniformity across the cross-section, and **(c)** direct comparison of the temperature history for similar fluences at both levels of fluence uniformities. Representative laser energy distributions for both fluence nonuniformities are shown in Figure 7-2.

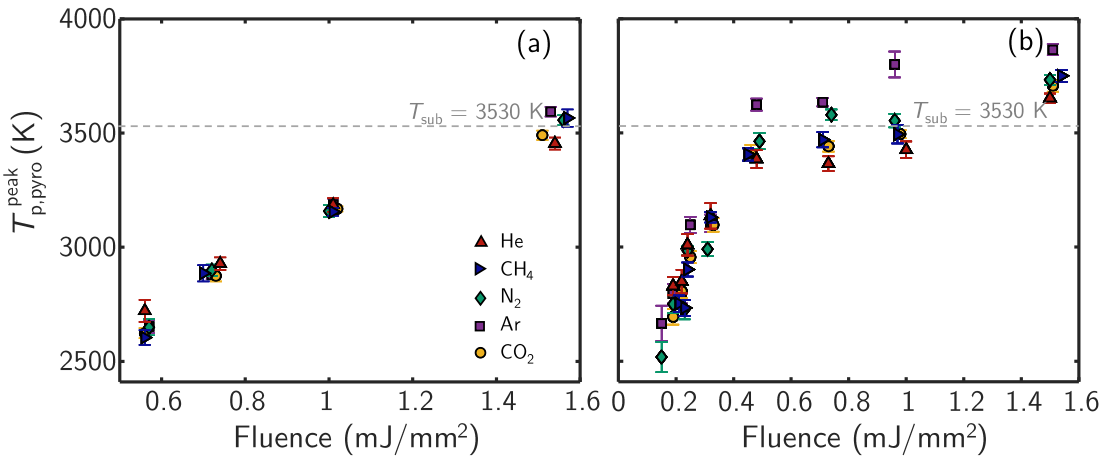


Figure 7-4: Peak pyrometric temperatures of soot heated with a laser of **(a)** weakly and **(b)** strongly nonuniformity across the cross-section.

As seen in Figure 7-4, at the same average fluence level, the peak pyrometric temperature is higher for the strongly nonuniform laser profile compared to the weakly nonuniform case. This is due to regions of high fluence that produce "hot spots" in the probe volume and the nonlinear fluence dependence of the LII signal. This is discussed further in Section 7.4.3. The effect of apparent anomalous cooling is associated with cases where the pyrometric temperatures remain below the sublimation temperature while decaying at a rate faster than that predicted by conduction cooling. In case of varying particle temperatures in the aerosol (for reasons discussed below), a fraction of the ensemble might reach the sublimation temperature and therefore contribute to unexpectedly fast signal decay. Figure 7-4 shows that in the case of temperature inhomogeneities caused by laser nonuniformity, the fluence threshold for (partial) sublimation (and thus the onset of apparent anomalous cooling) decreases with increasing beam nonuniformity.

7.4.2. Apparent anomalous cooling and calculation of the TAC

The pyrometric temperatures are regressed to the conduction model, Eq. (7.13), as shown in Figure 7-5 for weakly and strongly nonuniform fluence profiles. This analysis is carried out on data extracted between 80 and 150 ns after the peak intensity, a period over which $T_{\mathrm{pyro}}(t) - T_{\mathrm{g}}$ appears as a linear function when plotted on a semilog scale, indicating the exponential decay expected for conduction-dominated cooling. The pyrometric temperatures of both fluence profiles exhibit apparent anomalous cooling. At later cooling times, $T_{\mathrm{pyro}}(t)$ - T_{g} becomes nonlinear due to polydispersity within the probe volume [60].

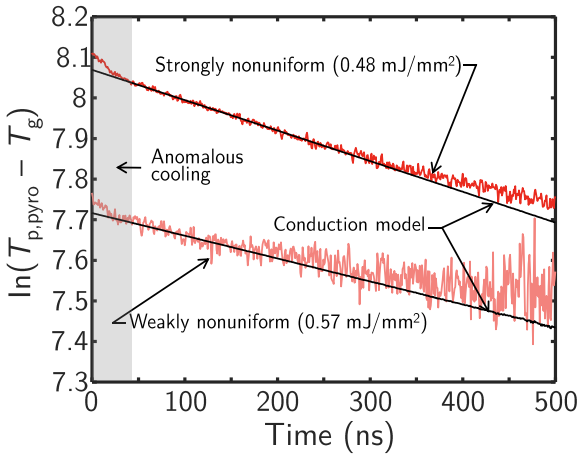


Figure 7-5: Pyrometric temperatures obtained from a weakly and strongly nonuniform laser profile at similar average fluence levels for soot aerosolized in Ar. Measurement and regression to the conduction model, Eq. (7.13).

Figure 7-6 shows the TACs obtained from the regression as a function of the ratio of the mass of the bath gas, m_g, to the mass of elemental carbon, m_c, for all fluences. These results are consistent with those inferred by Daun *et al.* [27] within experimental uncertainty.

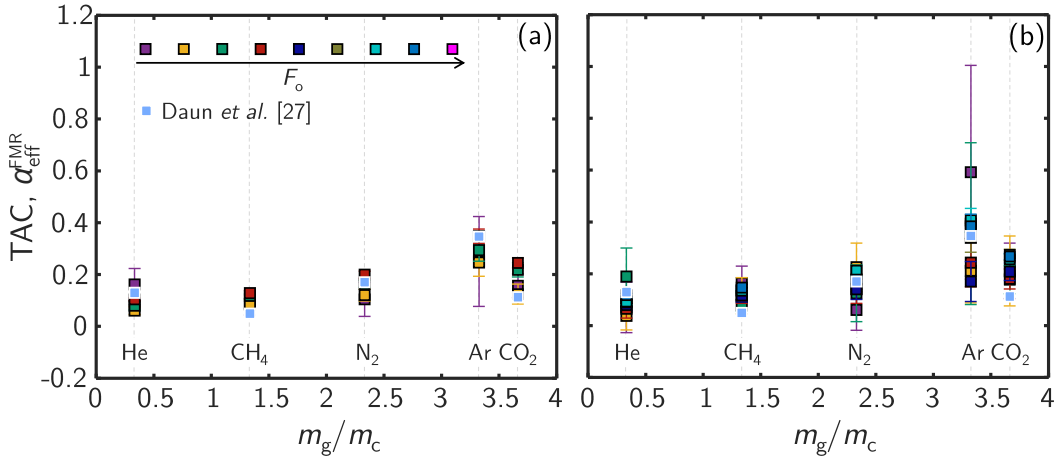


Figure 7-6: Inferred TACs at all considered fluences for soot heated with a laser of **(a)** weakly and **(b)** strongly nonuniformity across the cross-section. Uncertainty bounds represent one standard deviation of the mean. The corresponding fluences for the weakly and strongly nonuniform fluence profiles are comparable to those shown in Figure 7-3, for each respective case.

7.4.3. Effects of nonuniform fluence

For LII measurements, beam-shaping optics are often employed to promote a uniform laser fluence at the probe volume. These may include an aperture to select the most uniform portion of the laser beam [47,193,196], diffractive optical elements (DOE) that use controlled multiple refraction to smooth out intensity variations [193], and relay imaging to minimize beam distortion [197]. While the laser fluence may be adjusted by changing the Q-switch delay, this is known to distort the temporal and spatial beam profile [21,178]. Instead, the fluence should be adjusted using an energy attenuator consisting of a tunable dielectric beam splitter, a dump, and a compensator. Even with these measures, for each laser shot, the fluence profile contains various levels of spatial and temporal nonuniformity that impact the measurement.

Figure 7-7a shows that fluence nonuniformity results in faster-than-expected initial reduction in apparent pyrometric temperature with peak temperatures below the onset of sublimation. The pyrometric temperature profiles shown in Figure 7-7a are simulated for soot within a probe volume having a distribution of $d_\mathrm{p} \sim \mathcal{N}(28.3\ \mathrm{nm},\ 6.5\ \mathrm{nm})$ [194] and $N_\mathrm{p} \sim \ln\mathcal{N}(192,\ 1.98)$ [27], irradiated with a mean fluence of 0.6 $\mathrm{mJ/mm^2}$ (considered to be in the low fluence regime [178]) but having increasingly wide lognormal distributions about its mean, comparable to the measured laser energy distributions shown in Figure 7-2. The observed apparent anomalous cooling is more evident on a logarithmic scale as shown in Figure 7-7b for the corresponding temperature profiles in Figure 7-7a.

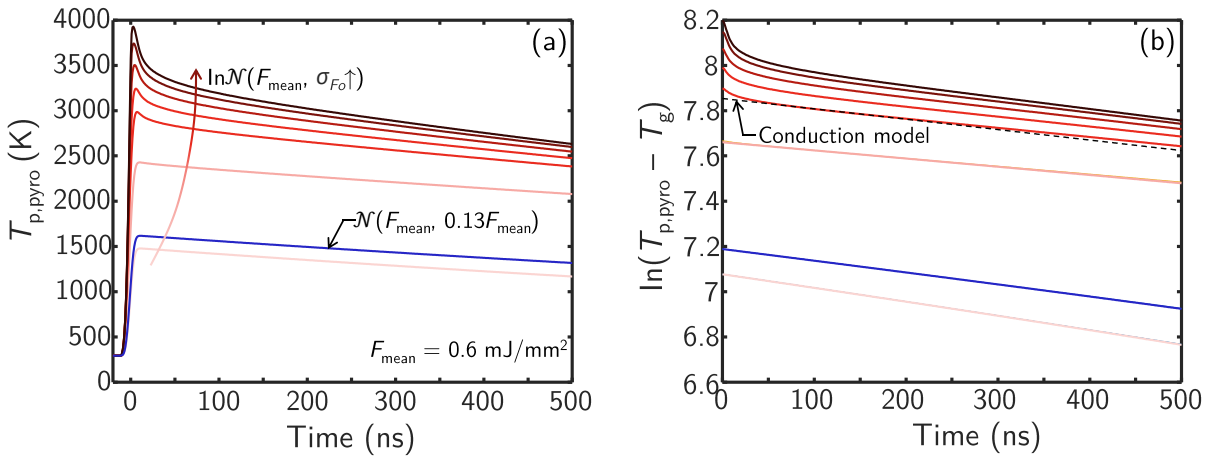


Figure 7-7: (a) Pyrometric temperatures obtained for fluence profiles with varying level of nonuniformity having a lognormal distribution with increasing geometric standard deviations (1.01, 1.35, 1.5, 1.6, 1.75, 2, and 2.5). Also shown are the results for a Gaussian fluence profile with a standard deviation of 13 % of the mean fluence, obtained from shot-to-shot measurements from Ref. [193]. **(b)** Corresponding pyrometric temperatures on a logarithmic scale with one set of pyrometric temperatures regressed to the conduction model (Eq. (7.13)). Bath gas: Ar (α = 0.25, T_{g} = 296 K).

At the narrow (most uniform) fluence distributions (σ_{Fo} = 1.01, 1.35, and the Gaussian distribution with a standard deviation of 0.13 F_{mean}), the pyrometric temperatures decay exponentially as expected for conduction-dominated cooling. As the fluence nonuniformity increases, apparent anomalous cooling becomes more pronounced even though the ensemble peak pyrometric temperature does not exceed the sublimation temperature.

Due to the approximately T^4 dependence of the LII signal intensity and thus the dominance of the hottest particles to the measured LII signal, it is of interest to estimate the contribution of particles within different regions of the laser cross-section (*i.e.*, different fluences) to the measured pyrometric temperature. The pyrometric temperature is calculated from a weighted combination of the respective signal responses from each particle, in all fluence regions, using the appropriate PDF of the fluence. The contribution of particles heated at a given fluence class is estimated by determining the sensitivity, $F_{\text{o}}^{\text{Sensitivity}}$, of each fluence class according to

$$F_{\text{o}}^{\text{Sensitivity}} = \frac{\int_{t^*} T_{\text{p,pyro}}^{F_{\text{o}}}\left(t^*\right)\mathrm{d}t^*}{\int_{t^*} T_{\text{p,pyro}}\left(t^*\right)\mathrm{d}t^*} - 1 \ , \tag{7.16}$$

where $T_{\mathrm{p,pyro}}$ is the pyrometric temperature estimated from the nonuniform fluence profile, $T_{\mathrm{p,pyro}}^{F_\mathrm{o}}$ is the pyrometric temperature estimated from the nonuniform fluence profile with fluence class F_o omitted from the distribution, and t^* is the simulation timescale (–20 ns to 800 ns). Figure 7-8a shows the resulting sensitivity of the pyrometric temperature to each fluence class as well as the underlying nonuniform fluence distribution.

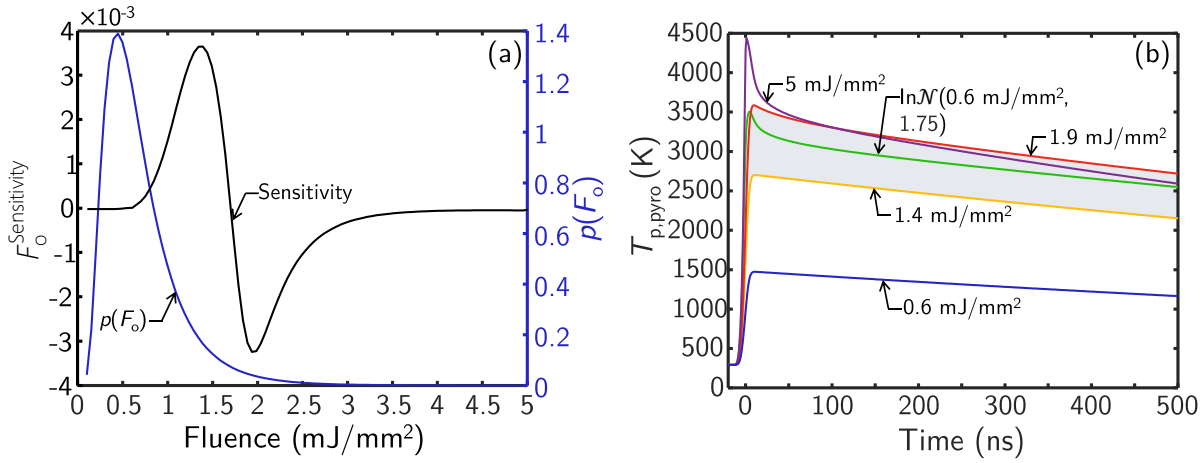


Figure 7-8: (a) Sensitivity of each fluence class to the pyrometric temperature for the related fluence profile of (In$\mathcal{N}$(0.6 mJ/mm^2, 1.75)). **(b)** Temporal variation of pyrometric temperature simulated with the same nonuniform fluence as in (a) compared to simulations with uniform fluences of 0.6, 1.4 (maximum positive sensitivity in (a)), 1.9 (maximum negative sensitivity in (a)), and 5 mJ/mm^2. The shaded area represents the region between the temperature profiles corresponding to the fluences associated with positive and negative peaks in sensitivity. Bath gas: Ar ($\alpha = 0.25$, $T_\mathrm{g} = 296$ K).

As seen from Figure 7-8a, there are two regions of high (either positive or negative) sensitivity that are caused by different physical effects influencing the pyrometric temperature profile shown in Figure 7-8b. When the particle ensemble reaches sublimation temperatures, the related rapid cooling occurs in the early phase of the cooling curve (< 50 ns), followed by conduction-dominated cooling. Having areas with above-average fluence leads to an increase in pyrometric temperature at early cooling times (*i.e.*, negative sensitivity) because the resulting hotter particles dominate the measured signal. With further increase in the local fluence, the effect vanishes for two reasons (a) due to the pdf, the relative weight decreases, and (b) particles sublimate at increasingly shorter time scales. At even higher fluences, this effect vanishes as well because of the multiplication by the near-zero PDF.

At later cooling times, the signal contribution of the initially hot particles is strongly reduced due to their mass loss, while the particles that have been heated to lower temperatures (at lower fluences) and that

maintained their original mass contribute to the signal. Considering the relative contributions of these lower fluence classes through $p(F_o)$ produces the positive sensitivity region.

For the fluence profile considered in Figure 7-8, the fluence classes of ~1.4 and ~1.9 mJ/mm^2 correspond to the positive and negative peaks in sensitivity, respectively. These two classes of fluence broadly represent the fluences responsible for the slower rate of cooling at longer cooling times (corresponding to the fluence at the positive peak) and those responsible for the rapid drop in temperatures (due to sublimation of some particles) following the peak temperatures (corresponding to the fluence at the negative peak). This is evident from Figure 7-8b, where the peak temperatures from uniform fluences of 1.9 and 5 mJ/mm^2 are above the temperatures associated with sublimation, and the corresponding temperature profiles show the accelerated decay. On the other hand, the peak temperatures from uniform fluences of 0.6 and 1.4 mJ/mm^2 are below that of the pyrometric temperature calculated for the nonuniform case, with no indication of sublimation (*i.e.*, no rapid initial temperature reduction). Rather, at later cooling times, the temperature decays more slowly than temperatures associated with the higher fluence classes. The measured pyrometric temperature lies between the envelope defined by the two temperature profiles corresponding to fluences at the (positive and negative) sensitivity peaks, with the earlier cooling times more influenced by the higher fluence classes and the later cooling times by the lower fluence classes.

7.4.4. Effects of particle size polydispersity

Another form of nonuniformity in particle heating and thus LII signal results from the polydisperse particle size distribution. Because soot particles absorb light in the Rayleigh regime, both their absorption cross-section and sensible energy are proportional to their volume, hence they reach approximately the same peak temperature [60,198]. Their subsequent cooling rate, on the other hand, depends strongly on their size as seen in Figure 7-9, which also shows that the rate of cooling is more sensitive to primary particle diameter compared to the size of the aggregate (via number of primary particles N_p); a result consistent with the literature [60,198]. Also note from Figure 7-9, that the rate of the temperature decay varies significantly across different aggregate morphologies. In addition, unlike metal nanoparticles, as discussed in Chapter 6, particle polydispersity does not result in a wide distribution of peak temperatures due to the volumetric laser absorption of soot.

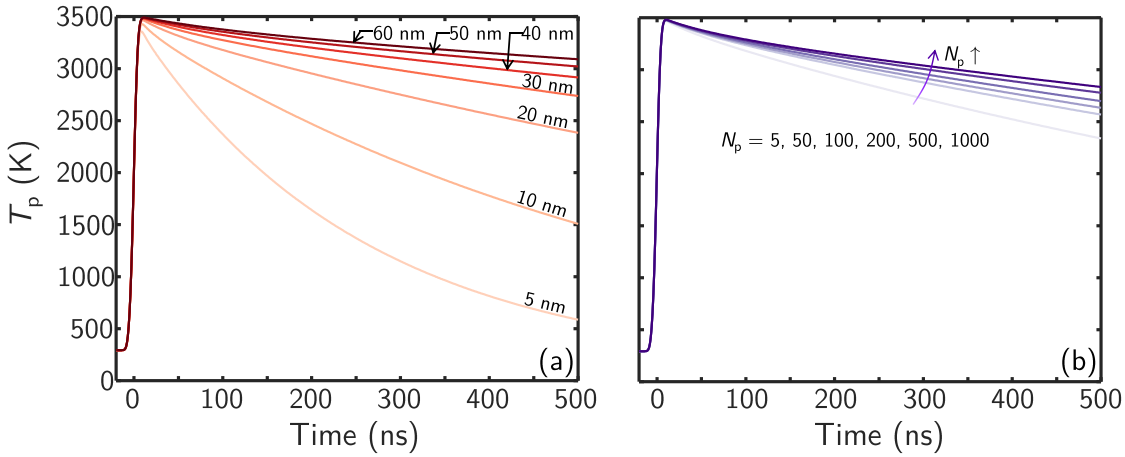


Figure 7-9: Temperature histories of **(a)** primary particle diameters for $N_p = 192$, and **(b)** aggregate sizes for $d_p = 28.3$ nm for a $F_o = 1.9$ mJ/mm^2. Aerosol bath gas is taken as Ar ($\alpha = 0.25$, $T_g = 296$ K).

Each particle size class contributes to the LII signal to a degree determined by its corresponding PDF. Figure 7-10 shows the apparent pyrometric temperatures for an aerosol of soot particles having particles distributed according to $d_p \sim \mathcal{N}(28.3\text{ nm}, \sigma_{dp})$ and $N_p \sim \ln\mathcal{N}(192, \sigma_{Np})$, irradiated at two uniform fluences, including 0.6 and 1.9 mJ/mm^2, where σ_{dp} and σ_{Np} are the standard deviations of the primary particle size and number of particles per aggregate distributions, respectively.

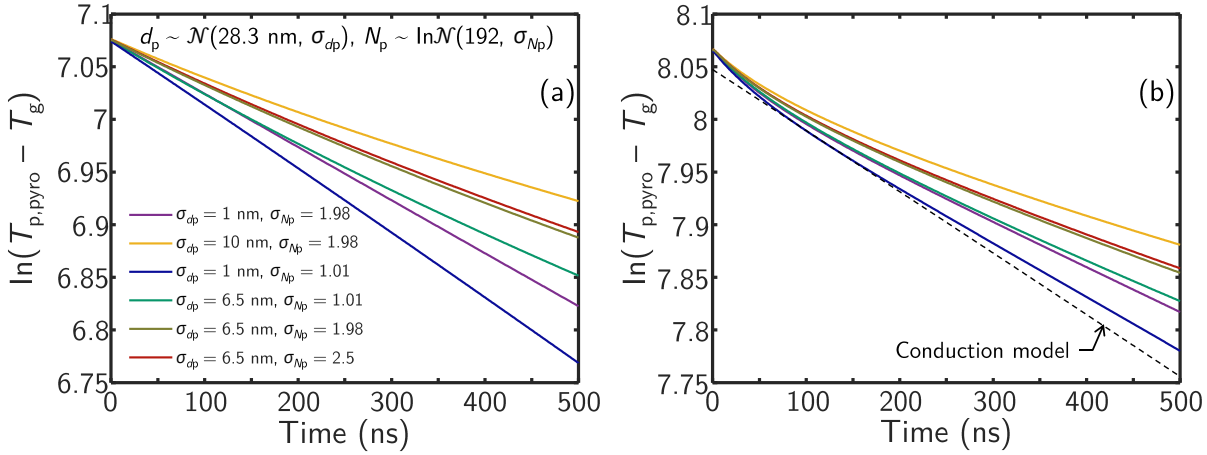


Figure 7-10: Pyrometric temperature histories for different aggregate distributions of soot irradiated at uniform fluences of **(a)** 0.6 mJ/mm^2, and **(b)** 1.9 mJ/mm^2. Bath gas: Ar ($\alpha = 0.25$, $T_g = 296$ K).

As shown in Figure 7-10, the low fluence of 0.6 mJ/mm^2, for the particle-size distributions considered, leads to peak pyrometric temperatures of ~1480 K and the expected conductive (exponential) cooling is observed, with the rate of cooling being influenced more by d_p than by N_p. On the other hand, at a uniform fluence

of 1.9 mJ/mm^2 a period of initial rapid reduction in pyrometric temperatures. While the extent of this apparent anomalous cooling appears similar for all aggregate size distributions considered, the cooling rates differ, again with more influence from d_p than from N_p. While particle polydispersity contributes to the reported excessive absorption for metal nanoparticles, as discussed in Chapter 6, this is not the case for soot since the particles absorb laser energy volumetrically and reach similar peak temperatures. Particle polydispersity, however, does contribute to apparent anomalous cooling for soot, but to a lesser extent compared to the influence of nonuniform fluence.

Figure 7-11 shows that rapid cooling is more likely to appear at higher fluences because the threshold of sublimation-dominated cooling shifts towards smaller particle and aggregate sizes with increasing fluence. That is, at higher fluences, while some particles may undergo conduction-dominated cooling, an increasing fraction of particles also undergo sublimation-dominated cooling, thereby influencing the overall pyrometric decay rate immediately following the peak temperature.

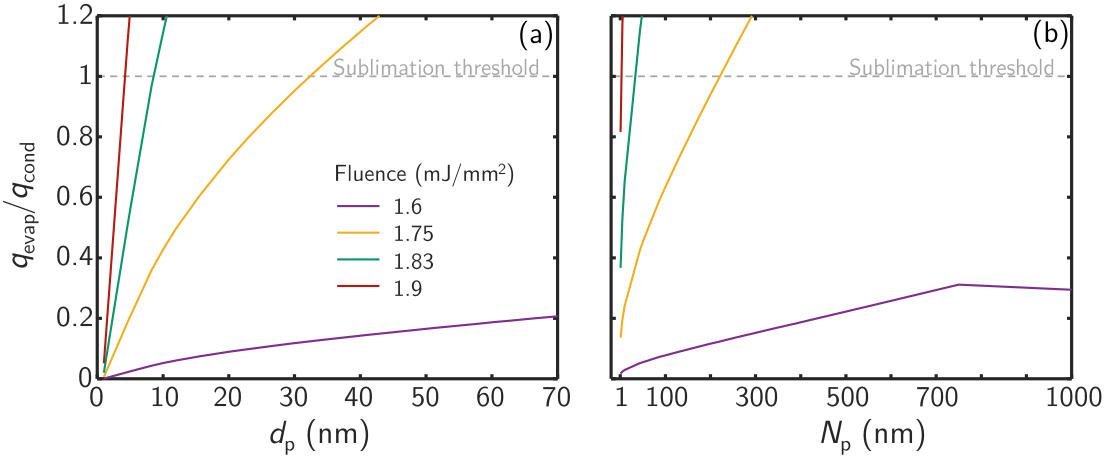


Figure 7-11: Comparing sublimative and conductive cooling powers, at peak temperature, for conditions of varying uniform fluences as a function of **(a)** primary particle diameters, and **(b)** aggregate sizes. Aerosol bath gas is taken as Ar ($\alpha = 0.25$, $T_g = 296$ K).

Figure 7-11 indicates that the contribution of sublimative cooling to the measured incandescence increases with aggregate sizes, and this effect increases with increasing fluence. For aerosols containing large aggregates or broad aggregate distributions that include large particles, an initial rapid cooling following peak temperatures is likely to occur due to sublimative cooling from the larger particles – a phenomenon that becomes more pronounced with increasing fluence.

7.4.5. Quantification of the magnitude of apparent anomalous cooling

The magnitude of apparent anomalous cooling, AC, is quantified by

$$AC = \int_0^t \left[q_{\text{inferred}}\left(t, T_{\text{p,pyro}}\right) - q_{\text{cond mod}}\left(t, \alpha_{\text{eff}}, T_{\text{p,pyro}}, d_{\text{p}}, N_{\text{p}}\right) \right] \mathrm{d}t \,, \tag{7.17}$$

where q_{inferred} is the inferred heat transfer rate found by taking the time derivative of the experimentally-obtained pyrometric temperatures using first-order Tikhonov regularization, and $q_{\text{cond mod}}$ is the predicted heat transfer rate using the estimated TAC, α_{eff}, inferred from regressing Eq. (7.13) to $T_{\text{pyro}}(t) - T_{\text{g}}$ on a semi-logarithmic scale. The integral is performed from $t = 0$ ns (at the peak pyrometric temperature) to $t = 150$ ns (the upper limit of the regression window). A typical set of q_{inferred} and $q_{\text{cond mod}}$ is shown in Figure 7-12.

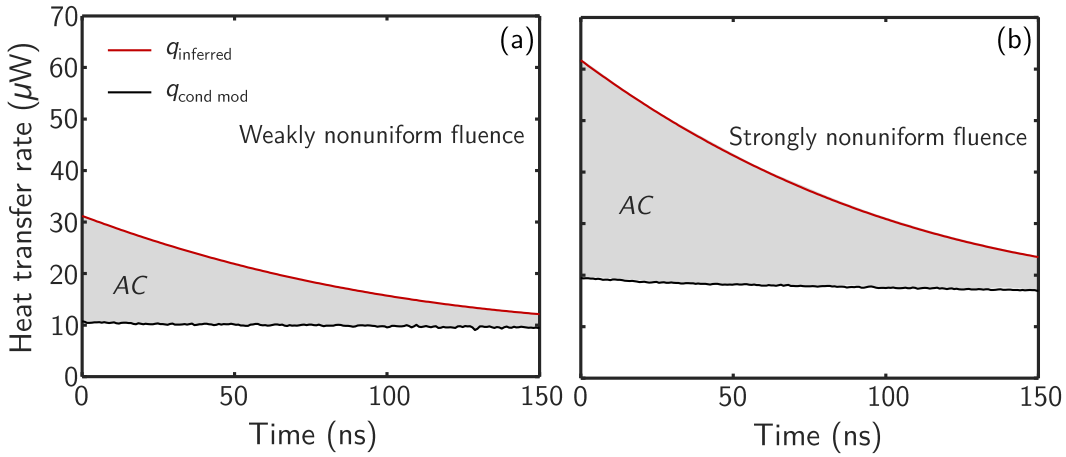


Figure 7-12: Inferred heat transfer rates from measured pyrometric temperatures compared to the heat transfer rates predicted by the conduction model for soot heated with a laser of **(a)** weak and **(b)** strong nonuniformity across the cross-section, having a measured mean fluence of 1.02 and 0.25 mJ/mm^2, respectively. The apparent anomalous cooling region is shaded. Bath gas: CO_2.

Figure 7-12 shows a large difference between q_{inferred} and $q_{\text{cond mod}}$ for both the weakly and strongly nonuniform fluences, although it is larger for the strongly nonuniform fluence. The magnitude of the anomalous cooling is shown in Figure 7-13 as it varies with fluence and $m_{\text{g}}/m_{\text{c}}$.

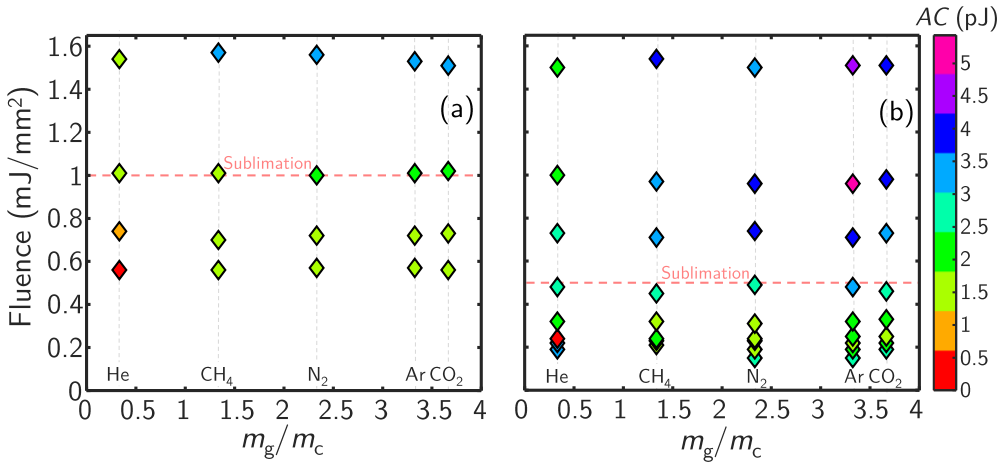


Figure 7-13: Estimated magnitude of apparent anomalous cooling (Eq. (7.17)) for soot heated with a laser of **(a)** weak and **(b)** strong nonuniformity across the cross-section at similar fluences.

Apparent anomalous cooling is associated with pyrometric temperatures below which sublimation should be minimal and cooling should be dominated by conduction to the bath gas. According to the fluence curves in Figure 7-4, the fluences below which conductive-dominated cooling is expected are ~1 and 0.5 mJ/mm^2, for the weakly and strongly nonuniform fluence profiles, respectively, which is consistent with the results in Figure 7-13. There is a general increase in AC with increasing fluence, even for fluences at which only conductive cooling is expected. Furthermore, at comparable fluences, AC is higher for the strongly nonuniform fluence profile compared to the weakly nonuniform one. This is consistent with the results shown in Figure 7-7, as the strongly nonuniform fluence likely includes greater number- and more intense-hot spots across the laser beam than the weakly uniform case. At a given average laser fluence, these hot spots can heat soot particles above their sublimation temperature, leading to immediate sublimative cooling following the peak temperature. The measured incandescence emission is then an integrated emission consisting of all fluence classes. In addition, as the mean of the distribution shifts towards higher fluences, there is a higher probability for higher classes of fluences, with enough energy to induce sublimative cooling, to be present.

The AC parameter varies with bath gas type. Figure 7-14 illustrates the dependence more evidently for fluences just below the threshold of sublimation, corresponding to 0.72 and 0.32 mJ/mm^2, for the weakly and strongly nonuniform fluence cases, respectively. This is aligned with the expectation that the type of bath gas is more relevant in cases in which cooling is dominated by conduction, not sublimation.

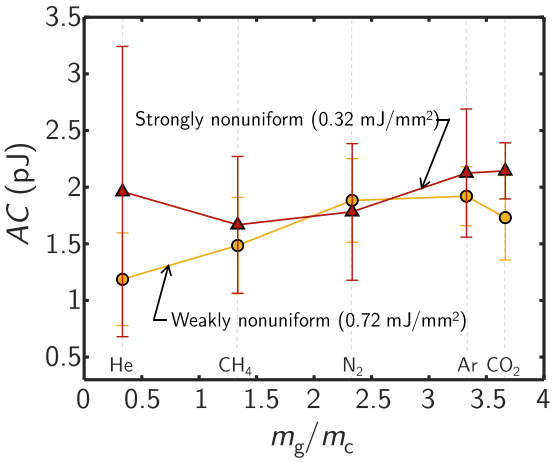


Figure 7-14: Estimated magnitude of apparent anomalous cooling for soot aerosolized in different bath gases and irradiated with laser fluence profiles of weak and strong nonuniformity.

The observed gas dependence is due to the characteristic conductive cooling capacity of each bath gas. While sublimative cooling (introduced by either high fluence classes or particles with high sublimative cooling power that contribute to the measured signal) may be primarily responsible for the observed anomalous cooling, as shown in Figure 7-15, the conductive cooling power also plays a role to an extent determined by the bath gas type. In particular, the higher the conductive cooling power of the gas, the less the contribution by sublimative cooling (*i.e.*, less apparent anomalous cooling). Figure 7-15 shows that for the gases considered, sublimative cooling contributes least to the overall particle cooling for He as the bath gas and contributes most for Ar as the bath gas. In addition, the gas-dependent trend observed in Figure 7-15 is consistent with that observed in Figure 7-14 within experimental uncertainty and model error.

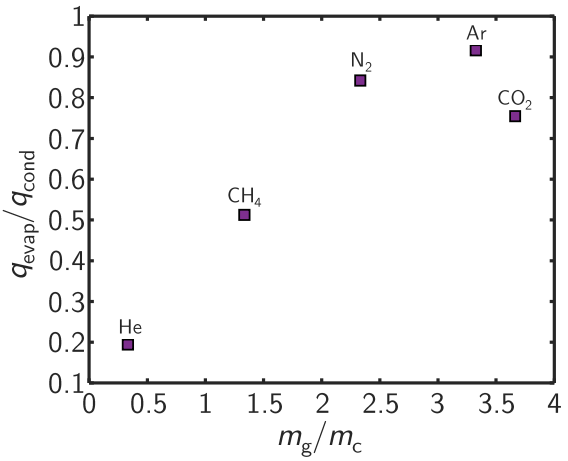


Figure 7-15: Comparing the conductive and sublimative cooling power, at peak temperature, for soot particles in different bath gases. Results are for $d_p = 28.3$ nm, $N_p = 192$, $F_o = 1.75$ mJ/mm^2 and $\alpha = 0.16$, 0.083, 0.1, 0.25, and 0.16, for He, CH_4, N_2, Ar, and CO_2, respectively, inferred from the current data set for the laser cross-section of weak nonuniformity (with a measured average fluence of ~0.57 mJ/mm^2).

Figure 7-16a shows the simulated pyrometric temperatures for He and CO_2 while keeping all other model parameters identical. It can be seen that the period of rapid cooling differs between both gases, with particles aerosolized in He, the gas having the highest conduction rate, approaching the expected conductive cooling model faster. Figure 7-16b shows that the estimated magnitude of anomalous cooling obtained from simulations, which are consistent with anomalous cooling magnitudes obtained from experiments (Figure 7-13) and also shows a gas-dependent trend consistent with Figure 7-14, Figure 7-15, and previous experiments [199].

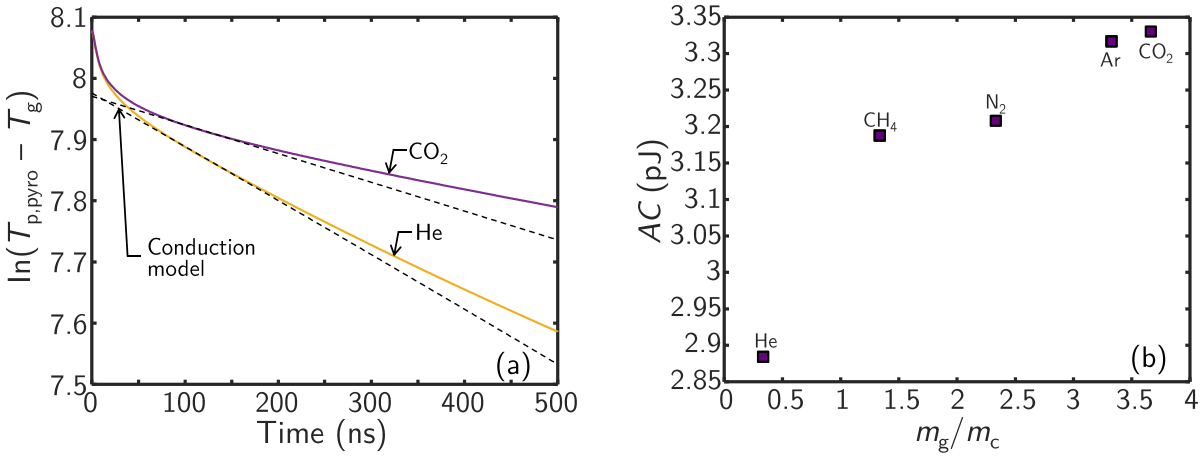


Figure 7-16: (a) Pyrometric temperature history of soot particles in He and CO_2. **(b)** Simulated magnitude of apparent anomalous cooling as a function of bath gas. Results are for $d_p \sim \mathcal{N}(28.3\text{ nm}, 6.5)$, $N_p \sim \ln\mathcal{N}(192, 1.98)$, $F_o = \ln\mathcal{N}(0.6\text{ mJ/mm}^2, 1.75)$ and $\alpha = 0.16$, 0.083, 0.1, 0.25, and 0.16, for He, CH_4, N_2, Ar, and CO_2, respectively, inferred from the current data set for the laser cross-section of weak nonuniformity (with a measured fluence of ~0.57 mJ/mm^2).

7.5. Conclusions

The apparent anomalous cooling of soot is a common and heretofore unexplained feature of many TiRe-LII datasets. In this chapter, experimental and theoretical investigations on soot extracted from a diffusion flame and entrained in different bath gases were carried out to explain the anomalous cooling phenomenon observed for soot.

Nonuniformities in the irradiating laser fluence profile create conditions that may result in anomalous cooling. Regions of fluences higher than the average measured fluence heat up particles within the probe volume to temperatures high enough to induce sublimation, which manifests in a decay in pyrometric temperatures immediately following the peak temperatures that exceed expected cooling rates. An increased degree of laser fluence nonuniformity increases the presence of anomalous cooling in the measured data. Additionally, particle polydispersity also contributes to anomalous cooling, although to a lesser extent, through particles within the probe volume that exhibit high levels of sublimative cooling that influence the overall measured incandescence.

Furthermore, it is shown that the bath-gas dependence of apparent anomalous cooling is due to the varying magnitude of the conductive cooling power of different bath gases, with soot aerosolized in bath gases with higher conductive cooling powers exhibiting less apparent anomalous cooling.

The main contributions of this thesis work are summarized in the next chapter, and pathways for future work are also discussed.

Chapter 8

Conclusions and future work

While time-resolved laser-induced incandescence (TiRe-LII) is a standard diagnostic for soot [64] and is becoming so for non-carbonaceous particles [91], there remain unexplained phenomena, commonly termed as "anomalies", that have been observed in the TiRe-LII data. Two of such anomalies are the excessive absorption phenomenon, observed for metal nanoparticles [16,19,90,139], where the nanoparticles reach higher-than-predicted peak pyrometric temperatures, and the anomalous cooling phenomenon, observed for both soot [27,28,184] and metal nanoparticles [19,139,172], where the pyrometric temperatures, immediately after the peak, decay faster than is predicted by the heat transfer submodel of the TiRe-LII instrument model. The goal of the analyses presented in this thesis work were to investigate the origins of these anomalies and improve the reliability of the TiRe-LII diagnostic technique. During the investigations, new information was revealed, which also laid the foundation for future work. A summary of the key contributions of this thesis work is presented in this chapter, along with several avenues for future work.

8.1. Summary and key contributions

The information presented in Chapter 1 provided the background and motivation for this thesis work, and in Chapter 2, the basic LII model used in literature and the underlying physical processes were discussed. Both these chapters laid the foundation for the investigations presented in this thesis, which provided additional insights into the TiRe-LII process. The key contributions of this thesis work are summarized as follows.

8.1.1. Aggregation effects

The analysis presented in Chapter 3 showed that metal nanoparticles, specifically iron nanoparticles, most often exist as aggregates within the aerosol. The aggregation of the nanoparticles enhances the absorption cross-sections, which allow the particles to reach higher peak temperatures; however, the peak temperatures predicted remained below experimentally observed pyrometric temperatures. Further analyses on aggregate effects were performed in Chapter 4, and it was shown that the absorption cross-section of the individual primary particles varied widely within the aggregates to a degree that increases with increasing aggregate sizes. Such absorption nonuniformities that exist within aggregates may contribute to excessive absorption due to the primary particles that have high absorption cross-sections and thus reach higher-than-expected peak temperatures. In addition, for aggregates with minimal overlap (*i.e.*, point contact) between primary particles, the particles with high absorption cross-sections may reach temperatures above which evaporation cooling is dominant; consequently, they cool down through evaporation, which manifests as an observed cooling in the measured data that is not predicted by the model. Furthermore, primary particles within the aggregates may be shielded from the EM-field at certain orientations, leading to increasingly nonuniform absorption and emission throughout the aggregate. However, the total absorption cross-section of the aggregate varies only slightly (< 10 %) over all orientations.

8.1.2. Sintering, coalescence, and morphology changes

Since the nanoparticles exist as aggregates, morphology changes occur upon laser irradiation that influence the measured incandescence. As shown in Chapter 3, laser-irradiated aggregates of low-melting-point materials, such as iron, sinter and coalesce into spheres through a viscous sintering process. For high-melting-point materials such as molybdenum, which undergo grain boundary sintering, it was shown that the duration of the apparent anomalous cooling phenomenon was consistent with the estimated timescales of grain boundary sintering, suggesting that such sintering processes may be contributing to the reported rapid cooling immediately following peak temperatures. It was also proposed that changes in the spectral absorption cross-section, as the particles sintered, may manifest as a rapid drop in the pyrometric temperatures. In Chapter 4, it was shown that as the aggregates sintered and coalesced, their absorption properties were enhanced due to increased electrical conductivity and morphological changes towards a structure that may promote the antenna effect. These enhancements were found to significantly increase the peak temperature of the partially sintered aggregates compared to the point-contact morphology. The

temperatures predicted from the partially sintered aggregate structure exhibited a rapid decay similar to apparent anomalous cooling, which was attributed to evaporative cooling due to the high peak temperatures reached.

The focus in Chapter 5 was on establishing the relevant timescales of aggregate sintering and coalescence and how they may impact the LII process. For iron aggregates, it was found that coalescence was likely to occur almost instantaneously once the laser-irradiated aggregates reached their melting point. When this occurs, absorption nonuniformities within the aggregate may no longer play a role, and the temperatures of coalesced spheres are impacted in the following ways: (i) the metal aggregates have a larger absorption cross-section compared to the coalesced spheres, hence, reducing the peak temperatures that may be reached; (ii) surface energy released during sintering and coalescence is converted to sensible energy of the particle, thereby increasing the temperatures reached, which, at least in part, may contribute to excessive absorption; (iii) the reduced surface-to-volume ratio reduces the heat transfer to the bath gas; (iv) fields-enhancements that may exist within the aggregate are reduced due to coalesce; (v) the wide variations in aggregate sizes is narrowed after coalescence, however, the resulting temperature distribution is wide, which increases the measured pyrometric temperature because of the bias towards hotter particles. Further analysis revealed that the proposed model still could not reliably reproduce the measured temperatures at early cooling times; nevertheless, the possibility of interference from non-incandescent emissions was discounted.

8.1.3. Particle polydispersity and nonuniform fluence effects

While aggregation and subsequent morphology changes may affect the measured LII data, particle polydispersity and laser nonuniform fluences also contribute significantly to the reported apparent anomalies. The investigations in Chapter 6 revealed that the particle polydispersity of metal nanoparticles results in widely varying temperatures in the aerosol, which are not accounted for in pyrometric temperature estimates. Although pyrometry is an attractive temperature metric in the TiRe-LII literature, due to its independence on particle size, it may not be an appropriate representative temperature of a metal nanoparticle ensemble within nanoaerosols of significant particle polydispersity. More importantly, the resulting pyrometric temperatures from considering particle polydispersity in the TiRe-LII instrument model exhibit peak temperatures that are higher than would be expected for a monodisperse aerosol irradiated with a uniform fluence profile. The temperatures also decay at rates faster than would be predicted if the

nonuniformities were not considered. These features are consistent with the excessive absorption and apparent anomalous cooling phenomena.

The analysis in Chapter 7 extends the discussion of particle polydispersity, introduced in Chapter 6, with the inclusion of nonuniform laser fluence, by applying these concepts to soot, for which apparent anomalous cooling was first reported. The analysis of soot was carried out through experimental and theoretical investigations. It was found that nonuniformities in the laser fluence contribute significantly to the apparent anomalous cooling that has been observed in the LII data for soot. In particular, soot in regions of fluences higher than the average measured fluence heats up to temperatures high enough to induce sublimation cooling, which manifests as a rapid decay in temperature immediately following the peak temperature. The magnitude of the rapid decay increases with an increase in the laser nonuniformity. While particle polydispersity contributes to the reported excessive absorption for metal nanoparticles, as discussed in Chapter 6, this is not the case for soot since the particles absorb laser energy volumetrically and reach similar peak temperatures regardless of their sizes. Particle polydispersity, however, does contribute to apparent anomalous cooling for soot, but to a lesser extent compared to the influence of nonuniform fluence.

8.2. Ongoing and future work

In addition to the key contributions of this thesis work, some ongoing research may provide further insights. The current ongoing research and avenues for future work are discussed in this section.

8.2.1. LII fluence curve and nonuniform fluence profiles for metal nanoparticles

Current LII models can reproduce the experimentally obtained fluence curves for soot [193,200]; however, even with the insights and advances of this thesis work, not much success has been made in reproducing the fluence curves from LII experiments on metal nanoparticles. The analysis presented in Section 5.4.3 showed that the peak pyrometric temperature at which iron nanoparticles plateau during LII experiments may vary between ~1800 K – 2800 K in the literature, with the datasets collected in this work plateauing at about ~3300 K and even showing signs of continued increase. The origins of differences between these datasets are not clear but may arise from differences in particle size or fluence distributions.

Using the current LII heat transfer model (with no consideration of aggregation, particle polydispersity, or nonuniform fluence) to evaluate the temperatures of iron nanoparticles with diameters of 10, 15, 20, 25, and 30 nm provides the LII fluence curves shown in Figure 8-1. Fluence curves presented in Figure 8-1 show signs of a plateau at fluences between 10–15 mJ/mm^2 as opposed to the experimental fluence range of ~ 1–6 mJ/mm^2.

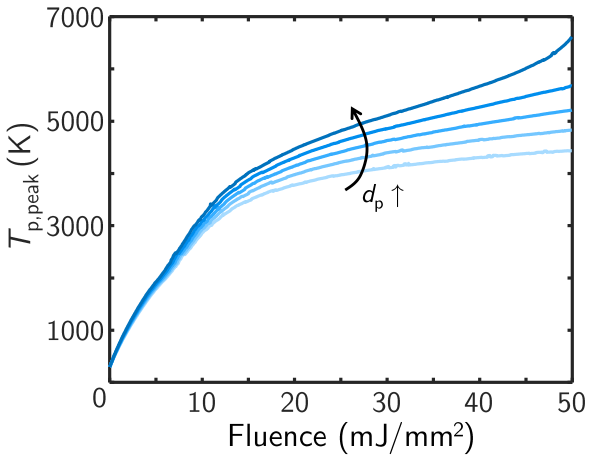


Figure 8-1: Simulated LII fluence curves for iron nanoparticles with diameters of 10, 15, 20, 25, and 30 nm. The particle thermodynamic temperatures are used the temperature metric.

Discussions in Appendix B propose that the fluence curves may be replicated with complete information of the fluence variations and particle polydispersity in the probe volume; however, this requires further investigation. In this regard, as was studied for soot, the impact of nonuniform fluence profiles on the LII data of metal nanoparticles also needs to be investigated. Preliminary work in this area is presented in Appendix B.

8.2.2. Consolidated LII-sintering-nonuniformities model

Investigations of this thesis work revealed that metal particle aggregation and subsequent morphology changes during the LII process can significantly impact the measured incandescence data. Low-melting-point materials such as iron are likely to coalesce, almost instantly, into spheres upon laser irradiation, which may allow one to ignore the sintering dynamics and approximate the particles as spheres during the cooling process; however, the validity of this approximation needs to be confirmed. In addition, particle polydispersity and nonuniformities in the irradiating laser beams also influence the measured incandescent. Furthermore, considering the presence of nonuniform fluences, there will be aggregates of varying degrees

of sintering depending on their locations in the probe volume. In the case of high-melting-point materials such as molybdenum, which sinter slowly, the sintering dynamics will be essential for an accurate model. Hence, a consolidation of a model that describes the sintering dynamics at each time step, an appropriate light absorption model to describe the absorption properties at each stage of sintering, and a TiRe-LII instrument model that considers particle polydispersity and fluence variations, will be vital for accurately modeling the measured incandescence.

8.2.3. Changes in successive LII signal traces

Occasionally, during TiRe-LII experiments, a sudden increase in signal intensity occurs between successive signal traces. The more intense signal traces also exhibit longer decay periods. While not extensively discussed in literature, it has been hypothesized that particles of a certain size class may be flowing through the probe volume and contributing significantly to the signal since they tend to reach much higher temperatures than particles well within the expected size distribution. Such instances of increased intensity between signal traces may be due to unstable particle generation by spark generation during LII experiments, which may sporadically affect the particle volume fraction. A uniform increase in volume fraction across all size classes (*i.e.,* unchanged $p(d_p)$) will not affect the estimated ensemble temperature between successive shots; however, this will not be the case if $p(d_p)$ changes significantly. A hypothetical worst-case scenario that will result in higher temperatures between shots is one where the volume fraction of the particles that reach the highest peak temperatures is greatly increased (*i.e.,* particles with diameters of ~250 nm, *cf.,* Figure 3-12a and Figure 6-5b). To estimate how the temperatures are affected by such a hypothetical change in volume fraction during particle generation, the lognormal distribution of $\ln\mathcal{N}$(56 nm, 2) is modified by adding a lognormal peak centered at 250 nm that follows a distribution of $A_{250}.\ln\mathcal{N}(250\text{ nm}, \sigma_{250})$, where A_{250} and σ_{250} are tuned so that size classes within 250 nm $\pm$ 5 % make up 5, 10, and 20 % of the probe volume, resulting in distributions as seen in Figure 8-2a.

Figure 8-2b shows that a 5 % addition of the 250 nm size class to the size distribution of $\ln\mathcal{N}$(56 nm, 2) can result in about a 60 % increase in peak thermodynamic temperature, and a 50–52 % increase at later cooling times. Additional increases of the 250 nm size result in higher percentage increases in the thermodynamic temperature. While the pyrometric temperature shows a similar trend for varying levels of the 250 nm size class, the magnitude of the percentage increase is significantly reduced due to the increasing underestimation of the thermodynamic temperatures at these size classes, as seen in Figure 8-2b.

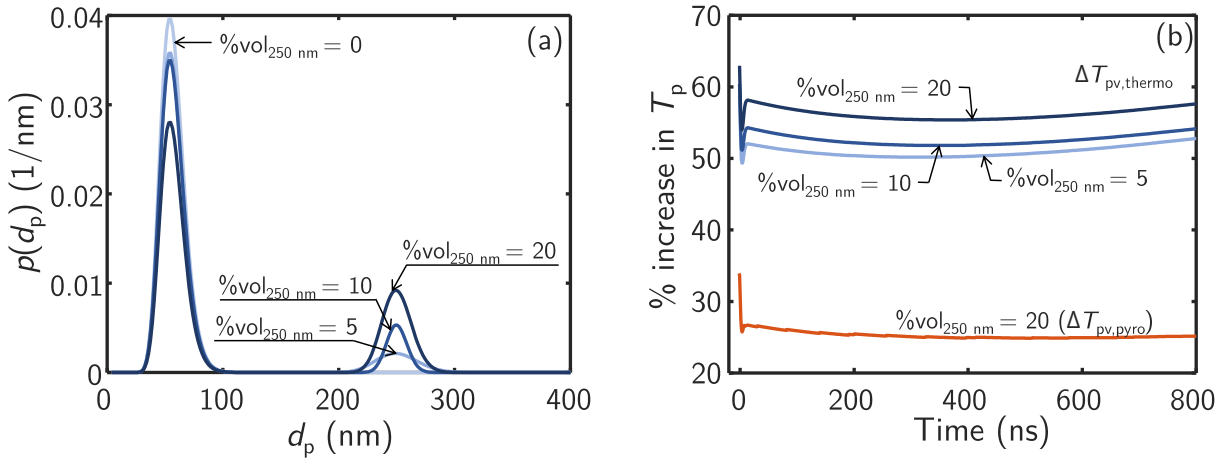


Figure 8-2: (a) PDFs described by $\ln\mathcal{N}(56\text{ nm}, 2)$ having different concentrations by volume (including 0%, 5%, 10%, and 20%) of particles having diameters of ~250 nm ± 5% in the probe volume, and **(b)** the corresponding increase in the temperature profiles computed from $T_{\text{pv,thermo}}$ and $T^{eff}_{\text{p,pyro}}$ (Only 20% covolume concentration level is shown for $T^{\text{eff}}_{\text{p,pyro}}$).

While the possibility that a volume fraction increase of the hottest particles may cause changes in successive signal traces, other situations and considerations will result in the same observation, for example, since the number of particles within the probe volume for each signal trace is finite, the particle distribution may change slightly from shot to shot. A detailed analysis of the problem will require the estimation of the various particle distributions occurring within the probe volume as a function of time, as well as a time-series analysis of the LII signal traces.

8.2.4. Appropriate light absorption models for metal nanoparticles

TEM micrographs of the synthesized aggregates show some level of primary particle overlap; hence, the point-contact approximation [110] may be invalid. Consequently, the applicability of the multi-sphere T-matrix method is likely limited as well. While the discrete dipole approximation (DDA) can be used to estimate the absorption properties of arbitrarily shaped particles, as discussed in Appendix A.6, its accuracy is limited for metals due to their high refractive indices. Considering these factors, other light scattering models that may be better suited for large refractive index materials such as the finite element method (FEM) [169] or the finite difference time domain method (FDTD) [170] may be used to more accurately compute the absorption cross-section of metal aggregates, although these methods may be more computationally intensive

than the DDA method [171]. Furthermore, with the consideration of particle overlap, the heat conduction model and the applicable sintering dynamics will also need modification.

Also worthy of note is that the metal nanoparticles may also be a combination of different phases, including either liquid and solid phases, or different oxide phases (*cf.*, Appendix A.2); consequently, there may be cases where there is no unique set of refractive indices, which may require extra care in modeling.

8.2.5. Quantifying uncertainties in estimated TACs

The TAC is usually inferred from the LII data either by (1) regressing the complete model to the time-resolved data (*cf.*, Chapter 5) or by (2) estimating the conduction cooling-dominated portion of the data and regressing this to the LII conduction cooling model. Both methods rely on information on the particle size. In the former method, the diameter is generally inferred simultaneously with the TAC, with the evaporative cooling portion providing the needed information on the particle diameter [19]. In the latter method, the diameter needs to be defined (*cf.*, Chapter 7). In cases of polydispersity of metal nanoparticles, while the first method may infer an effective particle diameter for which an associated TAC can also be inferred, for the second method, it is not clear which particle diameter should be used during inference. The uncertainty quantification of the inferred TACs should take this into account.

8.2.6. Optimal wavelength excitation for TiRe-LII on metal nanoparticles

It is more common to use lasers centered at a wavelength of 1064 nm to heat up aerosolized particles during LII experiments because, during the advent of the diagnostic technique for soot, it was revealed that other wavelengths, for example, 266, 355, or 532 nm, tend to result in non-incandescent interferences. In particular, signal interferences occur due to laser-induced fluorescence (LIF) emitted from polycyclic aromatic hydrocarbons (PAHs) when 266 or 532 nm laser excitation wavelengths are used [33,182] or from non-thermal C_2-Swan band and C_3-Swing band emissions, which are most pronounced at high fluences ($>$ 5 mJ/mm^2) and in the ~300–600 nm wavelength range [178,183]. These interferences are generally absent at longer excitation wavelengths of 1064 nm [127].

While shorter excitation wavelengths have been used for LII on metals [65,201], the practice of using 1064 nm persisted when LII was extended to non-carbonaceous particles. The drawback of using the 1064

nm laser wavelength for metal nanoparticles is that at this wavelength, metals generally have a lower absorption efficiency compared to soot, hence, the signal-to-noise ratio for metals can be poor. On the other hand, metals have much larger absorption efficiencies at shorter wavelengths, but the downside is that, much like soot, other non-thermal interferences may occur at shorter laser wavelengths due to elemental absorption lines that commonly occur at shorter wavelengths. As research was carried out to find appropriate excitation and detection wavelengths for soot, so does an explorative endeavor need to be carried out for non-carbonaceous particles.

In this regard, preliminary work was performed on spark-discharge-generated (SDG) iron nanoparticles, additionally irradiated at 355 nm and 532 nm, as well as the standard 1064 nm wavelength. The measured signals are shown in Figure 8-3 along with the estimated fluence curve.

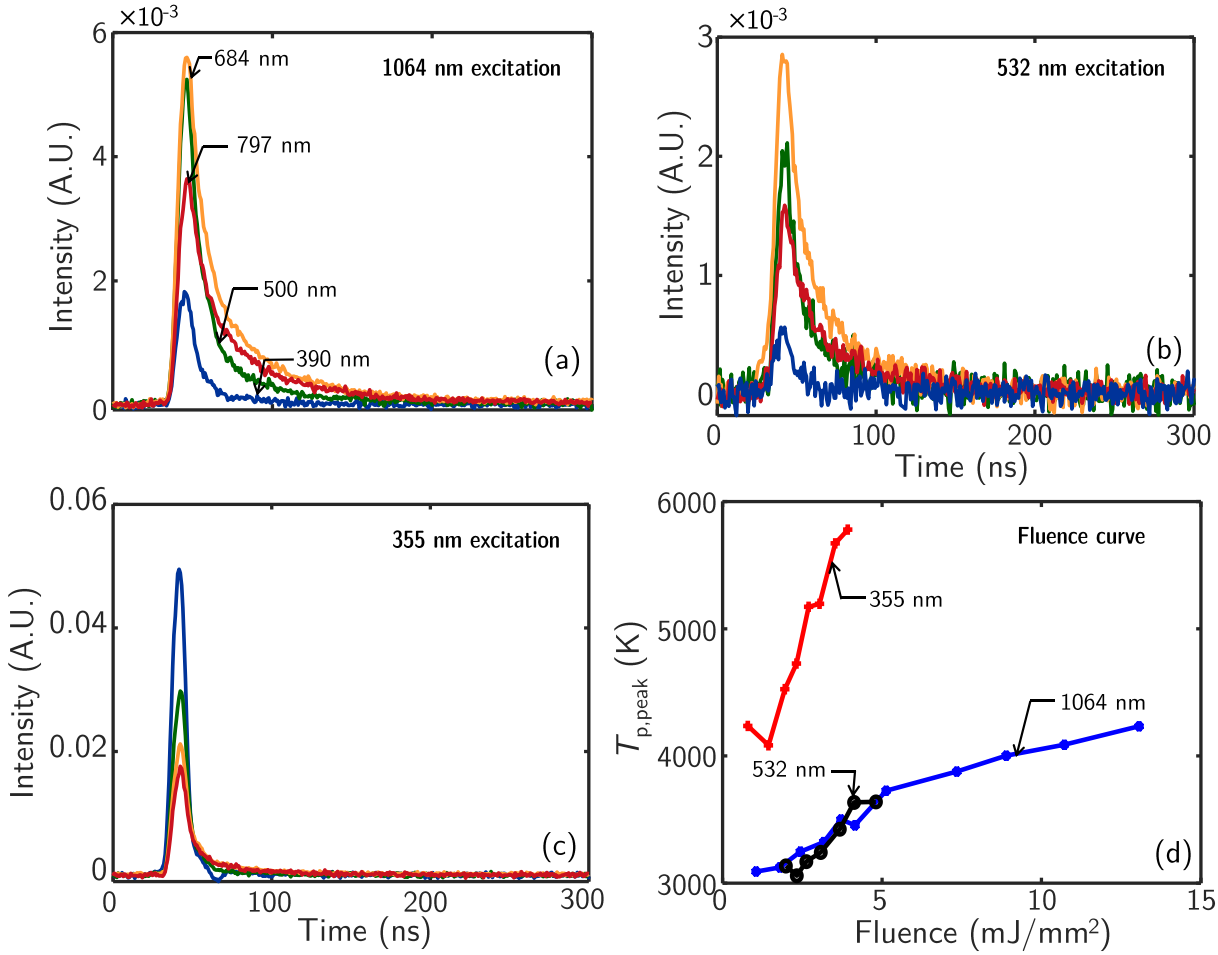


Figure 8-3: The calibrated intensities at detection wavelengths of 390 nm, 500 nm, 684 nm, and 797 nm from spark discharge-generated iron nanoparticles irradiated with laser wavelengths of **(a)** 1064 nm, **(b)** 532 nm, and **(c)** 355 nm; and their corresponding fluence curves.

At the same fluence of 1.8 mJ/mm^2, the magnitude of the measured signals for particles irradiated at 355 nm is an order of magnitude greater than the signals for particles irradiated at 532 nm and 1064 nm. In addition, the estimated fluence curves for particles irradiated at 532 nm and 1064 nm are consistent with each other and previous experiments, but that of 355 nm is atypical of what has been reported in the literature. This suggests that other non-incandescent interferences may be present in the measured signals for an irradiation wavelength of 355 nm. Additional investigations are needed to provide more insight into appropriate excitation wavelengths. A clear example where significant benefits in optimal excitation wavelengths could be realized is in the case of plasmonic nanoparticles such as gold and silver nanoparticles, which have absorption cross-sections at 1064 nm so small that they are not expected to heat up [90]. Heating

such particles at their respective plasmonic wavelengths may give way for an opportunity to probe them using the TiRe-LII technique.

8.2.7. Experiments on other elemental materials

A significant amount of this thesis work focused on iron nanoparticles as a case study for metal nanoparticles because it is the most investigated metal in the LII literature on non-carbonaceous materials [91]. However, factors such as sintering and coalescence dynamics, or absorption properties, may have varying impacts on that affect the measured LII signal depending on the material. For instance, refractory metals with higher melting and boiling points, such as molybdenum or tungsten, could be examined with the LII technique to gain additional insights. In particular, experiments on such materials can be useful as follows: (i) slower sintering, resulting in incomplete sintering by the LII peak, providing an opportunity to compare the spectral emission at the peak of the LII signal to that of a fully sintered particle, and (ii) high boiling point resulting in slower cooling rates that may be dominated by conduction cooling, hence avoiding the inclusion of the evaporation model and possibly the absence of the anomalous cooling phenomenon.

8.2.8. In-flame LII[8] and soot optical properties

Although the origins of the apparent anomalous cooling of re-aerosolized soot have been revealed, additional work was performed on in-flame soot by irradiating the soot directly in the flame, which is the more common method of LII experiments on soot in the literature. The results of this experiment are shown in Figure 8-4. Figure 8-4a shows that the effect of apparent anomalous cooling (AC) is more pronounced for re-aerosolized soot compared to in-flame soot. Figure 8-4b quantifies AC and shows that it is significantly less (>30x) for in-flame soot compared to re-aerosolized soot.

[8] Details of this issue are discussed further in the conference proceeding:
Robinson-Enebeli, S., Schulz, C., Daun, K. J., 2025, "Investigation of the Apparent Anomalous Cooling of Soot During Laser-Induced Incandescence." Proceedings of the 11th International Symposium on Radiative Transfer, RAD-25, Kuşadası Türkiye, 15–20 June 2025.

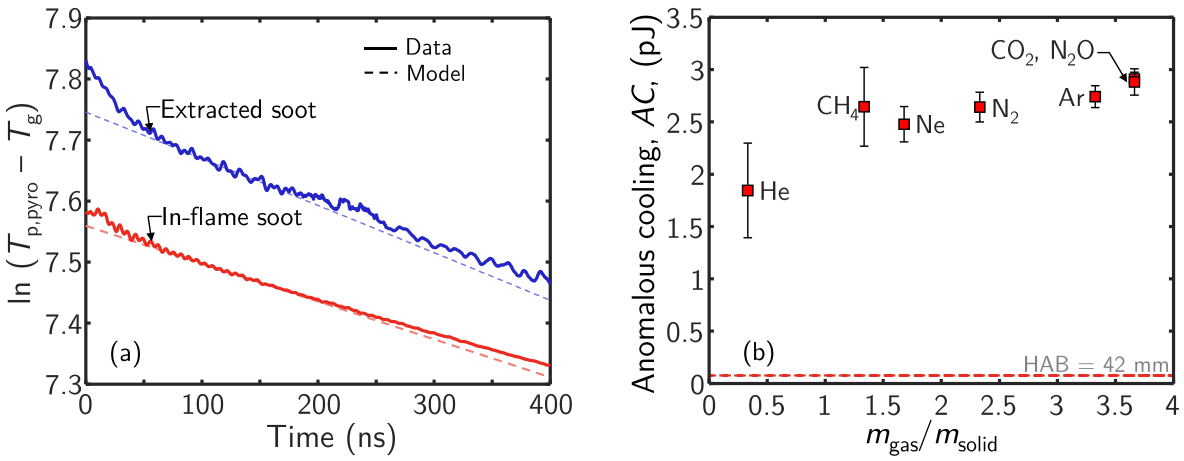


Figure 8-4: (a) Regression of the free molecular conduction model to the TiRe-LII data; in-flame soot at 42 mm HAB at a fluence of ~0.5 mJ/mm²and extracted soot diluted in Ar at a fluence of ~0.8 mJ/mm².; and **(b)** Magnitude of apparent anomalous cooling for extracted and in-flame soot (HAB = 42 mm) at a fluence of 0.566 mJ/mm² and 0.77 mJ/mm², respectively. Uncertainty bars represent one standard deviation of the mean.

The major differences between these two kinds of soot include: (i) In-flame soot has a higher initial temperature (1700 K) [58], compared to re-aerosolized soot (296 K); and (ii) Re-aerosolized soot tends to be more aggregated with a narrower distribution compared to in-flame soot. The disparity in the magnitude of the apparent anomalous cooling between these kinds of soot may arise from the above-stated differences.

In addition to this, further exploration of factors contributing to apparent anomalous cooling should include the effects of changes in soot optical properties caused by annealing or graphitization during laser irradiation. Moreover, the model can be extended to account for the subtle wavelength dependence of the soot absorption function.

8.3. Final remarks

Laser- and optical-based diagnostic techniques are attractive methods for probing particles because of their potential to provide *in situ*, and spatially- and time-resolved information. One such technique, TiRe-LII, can provide reliable information on particle diameter and concentration, given that the underlying process is well understood and the instrument model is accurate. While the experimentation and theoretical investigations in this thesis work were focused on resolving discrepancies between the current TiRe-LII instrument model and the measured data, the insights gained are beneficial to laser- and optical-based

processes that involve particle irradiation and subsequent signal acquisition. Specifically, the effects of metal aggregation and the subsequent sintering and coalescence of the aggregates, and the effects of particle polydispersity and nonuniformities in the irradiating laser, on the laser-particle interaction and the detected signals, have been revealed as important factors to consider when assessing and analyzing optically measured data from laser-irradiated particles.

References

[1] Beik, J., Abed, Z., Ghoreishi, F. S., Hosseini-Nami, S., Mehrzadi, S., Shakeri-Zadeh, A., and Kamrava, S. K., 2016, "Nanotechnology in Hyperthermia Cancer Therapy: From Fundamental Principles to Advanced Applications," J. Control. Release, **235**, pp. 205–221.

[2] Alkhalayfeh, M. A., Aziz, A. A., and Pakhuruddin, M. z., 2021, "An Overview of Enhanced Polymer Solar Cells with Embedded Plasmonic Nanoparticles," Renew. Sustain. Energy Rev. J., **141**(110726).

[3] Wang, L., Zheng, M., and Xie, Z., 2018, "Nanoscale Metal-Organic Frameworks for Drug Delivery: A Conventional Platform with New Promise," J. Mater. Chem. B, **6**(5), pp. 707–717.

[4] Guo, X., Yang, Z., Dong, H., Guan, X., Ren, Q., Lv, X., and Jin, X., 2016, "Simple Combination of Oxidants with Zero-Valent-Iron (ZVI) Achieved Very Rapid and Highly Efficient Removal of Heavy Metals from Water," Water Res., **88**, pp. 671–680.

[5] Lal, S., Link, S., and Halas, N. J., 2007, "Nano-Optics from Sensing to Waveguiding," Nat. Photonics, **1**(11), pp. 641–648.

[6] Stark, W. J., Stoessel, P. R., Wohlleben, W., and Hafner, A., 2015, "Industrial Applications of Nanoparticles," Chem. Soc. Rev., **44**(16), pp. 5793–5805.

[7] Tsuzuki, T., 2009, "Commercial Scale Production of Inorganic Nanoparticles," Int. J. Nanotechnol., **6**(5–6), pp. 567–578.

[8] Dreier, T., and Schulz, C., 2016, "Laser-Based Diagnostics in the Gas-Phase Synthesis of Inorganic Nanoparticles," Powder Technol., **287**, pp. 226–238.

[9] Gomes, J. F. P., Albuquerque, P. C. S., Miranda, R. M. M., and Vieira, M. T. F., 2012, "Determination of Airborne Nanoparticles from Welding Operations," J. Toxicol. Environ. Heal. Part A, **75**(13–15), pp. 747–755.

[10] Solomon, S., Qin, D., Manning, M., Alley, R. B. B., Berntsen, T., Bindoff, N. L. L., Chen, Z., et al., 2007, *Technical Summary. Climate Change 2007: The Physical Science Basis*, Cambridge University Press.

[11] Arias, P. A., Bellouin, N., Coppola, E., Jones, R. G., Krinner, G., Marotzke, J., Naik, V., et al., 2021, *Technical Summary. In Climate Change 2021: The Physical Science Basis.*, Cambridge University Press.

[12] Biskos, G., Vons, V., Yurteri, C. U., and Schmidt-Ott, A., 2008, "Generation and Sizing of Particles for Aerosol-Based Nanotechnology," KONA Powder Part. J., **26**(March), pp. 13–35.

[13] Tavakoli, F., and Olfert, J. S., 2013, "An Instrument for the Classification of Aerosols by Particle Relaxation Time: Theoretical Models of the Aerodynamic Aerosol Classifier," Aerosol Sci. Technol., **47**(8), pp. 916–926.

[14] Gurentsov, E. V., 2018, "A Review on Determining the Refractive Index Function, Thermal Accommodation Coefficient and Evaporation Temperature of Light-Absorbing Nanoparticles Suspended in the Gas Phase Using the Laser-Induced Incandescence," Nanotechnol. Rev., **7**(6), pp. 583–604.

[15] Stephens, M., Turner, N., and Sandberg, J., 2003, "Particle Identification by Laser-Induced Incandescence in a Solid-State Laser Cavity," Appl. Opt., **42**(19), p. 3726.

[16] Robinson-Enebeli, S., Talebi-Moghaddam, S., and Daun, K. J., 2021, "Time-Resolved Laser-Induced Incandescence Measurements on Aerosolized Nickel Nanoparticles," J. Phys. Chem. A, **125**(28), pp. 6273–6285.

[17] Melton, L. A., 1983, "Soot Diagnostics Based on Laser Heating," Appl. Opt., **23**(13), pp. 2201–2208.

[18] Michelsen, H. A., Liu, F., Kock, B. F., Bladh, H., Boiarciuc, A., Charwath, M., Dreier, T., et al., 2007, "Modeling Laser-Induced Incandescence of Soot: A Summary and Comparison of LII Models," Appl. Phys. B, **87**(3), pp. 503–521.

[19] Sipkens, T. A., Singh, N. R., and Daun, K. J., 2017, "Time-Resolved Laser-Induced Incandescence Characterization of Metal Nanoparticles," Appl. Phys. B, **123**(14).

[20] Talebi-Moghaddam, S., Sipkens, T. A., and Daun, K. J., 2019, "Laser-Induced Incandescence on Metal Nanoparticles: Validity of the Rayleigh Approximation," Appl. Phys. B, **125**(214).

[21] Schulz, C., Kock, B. F., Hofmann, M., Michelsen, H., Will, S., Bougie, B., Suntz, R., et al., 2006, "Laser-Induced Incandescence: Recent Trends and Current Questions," Appl. Phys. B, **83**(3), pp. 333–354.

[22] Kock, B. F., Kayan, C., Knipping, J., Orthner, H. R., and Roth, P., 2005, "Comparison of LII and TEM Sizing during Synthesis of Iron Particle Chains," Proc. Combust. Inst., **30**(1), pp. 1689–1697.

[23] Eremin, A., Gurentsov, E., Popova, E., and Priemchenko, K., 2011, "Size Dependence of Complex Refractive Index Function of Growing Nanoparticles," Appl. Phys. B, **104**(2), pp. 285–295.

[24] Eremin, A., and Gurentsov, E., 2019, "Evaporation Temperature Depression with Decrease of Iron Nanoparticle Size. Validation of Semi-Empirical Models," Mater. Chem. Phys., **228**, pp. 180–186.

[25] Sipkens, T. A., Hadwin, P. J., Grauer, S. J., and Daun, K. J., 2018, "Predicting the Heat of Vaporization of Iron at High Temperatures Using Time-Resolved Laser-Induced Incandescence and Bayesian Model Selection," J. Appl. Phys., **123**, p. 095103.

[26] Lang, P., Kücükmeric, E., Huber, F. J. T., and Will, S., 2024, "Investigation of Iron Oxide Nanoparticle Formation in a Spray-Flame Synthesis Process Using Laser-Induced Incandescence," Appl. Phys. B, **130**(11), pp. 1–20.

[27] Daun, K. J., Smallwood, G. J., and Liu, F., 2008, "Investigation of Thermal Accommodation Coefficients in Time-Resolved Laser-Induced Incandescence," J. Heat Transfer, **130**, pp. 121201-1-121201–9.

[28] Snelling, D. R., Thomson, K. A., Liu, F., and Smallwood, G. J., 2009, "Comparison of LII Derived Soot Temperature Measurements with LII Model Predictions for Soot in a Laminar Diffusion Flame," Appl. Phys. B, **96**(4), pp. 657–669.

[29] Weeks, R. W., and Duley, W. W., 1974, "Aerosol-Particle Sizes from Light Emission during Excitation by TEA CO2 Laser Pulses," J. Appl. Phys., **45**, p. 4661.

[30] Eckbreth, A. C., 1977, "Effects of Laser-Modulated Particulate Incandescence on Raman Scattering Diagnostics," J. Appl. Phys., **48**(11), pp. 4473–4479.

[31] Rohlfing, E. A., and Chandler, D. W., 1990, "Two-Color Pyrometric Imaging of Laser-Heated Carbon Particles in a Supersonic Flow," Chem. Phys. Lett., **170**(1), pp. 44–50.

[32] Hofeldt, D. L., 1993, "Real-Time Soot Concentration Measurement Technique for Engine Exhaust Streams," SAE Tech. Pap., (412).

[33] Bengtsson, P. E., and Aldén, M., 1995, "Soot-Visualization Strategies Using Laser Techniques," Appl. Phys. B, **60**(1), pp. 51–59.

[34] Will, S., Schraml, S., and Leipertz, A., 1995, "Two-Dimensional Soot-Particle Sizing by Time-Resolved Laser-Induced Incandescence," Opt. Lett., **20**(22), pp. 2342–2344.

[35] Mewes, B., and Seitzman, J. M., 1997, "Soot Volume Fraction and Particle Size Measurements with Laser-Induced Incandescence," Appl. Opt., **36**(3), p. 709.

[36] Roth, P., and Filippov, A. V., 1996, "In Situ Ultrafine Particle Sizing by a Combination of Pulsed Laser Heatup and Particle Thermal Emission," J. Aerosol Sci., **27**(1), pp. 95–104.

[37] Dasch, C. J., 1984, "Continuous-Wave Probe Laser Investigation of Laser Vaporization of Small Soot Particles in a Flame," Appl. Opt., **23**(13), p. 2209.

[38] Vander Wal, R. L., Choi, M. Y., and Lee, K. ook, 1995, "The Effects of Rapid Heating of Soot: Implications When Using Laser-Induced Incandescence for Soot Diagnostics," Combust. Flame, **102**(1–2), pp. 200–204.

[39] Vander Wal, R. L., and Choi, M. Y., 1999, "Pulsed Laser Heating of Soot: Morphological Changes," Carbon N. Y., **37**(2), pp. 231–239.

[40] Vander Wal, R. L., 1996, "Laser-Induced Incandescence: Detection Issues," Appl. Opt., **35**(33), p. 6548.

[41] Vander Wal, R. L. Vander, Ticich, T. M., and Stephens, A. B., 1998, "Optical and Microscopy Investigations of Soot Structure Alterations by Laser-Induced Incandescence," Appl. Phys. B, **67**, pp. 115–123.

[42] Wal, R. L. Vander, and Weiland, K. J., 1994, "Laser-Induced Incandescence: Development and Characterization towards a Measurement of Soot-Volume Fraction," App. Phys. B, **59**, pp. 445–452.

[43] Cignoli, F., Benecchi, S., and Zizak, G., 1994, "Time-Delayed Detection of Laser-Induced Incandescence for the Two-Dimensional Visualization of Soot in Flames," Appl. Opt., **33**(24), p. 5778.

[44] Vander Wal, R. L., 1996, "Soot Precursor Material: Visualization via Simultaneous LIF-LII and Characterization via Tem," Symp. Combust., **26**(2), pp. 2269–2275.

[45] Snelling, D. R., Smallwood, G. J., Liu, F., Gülder, Ö. L., and Bachalo, W. D., 2005, "A Calibration-Independent Laser-Induced Incandescence Technique for Soot Measurement by Detecting Absolute Light Intensity," Opt. Soc. Am., **44**(31), pp. 6773–6785.

[46] Snelling, D. R., Smallwood, G. J., Gülder, Ö. L., Bachalo, W. D., and Sankar, S., 2000, *Soot Volume Fraction Characterization Using the Laser-Induced Incandescence Detection Method*, National Research Council Canada.

[47] Mansmann, R., Sipkens, T. A., Menser, J., Daun, K. J., Dreier, T., and Schulz, C., 2019, "Detector Calibration and Measurement Issues in Multi-Color Time-Resolved Laser-Induced Incandescence," Appl. Phys. B, **125**(7), p. 126.

[48] Snelling, D., Liu, F., Smallwood, G., and Gülder, Ö. L., 2000, "Evaluation of the Nanoscale Heat and Mass Transfer Model of LII: Prediction of the Excitation Intensity," Proceedings of NHTC'00 34th National Heat Transfer Conference, Pittsburgh, Pennsylvania, August 20-22, 2000, pp. NHTC2000-12132.

[49] Snelling, D. R., Thomson, K. A., Smallwood, G. J., Gülder, Ö. L., Weckman, E. J., and Fraser, R. A., 2002, "Spectrally Resolved Measurement of Flame Radiation," AIAA J., **40**(9), p. 2002.

[50] Kock, B. F., Eckhardt, T., and Roth, P., 2002, "In-Cylinder Sizing of Diesel Particles by Time-Resolved Laser-Induced Incandescence (TR-LII)," Proc. Combust. Inst., **29**(2), pp. 2775–2782.

[51] Schraml, S., Dankers, S., Bader, K., Will, S., and Leipertz, A., 2000, "Soot Temperature Measurements and Implications for Time-Resolved Laser-Induced Incandescence (TIRE-LII)," Combust. Flame, **120**(4), pp. 439–450.

[52] Axelsson, B., Collin, R., and Bengtsson, P. E., 2001, "Laser-Induced Incandescence for Soot Particle Size and Volume Fraction Measurements Using on-Line Extinction Calibration," Appl. Phys. B, **72**(3), pp. 367–372.

[53] Axelsson, B., Collin, R., and Bengtsson, P.-E., 2000, "Laser-Induced Incandescence for Soot Particle Size Measurements in Premixed Flat Flames," Appl. Opt., **39**(21), p. 3683.

[54] Witze, P. O., Hochgreb, S., Kayes, D., Michelsen, H. A., and Shaddix, C. R., 2001, "Time-Resolved Laser-Induced Incandescence and Laser Elastic-Scattering Measurements in a Propane Diffusion Flame," Appl. Opt., **40**(15), p. 2443.

[55] McManus, K. R., Frank, J. H., Alien, M. G., and Rawlins, W. T., 1998, "Characterization of Laser-Heated Soot Particles Using Optical Pyrometry," 36th Aerospace Sciences Meeting and Exhibit, Reno, Nevada, USA, January 12 - 15, 1998.

[56] Smallwood, G. J., Snelling, D. R., Liu, F., and Gülder, Ö. L., 2001, "Clouds over Soot Evaporation: Errors in Modeling Laser-Induced Incandescence of Soot," J. Heat Transfer, **123**(4), pp. 814–818.

[57] Liu, F., Yang, M., Snelling, D. R., and Smallwood, G. J., 2005, "Numerical Calculations of Heat Conduction between Soot Aggregates and the Surrounding Gas in the Free-Molecular Regime Using the DSMC Method," Proceedings of the ASME Summer Heat Transfer Conference, American Society

of Mechanical Engineers Digital Collection, San Francisco, California, USA, July 17 - 22, 2005, pp. HT2005-72433.

[58] Snelling, D. R., Liu, F., Smallwood, G. J., and Gülder, Ö. L., 2004, "Determination of the Soot Absorption Function and Thermal Accommodation Coefficient Using Low-Fluence LII in a Laminar Coflow Ethylene Diffusion Flame," Combust. Flame, **136**(1–2), pp. 180–190.

[59] Kuhlmann, S. A., Reimann, J., and Will, S., 2006, "On Heat Conduction between Laser-Heated Nanoparticles and a Surrounding Gas," J. Aerosol Sci., **37**(12), pp. 1696–1716.

[60] Liu, F., Yang, M., Hill, F. A., Snelling, D. R., and Smallwood, G. J., 2006, "Influence of Polydisperse Distributions of Both Primary Particle and Aggregate Size on Soot Temperature in Low-Fluence LII," Appl. Phys. B, **83**(3), pp. 383–395.

[61] Liu, F., Snelling, D. R., Thomson, K. A., and Smallwood, G. J., 2009, "Sensitivity and Relative Error Analyses of Soot Temperature and Volume Fraction Determined by Two-Color LII," Appl Phys B, **96**, pp. 623–636.

[62] Maffi, S., Cignoli, F., Bellomunno, C., De Iuliis, S., and Zizak, G., 2008, "Spectral Effects in Laser Induced Incandescence Application to Flame-Made Titania Nanoparticles," Spectrochim. Acta Part B At. Spectrosc., **63**(2), pp. 202–209.

[63] Lemaire, R., and Mobtil, M., 2015, "Modeling Laser-Induced Incandescence of Soot: A New Approach Based on the Use of Inverse Techniques," Appl. Phys. B, **119**(4), pp. 577–606.

[64] Michelsen, H. A., Schulz, C., Smallwood, G. J., and Will, S., 2015, "Laser-Induced Incandescence: Particulate Diagnostics for Combustion, Atmospheric, and Industrial Applications," Prog. Energy Combust. Sci., **51**, pp. 2–48.

[65] Filippov, A. V, Markus, M. W., and Roth, P., 1999, "In-Situ Characterization of Ultrafine Particles by Laser-Induced Incandescence : Sizing and Particle Structure Determination," J. Aerosol Sci., **30**(1), pp. 71–87.

[66] Vander Wal, R. L., Ticich, T. M., and West, J. R., 1999, "Laser-Induced Incandescence Applied to Metal Nanostructures," Appl. Opt., **38**(27), p. 5867.

[67] Vander Wal, R. L., Berger, G. M., Ticich, T. M., and Patel, P. D., 2002, "Application of Laser-Induced Incandescence to the Detection of Carbon Nanotubes and Carbon Nanofibers," Appl. Opt., **41**(27), p. 5678.

[68] Starke, R., Kock, B., and Roth, P., 2003, "Nano-Particle Sizing by Laser-Induced-Incandescence (LII) in a Shock Wave Reactor," Shock Waves, **12**(5), pp. 351–360.

[69] Murakami, Y., Sugatani, T., and Nosaka, Y., 2005, "Laser-Induced Incandescence Study on the Metal Aerosol Particles as the Effect of the Surrounding Gas Medium," J. Phys. Chem. A, **109**(40), pp. 8994–9000.

[70] Eremin, A., Gurentsov, E., and Schulz, C., 2008, "Influence of the Bath Gas on the Condensation of Supersaturated Iron Atom Vapour at Room Temperature," J. Phys. D. Appl. Phys., **41**(5).

[71] Gurentsov, E. V., and Eremin, A. V., 2011, "Size Measurement of Carbon and Iron Nanoparticles by Laser Induced Incadescence," High Temp., **49**(5), pp. 667–673.

[72] Leipertz, A., and Dankers, S., 2003, "Characterization of Nano-Particles Using Laser-Induced Incandescence," Part. Part. Syst. Charact., **20**(2), pp. 81–93.

[73] Lehre, T., Suntz, R., and Bockhorn, H., 2005, "Time-Resolved Two-Color LII: Size Distributions of Nano-Particles from Gas-to-Particle Synthesis," Proc. Combust. Inst., **30**(2), pp. 2585–2593.

[74] De Iuliis, S., Migliorini, F., and Dondè, R., 2019, "Laser-Induced Emission of TiO2 Nanoparticles in Flame Spray Synthesis," Appl. Phys. B, **125**(11), p. 219.

[75] Sipkens, T. A., Mansmann, R., Daun, K. J., Petermann, N., Titantah, J. T., Karttunen, M., Wiggers, H., et al., 2014, "In Situ Nanoparticle Size Measurements of Gas-Borne Silicon Nanoparticles by Time-Resolved Laser-Induced Incandescence," Appl. Phys. B, **116**(3), pp. 623–636.

[76] Eom, G. S., Park, S., Park, C. W., Choe, W., Shin, Y.-H., Chung, K. H., and Hahn, J. W., 2004, "Size Monitoring of Nanoparticles Growing in Low-Pressure Plasma Using Laser-Induced Incandescence Technique," Jpn. J. Appl. Phys., **43**(9A), pp. 6494–6498.

[77] Menser, J., Daun, K., Dreier, T., and Schulz, C., 2016, "Laser-Induced Incandescence from Laser-Heated Silicon Nanoparticles," Appl. Phys. B, **122**, p. 277.

[78] Daun, K., Menser, J., Mansmann, R., Moghaddam, S. T., Dreier, T., and Schulz, C., 2017, "Spectroscopic Models for Laser-Heated Silicon and Copper Nanoparticles," J. Quant. Spectrosc. Radiat. Transf., **197**, pp. 3–11.

[79] Daun, K. J., Stagg, B. J., Liu, F., Smallwood, G. J., and Snelling, D. R., 2007, "Determining Aerosol Particle Size Distributions Using Time-Resolved Laser-Induced Incandescence," Appl. Phys. B, **87**, pp. 363–372.

[80] Sipkens, T., Joshi, G., Daun, K. J., and Murakami, Y., 2013, "Sizing of Molybdenum Nanoparticles Using Time-Resolved Laser-Induced Incandescence," J. Heat Transfer, **135**(5).

[81] Daun, K. J., Liu, F., and Smallwood, G. J., 2008, "Molecular Dynamics Simulations of Translational Thermal Accomodation Coefficients for Time-Resolved LII," Proceedings of 2008 ASME Summer Heat Transfer Conference, Jacksonville, Florida USA, August 10-14, 2008, pp. HT2008-56043 333–342.

[82] Daun, K. J., Titantah, J. T., and Karttunen, M., 2012, "Molecular Dynamics Simulation of Thermal Accommodation Coefficients for Laser-Induced Incandescence Sizing of Nickel Particles," Appl. Phys. B, **107**(1), pp. 221–228.

[83] Sipkens, T. A., and Daun, K. J., 2018, "Effect of Surface Interatomic Potential on Thermal Accommodation Coefficients Derived from Molecular Dynamics," J. Phys. Chem. C, **122**(35), pp. 20431–20443.

[84] Miller, J. C., 1969, "Optical Properties of Liquid Metals at High Temperatures," Philos. Mag., **20**(168), pp. 1115–1132.

[85] Querry, M. R., 1985, "Optical Constants," CRDC-CR-85034, Rep. No. AD-A158 623.

[86] Barnes, B. T., 1966, "Optical Constants of Incandescent Refractory Metals," J. Opt. Soc. Am., **56**(11), p. 1546.

[87] Eremin, A., Gurentsov, E., Mikheyeva, E., and Priemchenko, K., 2013, "Experimental Study of Carbon and Iron Nanoparticle Vaporization under Pulse Laser Heating," Appl. Phys. B, **112**(3), pp. 421–432.

[88] Sipkens, T. A., Singh, N. R., Daun, K. J., Bizmark, N., Ioannidis, M., Titantah, J. T., and Karttunen, M., 2014, "Time Resolved Laser Induced Incandescence For Sizing Aerosolized Iron Nanoparticles," Proceedings of the ASME 2014 International Mechanical Engineering Congress and Exposition, Montreal, Quebec, Canada, November 14-20, 2014, pp. IMECE2014-38515.

[89] Talebi Moghaddam, S., and Daun, K. J., 2018, "Plasma Emission during Time-Resolved Laser-Induced Incandescence Measurements of Aerosolized Metal Nanoparticles," Appl. Phys. B, **124**(159).

[90] Talebi-Moghaddam, S., Robinson-Enebeli, S., Musikhin, S., Clavel, D. J., Corbin, J. C., Klinkova, A., Smallwood, G. J., et al., 2021, "Multiphoton Induced Photoluminescence during Time-Resolved Laser-Induced Incandescence Experiments on Silver and Gold Nanoparticles," J. Appl. Phys., **129**(18), p. 183107.

[91] Sipkens, T. A., Menser, J., Dreier, T., Schulz, C., Smallwood, G. J., and Daun, K. J., 2022, "Laser-Induced Incandescence for Non-Soot Nanoparticles: Recent Trends and Current Challenges," Appl. Phys. B, **128**(72).

[92] Michelsen, H. A., 2003, "Understanding and Predicting the Temporal Response of Laser-Induced Incandescence from Carbonaceous Particles," J. Chem. Phys, **118**, pp. 7012–7045.

[93] Michelsen, H. A., Linne, M. A., Kock, · B F, Hofmann, · M, Tribalet, · B, Schulz, · C, Kock, B. F., et al., 2008, "Modeling Laser-Induced Incandescence of Soot: Enthalpy Changes during Sublimation, Conduction, and Oxidation," Appl Phys B, **93**, pp. 645–656.

[94] Bohren, C. F., and Huffman, D. R., 1998, *Absorption and Scattering of Light by Small Particles*, John Wiley & Sons, Inc., Canada.

[95] McCoy, B. J., and Cha, C. Y., 1974, "Transport Phenomena in the Rarefied Gas Transition Regime," Chem. Eng. Sci., **29**(2), pp. 381–388.

[96] Memarian, F., Liu, F., Thomson, K. A., Daun, K. J., Snelling, D. R., and Smallwood, G. J., 2015, "Effect of Recondensation of Sublimed Species on Nanoparticle Temperature Evolution in Time-Resolved Laser-Induced Incandescence," Appl. Phys. B, **119**(4), pp. 607–620.

[97] Nanda, K. K., Maisels, A., Kruis, F. E., Fissan, H., and Stappert, S., 2003, "Higher Surface Energy of Free Nanoparticles," Phys. Rev. Lett., **91**(10), pp. 1–4.

[98] Menser, J., Daun, K., Dreier, T., and Schulz, C., 2017, "Laser-Induced Atomic Emission of Silicon Nanoparticles during Laser-Induced Heating," Appl. Opt., **56**(11), p. E50.

[99] Sipkens, T. A., Singh, N. R., Daun, K. J., Bizmark, N., and Ioannidis, M., 2015, "Examination of the Thermal Accommodation Coefficient Used in the Sizing of Iron Nanoparticles by Time-Resolved Laser-Induced Incandescence," Appl. Phys. B, **119**(4), pp. 561–575.

[100] Daun, K. J., and Huberman, S. C., 2012, "Influence of Particle Curvature on Transition Regime Heat Conduction from Aerosolized Nanoparticles," Int. J. Heat Mass Transf., **55**, pp. 7668–7676.

[101] Daun, K. J., 2009, "Thermal Accommodation Coefficients between Polyatomic Gas Molecules and Soot in Laser-Induced Incandescence Experiments," Int. J. Heat Mass Transf., **52**(21–22), pp. 5081–5089.

[102] Daun, K. J., Titantah, J. T., and Karttunen, M., 2013, "Erratum to : Molecular Dynamics Simulation of Thermal Accommodation Coefficients for Laser-Induced Incandescence Sizing of Nickel Particles," pp. 599–600.

[103] Krishnan, S., Yugawa, K. J., and Nordine, P. C., 1997, "Optical Properties of Liquid Nickel and Iron," Phys. Rev. B, **55**(13), pp. 8201–8206.

[104] Shvarev, K. M., Baum, B. A., and Gel'd, P. V., 1975, "Optical Properties and Electronic Characteristics of Liquid Solutions of Nickel in Silicon," Sov. Phys. J., **18**(4), pp. 521–524.

[105] Daun, K. J., 2016, "Discussion of 'Normal Spectral Emissivity Measurement of Liquid Iron and Nickel Using Electromagnetic Levitation in Direct Current Magnetic Field.,'" Metall. Mater. Trans. A Phys. Metall. Mater. Sci., **47**(7), pp. 3300–3302.

[106] Sipkens, T. A., Menser, J., Mansmann, R., Schulz, C., and Daun, K. J., 2019, "Investigating Temporal Variation in the Apparent Volume Fraction Measured by Time-Resolved Laser-Induced Incandescence," Appl. Phys. B, **125**, p. 140.

[107] Gurentsov, A. V. ., and Eremin, E. V., 2015, "Sizing of Mo Nanoparticles Synthesised by Kr – F Laser Pulse Photo-Dissociation of Mo(CO)6," Appl. Phys. A Mater. Sci. Process., **119**, pp. 615–622.

[108] Altman, I., 2021, "Comment on 'Multiphoton Induced Photoluminescence during Time-Resolved Laser-Induced Incandescence Experiments on Silver and Gold Nanoparticles,'" J. Appl. Phys., **130**, p. 046101.

[109] Sorensen, C. M., 2001, "Light Scattering by Fractal Aggregates: A Review," Aerosol Sci. Technol., **35**(2), pp. 648–687.

[110] Filippov, A. V., Zurita, M., and Rosner, D. E., 2000, "Fractal-like Aggregates: Relation between Morphology and Physical Properties," J. Colloid Interface Sci., **229**, pp. 261–273.

[111] Liu, F., and Smallwood, G. J., 2010, "Effect of Aggregation on the Absorption Cross-Section of Fractal Soot Aggregates and Its Impact on LII Modelling," J. Quant. Spectrosc. Radiat. Transf., **111**(2), pp. 302–308.

[112] Watson, K. M., 1943, "Thermodynamics of the Liquid State," Ind. Eng. Chem., **35**(4), pp. 398–409.

[113] Liu, F., Daun, K. J., Snelling, D. R., and Smallwood, G. J., 2006, "Heat Conduction from a Spherical Nano-Particle: Status of Modeling Heat Conduction in Laser-Induced Incandescence," Appl. Phys. B, **83**(3), pp. 355–382.

[114] Hixson, R. S., Winkler, M. A., and Hodgdon, M. L., 1990, "Sound Speed and Thermophysical Properties of Liquid Iron and Nickel," Phys. Rev. B, **42**(10), pp. 6485–6491.

[115] Paradis, P. F., Ishikawa, T., and Yoda, S., 2002, "Noncontact Measurements of Thermophysical Properties of Molybdenum at High Temperatures," Int. J. Thermophys. 2002 232, **23**(2), pp. 555–569.

[116] Desai, P. D., 1986, "Thermodynamic Properties of Iron and Silicon," J. Phys. Chem. Ref. Data, **15**(3), p. 983.

[117] Dean, J. A., 1999, *Lange's Handbook of Chemistry*, Mcgraw-Hill, Inc.

[118] Young, D. A., and Alder, B. J., 1971, "Critical Point of Metals from the van Der Waals Model," Phys. Rev. A, **3**(1), pp. 364–371.

[119] Keene, B. J., 1988, "Review of Data for the Surface Tension of Iron and Its Binary Alloys," Int. Mater. Rev., **33**(1).

[120] Lu, H. M., and Jiang, Q., 2005, "Surface Tension and Its Temperature Coefficient for Liquid Metals," J. Phys. Chem. B, **109**(32), pp. 15463–15468.

[121] Sorensen, C. M., Maughan, J. B., and Moosmüller, H., 2019, "Spherical Particle Absorption over a Broad Range of Imaginary Refractive Index," J. Quant. Spectrosc. Radiat. Transf., **226**, pp. 81–86.

[122] Rahaman, M. N., 2007, *Sintering of Ceramics*, CRC Press, Taylor & Francis Group, Missouri-Rolla, USA.

[123] Yangchuan, X., and Rosner, D. E., 1999, "Prediction of Spherule Size in Gas Phase Nanoparticle Synthesis," J. Nanoparticle Res., **1**(2), pp. 277–291.

[124] Eggersdorfer, M. L., Kadau, D., Herrmann, H. J., and Pratsinis, S. E., 2012, "Aggregate Morphology Evolution by Sintering: Number and Diameter of Primary Particles," J. Aerosol Sci., **46**, pp. 7–19.

[125] Eggersdorfer, M. L., Kadau, D., Herrmann, H. J., and Pratsinis, S. E., 2011, "Multiparticle Sintering Dynamics: From Fractal-Like Aggregates to Compact Structures," Am. Chem. Soc., **27**, pp. 6358–6367.

[126] Eggersdorfer, M. L., and Pratsinis, S. E., 2014, "Agglomerates and Aggregates of Nanoparticles Made in the Gas Phase," Adv. Powder Technol., **25**(1), pp. 71–90.

[127] Robinson-enebeli, S. C., 2021, "Investigating Laser-Nanoparticle Interactions Using Time-Resolved Laser-Induced Incandescence," University of Waterloo.

[128] Tabrizi, N. S., Ullmann, M., Vons, V. A., Lafont, U., and Schmidt-Ott, A., 2008, "Generation of Nanoparticles by Spark Discharge," J. Nanoparticle Res. 2008 112, **11**(2), pp. 315–332.

[129] Rasband, W. S., "Image J," U. S. Natl. Institutes Heal. Bethesda, Maryland, USA, pp. 1997–2018.

[130] Samson, R. J., Mulholland, G. W., and Gentry1, J. W., 1987, "Structural Analysis of Soot Agglomerates," Langmuir, **3**, pp. 272–281.

[131] Mulholland, G. W., Bohren, C. F., and Fuller, K. A., 1994, "Light Scattering by Agglomerates: Coupled Electric and Magnetic Dipole Method," Langmuir, **10**, pp. 2533–2546.

[132] Deng, Y., Zhang, J., and Jiao, K., 2018, "Viscosity Measurement and Prediction Model of Molten Iron," Ironmak. Steelmak., **45**(8), pp. 773–777.

[133] Schönecker, S., Li, X., Johansson, B., Kwon, S. K., and Vitos, L., 2015, "Thermal Surface Free Energy and Stress of Iron," Sci. Rep., **5**(1), pp. 1–7.

[134] Wang, C., Baer, D. R., Amonette, J. E., Engelhard, M. H., Antony, J., and Qiang, Y., 2009, "Morphology and Electronic Structure of the Oxide Shell on the Surface of Iron Nanoparticles," J. Am. Chem. Soc., **131**(25), pp. 8824–8832.

[135] Askill, J., and Tomlin, D. H., 1963, "Self-Diffusion in Molybdenum," Philos. Mag., **8**(90), pp. 997–1001.

[136] Hodkin, E. N., Nicholas, M. G., and Poole, D. M., 1970, "The Surface Energies of Solid Molybdenum, Niobium, Tantalum and Tungsten," J. Less-Common Met., **20**(2), pp. 93–103.

[137] Paradis, P. F., Ishikawa, T., and Koike, N., 2007, "Non-Contact Measurements of the Surface Tension and Viscosity of Molybdenum Using an Electrostatic Levitation Furnace," Int. J. Refract. Met. Hard Mater., **25**(1), pp. 95–100.

[138] Wei, H., and Xu, H., 2013, "Hot Spots in Different Metal Nanostructures for Plasmon-Enhanced Raman Spectroscopy," Nanoscale, **5**(22), pp. 10794–10805.

[139] Robinson-Enebeli, S., Talebi-Moghaddam, S., and Daun, K. J., 2023, "Time-resolved Laser-induced Incandescence on Metal Nanoparticles : Effect of Nanoparticle Aggregation and Sintering," Appl. Phys. B, **129**(25).

[140] Doner, N., Liu, F., and Yon, J., 2017, "Impact of Necking and Overlapping on Radiative Properties of Coated Soot Aggregates," Aerosol Sci. Technol., **51**(4), pp. 532–542.

[141] Mackowski, D. W., and Mishchenko, M. I., 2011, "A Multiple Sphere T-Matrix Fortran Code for Use on Parallel Computer Clusters," J. Quant. Spectrosc. Radiat. Transf., **112**(13), pp. 2182–2192.

[142] Draine, B. T., and Flatau, P. J., 1994, "Discrete-Dipole Approximation For Scattering Calculations," J. Opt. Soc. Am. A, **11**(4), pp. 1491–1499.

[143] Liu, F., and Smallwood, G. J., 2011, "The Effect of Particle Aggregation on the Absorption and Emission Properties of Mono- and Polydisperse Soot Aggregates," Appl. Phys. B, **104**(2), pp. 343–355.

[144] Doner, N., and Liu, F., 2017, "Impact of Morphology on the Radiative Properties of Fractal Soot Aggregates," J. Quant. Spectrosc. Radiat. Transf., **187**, pp. 10–19.

[145] Mulholland, G. W., and Mountain, R. D., 1999, "Coupled Dipole Calculation of Extinction Coefficient and Polarization Ratio for Smoke Agglomerates," Combust. Flame, **119**, pp. 56–68.

[146] Yon, J., Liu, F., Bescond, A., Caumont-Prim, C., Rozé, C., Ouf, F. X., and Coppalle, A., 2014, "Effects of Multiple Scattering on Radiative Properties of Soot Fractal Aggregates," J. Quant. Spectrosc. Radiat. Transf., **133**, pp. 374–381.

[147] Quinten, M., 2001, "Local Fields Close to the Surface of Nanoparticles and Aggregates of Nanoparticles," Appl. Phys. B, **73**(3), pp. 245–255.

[148] Johnson, P. B., and Christy, R. W., 1974, "Optical Constants of Transition Metals: Ti, V, Cr, Mn, Fe, Co, Ni, and Pd," Phys. Rev. B, **9**(12), pp. 5056–5070.

[149] Shvarev, K. M.; Guschchin, V. S.; Baum, B., 1978, "The Effect of Temperature on Optical Constants of Iron," Teplofiz. Vys. Temp., **16**(3), pp. 520–525.

[150] Kreibig, U., and Vollmer, M., 1995, *Optical Properties of Metal Clusters*, Springer.

[151] Kreibig, U., 1974, "Electronic Properties of Small Silver Particles: The Optical Constants and Their Temperature Dependence," J. Phys. F Met. Phys., **4**, pp. 999–1014.

[152] Schäfer, J.-P., 2011, "Implementierung Und Anwendung Analytischer Und Numerischer Verfahren Zur Lösung Der Maxwellgleichungen Für Die Untersuchung Der Lichtausbreitung in Biologischem Gewebe," Universität Ulm.

[153] Mackowski, D. W., 1994, "Calculation of Total Cross Sections of Multiple-Sphere Clusters," J. Opt. Soc. Am. A, **11**(11), pp. 2851–2861.

[154] Draine, B. T., 1988, "The Discrete-Dipole Approximation and Its Application to Interstellar Graphite," Astrophys. J., **333**, pp. 848–872.

[155] Draine, B. T. ., and Flatau, P. J., 2020, *User Guide for the Discrete Dipole Approximation Code DDSCAT 7.3*.

[156] Markel, V. A., Muratov, L. S., Stockman, M. I., and George, T. F., 1991, "Theory and Numerical Simulation of Optical Properties of Fractal Clusters," Phys. Rev. B, **43**(10).

[157] Drachev, V. P., Perminov, S. V., Rautian, S. G., and Safonov, V. P., 2002, "Nonlinear Optical Effects and Selective Photomodification of Colloidal Silver Aggregates," Optical Properties of Nanostructured Random Media, Springer, Berlin, Heidelberg, pp. 113–148.

[158] Sorensen, C. M., Yon, J., Liu, F., Maughan, J., Heinson, W. R., and Berg, M. J., 2018, "Light Scattering and Absorption by Fractal Aggregates Including Soot," J. Quant. Spectrosc. Radiat. Transf., **217**, pp. 459–473.

[159] Stockman, M. I., 1997, "Inhomogeneous Eigenmode Localization, Chaos, and Correlations in Large Disordered Clusters," Phys. Rev. E, **56**(6), p. 6494.

[160] Safonov, V. P., Shalaev, V. M., Markel, V. A., Danilova, Y. E., Lepeshkin, N. N., Kim, W., Rautian, S. G., et al., 1998, "Spectral Dependence of Selective Photomodification in Fractal Aggregates of Colloidal Particles," Phys. Rev. Lett., **80**(5), pp. 1102–1105.

[161] Tsai, D. P., Kovacs, J., Wang, Z., Moskovits, M., Shalaev, V. M., Suh, J. S., and Botet, R., 1994, "Photon Scanning Tunneling Microscopy Images of Optical Excitations of Fractal Metal Colloid Clusters," Phys. Rev. Lett., **72**(26), pp. 4149–4152.

[162] Karpov, S. V, Gerasimov, V. S., Isaev, I. L., and Markel, V. A., 2005, "Local Anisotropy and Giant Enhancement of Local Electromagnetic Fields in Fractal Aggregates of Metal Nanoparticles," Phys. Rev. B - Condens. Matter Mater. Phys., **72**(20).

[163] Karpov, S. V., Gerasimov, V. S., Isaev, I. L., Podavalova, O. P., and Slabko, V. V., 2007, "The Origin of Anomalous Enhancement of Electromagnetic Fields in Fractal Aggregates of Metal Nanoparticles," Colloid J., **69**(2), pp. 159–169.

[164] Tong, Z., Li, S., Ruan, X., and Bao, H., 2019, "Comprehensive First-Principles Analysis of Phonon Thermal Conductivity and Electron-Phonon Coupling in Different Metals," Phys. Rev. B, **100**(14), p. 144306.

[165] Quinten, M., 1999, "Optical Effects Associated with Aggregates of Clusters," J. Clust. Sci., **10**(2), pp. 319–358.

[166] Eggersdorfer, M. L., and Pratsinis, S. E., 2013, "Restructuring of Aggregates and Their Primary Particle Size Distribution during Sintering," AIChE J., **59**(4), pp. 1118–1126.

[167] Sakat, E., Greffet, J.-J., Sauvan, C., Hugonin, J.-P., Besbes, M., and Wojszvzyk, L., 2018, "Enhancing Thermal Radiation with Nanoantennas to Create Infrared Sources with High Modulation Rates," Optica, **5**(2), pp. 175–179.

[168] Robinson-Enebeli, S., Schulz, C., and Daun, K. J., 2023, "Investigating the Absorption Properties of Metal Nanoparticle Aggregates during Time-Resolved Laser-Induced Incandescence.," Proceedings of the 10th International Symposium on Radiative Transfer, RAD-23, Begel House Inc., Thessaloniki, Greece, June 12–16, 2023, pp. 19–26.

[169] Coggon, J. H., 1985, "Electromagnetic and Electrical Modeling by the Finite Element Method.," Geophysics, **50**(11), pp. 132–155.

[170] Taflove, A., Hagness C., S., and Piket-May, M., 2004, "Computational Electromagnetics: The Finite-Difference Time-Domain Method," The Electrical Engineering Handbook, W.-K. Chen, ed., Elsevier Academic Press.

[171] Parsons, J., Burrows, C. P., Sambles, J. R., and Barnes, W. L., 2010, "A Comparison of Techniques Used to Simulate the Scattering of Electromagnetic Radiation by Metallic Nanostructures," J. Mod. Opt., **57**(5), pp. 356–365.

[172] Robinson-Enebeli, S., Schulz, C., and Daun, K. J., 2024, "Investigating the Absorption Properties of Metal Nanoparticle Aggregates during Time-Resolved Laser-Induced Incandescence," J. Quant. Spectrosc. Radiat. Transf., **322**, p. 109009.

[173] Sorensen, C. M., and Roberts, G. C., 1997, "The Prefactor of Fractal Aggregates," J. Colloid Interface Sci., **186**(2), pp. 447–452.

[174] Robinson-Enebeli, S., and Daun, K. J., 2021, "Effective Wavelength Data Arrangement for Time-Resolved Laser-Induced Incandescence Inference," NanoOntario, Remote/Online November 2021.

[175] Alba-Molina, D., Martín-Romero, M. T., Camacho, L., and Giner-Casares, J. J., 2017, "Ion-Mediated Aggregation of Gold Nanoparticles for Light-Induced Heating," Appl. Sci., **7**, p. 916.

[176] James, D. W., and Leak, G. M., 1965, "Grain Boundary Diffusion of Iron, Cobalt and Nickel in Alpha-Iron and of Iron in Gamma-Iron," Philos. Mag., **12**(117), pp. 491–503.

[177] Siegel, R. W., 1978, "Vacancy Concentrations in Metals," J. Nucl. Mater., **69**–**70**(C), pp. 117–146.

[178] Goulay, F., Schrader, P. E., Lopez-Yglesias, X., and Michelsen, H. A., 2013, "A Data Set for Validation of Models of Laser-Induced Incandescence from Soot: Temporal Profiles of LII Signal and Particle Temperature," Appl. Phys. B, **112**(3), pp. 287–306.

[179] Yi, J., Betrancourt, C., Darabiha, N., and Franzelli, B., 2023, "Initial Interpretation of Laser-Induced Incandescence (LII) Signals from Flame-Generated TiO2 Particles: Towards a Quantitative Characterization of the Flame Synthesis Processes," Appl. Energy Combust. Sci., **15**, p. 100190.

[180] Yi, J., Betrancourt, C., Darabiha, N., and Franzelli, B., 2023, "Characterization of Laser-Induced Emission of High-Purity TiO 2 Nanoparticles: Feasibility of Laser-Induced Incandescence," Appl. Phys. B, **129**(97).

[181] Hadwin, P. J., Sipkens, T. A., Thomson, K. A., Liu, F., and Daun, K. J., 2017, "Quantifying Uncertainty in Auto-Compensating Laser-Induced Incandescence Parameters Due to Multiple Nuisance Parameters," Appl. Phys. B, **123**(4), p. 114.

[182] Vander Wal, R. L., 1998, "Soot Precursor Carbonization: Visualization Using LIF and LII and Comparison Using Bright and Dark Field TEM," Combust. Flame, **112**(4), pp. 607–616.

[183] Goulay, F., Nemes, L., Schrader, P. E., and Michelsen, H. A., 2010, "Spontaneous Emission from C2(d 3Πg) and C3(A 1Πu) during Laser Irradiation of Soot Particles," Mol. Phys., **108**(7–9), pp. 1013–1025.

[184] Maffi, S., De Iuliis, S., Cignoli, F., and Zizak, G., 2011, "Investigation on Thermal Accommodation Coefficient and Soot Absorption Function with Two-Color Tire-LII Technique in Rich Premixed Flames," Appl. Phys. B, **104**, pp. 357–366.

[185] Cenker, E., Bruneaux, G., Dreier, T., and Schulz, C., 2015, "Determination of Small Soot Particles in the Presence of Large Ones from Time-resolved Laser-induced Incandescence," Appl. Phys. B, **118**(2), pp. 169–183.

[186] Hadwin, P. J., Sipkens, T. A., Thomson, K. A., Liu, F., and Daun, K. J., 2016, "Quantifying Uncertainty in Soot Volume Fraction Estimates Using Bayesian Inference of Auto-Correlated Laser-Induced Incandescence Measurements," Appl. Phys. B, **122**(1), pp. 1–16.

[187] Kock, B. F., Tribalet, B., Schulz, C., and Roth, P., 2006, "Two-Color Time-Resolved LII Applied to Soot Particle Sizing in the Cylinder of a Diesel Engine," Combust. Flame, **147**(1–2), pp. 79–92.

[188] Fried, L. E., and Howard, W. M., 2000, "Explicit Gibbs Free Energy Equation of State Applied to the Carbon Phase Diagram," Phys. Rev. B - Condens. Matter Mater. Phys., **61**(13), pp. 8734–8743.

[189] Leider, H. R., Krikorian, O. H., and Young, D. A., 1973, "Thermodynamic Properties of Carbon up to the Critical Point," Carbon N. Y., **11**(5), pp. 555–563.

[190] Bescond, A., Yon, J., Ouf, F. X., Rozé, C., Coppalle, A., Parent, P., Ferry, D., et al., 2016, "Soot Optical Properties Determined by Analyzing Extinction Spectra in the Visible Near-UV: Toward an Optical Speciation According to Constituents and Structure," J. Aerosol Sci., **101**, pp. 118–132.

[191] Bladh, H., and Bengtsson, P. E., 2004, "Characteristics of Laser-Induced Incandescence from Soot in Studies of a Time-Dependent Heat- and Mass-Transfer Model," Appl. Phys. B, **78**(2), pp. 241–248.

[192] Mobtil, M., and Lemaire, R., 2012, "Modeling Laser-Induced Incandescence of Soot Integrating Spatial and Temporal Dependences of Parameters Involved in Energy and Mass Balances," Proceedings of the 5th International Workshop and Meeting on Laser-Induced Incandescence, LII2012, CEUR Workshop Proceedings, Ed., Code 101856, Le Touquet Paris-Plage, France, May 8–11 2012, 865.

[193] Liu, F., Rogak, S., Snelling, D. R., Saffaripour, M., Thomson, K. A., and Smallwood, G. J., 2016, "Effects of Laser Fluence Non-Uniformity on Ambient-Temperature Soot Measurements Using the Auto-Compensating Laser-Induced Incandescence Technique," Appl. Phys. B, **122**(11), p. 286.

[194] Tian, K., Liu, F., Thomson, K. A., Snelling, D. R., Smallwood, G. J., and Wang, D., 2004, "Distribution of the Number of Primary Particles of Soot Aggregates in a Nonpremixed Laminar Flame," Combust. Flame, **138**(1–2), pp. 195–198.

[195] Mansmann, R., Dreier, T., and Schulz, C., 2017, "Performance of Photomultipliers in the Context of Laser-Induced Incandescence," Appl. Opt., **56**(28), p. 7849.

[196] De Iuliis, S., Cignoli, F., and Zizak, G., 2005, "Two-Color Laser-Induced Incandescence (2C-LII) Technique for Absolute Soot Volume Fraction Measurements in Flames," Appl. Opt., **44**(34), pp. 7414–7423.

[197] Michelsen, H. A., Witze, P. O., Kayes, D., and Hochgreb, S., 2003, "Time-Resolved Laser-Induced Incandescence of Soot: The Influence of Experimental Factors and Microphysical Mechanisms," Appl. Opt., **42**(27), p. 5577.

[198] Liu, F., Smallwood, G. J., and Snelling, D. R., 2005, "Effects of Primary Particle Diameter and Aggregate Size Distribution on the Temperature of Soot Particles Heated by Pulsed Lasers," J. Quant. Spectrosc. Radiat. Transf., **93**, pp. 301–312.

[199] Robinson-enebeli, S., Schulz, C., and Daun, K. J., 2025, "Investigation of the Apparent Anomalous Cooling of Soot During Laser-Induced Incandescence," Proceedings of the 11th International Symposium on Radiative Transfer, RAD-25 Kuşadası Türkiye, 15–20 June 2025.

[200] Sipkens, T. A., and Daun, K. J., 2017, "Defining Regimes and Analytical Expressions for Fluence Curves in Pulsed Laser Heating of Aerosolized Nanoparticles," Opt. Express, **25**(5), pp. 5684–5696.

[201] Kiefer, J., Sommer, R., Danova, K., Popovska, N., and Leipertz, A., 2009, "Temporally Resolved Characterization of Iron Nanoparticles Using a Time-Resolved Laser Technique," Conference on Lasers and Electro-Optics/International Quantum Electronics Conference, Optica Publishing Group, Baltimore, Maryland United States 31 May–5 June 2009, p. JWA73.

[202] Mätzler, C., 2002, *MATLAB Functions for Mie Scattering and Absorption Version 2 MATLAB Functions for Mie Scattering and Absorption*.

[203] Kobatake, H., and Fukuyama, H., 2016, "Amendments to the Discussion on the Paper Entitled 'Normal Spectral Emissivity Measurement of Liquid Iron and Nickel Using Electromagnetic Levitation in Direct Current Magnetic Field,'" Metall. Mater. Trans. A Phys. Metall. Mater. Sci., **47**(7), pp. 3303–3304.

[204] Buffat, P., and Borel, J. P., 1976, "Size Effect on the Melting Temperature of Gold Particles," Phys. Rev. A, **13**(6), pp. 2287–2298.

Extended analyses and supporting data

The main text of the thesis makes several references to the contents in the appendices of the document. These contents provide additional information and details on some of the topics that are briefly discussed in the text. In particular, the contents of Appendix A supplement several discussions in the main text and the contents in Appendix B further develop the analysis of the influence of nonuniform fluence on the TiRe-LII data for iron nanoparticles.

Appendix A

Supplementary information

This appendix contains information that supplements the analysis presented across all thesis chapters.

A.1 Melting model for metal nanoparticles

As opposed to soot particles that mostly sublime before melting at temperatures beyond 4450 K [92], most metal nanoparticles melt long before reaching their boiling point. Filippov *et al.* [65] note this and model melting with an expression similar to that of evaporation

$$q_{\mathrm{melt}} = \frac{\Delta H_{\mathrm{m}}\left(T_{\mathrm{p}}\right)}{M_{\mathrm{v}}} \frac{\mathrm{d}m_{\mathrm{p,m}}}{\mathrm{d}t}\,, \tag{A.1}$$

where $\Delta H_{\mathrm{m}}(T_{\mathrm{p}})$ is the temperature-dependent molar enthalpy of melting, M_{v} is the molar mass of the evaporated material, where the subscript 'v' stands for vapor and $\mathrm{d}m_{\mathrm{p,m}}/\mathrm{d}t$ is the rate of mass conversion from solid to liquid state (*i.e.*, the rate of phase transition). However, they do not provide an expression for $\mathrm{d}m_{\mathrm{p,m}}/\mathrm{d}t$; instead, the temperature of the nanoparticle is held constant until enough energy has been absorbed by (during heating) or removed from (during cooling) the nanoparticle, similar to the treatment

by Michelsen [92]. To determine a conservative estimate of the total energy required to completely melt the nanoparticle, Eq. (A.1) can be simplified to

$$q_{\mathrm{melt}} = \frac{\Delta H_{\mathrm{m}}\left(T_{\mathrm{p}}\right)}{M_{\mathrm{v}}} m_{\mathrm{tot}}\,, \tag{A.2}$$

where m_{tot} is the total mass of the aggregate before laser irradiation. Using the thermophysical properties: $M_{\mathrm{v}} = 55.85 \times 10^{-3}\,\mathrm{kg/mol}$ and $\Delta H_{\mathrm{m}} = 13.8 \times 10^{3}\,\mathrm{J/mol}$ [117], the required energy is in the order of 10^{-14} J, which is much less than the amount of energy deposited by the laser (10^{-10} J) within the first 1 ns. However, as shown in Figure A-1, melting temperatures are not reached until a significant amount of laser energy has been absorbed by the particle (q_{melt} is not included in the heat transfer model). This shows the highly dynamic nature of the irradiation process, *i.e.*, the energy required to melt the structure has been instantaneously deposited, but phase change and temperature increase require a finite time to take place, which ideally is described by $\mathrm{d}m_{\mathrm{p,m}}/\mathrm{d}t$ in Eq. (A.1). However, no reported measurement data has shown observable features of such phase transitions during LII experiments.

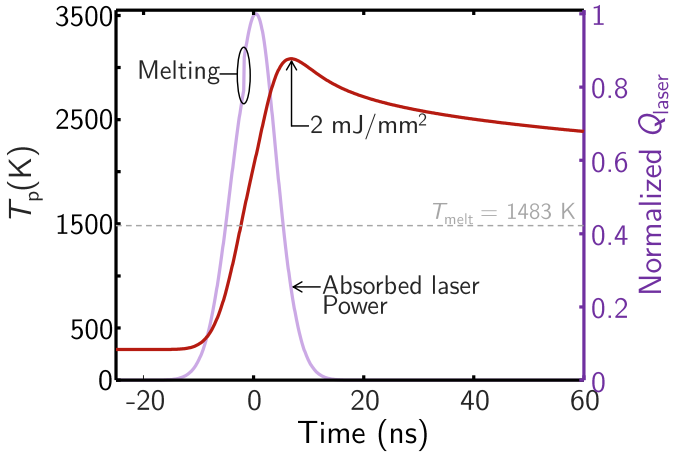


Figure A-1: Temporal temperature variation of a laser-irradiated iron aggregate ($N_{\mathrm{p}} = 135$) at 2 mJ/mm^2 (using Eq. (3.1)) compared to the absorbed laser energy, which shows the instant when melting is registered through change in mateiral properties. The change in morphology upon melting is not

A.2 Peak temperatures of core–oxide nanoparticle structures

Some coalesced spark-discharge-generated iron nanoparticles showed signs of an oxide layer, as shown in Figure A-2a, likely due to exposure to air upon exiting the spark-discharge generator. The MATLAB

implementation of the Mie predicted absorption properties of a coated sphere was obtained from Ref. [202]. The oxide layer of the iron cores was assumed to be hematite (Fe_2O_3) with radiative properties obtained from Ref. [85]. The peak thermodynamic temperatures of spherical iron spheres were compared to those of iron spheres coated with a 2.5 nm thick layer of hematite, as shown in Figure A-2b. The oxide layer seems to enhance the absorption properties of the iron nanoparticles, causing them to reach higher temperatures. However, it is not clear whether the oxide layer would remain intact as the particle heats up rapidly, expands, and evaporates.

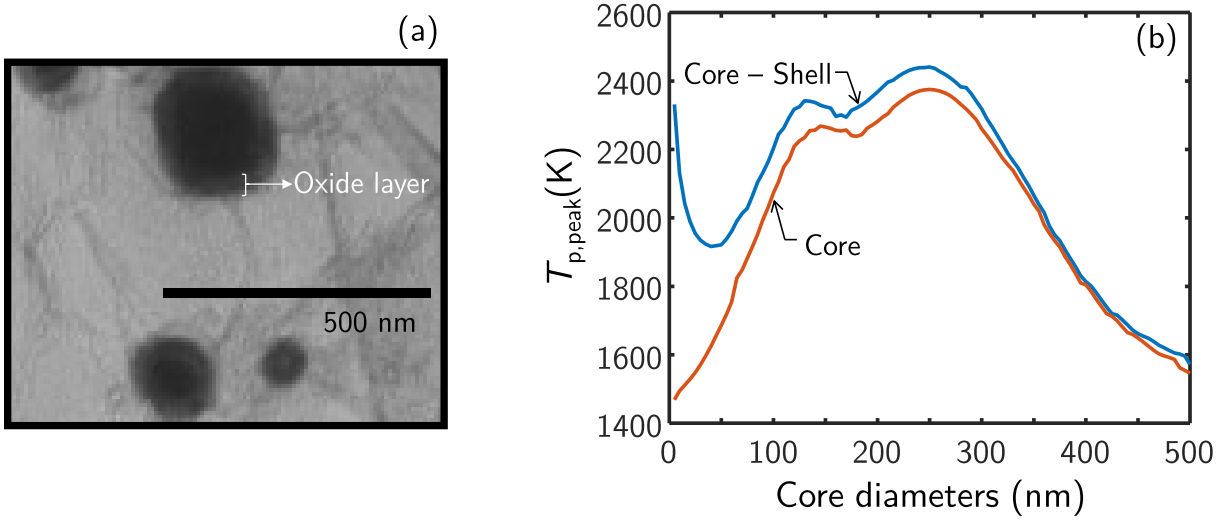


Figure A-2: (a) TEM micrograph of coalesced iron aggregates showing signs of an oxide layer, and **(b)** Comparing the thermodynamic peak temperatures of iron spheres to an iron core–shell structure with a 2.5 nm oxide laver thickness. Laser irradiation is assumed to be 2.45 mJ/mm^2.

A.3 Temperature history of molybdenum nanoparticles in different gases

Figure A-3 shows a 45 nm in diameter spherical molybdenum nanoparticle cooling down from a peak temperature of 4600 K in different gases. Similar to the experimental data in Figure 3-14b, the initial temperature decay in the different gases is similar and differs at later cooling times. This is due to the increasing dominance of conduction cooling, which differs by bath gas species.

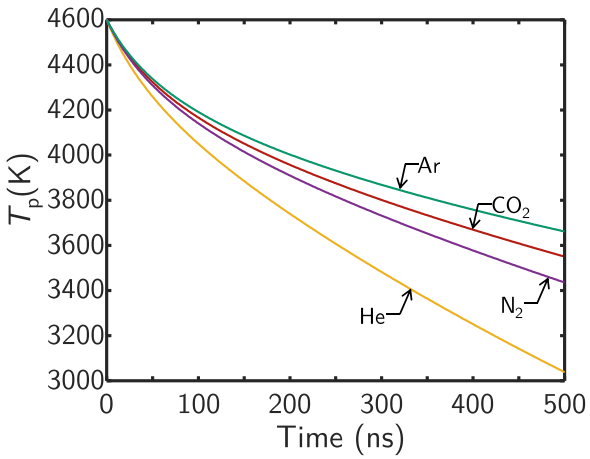


Figure A-3: A 45-nm diameter spherical molybdenum nanoparticle cooling down from peak temperature of 4600 K in different batch gases.

A.4 Refractive index of small particles

The computed temperatures depend on the spectral refractive index $\mathbf{m}_\lambda$ that is also used to compute $E(\mathbf{m}_\lambda)$. The primary particles within the spark discharge-generated aggregates are ~6nm in diameter, which may result in optical properties that differ from the bulk. At particle diameters smaller than 10 nm, the refractive index of the material may differ from the bulk due to changes in atomic structure or particle surface (caused by changes in electron localization or coordination number) [150]. To estimate the expected change for iron nanoparticles, a modified Drude model [150] is used to account for the increased collisions at the particle boundary,

$$\boldsymbol{\varepsilon}_{\mathrm{dp}} = \boldsymbol{\varepsilon}_{\mathrm{b}} + \omega_{\mathrm{p}}^2 \left[\frac{1}{\omega^2 + \Gamma_\infty^2} - \frac{1}{\omega^2 + \Gamma_{\mathrm{dp}}^2} \right] + \mathrm{i}\omega_{\mathrm{p}}^2 \left[\frac{\Gamma_{\mathrm{dp}}}{\omega\left(\omega^2 + \Gamma_{\mathrm{dp}}^2\right)} - \frac{\Gamma_\infty}{\omega\left(\omega^2 + \Gamma_\infty^2\right)} \right], \tag{A.3}$$

where $\varepsilon_{\mathrm{dp}}$ is the permittivity of the particle, a frequency, ω, modified from the permittivity of the bulk material ε_{b}, ω_{p} and Γ_∞ are the plasma and relaxation frequency of the bulk, respectively, and $\Gamma_{\mathrm{dp}} = 2A v_{\mathrm{F}}/d_{\mathrm{p}}$, is the relaxation frequency within the particle, A is a theory-dependent property on the order of 1, and v_{F} is the Fermi velocity. Values of ω_{p} and Γ_∞ are obtained from Ref. [203]. The permittivity of bulk iron is obtained from the refractive indices of bulk molten iron derived from ellipsometry [104]. Figure A-4 shows that, for iron nanoparticles with diameters greater than ~3 nm, the refractive indices do not differ significantly from those of the bulk; hence, in this work, it is assumed that the aggregate is molten upon

laser irradiation and uses measured data from ellipsometry for bulk molten iron obtained by Shvarev *et al.* [104].

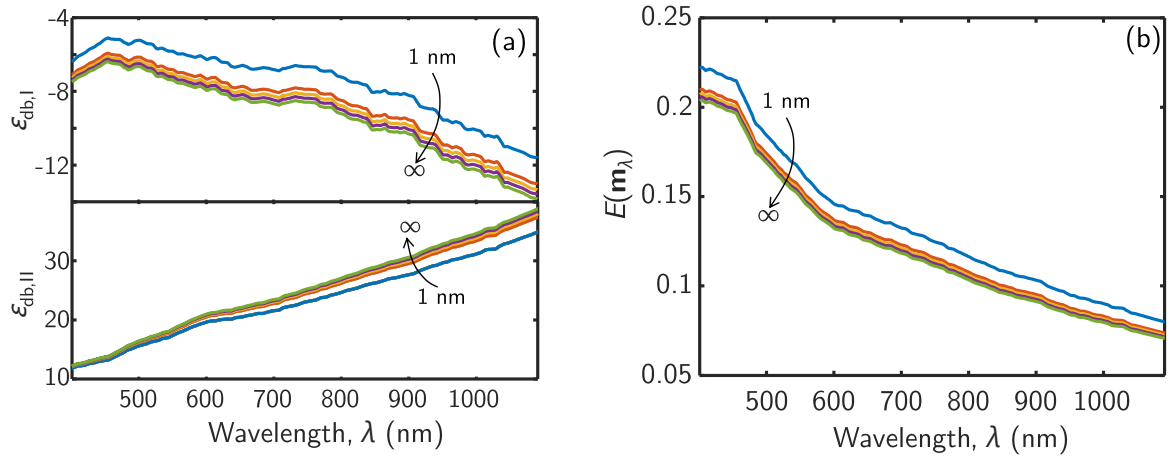


Figure A-4: (a) Size-dependent permittivity of iron nanoparticles computed from Eq. (A.3) **(b)** Corresponding absorption function. Data for particle diameters of 1, 3, 5, and 10 nm and bulk are shown.

A.5 Multisphere T-matrix method (MSTM) convergence study

When using the multisphere T-matrix method (MSTM) in the case of two touching spheres, with a size parameter $\ll 1$ and a large refractive index, it takes a large number of expansion orders to resolve the vector spherical harmonic expansion and reach convergence, *i.e.*, the inclusion of higher order terms [153] compared to, for example, soot that may require much less. Figure A-5 shows the number of higher-order terms needed to reach convergence when computing the absorption efficiency of a 70-primary particle iron aggregate irradiated at 1064 nm.

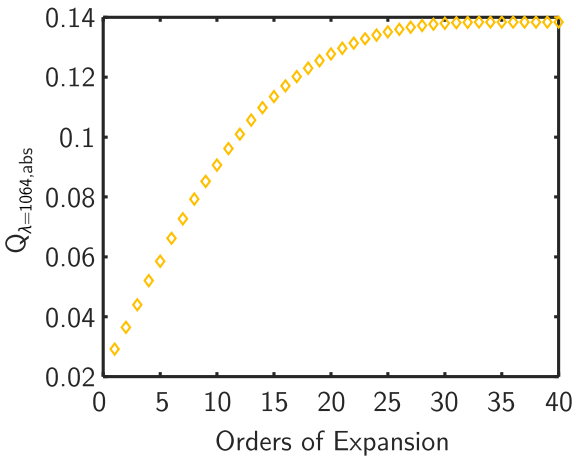


Figure A-5: MSTM computed absorption efficiency vs. number of orders of expansion required in the vector spherical harmonic expansion for a 70 primary-particle liquid iron aggregate.

As seen from Figure A-5, the results of $Q_{\text{abs},\lambda=1064}$ converge after about ~30 orders of expansion have been included. The exact number of expansion orders to reach convergence may vary depending on aggregate size and index of refraction. To strike a balance between computation effort and accuracy, 20 orders of magnitude are included in the calculations, which results in ~10 % difference relative to the highly converged result.

A.6 Discrete dipole approximation (DDA) mesh study

In addition to the requirement that the dipole spacing used in the discrete dipole approximation (DDA) calculation should be smaller than any structural features of the target structure, the dipole spacing should also follow the criteria: $|\mathbf{m}_\lambda|kd << 1$, where $\mathbf{m}_\lambda$ is the spectral refractive index of the material, $k = 2\pi/\lambda$ is the wavenumber, and d is the dipole spacing. These criteria are valid when $|\mathbf{m}_\lambda - 1| \lesssim 3$; however, when the refractive index is large, as in the case of metals, and the magnitude of the refractive index falls outside this range, much smaller dipole spacings are needed [155]. The DDA method tends to overestimate the absorption cross-section outside the valid range. Figure A-6 shows the evolution of the accuracy of DDA at different dipole spacings relative to the full Mie theory for a 6-nm diameter molten iron sphere.

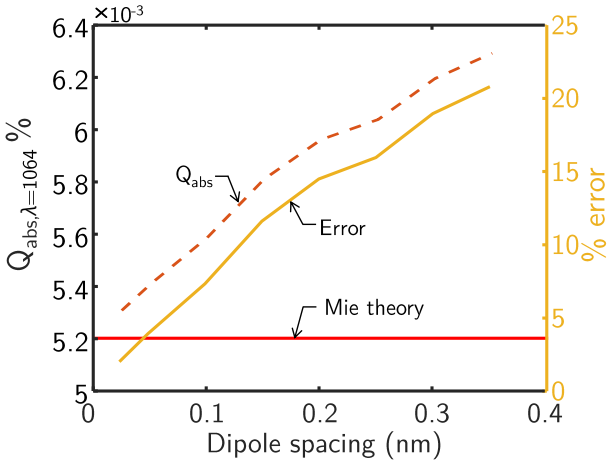


Figure A-6: Comparing the accuracy of the DDA method to that of Mie theory for a molten iron sphere with a diameter of 6 nm irradiated at 1064 nm. The refractive index of molten iron are used according to Ref. [104].

Significant computational efforts are required at smaller dipole spacings. For example, at a dipole spacing of 0.35 nm, the computation is completed in two minutes compared to three hours at a dipole spacing of 0.025 nm. While the results do not yet converge at smaller dipole spacing, the trend in Q_{abs} as a function of C_{OV} is consistent across dipole spacings. A dipole spacing of about 0.3 nm is chosen, which has a corresponding error of about 18 % according to Figure A-6. Other methods to compute light interactions with matter, such as the finite element method, have shown promise in producing more accurate results than DDA when investigating materials with high refractive indices [171].

A.7 Melting point depression

The melting point depression of the nanoparticles is calculated according to [204]

$$T_{\text{m,np}} = T_{\text{m,bulk}} \left(1 - \frac{2}{\rho_{\text{s}} \Delta H_{\text{m}} r_{\text{p,s}}} \left[\gamma_{\text{s}} - \gamma_{\text{l}} \left(\frac{\rho_{\text{s}}}{\rho_{\text{l}}} \right)^{2/3} \right] \right), \tag{A.4}$$

where $T_{\text{m,np}}$ is the melting point of the nanoparticles modified from the bulk value $T_{\text{m,bulk}}$, $r_{\text{p,s}}$ is the radius of the solid particle, ρ_{s} and γ_{s} are the density and surface tension of the material in the solid phase, and ρ_{l} and γ_{l} are the density and surface tension of the material in the liquid phase, and ΔH_{m} is the enthalpy of fusion. The melting point depression as a function of particle diameter is shown in Figure A-7.

A.8 Energy released from sintering

The energy released during the coalescence of an aggregate is computed by $\gamma_s \Delta A_s$, where γ is the surface energy and ΔA_s is the change of the surface area from an aggregate morphology to a sphere of equal mass. Using a temperature-dependent surface energy of γ_s [N/m] $= 1.826 - (T_p - T_m)\ 0.35\times10^{-3}$ N·m^{-1}·K^{-1}, where T_p and T_m are the temperature of the particle and the melting point [119], respectively; and using an aggregate with primary particle diameters ranging from 4–100 nm and a number of primary particles per aggregate of N_p = 10, 100, 200, 500, and 1000, the released energy is calculated (*cf.*, Figure A-7). For an aggregate with d_p = 6 nm and N_p = 200, the energy released after coalescence into a sphere is in the order of 10^{-14} J.

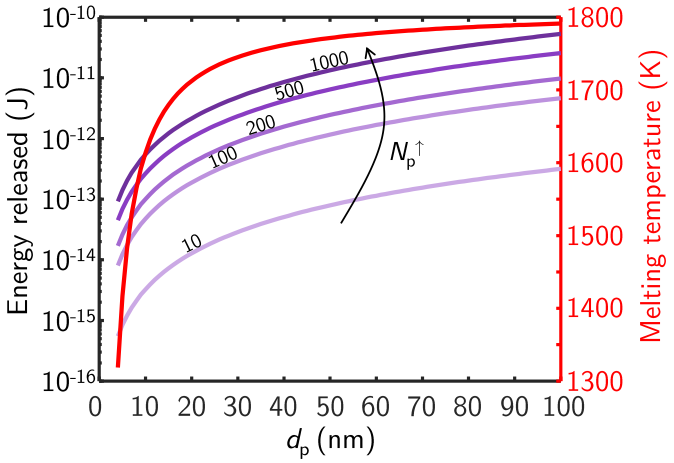


Figure A-7: The magnitude of energy released upon coalescence from aggregates with primary particle diameters ranging from 4–100 nm and N_p = 10, 100, 200, 500, and 1000, the energy released after coalescence. The melting point depression as a function of particle diameter is also shown.

A.9 Regression of the laser heating model to the LII signal

The current LII model is unable to predict the peak incandescence signal and temperature of iron nanoparticles for a given laser fluence and initial particle morphology, even when considering released surface energies. In particular, given the initial temperature of the aerosol and the laser fluence, there are no sets of QoIs including [d_p, σ, α] that can accurately model the measured signal, as shown in Figure A-8. This is mostly because there is no size distribution, at a particular fluence, that can model the observed peak temperatures, from which cooling begins. The analysis presented in Appendix B suggests that the consideration of nonuniformity in the laser fluence may improve the model and regression scheme.

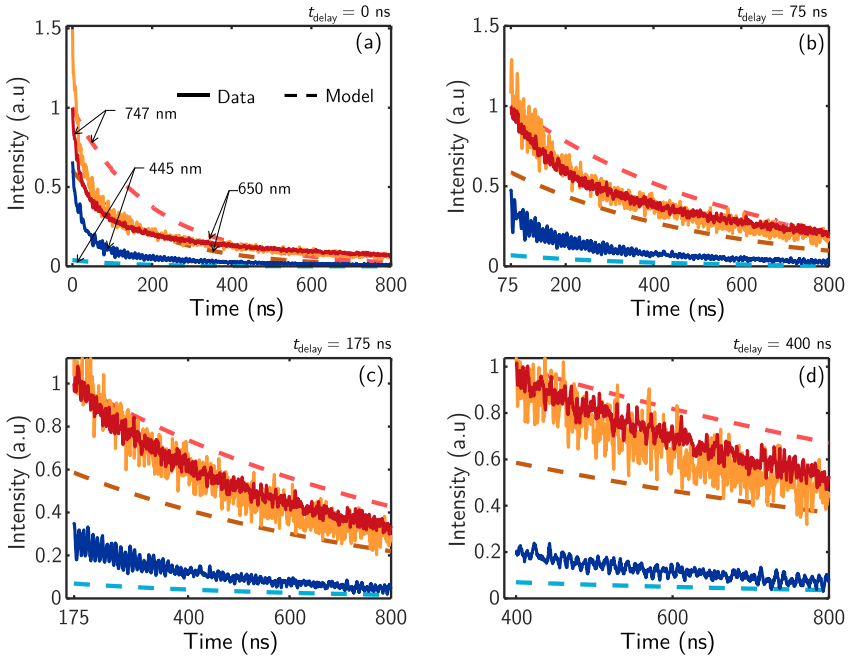


Figure A-8: Temporal variation of the LII signal for iron nanoparticles irradiated at varying laser fluence **(a)** Linear plot of signal detected at 747 nm. **(b)** Semi-logarithmic plot of the measured signal detected at 445 and 747 nm.

A.10 Sampling efficiency of soot particles

At a gas flow rate of 20 slm (standard liters per minute) through the venturi eductor, the amount of entrained into the probe volume increased with the molecular mass of the bath gas species, m_g, as indicated in Figure A-9, leading to a stronger signal as shown in Figure A-10. However, as confirmed by TEM micrographs shown in Figure A-11, this did not lead to significantly different levels of aggregation since the aerosol dilution is also increased for the heavier gases.

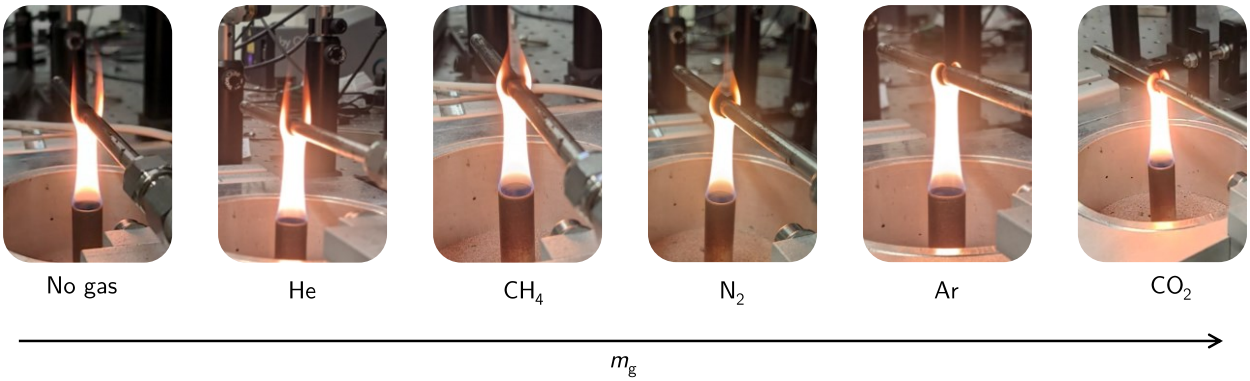


Figure A-9: Visual observation of the sampling efficiency of different bath gases.

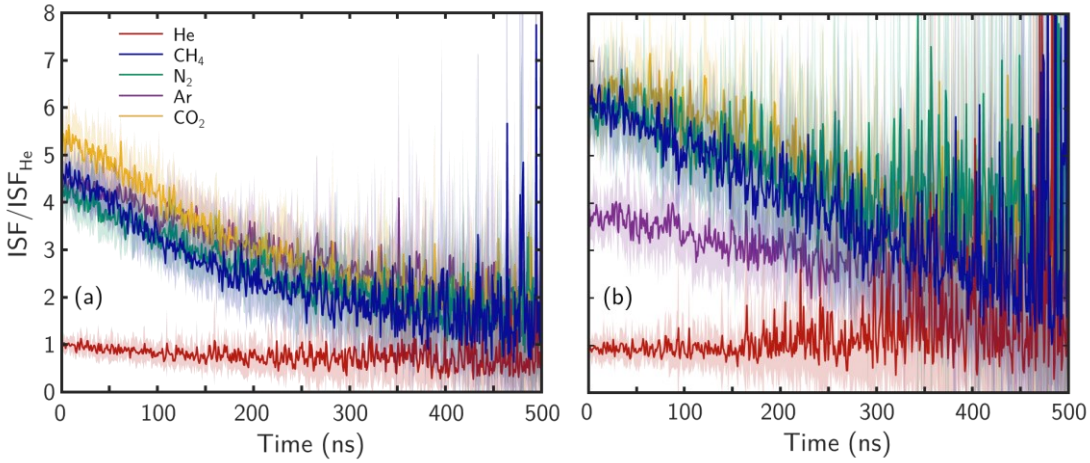


Figure A-10: Estimated soot volume fraction of soot aerosolized in differnt bath gases and irradiated with **(a)** a weakly nonuniform and **(b)** a strongly nonuniform fluence.

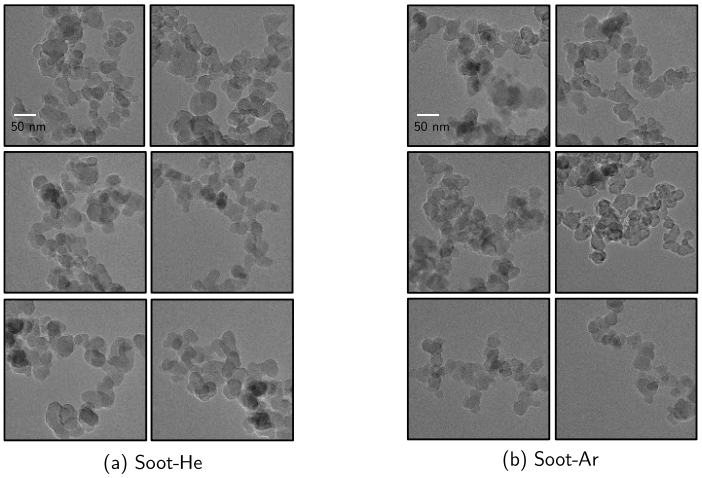


Figure A-11: TEM micrographs of soot aerosolized in **(a)** He and **(b)** Ar.

Appendix B

Influence of nonuniform fluences on iron nanoparticle pyrometric temperatures

The preliminary work presented in this appendix extends the analysis presented in Chapter 6 to include the influence of spatially nonuniform fluences during the LII experiments on iron nanoparticles. It is shown that, with the consideration of fluence variations across the laser cross-section, the model is able to regress well to the prompt data, hence showing model improvements from Chapter 5 and Appendix A.9.

B.1 Modeling the spatially nonuniform fluence for iron nanoparticles

The preliminary work presented in this appendix extends the analysis presented in Chapter 6 to include the influence of spatially nonuniform fluences during the LII experiments on iron nanoparticles. While it is typical to model the fluence distribution as top-hat, wide distributions in the fluence across the beam cross-section, combined with polydisperse particle distributions, reproduce the observed discrepancies between the TiRe-LII model and the measured data. Conditions in the probe volume involving wide or irregular distributions in fluence widen the temperature variations caused by particle polydispersity. It is shown that when all experimental variations are considered, quantities-of-interest (QoIs) that are more consistent with the ground truth can be inferred from the TiRe-LII experimental measurements.

The spectral incandescence model is modified to include the variation in fluence,

$$J_\lambda\left(t\right) = A_\lambda \Lambda \int_{F_\mathrm{o}} \int_{d_\mathrm{p}} p(F_\mathrm{o}) p(d_\mathrm{p}) C_{\mathrm{abs},\lambda}\left(\mathbf{m}_\lambda, d_\mathrm{p}\right) I_{\mathrm{b},\lambda}\left[T_\mathrm{p}\left(t, d_\mathrm{p}\right)\right] \mathrm{d}d_\mathrm{p}\, \mathrm{d}F_\mathrm{o}\,. \tag{B.1}$$

The measured incandescence is an integral of the various incandescence signals emitted from the probe volume due to the different diameters, d_p, and fluences, F_o, which are weighted by the corresponding probability density functions $p(d_\mathrm{p})$, and $p(F_\mathrm{o})$, respectively. Figure B-1 illustrates, for a 56-nm diameter particle, how the heat transfer and spectroscopic submodels are used to obtain pyrometric temperatures in this work. Observed discontinuities in the simulated signals and temperatures are a result of the change in

the refractive index upon melting or resolidification of the metal. Such discontinuities have not been observed in the data, since it is expected that, in reality, they would be blended out by the fact that the incandescence is emitted from the particle ensemble and at each instant, the particles have a distribution of temperatures. The appearance of the discontinuities in the simulated results may be a result of not using a large enough particle population size during simulations.

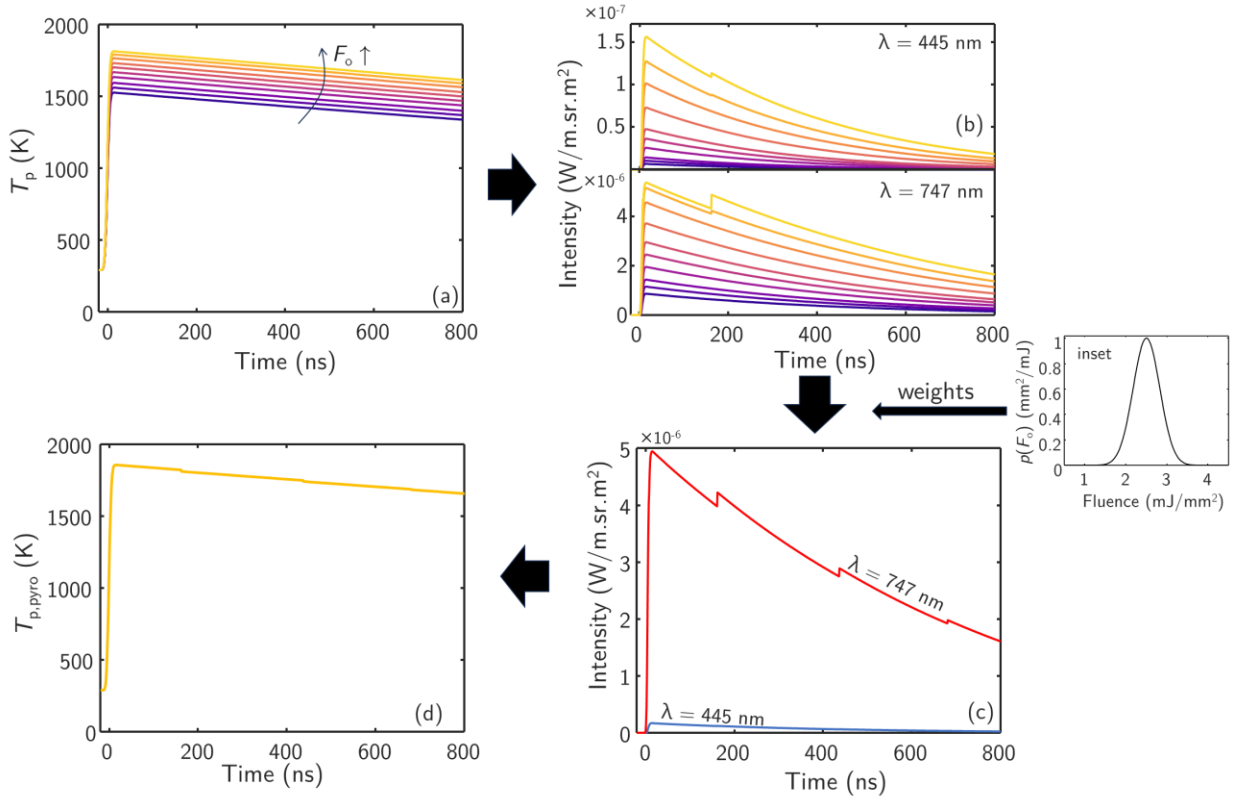


Figure B-1: Demonstrating the computation of the pyrometric temperatures using the condition of non-uniform fluence with uniform particle sizes (56 nm). Shown here: **(a)** Several temperature evolutions of the particles irradiated with the various fluences present in the probe volume; **(b)** incandescence emissions of the irradiated particles at detection wavelengths of 445 and 747 nm; **(c)** integrated intensity obtained from integrating incandescence emissions that have been weighted by the fluence distribution $p(F_o)$, shown in the inset; **(d)** the pyrometric temperature obtained from color pyrometry of the integrated incandescent emissions from a probe volume irradiated with a non-uniform fluence profile. The observed discontinuities in the temperature and intensity profiles are due to change in refractive index between the solid and liquid phases of iron.

Different distributions of laser fluence are considered, including a top-hat distribution, Gaussian distributions with standard deviations that are varying percentages of the mean fluence, and a distribution with "hot" and "cold" spots (here called irregular distribution) in the laser beam cross-section. All considered

fluence distributions have an average fluence of 2.5 mJ/mm². The Gaussian fluence distributions are equivalent to the "Gaussian beam" spatial distribution used by Bladh *et al.* [191], and the irregular distribution is comparable to the "double δ" fluence distribution described by Liu *et al.* [193]. Typical fluence distribution widths are also informed by experimental measurements by Liu *et al.* [193]. Figure B-2a shows the varying distributions, and Figure B-2b visually illustrates the fluence deviations within the probe volume.

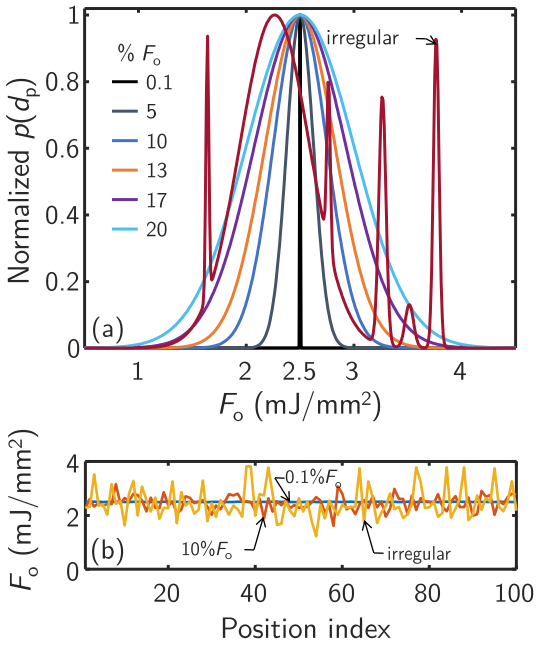


Figure B-2: (a) PDFs of different fluence distributions considered, and **(b)** a visual illustration of randomly sampled fluence values present in the probe volume for a top-hat, irregular and normal (σ = 10% F_o) distribution.

For a monodisperse size distribution of 56 nm, Figure B-3a shows the effective pyrometric temperatures resulting from the considered fluence distributions. As observed, the deviation between the effective pyrometric temperatures and those predicted by a uniform fluence increases as the distribution widths of the laser fluence widen, with the irregular fluence distribution producing the highest temperatures. Figure B-3b shows that the percent increase in the effective pyrometric temperature is as high as 25 % at the peak when "hot" and "cold" (*i.e.*, irregular fluence distribution) spots are considered.

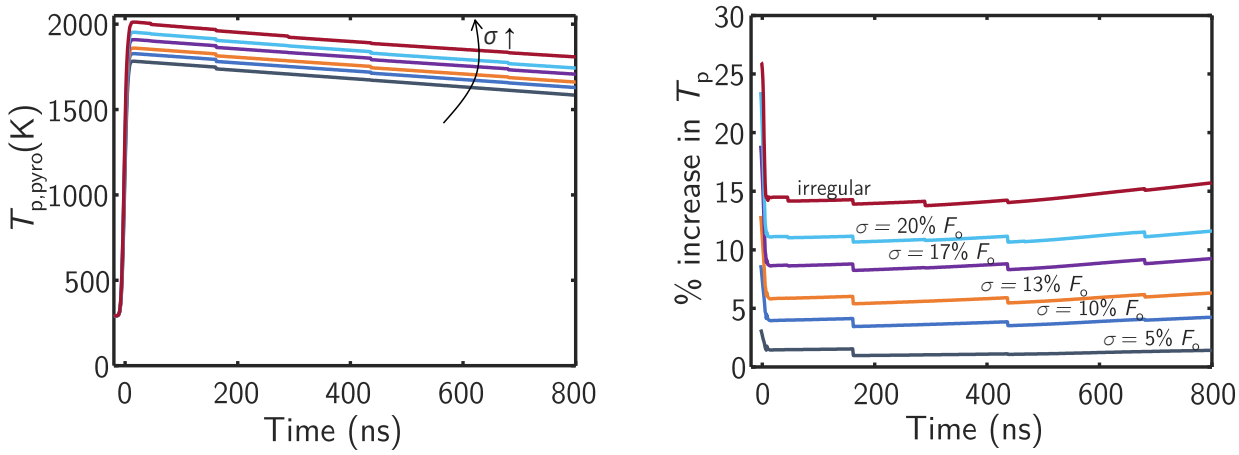


Figure B-3: (a) Temperature profiles of a monodisperse aerosol with particle diameters of 56 nm, irradiated with increasingly wide fluence distributions with a mean of 2.5 mJ/mm^2, and **(b)** the corresponding increase in the $T_{p,pyro}^{eff}$ for the different fluence distributions considered.

B.2 Combined effects of polydispersity and nonuniform fluence on the effective pyrometric temperature

Simulations considering both polydispersity and nonuniform laser fluence were performed with a diameter size distribution of ln$\mathcal{N}$(56 nm, 2) and the fluence distribution is taken as $\mathcal{N}$(2.5 mJ/mm^2, σ_F), where σ_F is about 13% of the mean fluence as determined from a typical laser fluence distribution [193]. The simulated effective pyrometric temperature is shown in Figure B-4 and is compared to the pyrometric temperatures for conditions of monodispersity and top-hat fluence profiles. Two monodisperse cases are considered with diameters at the mean of the lognormal distribution (56 nm) and above the mean of the distribution (200 nm). Two top-hat fluence profiles are also considered, including the mean of the Gaussian fluence distribution (2.5 mJ/mm^2) and about three standard deviations above the mean of the distribution (3.5 mJ/mm^2). For each of the conditions considered, the temperature profiles of the different size classes in different portions of the laser beam cross-section are shown in Figure B-5 along with the corresponding effective pyrometric temperature obtained from the temperature profiles.

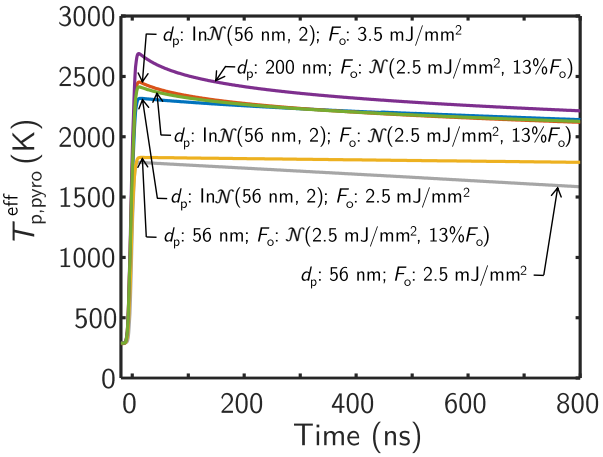


Figure B-4: Effective pyrometric temperatures of various conditions of mono- and polydispersity of the size distribution and uniform and nonuniform distribution of the laser fluence.

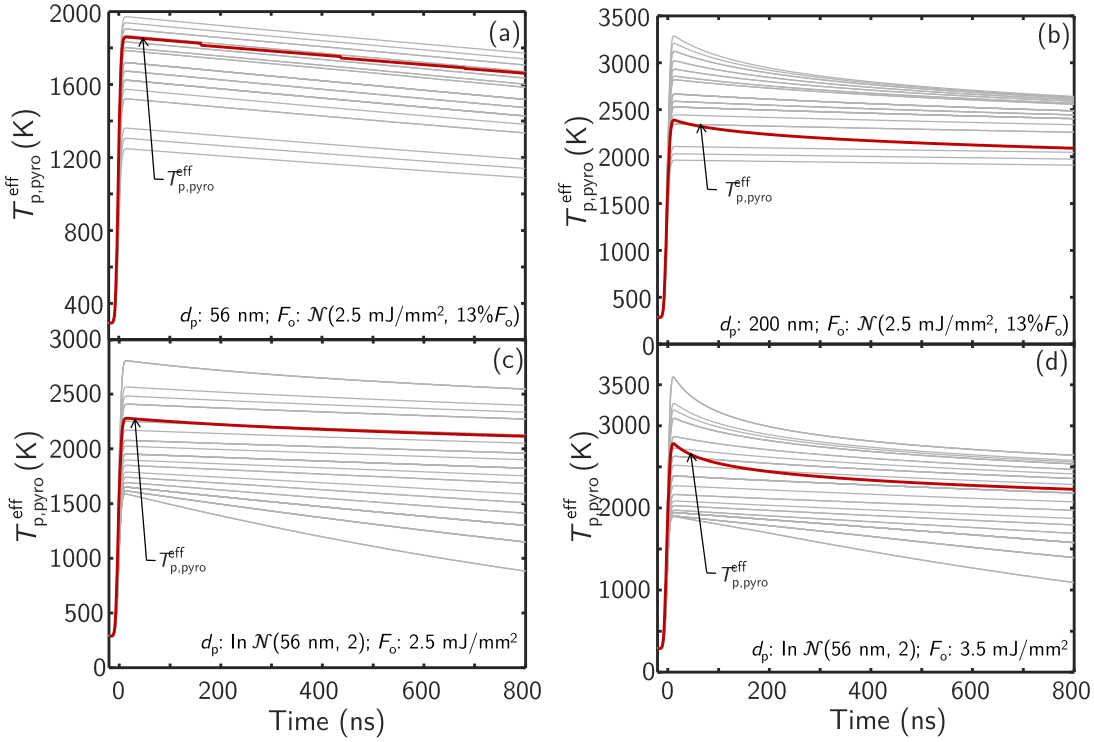


Figure B-5: The effective pyrometric temperature of different conditions of size and fluence distributions within the probe volume including a monodisperse aerosol with **(a)** 56 nm and **(b)** 200 nm particles in diameter and a normally distributed fluence of $\mathcal{N}(2.5\ \mathrm{mJ/mm^2}, 13\%\mathrm{F_o})$, and a top-hat laser fluence of **(c)** 2.5 mJ/mm^2 and **(d)** 2.5 mJ/mm^2 irradiating particles that distributed as ln$\mathcal{N}(56\ \mathrm{nm}, 2)$. The grey curves are the various size classes and fluence regions within the probe volume.

As shown in Figure B-4, for a monodisperse case of 56 nm irradiated with a non-uniform fluence ($\mathcal{N}$(2.5 mJ/mm^2, 13%F_o)), one would expect the peak pyrometric temperature to be lower than that of the overall effective pyrometric temperature (determined from the condition of ln$\mathcal{N}$(56 nm, 2) and $\mathcal{N}$(2.5 mJ/mm^2, 13%F_o)), and decay approximately linearly as a function of time following the peak temperature since temperatures remain below the point where evaporation cooling is dominant (~2600 K, as determined for a 56 nm diameter iron nanoparticle). This is also consistent with the case of uniform fluence at 2.5 mJ/mm^2 with polydispersity considered. On the other hand, for a monodisperse size distribution and uniform fluence higher than the means of the respective distributions (*i.e.*, 200 nm monodisperse distribution and 3.5 mJ/mm^2 top hat laser fluence profile), the peak temperatures are higher, compared to the overall effective pyrometric temperature, with significant evaporative cooling following the peak temperatures. This is a result of the particles in the different fluence regions and particles in larger size classes that reach higher temperatures (superheated in some cases, *i.e.,* higher than the boiling point of iron – 3135 K) as seen in Figure B-5. It is the contributions from such fluence regions and size classes that result in the overall effective pyrometric temperature exhibiting a rapid drop in temperature immediately following the peak temperature, similar to evaporative cooling, despite remaining below the threshold at which evaporative cooling is dominant for iron.

Upon further observation, the following features of the overall effective pyrometric temperature are evident:

i. The evaporation-like temperature decay below the dominant evaporative cooling threshold is consistent with the apparent "anomalous" cooling phenomenon, which was first reported for soot [27] and then for molybdenum and iron [19,172].
ii. The high temperatures of the overall effective pyrometric temperature profile compared to the expected pyrometric temperatures that do not consider nonuniformities in the particle diameters or fluence are consistent with the apparent excessive absorption phenomenon that is observed for metal nanoparticles [16,139,181].

These observations directly result from particles in the probe volume reaching temperatures above the dominant evaporative cooling threshold. These particles contribute to the emitted incandescence, which may manifest, at least in part, as the apparent anomalies in the experimentally measured effective pyrometric temperature. Note that while nonuniformities in particle distribution and fluences reproduce

features of the apparent anomalies, the effects of aggregation, field enhancements, aggregate sintering and coalescence have not been considered here. As established in previous chapters, these effects also contribute to the observed apparent anomalies and would likely exacerbate the features reproduced here.

B.3 Assessing the simulated fluence curve

The fluence curve has traditionally been a tool to assess the cooling regimes of the nanoparticle ensemble [200]. The three fluence regimes include the low fluence regime where the peak temperature of the particle linearly increases with laser fluence (conduction-dominated cooling), the high fluence regime where the peak temperature is independent of laser fluence and remains mostly constant (also referred to as the plateau regime; evaporation-dominated cooling), and the transition regime that exist between the low and high fluence regimes. While LII experiments on iron nanoparticles have shown that the plateau regime of synthesized iron nanoparticle ensembles begins at fluences of ~1 mJ/mm^2, the LII model has not been able to reproduce this behaviour even when polydispersity is considered (*cf.*, Figure 5-8). As seen in Figure B-6, additional consideration of nonuniform, normally distributed fluences also does not reproduce the experimentally observed plateau regime.

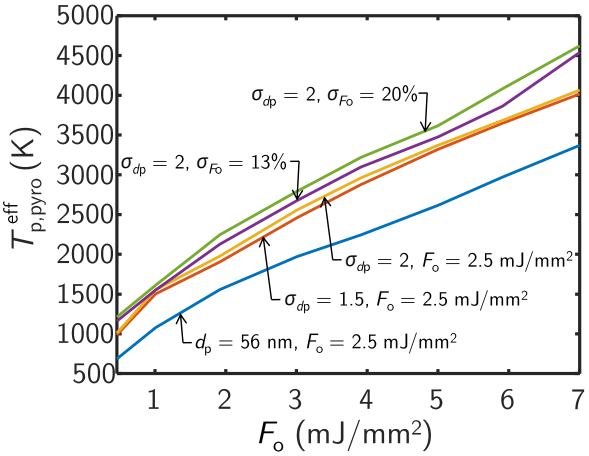


Figure B-6: Simulated fluence curves for different combinations of distributions in size and fluence. Polydisperse size distributions have a mean of 56 nm and nonuniform fluence distributions have a mean of 2.5 mJ/mm^2.

Figure B-6 also shows that the fluence curves are translated to higher temperatures as the distribution widths of the particle size and fluence widen. Since the standard LII models have reproduced the plateau regime for soot [193], it is possible that additional phenomena, not considered in this work, including aggregation and subsequent coalescence, may be a significant contributing factor to the measured

incandescence signal from metal nanoparticles. It may also be that other fluence distributions are more appropriate to reproduce the plateau regime.

B.4 Assessing the inference technique

In this section, the accuracy of the QoIs that are commonly inferred from the experimental TiRe-LII data is assessed for conditions where the fluence distribution is not considered in the model, as it is typically performed in the literature. The information on the fluence distribution is then included in the inference, and the QoIs are re-inferred.

TiRe-LII experimental signals from an iron aerosol are simulated by evaluating Eq. (5.1) at four detection wavelengths, namely, 445, 550, 650, and 747 nm, with normally distributed random noise characterized as 2 % of the peak signal. The particle size and fluence distribution were taken as $\ln\mathcal{N}(56$ nm, $\sigma_g)$ and $\mathcal{N}(2.5$ mJ/mm^2, $\sigma_F)$, respectively, and the TAC was 0.08 [19]. The simulated signals are regressed to Eq. (5.1) with the assumption of uniform fluence, following the inference strategy in Chapter 5 and Ref. [16]. Since the model is not regressed to the pyrometric temperatures, the procedure avoids the uncertainties and approximations introduced by pyrometry. The peaks of the signals are normalized to one of the detection wavelengths, and regression occurs from the signal peak. The free parameters are the particle diameter d_p, the geometric standard deviation of an assumed log-normal particle-size distribution, σ_g, the TAC, α, and the peak temperature from which the particles cool, T_{peak}. The QoI, T_{peak}, is a model parameter that acts as an effective peak temperature from which the particle ensemble cools. This treatment consequently imposes a uniform peak temperature for all particle size classes in the ensemble, similar to the procedure in Chapter 5. Priors are included for each of the QoIs.

The inference strategy is assessed for assumed experimental conditions of narrowly distributed particle diameters and fluences with σ_g and σ_F taken as 1.001 and $0.1\%F_o$ (approximately monodisperse with a uniform fluence), respectively, and for plausible experimental variations with σ_g and σ_F taken as 2 and $13\%F_o$, respectively. Figure B-7a and b show how well the inferred signals regress to the simulated experimental signals for the two conditions considered. For conditions of narrow distributions, the inferred signals regress quite well to the simulated experimental signals, while for the conditions of plausible experimental variations, the inferred signals do not accurately capture the signal decay in the first ~400 ns. This discrepancy between the inferred and experimental signals has been observed for nickel [16] and iron (*cf.*,

Figure 5-10) nanoparticles, which often leads to the exclusion of the first few nanoseconds following the peak signal (*i.e.*, prompt signals) from the inference. Additionally, Figure B-7b shows, for an iron aerosol, that the combined effects of widely distributed particle sizes and fluences significantly contribute to the rapid drop in experimental signals following the peak; a feature that cannot be captured by a model that does not consider fluence variations. Excluding this portion of the signal from the inference causes the loss of information on the size distribution and promotes the inference of narrow size distributions, as seen in Figure 5-11.

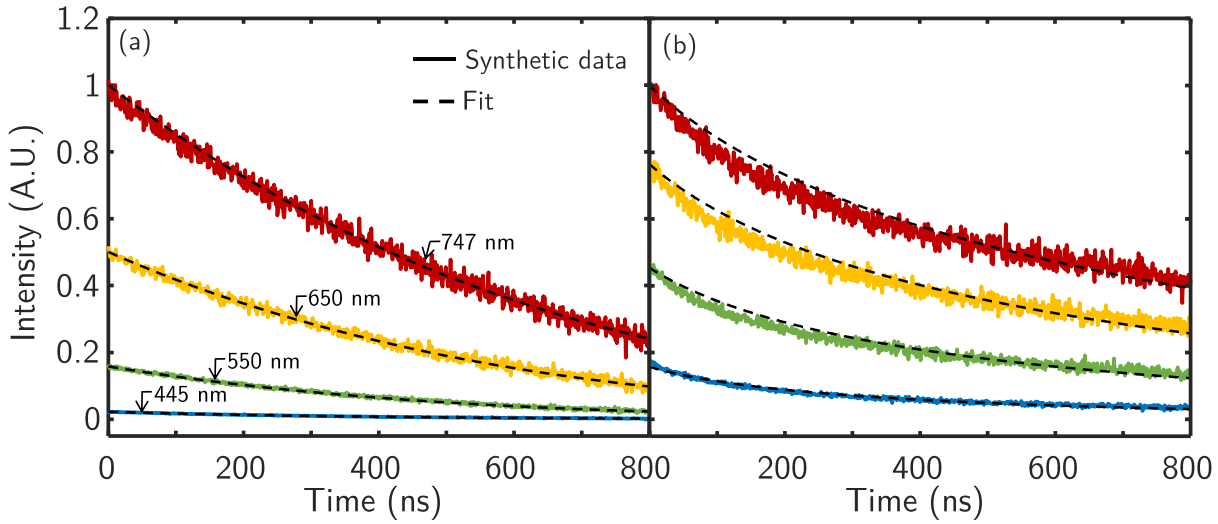


Figure B-7: Comparing the model fit to the synthetic data for **(a)** a narrow distribution in size, $\ln\mathcal{N}(56$ nm, 1.001) and fluence, $\mathcal{N}(2.5\text{mJ/mm}^2, 0.01\%F_\text{o})$, and **(b)** a wide distribution in size, $\ln\mathcal{N}(56$ nm, 2) and fluence, $\mathcal{N}(2.5\text{mJ/mm}^2, 13\%F_\text{o})$.

The inferred QoIs from the two conditions are shown in Table B-1 along with the percent differences ($T_\text{pv,thermo}$ is considered the ground truth temperature). As the recorded incandescence signal is a combination of all radiative emissions within the probe volume, from which the pyrometric temperature is generally determined, the task of unravelling the measured signal is strongly ill-posed. The following Gaussian priors were used for d_p, σ, α, and T_peak, respectively: $\mathcal{N}(50$ nm, 7.5), $\mathcal{N}(1.1, 0.165)$, $\mathcal{N}(0.1, 0.015)$, and $\mathcal{N}(1800, 270)$. The standard deviations of the priors were set to about 15% of the respective means. For the condition of narrow distributions, the inferred QoIs are fairly consistent with the true values. For the conditions of wide distributions in particle size and fluence, the inferred QoIs are less consistent with the true values, with a larger percentage difference compared to the case of narrow distributions in diameter and fluence. The leading cause of the increased difference is the assumption of a uniform fluence distribution.

Table B-1: Inferred QoIs with a narrow distribution in size, $\mathrm{In}\mathcal{N}(56\text{ nm}, 1.001)$ and fluence, $\mathcal{N}(2.5\text{mJ/mm}^2, 0.01\%F_\mathrm{o})$, and a wide distribution in size, $\mathrm{In}\mathcal{N}(56\text{ nm}, 2)$ and fluence, $\mathcal{N}(2.5\text{mJ/mm2}, 13\%F_\mathrm{o})$.

Simulation conditions	$d_\mathrm{p} \sim \mathrm{In}\mathcal{N}(56\text{ nm}, 1.001)$; $F_\mathrm{o} \sim \mathcal{N}(2.5\text{mJ/mm}^2, 0.01\%F_\mathrm{o})$		$d_\mathrm{p} \sim \mathrm{In}\mathcal{N}(56\text{ nm}, 2)$; $F_\mathrm{o} \sim \mathcal{N}(2.5\text{mJ/mm}^2, 13\%F_\mathrm{o})$	
	Point estimate	% Diff.	Point estimate	% Diff.
d_p (nm)	57	1.75	60	6.67
σ_g (-)	1.1	9	2.7	23
α (-)	0.084	4.76	0.21	60
T_peak (K)	1770	0.9	2785	10.2

However, when the fluence distribution across the laser cross-section is measured and considered in the regression, it is possible to regress to the experimental signals and capture the rapid decay following the peak temperature, as shown in Figure B-8. The same priors from the case of assumed uniform fluence were used here. Figure B-8 is obtained by simulating experimental signals with a fluence distribution of $\mathcal{N}(2.5$ mJ/mm^2, $13\%F_\mathrm{o})$, and the regression is performed such that for each set of QoIs – d_p, σ_g, α, the predicted signals are evaluated by integrating across all signals produced with the fluence distribution from the simulated signals. The simulated experimentally measured incandescence signal, including heat-up and cool-down, is regressed, with no need to infer a model peak temperature. This treatment eliminates the inaccuracies of imposing a uniform peak temperature, an approximation that hinders the inference of QoIs when the heat-up phase of the signals is considered (*cf.*, Appendix A.9). The inferred QoIs shown in Table B-2 are consistent with the true values. This suggests accurate QoIs can be inferred from TiRe-LII data when the model considers the possible variations in both particle size and fluence within the probe volume.

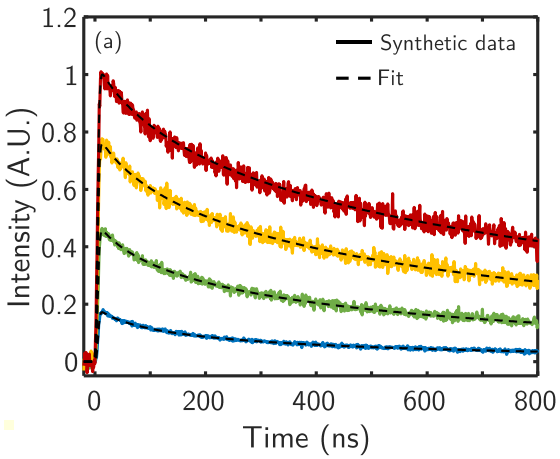


Figure B-8: Including the information on fluence distribution in the inference and comparing the fit to the synthetic data

Table B-2: Infered QoIs and associated percent difference when including the fluence distribution in the inference procedure.

	Point estimate	% Diff.
d_{p} (nm)	53	5.36
σ (-)	2.02	1
α (-)	0.89	10.11